UNIVERSITA' DEGLI STUDI DI CATANIA
Facoltá di Scienze Matematiche Fisiche e Naturali
Corso di Dottorato di Ricerca in Fisica, XIX Ciclo

Hyperon production at the HERMES experiment

Tutore Interno:
Prof. FRANCESCO RIGGI
Universitá degli studi di Catania

Tutore Esterno:
Prof. PAOLA FERRETTI DALPIAZ
Universitá degli studi di Ferrara

Dottorando:
CARMEN BONOMO

2004 - 2006

Contents

Chapter 1

Introduction

In this work, the production mechanism of strange-baryons in deep-inelastic scattering reactions is investigated. The aim is twofold. From one side to study the way confinement arises or how, in the hadronization process, the quark struck by the beam probe is finally embedded in a new-type baryon. From the other side to measure basic quantities such as the photoproduction cross sections, which can be used to test predictions and constrain physics parameters of any model of hadronic interactions, or the fragmentation functions, which should be used when extracting the original partonic information from measured observables.

The analysis presented in this thesis has been performed at the HERMES experiment that is devoted to the investigation of the internal structure of the nucleons via the **Deep Inelastic Scattering** (DIS) process, in which a high energy lepton beam interacts with a nucleon target. The first DIS experiment was performed at SLAC (Stanford Linear Accelerator Center) in the late 1960s: the results of this experiment presented the first evidence for the point-like substructure of the nucleon [1].
The successes of the quark-parton model in interpreting the first Deep Inelastic Scattering results led, in 1972, to the formulation of **Quantum Chromo Dynamics** (QCD) [2], as a fundamental gauge theory of hadronic physics. QCD, the basic theory of the strong interactions, is at short distances a perturbation theory of the pointlike constituents of hadrons. Perturbative QCD (pQCD) is a highly sophisticated and well developed subject, and it is widely accepted as the theory of high energy scattering processes.
The phenomenology of strong interactions contains two fundamental ingredients: *asymptotic freedom* and the *confinement* of colour charges. The *confinement* conjecture is originated from the experimental evidence that quarks and gluons appear to be *confined* in nature. This means that only hadrons, leptons and photons but no quarks or gluons are observed in experiments. There is pretty good evidence for this conjecture from experimental facts, as the Regge trajectories,or quarkonia spectra interpreted in the lattice string models (see Chapter4). Today almost no one seriously doubts that quantum chromodynamics confines quarks. Nevertheless, there is as yet no consensus amongst theorists about the mechanism that is responsible for *confinement* . From the other hand, the belief that QCD is a well grounded theory at all distance scales, rests on the hypothesis of *confinement* , that is probably the leading outstanding problem in hadronic physics.

Hadronic physics can be divided into four regions of 'phase space':

1- very low energy

2- spectrum, or low energy

3- high energy, corresponding to small angles

4- high energy, corresponding to large angles.

Perturbative QCD describes high energy at large angles, and to a lesser extent at small angles (total cross sections and related processes). At very low energy QCD is a theory of pions and nucleons (and their strange counterparts), and is characterized by spontaneous symmetry breaking of the approximate chiral symmetry of QCD. At intermediate energy scales, or low energy, there is a complex scenario, with *e.g* hadron resonances, Regge trajectories, soft diffractions, hadronozation of the partons, just to name a few of many topics (An elementary introduction to the the string models and the Regge theory may be found in appendix A).
Thus, while the perturbative QCD has been very successful in describing the hard processes between the quasi-free quarks and gluons at short distances and time scales, it can not be applied in the domain of long distances, where the strong coupling constant α_s becomes large and perturbative expansions diverge. A way to explain how hadrons develop out of quarks and gluons is to use the **Factorization** concept. In this scenario, a QCD process, like DIS, is splitted into the hard partonic sub-process (the photon-quark scattering) calculable by pQCD, and the long range part related to the initial and final state particles. This second part, that can not be treated by pQCD, is studied through the definition of the *Parton Distribution Functions*, that describe the initial state nucleon, and the *Fragmentation Functions*, that describe the hadronization into the final state.
The above parametrizations represent a valid approximation in the study of a complex problem that can not be solved by using *first principles* alone. Therefore, it is desirable to test experimentally model assumptions, to gain control over approximations and, eventually, to derive low-energy effective Lagrangians from QCD.

Other phenomenologically important questions are posed in low-energy QCD that eagerly await an answer: is the same set of fundamental parameters (QCD coupling and quark masses) that describes for instance the hadron spectrum consistent with high energy QCD or is there place for new physics? Are all hadronic states correctly classified by the naïve quark model or do glueballs, hybrid states and molecules play a rôle? At what temperatures/densities does the transition to a quark-gluon plasma occur? What are the experimental signatures of quark-gluon matter? Can we solve nuclear physics on the quark and gluon level?

It is worthwhile to stress, however, that the physics at all distance scales is linked, and it is hard to find a situation, even within the relatively clean perturbative regime, where the non-perturbative effects do not enter. Furthermore, without understanding non-perturbative aspects of QCD, it can not be explained why pQCD works at all. The confinement problem is closely linked to the problem of vacuum structure. In the past decades, many explanations of the confinement mechanism have been proposed, most of which share the feature that topological excitations of the vacuum play a major rôle. A list of these theories includes the dual superconductor picture of confinement [3, 4], the centre vortex model [5], the instanton liquid model [6], and the anti-ferromagnetic vacuum [7]. All these interpretations have been explored in lattice studies, initiated in 1980 by Creutz [8]. The situation with respect to an anti-ferromagnetic vacuum is still somewhat inconclusive [9]. Instantons seem to be more vital for chiral symmetry related properties than for confinement [10]. Depending on the picture, the excitations giving rise to confinement are thought to be magnetic monopoles, instantons, dyons, centre vortices, etc. It is worthwhile to stress here that the above ideas are not completely disjoint and do not necessarily exclude each other. For instance, all the above mentioned topological excitations are found to be correlated with each other in numerical as well as analytical studies.

Despite all the efforts, a mathematically rigorous proof that QCD as the *microscopic* theory of *strong interactions* indeed gives rise to the *macroscopic* property of linear quark *confinement* as indicated by Regge trajectories and quarkonia spectra is, after more then thirty years, still lacking.

The difficulty in deriving infra-red properties of QCD illustrates that something qualitatively new is happening. Unlike in previously existing elementary physical theories, it is not possible to reduce everything down to two-body interactions but collective excitations of quark and gluon states have to be accounted for.

The Standard Model predicts a collective bulk phenomenon: the occurrence of phase transitions in quantum fields at characteristic energy densities. Within the framework of the Standard Model, the appearance of phase transitions involving elementary quantum fields is intrinsically connected to the breaking of fundamental symmetries of nature and thus to the origin of mass. In general, intrinsic symmetries of the theory, which are valid at high-energy densities, are broken below certain critical energy densities. Particle content and particle masses originate as a direct consequence of the symmetry-breaking mechanism. For the first time, excitations of the vacuum that are considered to be fundamental do not occur as initial or final states anymore.

Even before QCD was established as the fundamental theory of strong interactions it had been argued that the mass spectrum of resonance produced in hadronic collisions implies some form of critical behaviour at high temperature and/or density [11] The subsequent formulation of QCD and the oservation that QCD is an asymptotically free theory led to the suggestion that this critical behaviour is related to a phase transition [12]. Infact, the most fascinating aspect of QCD thermodynamics is the theoretically well supported expectation that strongly interacting matter can exist in different phases.

The existence of a phase transition to a new state of matter, the quark-gluon plasma, QGP, at high temperature has been convincingly demonstrated in lattice calculation. The lattice calculations predict that at a critical temperature of $\approx 170MeV$, corresponding to an energy density of $\epsilon_c \approx 1GeV fm^{-3}$ the hadronic matter undergoes a phase transition to a deconfined state of quarks and gluons. At this temperature, in addition, chiral symmetry is approximately restored and quark masses are reduced from their large effective values in hadronic matter to their small bare ones. At low temperature and large values of the chemical potential, the basic properties of the hadronic matter can be described in terms of nearly degenerate, interacting Fermi gases. In a degenerate Fermi gas an attractive interaction will lead to quark-quark pairing, and thus to the formation of a color superconducting phase [13] - [14]

This new theorethical approach affects crucially our current understanding of the Standard Model at low energy, and give a clue to the *confinement* puzzle, investigating the quarks and gluons *deconfinement* processes.

In nature it is already possible to obtain critical temperature or energy densities which reach and exceed the critical energy density ϵ_c, thus making possible the QCD phase transition, the only one predicted by the Standard Model that is within reach of experimental validation.

According to QCD a phase transition from hadronic matter to a deconfined quark phase should occur at a density of a few times nuclear matter saturation density. Consequently, the core of the more massive *neutron stars* is one of the best candidates in the Universe where such deconfined phase of quark and gluons matter could be found. The bulk properties and the internal structure of these stars chiefly depends upon the equation of state (EOS) of dense hadronic matter. Different models for the EOS of dense matter predict a neutron star maximum mass (M_{max}) in the range of 1.4 – 2.2 $M_\odot$, and a corresponding central density in range of 4 – 8 times the saturation density ($\rho_0 \sim 2.8 \times 10^{14}$g/cm^3) of nuclear matter (e.g. Shapiro & Teukolsky

1983; Haensel 2003). In the case of a star with $M \sim 1.4\ M_\odot$, different EOS models predict a radius in the range of 7 – 16 km (Shapiro & Teukolsky 1983; Haensel 2003; Dey et al. 1998).

In a simplistic picture the core of a neutron star is modeled as a uniform fluid of neutron rich nuclear matter in equilibrium with respect to the weak interaction (β-stable nuclear matter). However, due to the large value of the stellar central density and to the rapid increase of the nucleon chemical potentials with density, the presence of hevier particles is expected. Since the hevay quarks charm, bottom and top are to hevy to play any role in the vicinity of the phase transition, the strange quark mass, which is of the order of the phase-transition temperature, plays a decisive role in determining the nature of the transition at vanishing chemical potential μ_B (baryon-number density). Hyperons (Λ, Σ^-, Σ^0, Σ^+, Ξ^- and Ξ^0 particles) are, therfore, expected to appear in the inner core of the star.

The true nature of the ultra-dense compact *neutron stars* is considered one of the most fascinating enigma in modern astrophysics. Recently, the fluid oscillations governed by the Coriolis force, the r-modes[1], of rapidly rotating neutron stars have attracted much interest as posible sources of gravitational waves and mechanisms for regulating the spins of neutron stars . The bulk-viscosity of mixed netron-hyperon stars has been studied in an impressive number of recent publications [16]. It is worthwhile to note that several autors make use of the known hyperon production cross sections, in the EOS evaluation.

The critical energy density ϵ_c will be hopefully obtained in ultra-relativistic heavy-ion collisions. ALICE at LHC is designed to study the QGP in ultrarelativistic nucleus-nucleus interactions [17]. The STAR collaboration at RHIC is wondering on their results [18]. The theory-experiment comparison suggests that central Au+Au collisions at RHIC produce dense, rapidly thermalizing matter characterized by: (1) initial energy densities above the critical values predicted by lattice QCD for establishment of a Quark-Gluon Plasma (QGP); (2) nearly ideal fluid flow, marked by constituent interactions of very short mean free path, established most probably at a stage preceding hadron formation; and (3) opacity to jets. Many of the observations are consistent with models incorporating QGP formation in the early collision stages, and have not found ready explanation in a hadronic framework. However, the measurements themselves do not yet establish unequivocal evidence for a transition to this new form of matter.

It is, however, very interisting to notice that the interest to nucleus-nucleus collisions at incident energies $E_{lab} \simeq$ (10–40)A GeV has been recently revived, since the highest baryon densities [19, 20, 21] and highest relative strangeness [22, 23] at moderate temperatures are expected in this energy range. The onset of deconfinement is also expected in this domain. In particular, the energy-scan SPS program [24] is dedicated to the search for the onset of deconfinement in heavy-ion collisions. Moreover, a critical end point [25] of the QCD phase diagram may be accessible in these reactions [26, 27]. The above expectations motivated the project of the new accelerator facility FAIR at GSI [28], the heavy-ion program of which is precisely dedicated to study dense baryonic matter with the emphasis on the onset of deconfinement and the critical end point. The future SPS [29] and RHIC [30] programs are also devoted to the same problems. These programs will run even before FAIR.

This thesis is organized as follows: the framework of the Deep Inelastic Scattering and quark fragmentation is reviewed in Chapter3. In Chapter5 the HERMES experiment is introduced with its main components: the polarized target, the tracking and particle identification detectors of the spectrometer and the data acquisition and processing. Chapter4 gives an overview about the Monte Carlo tools used in the collaboration. Chapter6 and 7 are devoted to the analysis of

[1]See Ref. [15] for a recent review of the many physical and astrophysical issues related to the r-modes

the Λ ($\overline{\Lambda}$) and of the heavier hyperons, respectively. The inavriant masses are first reconstructed and then corrected for the background subtraction. The photoproduction cross sections are finally extracted.

Chapter 2

Strange Baryons: an historical overview

2.1 The discovery of the Strangeness

With the discovery in 1947 of the pion, which was assumed to provide the nuclear binding force, a relatively simple picture of elementary particles emerged. However this simple interpretation did not go unchallenged for long. In the same year, a cloud chamber picture of cosmic rays indicated the existence of new particles. The pictures showed a 'V-track', indicating the decay of a neutral particle, later identified with the Λ, into two charged particles. Two more strange particles, the Ξ^- and the Σ, were discovered shortly after the Λ. Since 1947, many observations of these new particles have been made in cosmic-ray studies.
The year 1952 was a milestone in particle physics. It saw the invention of a new type of detector, the bubble chamber, which was to dominate discoveries for the subsequent three decades; and it witnessed the first of a new breed of accelerators, the synchrotron, designed with the express purpose of creating man-made versions of the particles found in cosmic rays.
Experiments at accelerators allowed the physicists to fill the gaps in the pattern of particles that was beginning to emerge. The first particle to be discovered at an accelerator, the neutral pion, completed the pion family. Similarly, the neutral Ξ, when at last discovered in a bubble chamber, provided a partner for the negative Ξ, which had been found in cosmic rays. With increasing amount of energy at their disposal, experimenters also confirmed Dirac's theory of antimatter, finding antiparticles for each of the known particles.

In 1953, the first machine capable of producing the new particles, the Cosmotron, went into operation at the Brookhaven National Laboratory (BNL). This machine permitted a systematic study of the particle production and decay reactions. Both the cosmic-ray experiments and those done at accelerators showed the decay lifetimes of the new particles to be on the order of 10^{-10} sec, extremely long compared to the particle production time of 10^{-23} sec. To account for this discrepancy, the concept of associated production was suggested, according to which a Λ is produced along with another strange particle, such as the Kaon. Confirmation of this came in 1954 from the BNL experiments. This concept was formalized by Gell-Mann and Nishijima with the introduction of a 'strangeness' quantum number. The strangeness was taken to be conserved in strong nuclear interactions. That assumption implied that a particle produced with a certain strangeness would always be accompanied by a particle or particles totaling an equal but an opposite strangeness. If the strangeness quantum number were to be absolutely conserved, as is, for example, electric charge, the strange particle would be stable. The long decay lifetime of the newly observed particles indicated that strangeness is not conserved in weak interactions. Indeed, once created, two strange particles go their separate ways and usually decay via the weak force. The heavier strange particles, the Ξ^- and the Σ, can decay to lighter strange particles as long as overall strangeness is conserved. But the two lightest strange particles, the Kaon and the Λ, can not decay into lighter strange particles; instead they decay separately into non-strange particles. Thus, whereas electric charge is conserved always, strangeness leaks away when the weak force acts.

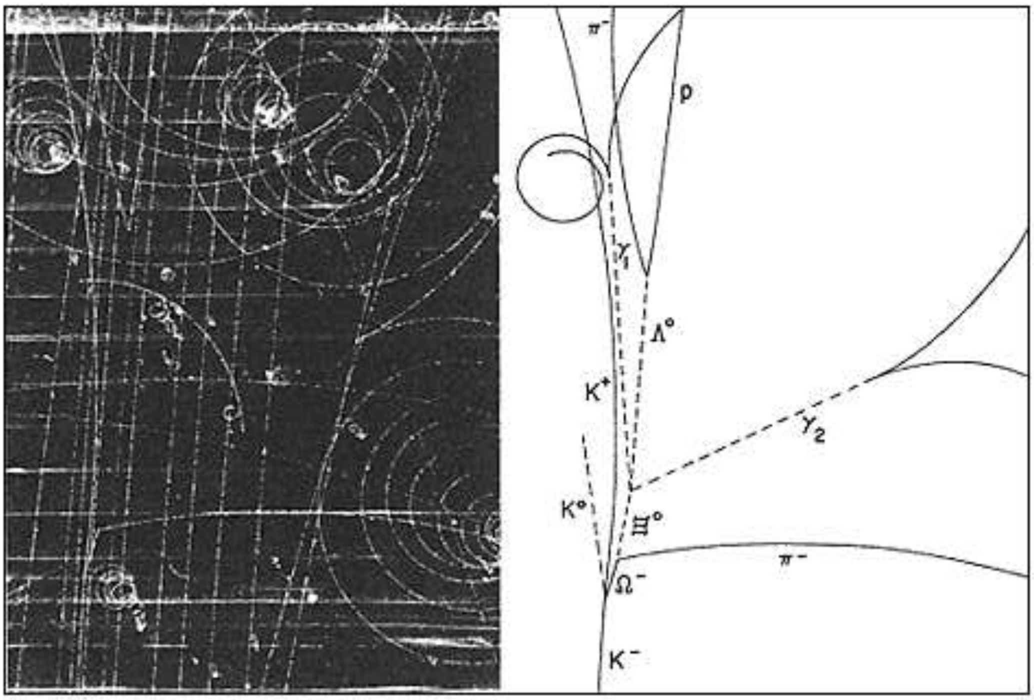

Figure 2.1: The bubble chamber picture of the first Ω^- observed. An incoming K^- meson interacts with a proton and produces an Ω^-, a K^0 and K^+ meson which all decay into other particles. The Ω^- decays into a negative pion and a Ξ^0, that in turn decays into two photons and a Λ particle. Neutral particles which produce no tracks in the chamber are shown by dashed lines.

In $1960-1$, Gell-Mann and Ne'eman independently proposed a method for classifying all the particles then known. This method became known as the *Eightfold Way*, as suggested by Gell-Mann. In the *Eightfold Way*, the particles are classified into 'families' according to their electric charge and their strangeness. Fig.2.2 shows two such families, one with eight members (an 'octect') and one with ten members (a 'decuplet'). Each particle has a particular position in its family, according to the amount of electric charge and strangeness the particle has. These properties, together with the particle's spin, completely define that particle in the *Eightfold Way*.

In 1962 the *Eightfold Way* was still very new and poorly understood by most of the theorists. The discovery of two new resonances, the Ξ^{*0} and the Ξ^{*0}, in 1962 and of the Ω^- in 1964 (see Fig.2.1) dramatically confirmed the predictive power of the strangeness scheme, which could now be used as a firm basis for ideas of a more fundamental nature.

The regularities such as that of the decuplet can be accounted for by postulating three types of fermions constituent in a baryon, called **quarks**, with the quantum numbers shown in Tab.2.1

The quark hypothesis was put forward in 1964 by Gell-Mann and Zweig. These quarks

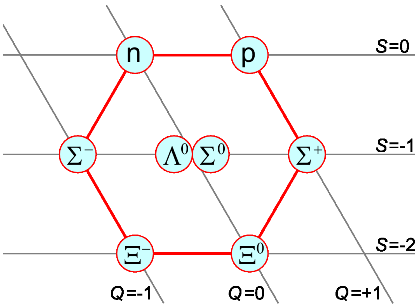

(a) Octet

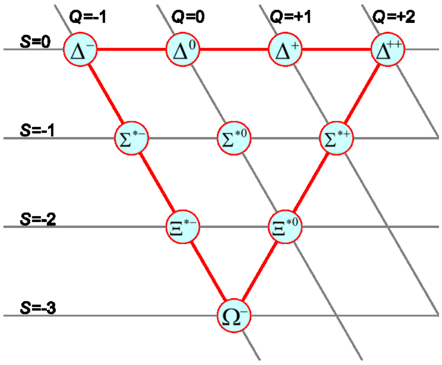

(b) Decuplet

Figure 2.2: The S=1/2 octet and the S=3/2 decuplet of baryons in the SU(3) symmetry.

Flavor	B	J	I	I_3	S	Q/e
u	$1/3$	$1/2$	$1/2$	$+1/2$	0	$+2/3$
d	$1/3$	$1/2$	$1/2$	$-1/2$	0	$-1/3$
s	$1/3$	$1/2$	0	0	-1	$-1/3$

Table 2.1: Quark quantum numbers.

consist of an $S = 0$ isospin doublet, labeled u and d (standing for $I_3 = +1/2$ (*up*) and $I_3 = -1/2$ (*down*), respectively) and a $S = -1$ isosinglet, labeled s (for *strange*). Baryons are assumed to be composed of three quarks each with baryon number $B = 1/3$. From the relation:

$$Q/e = \frac{1}{2}(B + S) + I_3 \tag{2.1}$$

where the combination $Y = B + S$ is called hypercharge, it follows that quarks must also carry fractional charges of $2/3$ and $-1/3$. The appropriate combinations of quarks indicated in Fig.2.2 can then account for the quantum numbers I, I_3, S (or Y) and electric charges of the members of the decuplet (Fig.2.3) and of the octect.

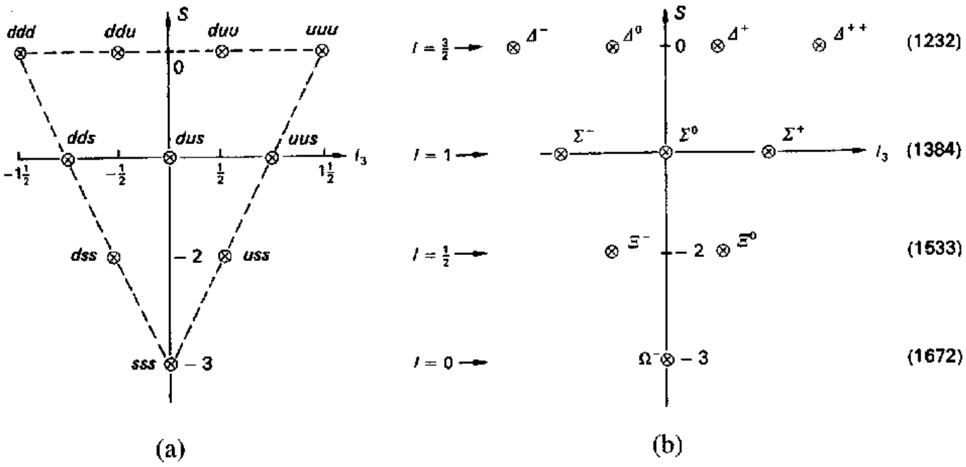

Figure 2.3: (a) Quark level conterpart of the baryon decuplet. (b) The observed decuplet of baryon states of spin-parity $3/2^+$. The mean mass of each isospin multiplet is given in brackets ([31]).

The masses of u and d quarks are expected to be nearly equal, since any difference must be of the order of the electromagnetic mass differences among the members of an isospin multiplet. The progressive increase in mass of the decuplet and octect members with decreasing S can then be simply ascribed to an increasing number of s quarks involved.
The first solid evidence for quarks came towards the end of '60s from Deep Inelastic Scattering experiments at the Stanford Linear Accelerator Center (SLAC) in which electrons accelerated to high energy in the SLAC's linear accelerator were fired on a proton target (a detailed description of the DIS process is reported in Chapter 3). The quarks proposed by Gell-Mann were indeed identified with the point-like constituents (*partons*) of the baryons struck by the incident electrons in DIS experiments and later incorporated in the more general framework of QCD.

Regularities among the baryons (and mesons) also emerge from a completely different approach based on the Regge theory: the Regge trajectories. Introduced for the first time in 1959, the Regge trajectories represented an active area of research during the '60. However the interest in Regge trajectories recently resurged due to the amount of new data and new quark models available.
The Regge trajectories are graphs of the total angular momentum J versus mass squared M^2 over a set of particles of fixed principal quantum number N, isospin I, dimensionality of the symmetry group D, spin S and flavor. Along a Regge trajectory, D, S, flavor, strangeness and isospin are fixed and only the orbital angular momentum L is allowed to vary (variations in J and L are equivalent when S is fixed). More details about the Regge trajectories are provided in Appendix A. Regge trajectories for relativistic scattering are to a good approximation straight lines over a considerable range of energy. Figs.2.4, 2.5 and 2.6 show examples of the Regge trajectories for strange baryons.

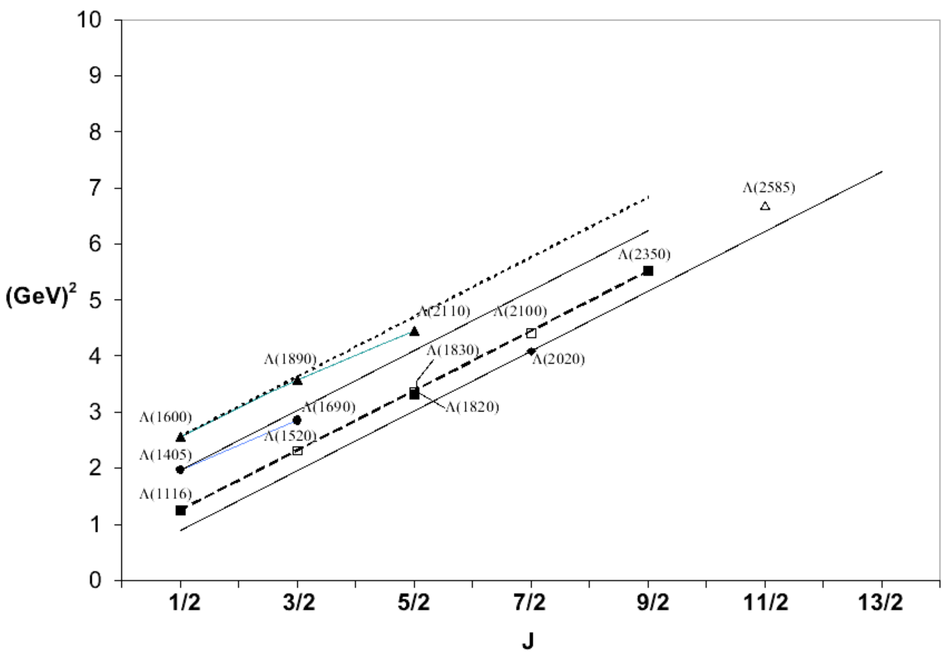

Figure 2.4: Regge trajectories for Λ baryons.

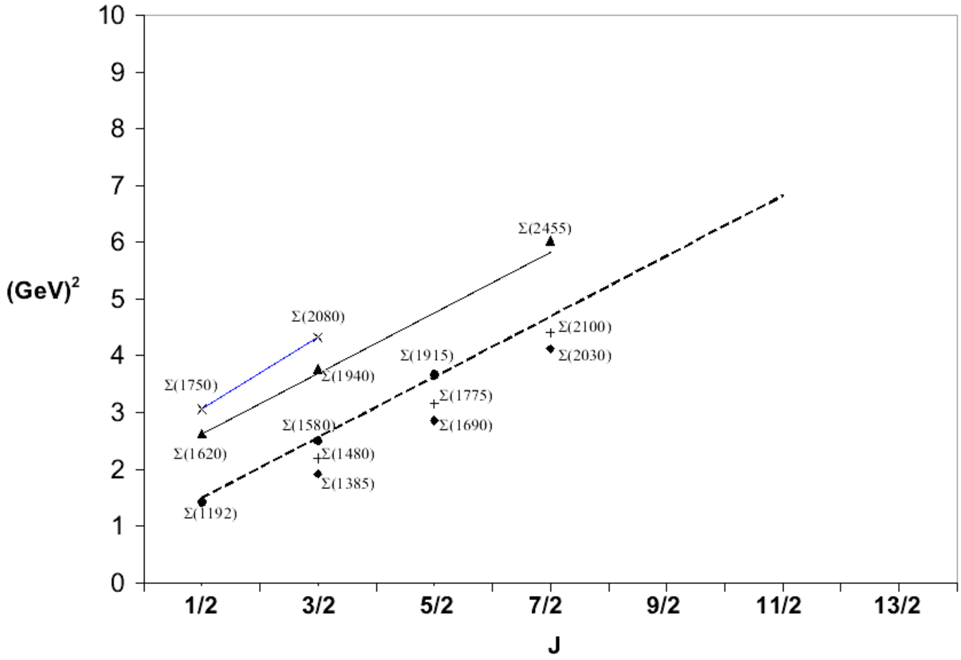

Figure 2.5: Regge trajectories for Σ baryons.

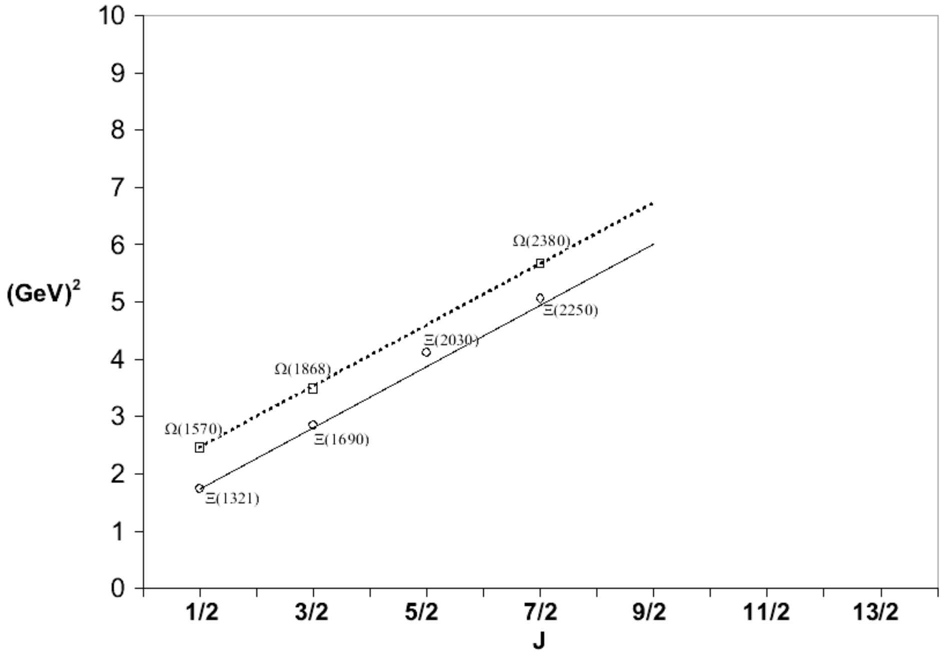

Figure 2.6: Regge trajectories for Ξ and Ω baryons.

2.2 Properties of selected Strange Baryons

In this section some relevant properties of the five strange baryons analyzed in this thesis (Chapters 6 and 7) are reported from a hystorical prospective.

2.2.1 Λ (uds) [$\mathbf{I} = 0$, $\mathbf{J}^P = \frac{1}{2}^+$, $\mathbf{S} = -1$]

Mass

The mass of the Λ hyperon was measured by a number of emulsion and Bubble Chamber experiments during the '60s, as reported in Fig.2.7 [32].

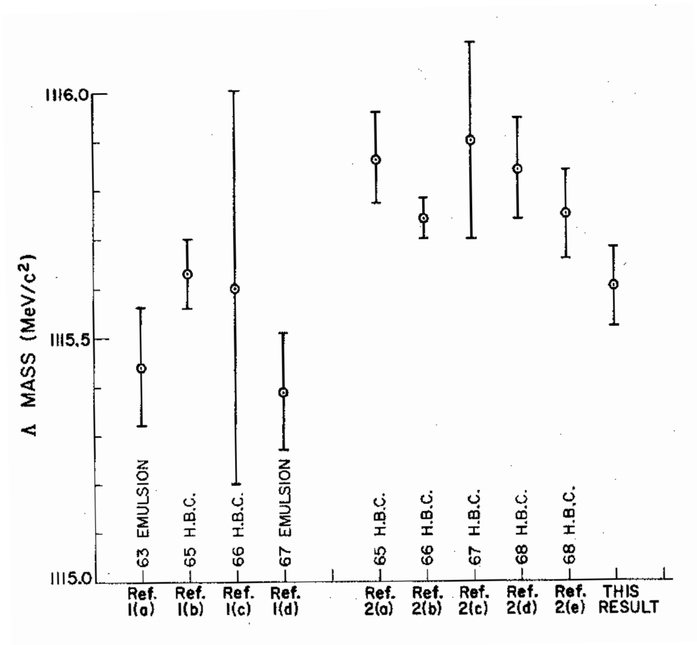

Figure 2.7: Summary of the measurements of the Λ Mass till 1972. $1(a), 1(b), 1(c), 1(d)$ correspond to ref. [33], [34], [35] and [36], respectively. $2(a), 2(b), 2(c), 2(d)$ and $2(e)$ correspond to ref. [37], [38], [39], [40] and [41], respectively.

Among these experiments the one that provided the estimation of the mass based on the highest statistics (935 events) is reported in [32]. In this experiment, performed at the He^4 bubble chamber of the Argonne National Laboratory, the Λ mass was measured through the reactions:

1. K^-+He$^4 \rightarrow \pi^- + \Lambda^0$+ He^3
2. K^-+He$^4 \rightarrow \pi^- + \Lambda^0$+ p + d
3. K^-+He$^4 \rightarrow \pi^- + \Lambda^0$+ p + p + n

and a final result of $M_\Lambda = 1115.59 \pm 0.08$ MeV/c^2 was reported.

However, the necessity to better constrain quark models and test the predictions of mass relations and QCD calculations of hyperfine interactions such as the $\Sigma^0 \rightarrow \Lambda^0$ transition demanded new higher precision measurements of the Λ mass. Such a measurement was eventually performed at the Alternating Gradient Synchrotron (AGS) at Brookhaven National Laboratories by the E766 collaboration in 1994 [42]. 20138 Λ^0 events were selected in pp interactions using a proton beam with an average momentum of 27.5 GeV/c off a 12-in long liquid hydrogen target. A Gaussian fit of the invariant mass distribution provided the highest precision measurement to date:

$$\mathrm{M}_\Lambda = 1115.678 \pm 0.006 \pm 0.006 \ \mathrm{MeV/c}^2$$

This experiment also measured the $\overline{\Lambda}$ mass with a comparable precision:

$$\mathrm{M}_{\overline{\Lambda}} = 1115.690 \pm 0.008 \pm 0.006 \ \mathrm{MeV/c}^2$$

providing a stringent test for the CPT invariance theorem:

$$\frac{M_\Lambda - M_{\overline{\Lambda}}}{M_\Lambda} = -(1.08 \pm 0.90) \cdot 10^{-5} \tag{2.2}$$

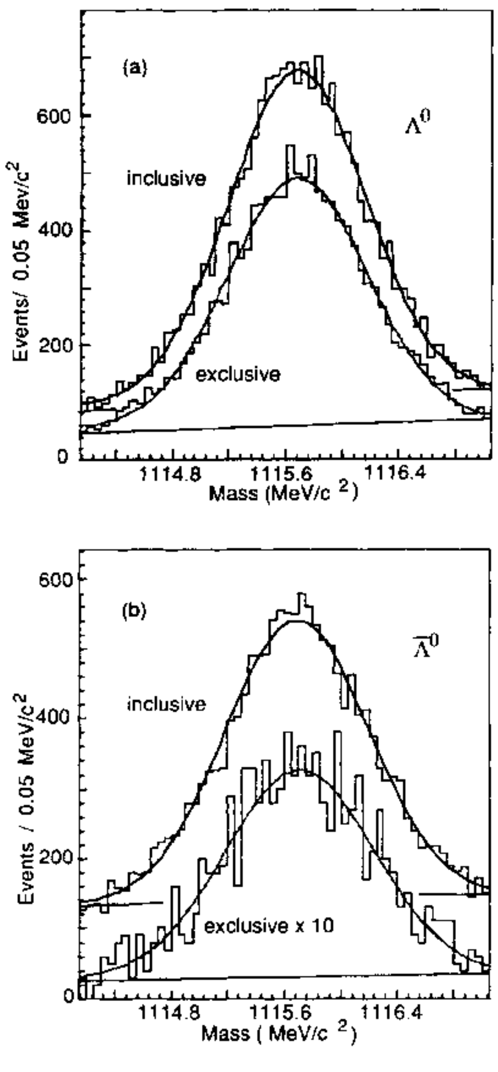

Figure 2.8: Invariant mass for (a) Λ^0 and (b) $\overline{\Lambda}^0$. Gaussians fits with linear backgrounds are shown explicitly [42].

Lifetime

This fundamental property of the Λ hyperon has been widely measured over the '60s and '70s. Most of the results are reported in Fig. 2.9 [43] together with the former (1973) world averaged value provided by the PDG. In [43] the data coming from three different K^-p bubble chamber experiments are reported:

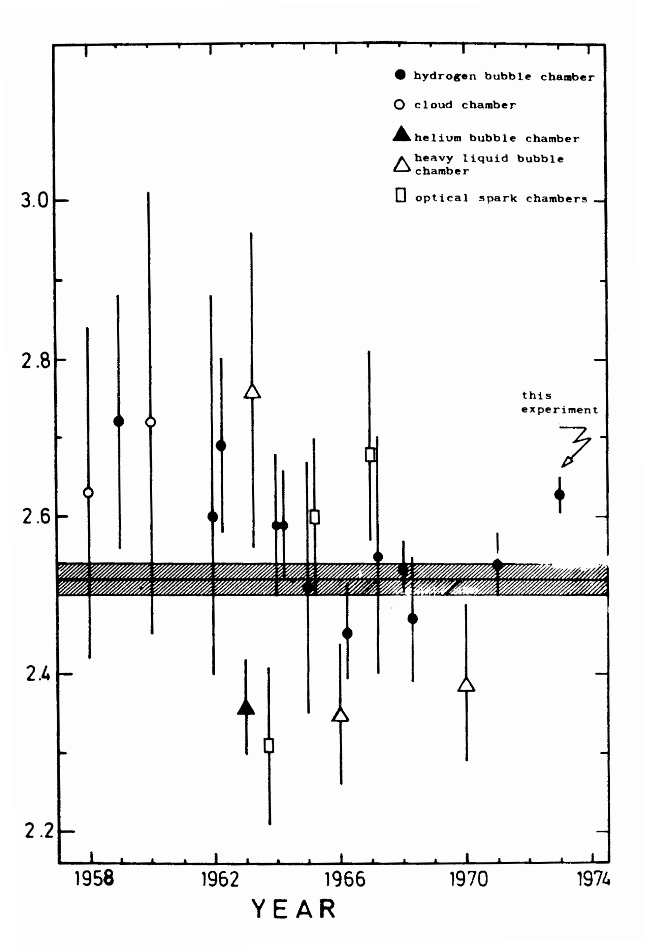

Figure 2.9: Summary of the measurements of the Λ lifetime till 1973 [42]. Shaded area corresponds to the world average value reported in [44].

1. (CERN Heidelberg Saclay (CHS) Collaboration) with 81 cm Saclay bubble chamber at CERN in a K^- momentum range of 0.43 to 1.43 GeV/c;
2. (College de France Rutherford Saclay (CRS) Collaboration) with 180 l bubble chamber at Nimrod in a K^- momentum range of 1.26 to 1.84 GeV/c;
3. (College de France Saclay (CS) Collaboration) with the 2 m CERN bubble chamber in a K^- momentum range of 1.94 to 2.34 GeV/c.

The Λ lifetime was measured through the reactions:

1. $K^- + p \rightarrow \Lambda^0 + \pi^+ + \pi^-$
2. $K^- + p \rightarrow \Lambda^0 + \pi^+ + \pi^- + \pi^0$

The final value of

$$\tau = (2.626 \pm 0.020) \cdot 10^{-10} \text{ sec}$$

was reported.

Two additional measurements have been done in 1975 [45] and 1977 [46] at CERN providing comparable results.
The first one used the CERN 2m hydrogen bubble chamber with a K^- beam of momentum range between 0.96 and 1.36 GeV/c.
In the second one the lifetime of the Λ hyperon has been measured at the CERN proton Synchrotron with a 24 GeV/c proton beam hitting a platinum target. Λ decay has been identified by measuring its decay products in a magnetic spectrometer and in a lead glass hodoscope. The final values reported in these three papers have been combined by the PDG [47] providing the present world average value of

$$\tau = (2.631 \pm 0.020) \cdot 10^{-10} sec \tag{2.3}$$

Decay Modes and Branching Ratios

The Λ hyperon decays through the following channels:

- Γ^1 $\Lambda \rightarrow p\pi^-$ $(63.9 \pm 0.5)\%$
- Γ^2 $\Lambda \rightarrow n\pi^0$ $(35.8 \pm 0.5)\%$
- Γ^3 $\Lambda \rightarrow p\gamma$ $(1.75 \pm 0.15) \cdot 10^{-3}$
- Γ^4 $\Lambda \rightarrow p\pi^-\gamma$ $(8.4 \pm 1.4) \cdot 10^{-4}$
- Γ^5 $\Lambda \rightarrow pe^-\overline{\nu}_e$ $(8.32 \pm 0.14) \cdot 10^{-4}$
- Γ^6 $\Lambda \rightarrow p\mu^-\overline{\nu}_\mu$ $(1.57 \pm 0.35) \cdot 10^{-4}$

The Branching Ratios for the first two channels were measured since the late '50s. The decay branching ratio of the Λ has often been cited as part of the evidence for the phenomenological selection rule $|\Delta I| = \frac{1}{2}$ for non-leptonic weak decays of baryons. This rule predicts, on the basis of isospin analysis of the initial and final states, that

$$R_\Lambda = \frac{\Lambda \rightarrow p\pi^-}{\Lambda \rightarrow p\pi^- + \Lambda \rightarrow n\pi^0} = \frac{\Gamma^1}{\Gamma^1 + \Gamma^2} = \frac{2}{3}. \tag{2.4}$$

The first measurement was performed at the hydrogen bubble chamber of the Lawrence Radiation Laboratory [48] providing the value $R_\Lambda = 0.624 \pm 0.030$.
Subsequent experiments confirmed this result with higher statistical accuracy. The most recent result of $R_\Lambda = 0.646 \pm 0.008$ was published in 1971 [49]. In this experiment more than 10000 Λ decay events were collected by the Brookhaven National Laboratory 30-in hydrogen bubble chamber.

Since γ-rays, neutral pions and neutrons are not detected efficiently in bubble chambers and nuclear emulsions, decays involving uncharged products must be studied indirectly by assuming

that a momentum and energy imbalance among the charged products is due to neutral products or that totally unseen decays occur according to decay schemes expected on theoretical grounds. The only two measurements available for the branching ratio for the channel $\Lambda \rightarrow \mathrm{n}\pi^0$ have been achieved in two separate experiments in the early '60s and published in [50] and [51], respectively.
In particular the former experiment was performed at the Berkeley Bevatron using a 21 l liquid Xenon bubble chamber exposed to 1.0 GeV/c and 1.1 GeV/c π^- beams. The reported result was

$$R_\Lambda = \frac{\Gamma^2}{\Gamma^1 + \Gamma^2} = 0.35 \pm 0.05. \tag{2.5}$$

The latter was performed at the Brookhaven National Laboratory using the π^- Cosmotron beam off a 15-in bubble chamber filled with methyl-iodide, propane and ethane. The resulting value was

$$R_\Lambda = \frac{\Gamma^2}{\Gamma^1 + \Gamma^2} = 0.291 \pm 0.034. \tag{2.6}$$

All the other branching ratios (see Tab.2.2.1), which are order of magnitude smaller than the two discussed above, have been measured in a number of high precision experiments till the early '90s as reported in the [47].

2.2.2 Σ^0 (uds) [$\mathbf{I} = 1$, $\mathbf{J}^P = \frac{1}{2}^+$, $\mathbf{S} = -1$]

Mass

The first attempts to measure the $\Sigma^0 - \Lambda^0$ mass difference were based on analyses of limited statistics data collected by emulsion and bubble chamber experiments performed more than 3 decades ago [52]. Among them, the best experimental determinations of the Σ^0 hyperon mass and $\Sigma^0 - \Lambda^0$ mass difference are those of [52]:

$$M_{\Sigma^0} = 1192.41 \pm 0.14 \quad MeV/c^2 \tag{2.7}$$

$$M_{\Sigma^0} - M_{\Lambda^0} = 76.63 \pm 0.28 \quad MeV/c^2 \tag{2.8}$$

which were determined in 1965 with 208 events in a hydrogen bubble chamber.
A significantly more precise determination of the Σ^0 mass has been obtained with the data collected in 1997 by the experiment E766 at the Brookhaven National Laboratory (AGS) [53]. A spectrometer consisting of six narrow-wire-spacing high rate drift chambers was used to detect charged particles produced by 27.5 GeV/c proton interactions in a 30 cm long liquid hydrogen target. A fit of the invariant mass distribution of 3327 $\Sigma^0 \rightarrow \Lambda^0 + \gamma$ decays (see Fig.2.10) yield [53]

$$M_{\Sigma^0} = 1192.65 \pm 0.020 \pm 0.014 \quad \mathrm{MeV/c^2} \tag{2.9}$$

$$M_{\Sigma^0} - M_{\Lambda^0} = 76.966 \pm 0.020 \pm 0.013 \quad \mathrm{MeV/c^2} \tag{2.10}$$

which represent the most precise determinations of the Σ^0 mass and of the $\Sigma^0 - \Lambda^0$ mass difference to date.

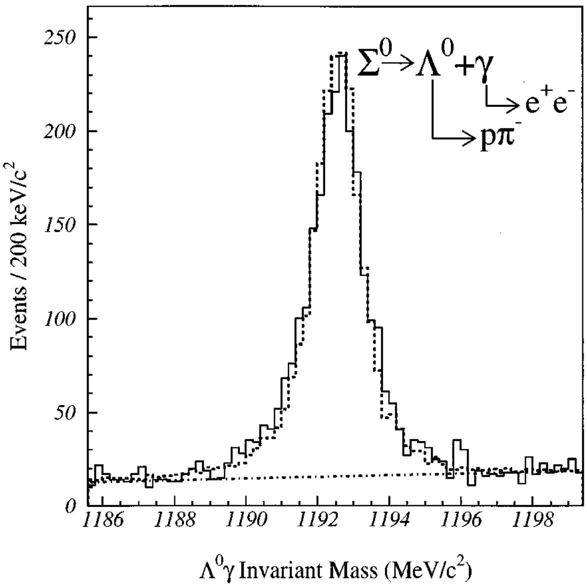

Figure 2.10: Fit of the invariant mass for the $\Sigma^0 \to \Lambda^0 + \gamma$ distribution [**?**]

Lifetime, Decay Modes and Branching Ratios

The dominant decay mode of the Σ^0 hyperon is:

- $\Gamma^1 \quad \Sigma^0 \to \Lambda^0 + \gamma$

and its lifetime was determined by the $\Sigma^0 - \Lambda^0$ magnetic transition moment $|\mu_{\Sigma\Lambda}|$ through the measurement of the cross section of the Primakoff process [54]

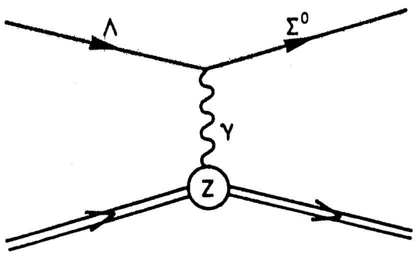

Figure 2.11: Primakoff production of Σ^0 hyperons on nuclei.

$$\Lambda + \mathrm{Z} \to \Sigma^0 + \mathrm{Z}$$

where Z stands for the Coulomb field of a nucleus.
The first determination of the Σ^0 lifetime is reported in [54] and was obtained by measuring the Coulomb production of Σ^0 hyperons through the interaction of a beam of Λ hyperons at the CERN Proton Synchrotron with Uranium and Nickel nuclei. The results for the Σ^0 lifetime and for the $\Sigma^0 - \Lambda^0$ magnetic transition moment were:

$$\tau_{\Sigma^0} = (0.58 \pm 0.13) \cdot 10^{-19} \ \text{sec} \tag{2.11}$$

$$|\mu_{\Sigma\Lambda}| = (1.82^{+0.25}_{-0.18}) \text{ nuclear magnetons} \tag{2.12}$$

respectively. Both are in agreement with SU(3) predictions.
A subsequent experiment was performed in 1986 using a similar approach [55] in the Fermilab Proton Center beam line using a 400 GeV proton beam onto three targets (Be, Sn and Pb). The results for the Σ^0 lifetime and for the $\Sigma^0 - \Lambda^0$ magnetic transition moment were:

$$\tau_{\Sigma^0} = (0.76 \pm 0.05 \pm 0.07) \cdot 10^{-19} \text{ sec} \tag{2.13}$$

$$|\mu_{\Sigma\Lambda}| = (1.59 \pm 0.05 \pm 0.07) \text{ nuclear magnetons} \tag{2.14}$$

A recalculation of the experimental results of [54] removing a numerical approximation made in that work yield [56]:

$$\tau_{\Sigma^0} = (0.65^{0.17}_{0.11}) \cdot 10^{-19} \text{ sec} \tag{2.15}$$

$$|\mu_{\Sigma\Lambda}| = (1.72^{0.17}_{0.19}) \text{ nuclear magnetons} \tag{2.16}$$

Two other suppressed decay modes are foreseen:

- Γ^2 $\quad \Sigma^0 \to \Lambda^0 + \gamma\gamma$
- Γ^3 $\quad \Sigma^0 \to \Lambda^0 + e^+e^-$

For Γ^2 only an upper limit (< 3 CL 90%) exists as reported in [57] while for Γ^3 only a theoretical QED calculation ($5 \cdot 10^{-3}$) exist as reported in [58].

2.2.3 Σ^{*+} (uds) and Σ^{*-} (dds) [I $= 1$, J$^P = \frac{3}{2}^+$, S $= -1$]

Masses and Widths

Several experiments have been performed over the past decades in order to measure the masses of the Σ^{*+} and Σ^{*-} hyperons and their widths.
The first determination was obtained at the Lawrence Radiation Laboratory (Berkeley) Bevatron in 1961 [59] in the interaction of 1.11 ± 0.03 GeV/c K$^-$ beams in a 30-in propane bubble chamber via the reaction (see Fig.2.12)

$$\mathrm{K}^- + \mathrm{p} \to \Lambda + \pi^+ + \pi^-$$

The results reported for the Σ^{*+} and Σ^{*-} masses and widths are:

$$M_{\Sigma^{*+}} = 1376.0 \pm 3.9 \text{ MeV/c}^2 \qquad \Gamma_{\Sigma^{*+}} = 48 \pm 16 \text{ MeV/c}^2 \tag{2.17}$$

$$M_{\Sigma^{*-}} = 1376.0 \pm 4.4 \text{ MeV/c}^2 \qquad \Gamma_{\Sigma^{*-}} = 66 \pm 18 \text{ MeV/c}^2 \tag{2.18}$$

A number of subsequent experiments have been performed with increasing accuracy till 1984 when a high statistics experiment involving $5.3 \cdot 10^6$ photographs of the CERN 2m hydrogen bubble chamber exposed to a K$^-$ beam of mean momentum 8.33 GeV/c was performed [60].
The actual world average values of the Σ^{*+} and Σ^{*-} masses and widths are [47]:

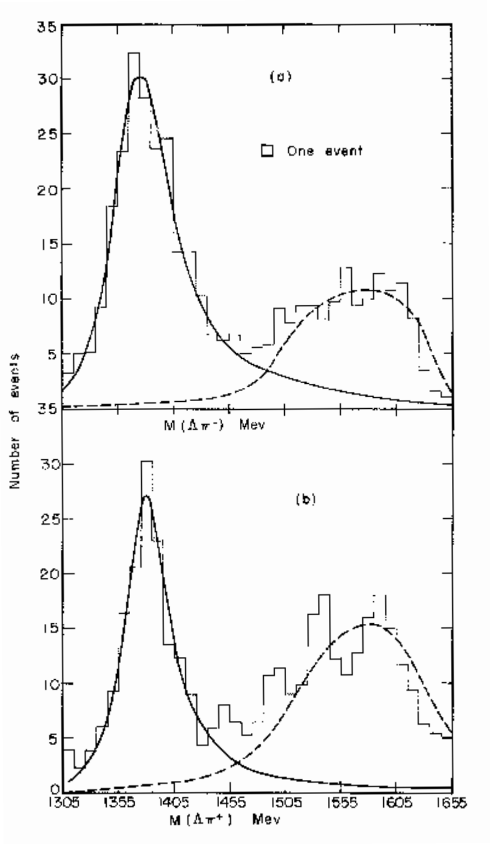

Figure 2.12: Invariant mass distributions for the (a) Σ^{*-} and (b) Σ^{*+}. The solid lines are the fits of the resonance regions [59].

$$M_{\Sigma^{*+}} = 1382.8 \pm 0.4 \quad \text{MeV/c}^2 \qquad \Gamma_{\Sigma^{*+}} = 35.8 \pm 0.8 \quad \text{MeV/c}^2 \tag{2.19}$$

$$M_{\Sigma^{*-}} = 1387.2 \pm 0.5 \quad \text{MeV/c}^2 \qquad \Gamma_{\Sigma^{*-}} = 39.4 \pm 2.1 \quad \text{MeV/c}^2 \tag{2.20}$$

Decay Modes and Branching Ratios

The Σ^{*+} and Σ^{*-} hyperons decay through the channels:

- Γ^1 $\quad \Sigma^* \to \Lambda^0 + \pi$ $\quad (87.0 \pm 1.5)\%$
- Γ^2 $\quad \Sigma^* \to \Sigma + \pi$ $\quad (11.7 \pm 1.5)\%$
- Γ^3 $\quad \Sigma^* \to \Lambda^0 + \gamma$ $\quad (1.3 \pm 0.4)\%$
- Γ^4 $\quad \Sigma^* \to \Sigma^- + \gamma$ $\quad (< 2.4 \cdot 10^{-4})$ (CL 90%)

The ratio Γ^2/Γ^1 has been measured in several hydrogen bubble chambers experiments during the '60s and '70s through the study of Kp and πp interactions. The present world average for the ratio Γ^2/Γ^1 is 0.135 ± 0.011 [47].

The ratio Γ^3/Γ^1 has been recently measured by the CLAS collaboration at JLAB [61] which reported the result:

$$\Gamma^3/\Gamma^1 = (1.53 \pm 0.39^{+0.15}_{-0.24}) \cdot 10^{-2} \tag{2.21}$$

superseding an old measurement which only provided an upper limit (<6 CL 90%) [57].
The ratio Γ^4/Γ^{Tot} has also been measured very recently. The experiment performed at FNAL by the SELEX collaboration [62] provided an upper limit ($< 2.4 \cdot 10^{-4}$ CL 90%) which superseded the upper limit of $< 6.1 \cdot 10^{-4}$ (CL 90%) estimated 3 decades earlier by [63].

2.2.4 Ξ^- (dss) [I $= \frac{1}{2}$, J^P $= \frac{3}{2}^+$, S $= -2$]

Mass

In a exposure of the CERN 32 cm hydrogen bubble chamber to a beam of K$^-$ mesons having a momentum of 1.455 ± 0.025 GeV/c 62 Ξ^- events were selected in 1963 providing the first measure of its relevant parameters [64]. In particular the value reported for the mass is:

$$M_{\Xi^-} = 1321.1 \pm 0.65 \quad \text{MeV/c}^2 \tag{2.22}$$

This result has been confirmed by several experiments performed during the ’60s and ’70s, the most recent of which is reported in [65]. In this experiment cross sections, mass spectra, angular distributions and several other features of Ξ^- production from protons and neutrons in K$^-$d interactions at 4.93 GeV/c in the Berkeley National Laboratory 80-in bubble chamber were measured. The reported result for the Ξ^- mass is:

$$M_{\Xi^-} = 1321.46 \pm 0.34 \quad \text{MeV/c}^2 \tag{2.23}$$

The present world average reported in the PDG [47] is:

$$M_{\Xi^-} = 1321.34 \pm 0.14 \quad \text{MeV/c}^2 \tag{2.24}$$

In the same period, similar measurements were done for the Ξ^- antiparticle ($\overline{\Xi}^+$) mass yielding to the world average value:

$$M_{\overline{\Xi}^+} = 1321.20 \pm 0.33 \quad \text{MeV/c}^2 \tag{2.25}$$

The ratio $\frac{M_{\Xi^-} - M_{\overline{\Xi}^+}}{M_{\Xi^-}}$ has been evaluated as a test of CPT invariance using the world average Ξ^- and $\overline{\Xi}^+$ masses above yielding (1.1 ± 2.7) $\cdot 10^{-4}$ [47].

Mean Life and Decay Modes

The Ξ^- mean life has been measured in a number of experiments which covered more than 2 decades from the early ’60s.
The most statistically accurated measurements was performed in 1978 [66] with the CERN 2m hydrogen bubble chamber exposed to a K$^-$ beam of nominal momentum 4.2 GeV/c. 4286 Ξ^- events were analyzed providing the value:

$$\tau_{\Xi^-} = (1.609 \pm 0.028) \cdot 10^{-10} \quad \text{sec.} \tag{2.26}$$

The world average reported by the PDG is [47]:

$$\tau_{\Xi^-} = (1.639 \pm 0.051) \cdot 10^{-10} \ \text{sec.} \tag{2.27}$$

Similar measurements were performed with a much lower statistics for the determination of the $\overline{\Xi^+}$ mean life yielding to the world average:

$$\tau_{\overline{\Xi}^+} = (1.6 \pm 0.3) \cdot 10^{-10} \ \text{sec.} \tag{2.28}$$

A full list of the Ξ^- decay modes can be found in [47]. The most probable decay channel is by far $\Xi^- \to \Lambda + \pi^-$ with a branching ratio of $(99.887 \pm 0.035)\%$.

2.2.5 The present world averages

The present world average [47] of the strange baryons properties described above are summarized in Tab.2.2.

Strange Baryons	I(J^P)	Mass (MeV)	Lifetime or Full Widths	Dominant Decay Modes	Branching Ratios
$\Lambda^0(usd)$	$0(\frac{1}{2}^+)$	1115.683 ± 0.006	$(2.631 \pm 0.020) \cdot 10^{-10}$ sec	pπ^-	$(63.9 \pm 0.5)\%$
				nπ^0	$(35.8 \pm 0.5)\%$
$\Sigma^0(uds)$	$1(\frac{1}{2}^+)$	1192.642 ± 0.024	$(7.4 \pm 0.7) \cdot 10^{-20}$ sec	$\Lambda\gamma$	100%
$\Sigma^{*-}(dds)$	$1(\frac{3}{2}^+)$	1387.2 ± 0.5	39.4 ± 2.1 MeV	$\Lambda\pi^-$	$(88 \pm 2)\%$
				$\Sigma\pi$	$(11.7 \pm 1.5)\%$
$\Sigma^{*+}(uus)$	$1(\frac{3}{2}^+)$	1382.8 ± 0.4	35.8 ± 0.8 MeV	$\Lambda\pi^+$	$(88 \pm 2)\%$
				$\Sigma\pi$	$(11.7 \pm 1.5)\%$
$\Xi^-(dss)$	$1(\frac{1}{2}^+)$	1321.31 ± 0.13	$(1.639 \pm 0.015) \cdot 10^{-10}$ sec	$\Lambda\pi^-$	$(99.887 \pm 0.035)\%$

Table 2.2: Summary of the properties of the strange baryons analyzed in this thesis.

Chapter 3

HERMES Physics

3.1 Kinematics

In a deep-inelastic scattering (DIS) process the lepton interacts with the nucleon in such a way that it leaves a continuous spectrum of hadrons in the final state, denoted with X.

$$l + N \rightarrow l' + X \tag{3.1}$$

Fig.3.1 shows a sketch of the DIS process in the one-photon exchange approximation. The interaction between the lepton and the target takes place via the exchange of a virtual boson with mass $q^2 = -Q^2$ and $q = k - k'$. The type of the exchange boson depends on the lepton type and on the involved energies. At HERMES, the beam energy of 27.5 GeV (corresponding to a center of mass energy $\sqrt{s} \approx 7.1$ GeV ([1]) is well below the Z^0 mass, thus the contribution from the Z^0 boson is completely negligible and the virtual photons,denoted with γ^* are the dominant exchange bosons.

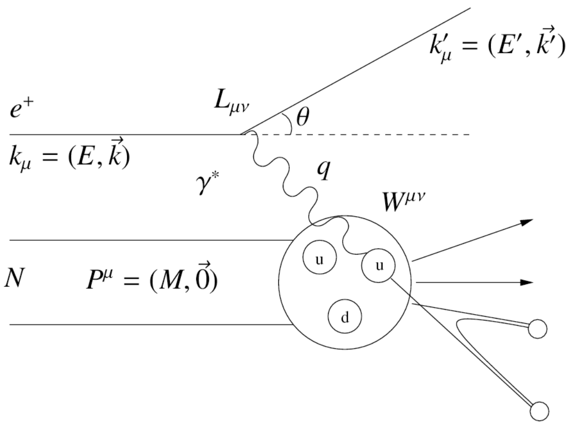

Figure 3.1: Schematic view of a deep inelastic scattering event on a proton target.

[1]The center of mass energy s is defined as:

$$s = (k + P)^2 \overset{lab}{=} 2ME - M^2 \tag{3.2}$$

In inclusive measurements only the scattered lepton l' is detected. The variables reported in tab.3.1 are commonly used to describe DIS processes.

$\mathbf{k} = (E, \vec{k}); \mathbf{k}' = (E', \vec{k'});$	$4-$momenta of incoming and outgoing e^+
$\mathbf{P} \overset{lab}{=} (M, \vec{0})$	$4-$momenta of the target nucleon
θ, ϕ	polar and azimuthal scattering angles
$\mathbf{q} = (\nu, \vec{q})$	$4-$momenta of the virtual photon
$Q^2 = -q^2 \overset{lab}{=} 4EE'sin^2(\theta/2)$	negative squared $4-$momentum transfer
$\nu = \frac{\mathbf{P}\cdot\mathbf{q}}{M} \overset{lab}{=} E - E'$	energy transfer from the incoming lepton to the target nucleon
$x = \frac{Q^2}{2\mathbf{P}\cdot\mathbf{q}} \overset{lab}{=} \frac{Q^2}{2M\nu}$	Bjørken scaling variable
$y = \frac{\mathbf{P}\cdot\mathbf{q}}{\mathbf{P}\cdot\mathbf{k}} \overset{lab}{=} \frac{\nu}{E}$	fractional energy of the virtual photon
$W^2 = (\mathbf{P} + \mathbf{q})^2 \overset{lab}{=} M^2 + 2M\nu - Q^2$	squared invariant mass of the hadronic final state
$p = (E_h, \vec{p})$	$4-$momentum of a final state hadron
$z = \frac{\mathbf{P}\cdot\mathbf{p}}{\mathbf{P}\cdot\mathbf{q}} \overset{lab}{=} \frac{E_h}{\nu}$	fractional energy of the final state hadron
$p^{\parallel}_{CM} = \vec{p} \cdot \frac{\vec{q}}{\lvert\vec{q}\rvert}\Big\rvert_{\gamma^*-N}$	hadron momentum component parallel to the photon momentum in the center of mass frame
$x_F = \frac{p^{\parallel}_{CM}}{\lvert\vec{q}\rvert} \simeq \frac{2p^{\parallel}_{CM}}{W}$	Feynman scaling variable

Table 3.1: Definition of the most important kinematic variables used in deep-inelastic scattering.

The kinematics of a scattering event is described by the $4-$momenta of the lepton before and after the scattering ($k = (E, \vec{k})$ and $k' = (E', \vec{k'})$, respectively) and by the corresponding $4-$vector of the target nucleon, $P = (E_N, \vec{P})$.
The spatial resolution of scattering process is inversely proportional to the negative squared $4-$momentum Q^2 of the virtual photon, where:

$$Q^2 = -q^2 = -(\mathbf{k} - \mathbf{k}') \overset{lab}{\simeq} 4EE'sin^2(\theta/2) \tag{3.3}$$

Furthermore, the energy transfer ν from the incoming lepton to the target nucleon is defined as:

$$\nu = \frac{Pq}{M} \overset{lab}{=} E - E' \tag{3.4}$$

and the total invariant mass of the final hadronic state

$$W^2 = (\mathbf{P} + \mathbf{q})^2 \overset{lab}{=} M^2 + 2M\nu - Q^2 \tag{3.5}$$

Here, M denotes the nucleon. The expression in the laboratory frame hold for fixed targets ($P = (M, 0)$) and energies high enough to neglect the lepton mass.
For elastic scattering, $W^2 = M^2$ so that $Q^2 - 2M\nu = 0$.

The Bjørken scaling variable is defined as:

$$x = \frac{Q^2}{2\mathbf{P} \cdot \mathbf{q}} \stackrel{lab}{=} \frac{Q^2}{2M\nu} \tag{3.6}$$

thus yields $x = 1$ for elastic and $0 < x < 1$ for inelastic events and can be understood as a measure for the inelasticity of the event.
The DIS reaction can be described as scattering off the individual quarks in the target nucleon, which subsequently breaks apart. The DIS domain is approximately given by:

$$Q^2 \geq 1GeV^2 \quad and \quad W^2 \geq 4GeV^2. \tag{3.7}$$

These conditions ensure a high enough resolution to probe the internal structure of the nucleon. Furthermore, the W^2 requirement avoids the elastic scattering region, as well as inelastic scattering in resonance regions with $W^2 = M_R$ (where M_R is the mass of the resonance).
All the variables reported above are well defined by the properties of the scattered lepton and thus can be calculated from an inclusive measurement. In semi-inclusive measurements, hadrons are detected in coincidence with the outgoing lepton. Semi-inclusive variables define the characteristics of the individual hadrons. The most important ones are z, the longitudinal momentum fraction carried away by the produced hadron, the Feynman variable x_F and the rapidity η:

$$z \equiv \frac{E_h}{\nu} \tag{3.8}$$

$$x_F \equiv \frac{2p^{\|}_{CM}}{W} \tag{3.9}$$

$$\eta \equiv \frac{1}{2} \cdot ln \left(\frac{E^h_{CM} + p^{\|}_{CM}}{E^h_{CM} - p^{\|}_{CM}} \right) \tag{3.10}$$

here $p^{\|}_{CM}$ denotes the projection of the hadron momentum in the direction of the virtual photon in the photon-nucleon center of mass system. In this reference frame, the Feynman variable x_F scales the momentum component collinear to the photon momentum to its maximum possible value ($-1 \leq x_F \leq 1$). The rapidity η is a commonly used variable in high energy hadronic scattering since it conveniently transforms additively under boosts along a special axis (where the natural choice is the collision axis, given by the virtual photon momentum) [67]. In the non-relativistic limit, η becomes the particle velocity along this axis. The variables η and x_F enable to define a forward region in which

$$x_F > 0 \quad and \quad \eta > 0 \tag{3.11}$$

and a backward region where both the variables are negative. Around 0 there is the so-called *central region*.

3.2 The DIS Cross Section

The inclusive DIS cross section can be defined in terms of the leptonic tensor $L_{\mu\nu}$, that describes the leptonic interaction part $l \rightarrow \gamma^* l'$, and the hadronic tensor $W^{\mu\nu}$, that describes the hadronic interaction part $P + \gamma^* \rightarrow P'$.

$$\frac{d^2\sigma}{dE'd\Omega} = \frac{\alpha^2}{2MQ^4} \cdot \frac{E'}{E} \cdot L_{\mu\nu} W^{\mu\nu} \tag{3.12}$$

Here, $\alpha = e^2/(4\pi) \approx (1/137)$ is the fine structure constant. As in classical Rutherford scattering, a typical $Q^{/4}$ dependence is obtained.
For the point-like leptons, the tensor $L_{\mu\nu}$ can be exactly calculated in QED. For unpolarized scattering it is given in leading order by:

$$L_{\mu\nu} = 2 \cdot \left[k'_\mu k_\nu + k'_\nu k_\mu - g_{\mu\nu}\left(\mathbf{k}' \cdot \mathbf{k} - m^2\right)\right] \tag{3.13}$$

with m denoting the lepton mass and $g_{\mu\nu}$ the Minkowski metric.
The hadronic tensor has to reflect the hadronic substructure of the target nucleon and thus can not be calculated exactly. Fortunately, its structure can be constrained by symmetry requirements like Lorentz and gauge invariance as well as current parity conservation. For the unpolarized (or spin-averaged) case, only two independent structure functions remain:

$$\frac{1}{2M} W_{\mu\nu} = \left(-g_{\mu\nu} - \frac{q_\mu q_\nu}{Q^2}\right) \cdot W_1(\nu, Q^2) + \frac{1}{M^2}\left(p_\mu + \frac{\mathbf{p}\cdot\mathbf{q}}{Q^2} q_\mu\right)\left(p_\nu + \frac{\mathbf{p}\cdot\mathbf{q}}{Q^2} q_\nu\right) \cdot W_2(\nu, Q^2). \tag{3.14}$$

The combination of eqs. 3.12, 3.13 and 3.14 leads to:

$$\frac{d^2\sigma}{dE'd\Omega} = \left(\frac{d\sigma}{d\Omega}\right)_{Mott} \cdot \left[W_2(\nu, Q^2) + 2W_1(\nu, Q^2) tan^2\left(\frac{\theta}{2}\right)\right] \tag{3.15}$$

where

$$\left(\frac{d\sigma}{d\Omega}\right)_{Mott} = \frac{4\alpha^2 E'^2}{Q^4} cos^2\left(\frac{\theta}{2}\right) \tag{3.16}$$

denotes the Mott cross section which describes the scattering of leptons off a spin-less and point-like particle. The structure functions parameterize the deviation of the nucleon cross section from this point-like particle behavior, where specifically the additional tan^2-dependence is due to the interaction of the positrons with the magnetic moment of the nucleon. In the elastic limit ($\nu \to Q^2/(2M)$), the structure functions W_1 and W_2 are related to the electric and magnetic nucleon form factors:

$$W_1(\nu, Q^2) = \frac{Q^2}{4M^2} G_M^2(Q^2)\delta\left(\nu - \frac{Q^2}{2M}\right) \tag{3.17}$$

$$W_2(\nu, Q^2) = \frac{G_E^2(Q^2) + \frac{Q^2}{4M^2} G_M^2(Q^2)}{1 + \frac{Q^2}{4M^2}} \delta\left(\nu - \frac{Q^2}{2M}\right) \tag{3.18}$$

Usually, the cross section is expressed in terms of the dimensionless structure functions $F_1(x, Q^2)$ and $F_2(x, Q^2)$. In the limit of $Q^2 \to \infty$ for a fixed ratio of $\frac{Q^2}{P\cdot q}$ the so-called Bjørken limit, they become a function of the Bjørken scaling variable (3.6) alone:

$$MW_1(\nu, Q^2) = F_1(x, Q^2) \to F_1(x) \tag{3.19}$$

$$\nu W_2(\nu, Q^2) = F_2(x, Q^2) \to F_2(x) \tag{3.20}$$

This behavior has been predicted by Bjørken [68] and Feynman [69] and has subsequently been measured at SLAC [70]. It indicates that, at sufficiently high energies, the scattering process occurs on point-like particles that form the constituents of the nucleon. These predictions and measurements form the basis of the quark parton model.
Comparing A.10 with the cross section for scattering off point-like spin $1/2$ particles

$$\frac{d\sigma}{d\Omega} = \left(\frac{d\sigma}{d\Omega}\right)_{Mott} \cdot \left[1 + \frac{Q^2}{2M^2} tan^2\left(\frac{\theta}{2}\right)\right] \tag{3.21}$$

yields (taking into account eqs. 3.19 and 3.19)

$$2xF_1(x) = F_2(x) \tag{3.22}$$

This equation is known as the Callan-Gross realtion [71]. Its experimental verification confirmed that the charged partons in the nucleon are indeed spin $1/2$ objects.
Experimentally, the F_2 structure function is well known from the H1 and ZEUS data at HERA. Fig.3.2 shows the Q^2 dependence of the structure function $F_2(x, Q^2)$. For intermediate x (around 0.25) the function is independent of Q^2, as expected from the quark parton model (eq.3.2). However, for larger and smaller x, this independence is lost. This scale-breaking effect can be explained if interactions between the partons are introduced into the quark parton model, which so far have been neglected.

The cross section is often written as a function of Q^2 and x. In terms of the dimensionless structure functions F_1 and F_2 it is given by:

$$\frac{d^2\sigma}{dxdQ^2} = \frac{4\pi\alpha^2}{xQ^4}\left[y^2 x F_1(x, Q^2) + (1-y)F_2(x, Q^2)\right] \tag{3.23}$$

Here, y denotes the fraction of the lepton energy transferred to the target (see tab.3.1).

3.3 The Quark Parton Model

The Quark Parton Model provides an intuitive explanation for the observed Bjørken scaling. The nucleon is considered to be composed of point-like constituents, the **partons**. It is formulated in a reference frame where the nucleon is moving with high momentum, such that the transverse momentum components and the rest mass of the constituents and the nucleon itself can be neglected (*infinite momentum frame* see fig.3.3). In this model, the DIS occurs as elastic scattering on these constituents.

The model implies that the interaction between the individual partons is weak on short distances. If the scattering occurs on sufficiently short time scales, the particles can thus be regarded as quasi-free, and the $4-$momentum of a parton after scattering is given by:

$$(\xi\mathbf{P} + \mathbf{q})^2 = \xi^2 M^2 + 2\xi\mathbf{P}\cdot\mathbf{q} - Q^2 \approx 0 \tag{3.24}$$

where ξ denotes the fraction of the nucleon momentum carried by the struck quark. Neglecting the target mass yields $\xi \approx Q^2/(2P \cdot q)$ and thus allows to relate the momentum fraction with the Bjørken scaling variable x in the given approximation (see eq.3.6).
In the QPM interpretation the structure function $F_2(x, Q^2)$ can be rewritten as:

$$F_2(x, Q^2) = x \cdot \sum_f e_f^2 \cdot q_f(x, Q^2) \tag{3.25}$$

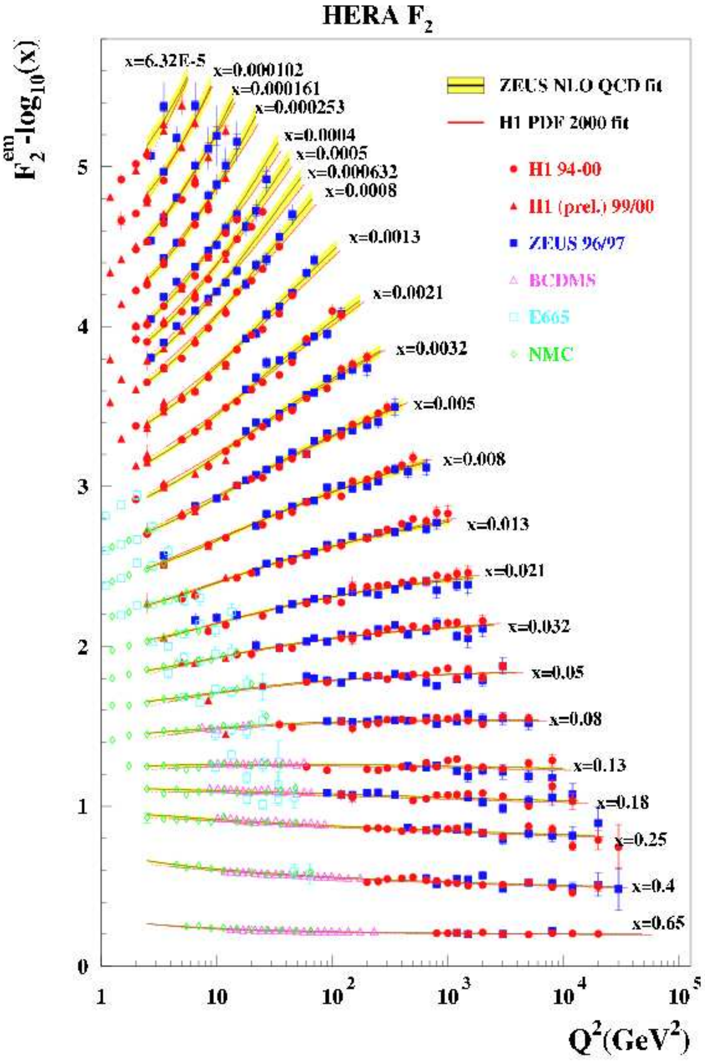

Figure 3.2: World data on $F_2(x, Q^2)$ from H1, ZEUS, NMC, E665 and the BCDMS collaborations.

The sum runs over all quark flavors $q \in [u, d, s, c, b, t]$ and the corresponding antiquarks. Here e_f is the fractional charge carried by the considered quark flavor and $q_f(x, Q^2)$ is the so-called *Parton Density Function* (PDF) that represents the expectation value for the number f quarks of type f to be found in the nucleon with a momentum fraction between x and $x + dx$. For HERMES the relevant flavors are u, d and s, with fractional charge $+2/3$ (u) and $-1/3$ (d and s). The structure function can be rewritten in terms of the individual quark distributions([2]). For the proton and the neutron it becomes:

$$\frac{1}{x} \cdot F_2^p = \left[\frac{4}{9} \cdot (u_v^p + u_s + \overline{u}_s) + \frac{1}{9} \cdot (d_v^p + d_s + \overline{d}_s) + \frac{1}{9} \cdot (s_s + \overline{s}_s)\right] \tag{3.26}$$

$$\frac{1}{x} \cdot F_2^n = \left[\frac{4}{9} \cdot (u_v^n + u_s + \overline{u}_s) + \frac{1}{9} \cdot (d_v^n + d_s + \overline{d}_s) + \frac{1}{9} \cdot (s_s + \overline{s}_s)\right] \tag{3.27}$$

[2]The $u, d, s-$quark distributions $q_{(u,d,s)}(x)$ are denoted with $u(x)$, $d(x)$ and $s(x)$, respectively

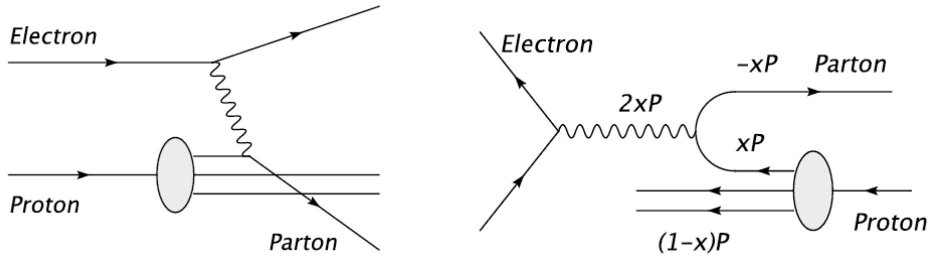

Figure 3.3: Schematic view of the DIS process in the laboratory frame (left) and in the Breit frame (right).

where the subindeces v and s denotes the *valence quark* distributions and the *sea quark* distributions, respectively. The proton and the neutron are partners in an isospin doublet ($I = 1/2$). Therefore their quark distributions are subject to a number of symmetry relations

$$u_v^p(x) = d_v^n(x) \qquad d_v^p(x) = u_v^n(x) \tag{3.28}$$

$$u_s^p(x) = d_s^p(x) = d_s^n(x) = u_s^n(x) \tag{3.29}$$

Since the sea quarks are always created in quark - antiquark pairs of the same flavor, it is possible to equate $u_s(x) = \overline{u}_s(x)$ and analogous for the other quark flavors. A number of sum rules in terms of the total quark and anti-quark distributions can be written. For the proton:

$$\int_0^1 dx[u(x) - \overline{u}(x)] = \int_0^1 dx u_v(x) = 2 \tag{3.30}$$

$$\int_0^1 dx[d(x) - \overline{d}(x)] = \int_0^1 dx d_v(x) = 1 \tag{3.31}$$

$$\int_0^1 dx[s(x) - \overline{s}(x)] = 0 \tag{3.32}$$

3.3.1 The QCD-improved Quark Parton Model

In the so-called QCD-improved quark parton model, quarks interact by the exchange of gluons, which mediate the strong interaction. Fig.3.4 depicts the basic processes possible in strong interaction: quarks can radiate gluons, gluons can split into a $q\overline{q}$ pair and gluons can couple with other gluons.

Similar to QED, the interaction strength arises from a coupling strength $\alpha_s = g^2/4\pi$. It is given in first order QCD as

$$\alpha_s(\mu^2) = \frac{12\pi}{(33 - 2n_f) \cdot log(\mu^2/\Lambda_{QCD}^2)} \tag{3.33}$$

μ is the renormalization scale, which effectively poses a cut on the time scale in which virtual fluctuations are taken into account. For DIS, it is usually set to Q. The number of quark flavors is given by n_f, where usually all flavors with a mass smaller than μ are taken into account. Λ_{QCD} finally is the QCD parameter.

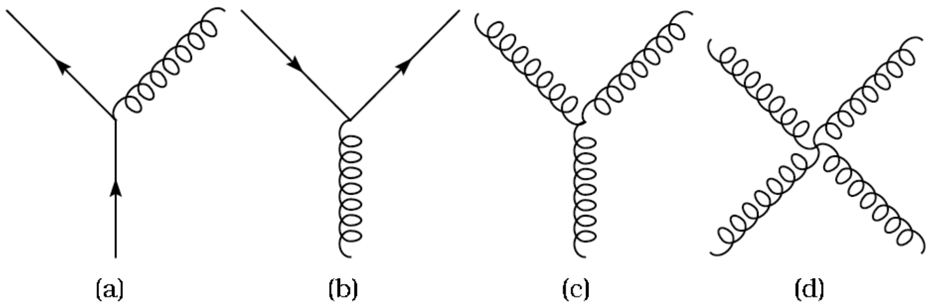

Figure 3.4: The four basic gluon interactions. (a) gluon radiation by a quark, (b) splitting of a gluon in a quark - antiquark pair, (c) splitting of a gluon in two gluons and (d) a gluon four - vertex.

For the applicability of perturbation theory, α_s must be less than 1, so Λ sets the scale for the breakdown of perturbation theory. Depending on the renormalization scheme and the number of quark flavors, Λ has a value f $200 - 300$ MeV.
Unlike the electromagnetic coupling constant α, α_s exhibits a strong μ^2 (or for DIS Q^2) dependence. α_s becomes large as Q^2 decreases: this property shows the tendency towards **confinement** and it is essential to understand the fragmentation process of quarks into hadrons. A low energy, the quarks are bound very strongly together into a color singlet. The coupling constant decreases when Q^2 increases and approaches 0 as $Q^2 \to \infty$. Quarks behave as if they move freely and unbound. This property is called **asymptotic freedom**.

The interactions of the partons by the processes shown in fig.3.4 together with the Q^2 dependence of the coupling strength explain the scaling violations observed in the structure functions. A photon with a larger $4-$momentum probes the nucleon with a higher resolution. With increasing resolution the nucleons appear to be composed of a larger number of resolved quarks and gluons, all sharing the total nucleon momentum. The fraction of partons which possess a high share x of the total momentum thus decreases, while the number of partons with low x increases.
Quantitatively, this behavior can be described by the DGLAP[3] evolution equations ([72], [73], [74], [75]). For the quark distributions $q(x, Q^2)$ and the gluon distributions $g(x, Q^2)$, they are given as

$$\frac{dq(x,Q^2)}{dlnQ^2} = \int_x^1 \frac{dx'}{x'}\left[q(x',Q^2)\cdot P_{qq}\left(\frac{x}{x'}\right) + g(x',Q^2)\cdot P_{qg}\left(\frac{x}{x'}\right)\right] \tag{3.34}$$

$$\frac{dg(x,Q^2)}{dlnQ^2} = \int_x^1 \frac{dx'}{x'}\left[g(x',Q^2)\cdot P_{gg}\left(\frac{x}{x'}\right) + \sum_q q(x',Q^2)\cdot P_{gq}\left(\frac{x}{x'}\right)\right] \tag{3.35}$$

They mathematically express the fact that, at a given resolution Q^2, e.g. a quark of flavor q, carrying the momentum fraction x, could have been radiated from a parent parton (quark or gluon) which carried a higher fraction x'. The splitting functions $P_{ab}(x/x')$ specify the probability that a parton b with momentum fraction x' is the origin of a parton a with momentum fraction x. Or, speaking in terms of resolution, they give the probability to find object a inside of object b with a fraction x/x' of b's momentum. Once the parton distributions are known at

[3]DGLAP=Dokshitzer,Gribov,Lipatov,Altarelli,Parisi

some scale, the DGLAP equations allow to calculate PDFs at other scales where perturbation theory holds.

3.4 Hadronic Final States and Fragmentation Functions

The energy at which the scattering interaction occurs is much higher than the force that holds the partons together, so one would expect them to be 'kicked out' of the nucleon. However, the principle of confinement dictates that quarks cannot exist as free particles in nature (long distance behavior). They are always bound together into color neutral objects: baryons consisting of three differently colored quarks (q_{c1}, q_{c2}, q_{c3}) or mesons, being a bound state of a quark and an antiquark ($q_c, \overline{q}_c$). The process in which the final hadrons emerge from the deep inelastic scattering is called **Fragmentation** or **Hadronization** and cannot be tackled using perturbative QCD as the strong coupling constant α_s becomes too large at low energy, which is exactly where hadronization occurs.

A concept essential to the description of DIS is factorization. It is assumed that the scattering process of the virtual photon off a nucleon can be divided into two parts: the hard short distance scattering of the proton off one of the nucleon's constituents (the cross section σ calculable from perturbation theory) and the selection of these constituents according to a soft, long range parton density function. The factorization theorem for hadron production in semi-inclusive DIS is contained in the following expression for the hadron production cross section:

$$\frac{d^3\sigma^h}{dxdQ^2dz} = \frac{\sum_f e_f^2 q_f(x,Q^2) D_f^h(z,Q^2)}{\sum_f e_f^2 q_f(x,Q^2)} \cdot \frac{d^2\sigma^{DIS}}{dxdQ^2} \tag{3.36}$$

The hadron production is given by the $D_f^h(z, Q^2)$ functions, called *Fragmentation Functions*; they factorize from the parton distribution functions $q_f(x, Q^2)$ and depend mostly on the z variable.

The fragmentation functions have to be derived from fit of the experimental data because they cannot be directly calculated. The hadronization process is implemented in Monte Carlo simulation by using phenomenolocical models, whose parameters have to be tuned to reproduce the experimental data. The fragmentation model have been tuned by fitting the data from the collider e^+e^- experiments at several energies. The tuning of the LUND model to the HERMES data has been obtained by measuring the hadron multiplicities versus various variables ([76] and [77]).

The three main fragmentation models are described in Sec.4.3. Particular emphasis is given to the LUND model, based on the string fragmentation model, that is the default model for all PYTHIA applications.

Chapter 4

Monte Carlo Simulation

Monte Carlo simulations represent a very important tool in high energy physics. Parametrization and models allow to simulate on a statistical basis, many aspects that can not be calculated in an analytical way and that are necessary for a complete understanding of the physical problems.
For the analysis presented in this thesis, a Monte Carlo simulation based on **PYTHIA** 6.2 [78] generator and **GEANT**3 [79] was used for two main issues: the calculation of the geometrical acceptance, that, due to the limited angular coverage of the HERMES spectrometer, is of fundamental importance in the evaluation of the 4π hyperons photoproduction cross section, and the study of the background of the heavier hyperons. In this chapter a short overview about the Monte Carlo techniques is given; the HERMES Monte Carlo chain is then described. Finally the comparison between the Monte Carlo generated distributions and the experimental distributions is shown.

4.1 The HERMES Monte Carlo Implementation

The HERMES Monte Carlo consists of a set of programs which act as building blocks for the complete Monte Carlo chain shown in fig. 4.1. Each MC production starts with a **Generator Monte Carlo (GMC)** program. Several events generators are available which are suitable to simulate different aspects of HERMES physics. Their outputs can be considered as a simulation of what 'really' happens on the physics level. For a reasonable comparison with experimental data, however, further effects have to be taken into account which are inevitably introduced by the measuring process: depending on their kinematics, only a certain fraction of the particles produced in the reaction traverse the active area of the detector.
They might interact with target material and detector before their kinematic properties can actually be measured. In the form of (multiple) scattering, these interactions influence the energies and the measured angles of the tracks. Since the particle momentum is determined by the bending of the tracks induced by the spectrometer magnet, also the momentum determination is affected. Additionally, the radiation of Bremsstrahlung photons biases the detected energy of the particles. Finally, the detector signals have to be interpreted by the reconstruction program. The reconstructed track properties (momentum, angles, particle types...) are subject to inefficiencies like the limited detector resolution, misidentifications or even complete particle loss if the signal does not allow to decode the information.

It thus produces a response function which is very similar to the actual detector's one, except that it contains in addition the Monte Carlo information such as particle type and the originally

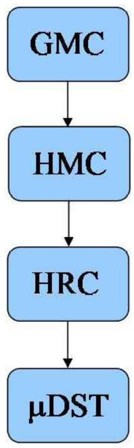

Figure 4.1: Schematic view of the HERMES Monte Carlo chain.

generated particle kinematics. Due to the compatible data format, the HMC output can be fed directly into the **HERMES Reconstruction (HRC)** program, which is also used to decode the response of the real detector. Since the procedure to transfer the detector response into actual track properties is thus identical for experiment and simulation, all possible biases introduced at this stage are automatically accounted for. As a last step, the data is usually passed through the μDST writer to be saved on disk in a compact format, see Sec. 5.4.7. The acceptance and particle interaction effects are calculated by a program called **HERMES Monte Carlo (HMC)**. It contains a model of the HERMES detector and the target based on the GEANT3 tool-kit [79]. For each particle, the transition through the detector is simulated taking into account the interaction cross sections with the materials it traverses. The HMC output contains the response of the detector components, such as the signals from the individual wires of the tracking chambers.

4.2 The PYTHIA 6.2 Generator

In this section some general basics of Monte Carlo working principles and a detailed description of PYTHIA 6.2 will be introduced.

4.2.1 Monte Carlo Methods

The general problem is to generate events according to a known distribution $f(x)$ that has to be non-negative within the allowed range $x_{min} \leq x \leq x_{max}$. A phase space variable x has to be selected randomly, in such a way that the probability to find an event in a small interval *dx* around *x* is proportional to $f(x)dx$. There are three basic methods to find such an x:

1) If $f(x)$ is a simple function that can be analytically integrated and $F(x)$ is the primitive function of $f(x)$, then the integral of the distribution is the total area under $f(x)$. Then one has:

$$\int_{xmin}^{x} f(x)dx = R\int_{x_{min}}^{x_{max}} f(x)dx = R(F(x_{max}) - F(x_{min})), \qquad 0 \leq R \leq 1 \tag{4.1}$$

if the integral is invertible, then

$$x = F^{-1}[F(x_{min}) + R(F(x_{max}) - F(x_{min}))] \quad (4.2)$$

thus selecting a series of random numbers R_i, the distribution of x_i follows $f(x)$ by construction.

2) Often the function of interest is not as simple as in method 1), for example the function is not integrable. In this case, if the maximum of the distribution is known ($f(x) \leq f_{max}$ $\forall x$) the 'accept-reject' method can be applied:

   a) in the first step, a random number R_1 ($0 \leq R_1 \leq 1$) is selected, then x is chosen with uniform probability in the allowed range: $x = x_{min} + R_1(x_{max} - x_{min})$.
   b) in the next step, a new random number R_2 ($0 \leq R_2 \leq 1$) is selected and compared with the ratio $f(x)/f_{max}$, if $R_2 < f(x)/f_{max}$, x is retained, otherwise it is rejected and the process is started again from point a).

   The probability that $f(x)/f_{max} > R_2$ is proportional to $f(x)$, so again the distribution of the x_i follows $f(x)$. This 'hit or miss' method has of course a smaller efficiency then method 1), but has the advantage that no integration is needed.

3) If a simple function $g(x)$ exists, for which the integral and the inverse of the integral is known, and for which $f(x) \leq g(x)$ for all x of interest, a combination of method 1). and 2). can be applied:

   a) in the first step, x is selected from $g(x)$ using method 1).
   b) in the next step, a new random number R_2 ($0 \leq R_2 \leq 1$) is compared with the ratio $f(x)/g(x)$ and the value is retained if $R_2 < f(x)/g(x)$. If this is not true, the chosen x is rejected and a new value needs to be picked from point a).

   The probability to choose a point x in step a) is $P_1(x) = g(x)dx$, the probability to keep this value in step b) is $P_2(x) = f(x)/g(x)$, the total probability to choose a particular x is then $P(x) = P_1(x)P_2(x) = f(x)dx$ which is what is desired.

Several other more complicated methods are available in order to improve the efficiency and to comply with more complicated situations. A description of the presented and other methods can be found, in more detail, for instance in Refs. [78] and [80].

4.3 Fragmentation Models

Hadronization or Fragmentation processes take place in the confinement regime where the perturbative QCD theory doesn't work. In such processes colored partons are transformed into colorless hadrons that constitute the final particle states observed in the detectors.
The fragmentation process is not yet understood from first principles, i.e. starting from the QCD Lagrangian. For this reason, a variety of different phenomenological models have been developed over the past decades. Three main categories are usually distinguished:

- string fragmentation (SF),

- independent fragmentation (IF),
- cluster fragmentation (CF),

but many variants and hybrids exist.
In the following only the first model is described in some details. It represents the most widely used model and the default model for all PYTHIA applications.

4.3.1 String Fragmentation

In the **LUND** Model the fragmentation process is described in a probabilistic and iterative way, in terms of one or a few simple underlying branchings, of the type:

$$\text{jet} \rightarrow \text{hadron} + \text{remainder-jet}$$

$$\text{string} \rightarrow \text{hadron} + \text{remainder-string}$$

and so on. At each branching, probabilistic rules are given for the production of new flavors, and for the sharing of energy and momentum between the products.

This is illustrated in fig.4.2 for a color-singlet $q\overline{q}$ 2-jet event, as produced in e^+e^- annihilation.

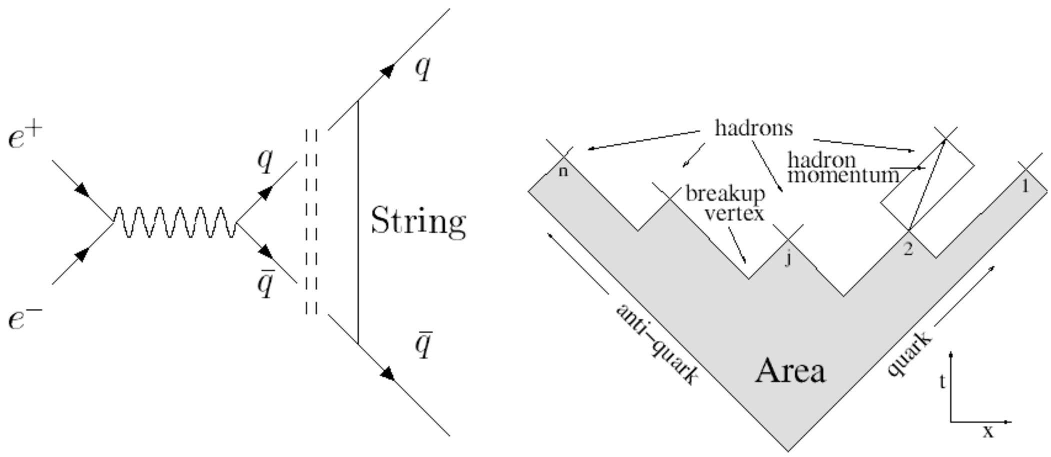

Figure 4.2: Schematic view of a typical LUND string break up.

Lattice QCD studies support a linear confinement picture, i.e. the energy stored in the color dipole field between a charge and an anticharge increases linearly with the separation between the charges, if the short-distance Coulomb term is neglected.

The assumption of linear confinement provides the starting point for the string model. The $q\overline{q}$ pair is produced in a single point in space-time, then the two quarks start to move apart from their common production vertex in opposite directions; the physical picture is that of a color flux tube being stretched between the q and the $\overline{q}$. The transverse dimensions of the tube are of typical hadronic sizes, roughly 1 fm. If the tube is assumed to be uniform along its length, this automatically leads to a confinement picture with a linearly rising potential. The dynamics of

the massless relativistic string with no transverse degrees of freedom is used in order to obtain a Lorentz covariant and causal description of the energy flow due to this linear confinement. The constant force κ caused by this string gives rise to a linear potential. Thus a stable meson configuration produces a so called *yo-yo* mode, in which the system oscillates between states where all energy is contained in the particle's momentum (t_0, t_2) and the turning points where the energy is contained in the string of length Δx stretched between the particles ($E = \kappa \cdot \Delta x$). The string constant, i.e. the amount of energy per unit length, is deduced to be $\kappa \approx 1$ GeV/fm from hadron spectroscopy.
As the q and $\overline{q}$ move apart, the potential energy stored in the string increases, and the string may break by the production of a new $q'\overline{q}'$ pair, so that the system splits into two color-singlet systems $q\overline{q}'$ and $q'\overline{q}$. If the invariant mass of either of these string pieces is large enough, further breaks may occur. In the Lund string model, the string break-up process is assumed to proceed until only on-mass-shell hadrons remain, each hadron corresponding to a small piece of string with a quark in one end and an antiquark in the other.

As already mentioned, the LUND model uses an iterative approach to simulate the fragmentation process. In a first step, the flavor of the new $q\overline{q}$ pair is chosen. Massless quarks without transverse momentum could be produced at one point in space-time and then be pulled apart by the force field. If the quark masses m and transverse momentum $p_\perp$ are taken into account, the quark and antiquark have to be produced at a certain distance from each other to account for the energy contained in the transverse mass $m_\perp = \sqrt{m^2 + p_\perp^2}$. In a quantum mechanical picture, the quarks may be produced at one point and then tunnel out into the classically allowed region, with a tunneling probability:

$$P \sim exp\left(-\frac{\pi m_\perp^2}{\kappa}\right) = exp\left(-\frac{\pi m^2}{\kappa}\right) \cdot exp\left(-\frac{\pi p_\perp^2}{\kappa}\right) \tag{4.3}$$

The tunneling picture implies a suppression of heavy-quark production, $u : d : s : c \approx 1 : 1 : 0.3 : \ 10^{-11}$. Charm and heavier quarks hence are not expected to be produced in the soft fragmentation, but only in perturbative parton-shower branchings $g \rightarrow q\overline{q}$. The $s\overline{s}$ production probability relative to the lighter quarks is a free parameter of the model, since the quark masses are difficult to assign. At HERMES, an example of the difficulty in correctly taking into account the s quark contribution is shown in the disagreement between the experimental and the simulated multiplicities for the Kaon [76] and [77]

In a second step, when the quark and antiquark from two adjacent string breaks are combined to form a meson, the spin and the angular momentum of the new compound state have to be decided. Concerning the two possible spin couplings, a vector meson to pseudo scalar meson ratio of $1:3$ could be expected due to the relative number of available spin states. However, this effect is countered by the spin-spin interaction of the constituents, which suppresses the vector meson production with respect to pseudo-scalar meson production, that is a free parameter of the model.
While mesons emerge rather naturally as bound states consisting of a string with a q and $\overline{q}$ as end points, there is no clear and unique way to produce baryons in this model. Two alternatives are implemented in JETSET. In the simplest form, baryons arise by replacing the $q-\overline{q}$ pair with a $\overline{qq} - qq$ configuration (both qq and $\overline{q}$ are color anti-triplet states). While in this simple model baryons and antibaryons are automatically produced as nearest neighbors, the alternative **POPCORN** model allows for one ([81]) or several (advanced popcorn [82]) mesons to be produced

in-between. No di-quarks are produced, but baryons arise from the successive production of several $q_i\overline{q_i}$ pairs with different colors.

At this stage, the hadron (and thus its mass) has already been depicted upon, as well as the transverse momentum components. What remains to be determined is the energy and longitudinal momentum of the hadron. Only one variable can be selected independently, since the momentum of the hadron is constrained by the already determined hadron transverse mass $m_\perp$,

$$(E + p_z)(E - p_z) = E^2 - p_z^2 = m_\perp^2 = m^2 + p_x^2 + p_y^2\ . \tag{4.4}$$

The fraction z of the total available energy to be assigned to the new particle is given by the Lund symmetric fragmentation function $f(z)$, which expresses the probability that a given z is picked and ensures the validity of the 'left-right symmetry', that requires that the fragmentation process as a whole should look the same, irrespectively of whether the iterative procedure is performed from the q end or the $\overline{q}$:

$$f(z) \propto \frac{1}{z} z^{a_\alpha} \left(\frac{1-z}{z}\right)^{a_\beta} \exp\left(-\frac{bm_\perp^2}{z}\right) \tag{4.5}$$

There is one separate parameter a for each flavor, with the index α corresponding to the 'old' flavor in the iteration process, and β to the 'new' flavor. It is customary to put all $a_{\alpha,\beta}$ the same, and thus arrive at the simplified expression:

$$f(z) \propto z^{-1}(1-z)^a \exp\left(-\frac{bm_\perp^2}{z}\right)\ . \tag{4.6}$$

The variables a and b are needed to regulate the distribution of energy across the final states. The functional form of eq. 4.6 is motivated by the requirement that the fragmentation process should be independent of the choice of the direction the fragmentation is performed along the string ([83]). In fact, at iteration the Lund algorithm randomly chooses a string end from which the fragmentation takes place. Once the remaining energy has dropped below a given value, two hadrons are produced after a final string break. This avoids the problem of putting the last hadron on the mass shell while being at the same time completely constraint by energy and momentum conservation.

In the following sections the other two models, Independent Fragmentation and Cluster Fragmentation, respectively, are briefly described.

4.3.2 Independent Fragmentation

In the **Independent Fragmentation** model, it is assumed that the fragmentation of any system of partons can be described as an incoherent sum of independent fragmentation procedures for each parton separately. The process is to be carried out in the overall c.m. frame of the jet system, with each jet fragmentation axis given by the direction of motion of the corresponding parton in that frame.

Also in this case, an iterative procedure is used to describe the successive hadrons production. An initial quark, carrying a well-defined amount of energy and momentum, is split into a hadron $q\overline{q}_1$ and a remainder-jet q_1, essentially collinear with each other. The energy fraction z

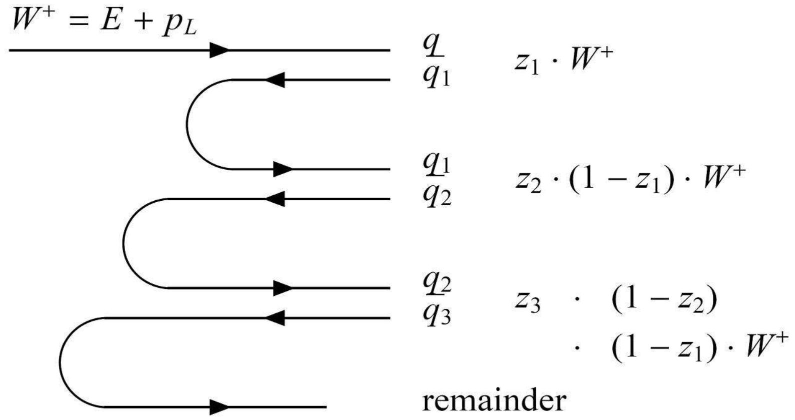

Figure 4.3: Schematic view of the Independent Fragmentation Model.

taken by the new meson $q\overline{q}_1$ is again determined by a distribution function $f(z)$. Several functions can be chosen, but the common forms are the Lund symmetric fragmentation function and the Field-Feynman parametrisation:

$$f(z) = 1 - a + 3a(1 - z)^2 \tag{4.7}$$

with a default value of $a = 0.77$ ([84]).

The Independent Fragmentation model has some problems that are not present in the String Fragmentation model. For example, flavor is conserved locally in each $q_i\overline{q}_i$ splitting, but not in the jet as a whole. In the production of the last meson $q_{n-1}\overline{q}_n$ generated in the jet, an unpaired quark flavor q_n with an energy below a certain threshold is discarded. Furthermore, particles produced with a very small energy fraction z move backwards in the jet ($p_L < 0$) and are usually discarded. Several model extensions exist which fix these issues, the implementation most commonly used are the Hoyer er al. ([85]) and Ali et al. ([86]) programs.
The other problem of the Independent Fragmentation is that its formalism is not Lorentz invariant, the outcome depending on the chosen reference frame. The fragmentation is always carried out in the c.m. frame. However, there is no physical motivation for this restriction.

4.3.3 Cluster Fragmentation

The **Cluster Fragmentation** model uses a QCD parton branching mechanism to obtain the multitude of final state particles. The fragmentation process is basically divided into three steps:

- parton showers evolve the initial partons far off mass-shell into partons nearer to mass-shell. The energy sharing in the branching vertices $q \rightarrow qg$, $g \rightarrow q\overline{q}$ and $g \rightarrow gg$ is given by the corresponding Altarelli-Parisi splitting functions P_{ab};
- in a second step, partners in the same region of phase-space are grouped together into clusters, which in case of high masses fragment into smaller ones.
- Finally, the cluster decays isotropically into hadrons.

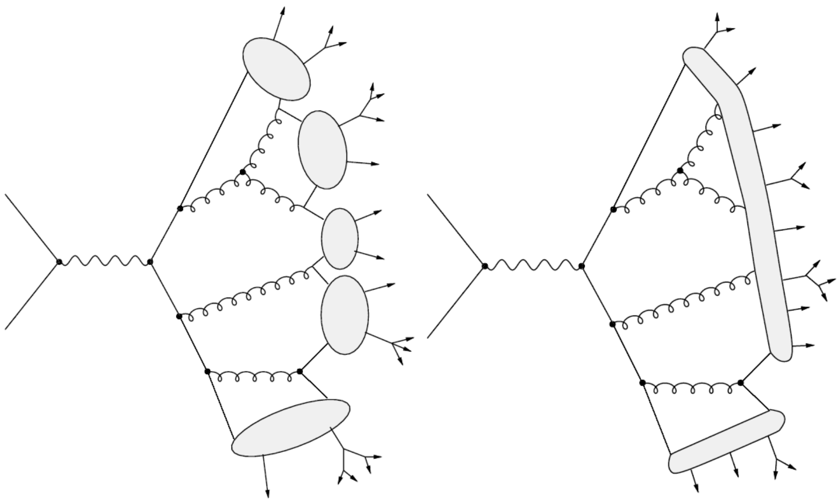

Figure 4.4: Schematic view of the cluster fragmentation.

In general the cluster model contains few adjustable parameters, like the QCD scale parameter Λ_{QCD} and energy cut-offs. Again various implementations exist, the most prominent ones being the Webber model ([87], [88]) implemented in the HERWIG program ([89]) and the CALTECH-II model ([90]).

4.3.4 The Physics of PYTHIA 6.2

According to the model proposed by Schuler and Sj$\ddot{o}$strand ([91]) and further updated in [92], the $\gamma^* p$ cross section can be divided into a photoproduction component and a DIS component. In the limit $Q^2 \to 0$, the DIS process $\gamma^* q \to q$ becomes kinematically forbidden and only the photoproduction component remains. In contrast, when Q^2 increases from zero to high values, the photoproduction component decreases in importance and finally only the DIS process remains. PYTHIA 6.2 is based on a smooth interpolation between real photoproduction (Q$^2 = 0$) data and the truly deep inelastic region (Q$^2 \to \infty$).

Photoproduction ($Q^2 \to 0$)

The strongly interacting fluctuations $\gamma \to q\overline{q}$ provide the main contribution to the total γp cross section. The total rate of $q\overline{q}$ fluctuations is not perturbatively calculable. For this reason, the spectrum of fluctuations is normally split into a low-virtuality and a high virtuality part. The former part can be approximated by a sum over low mass vector-meson states (VMD), while the high-virtuality part should be perturbatively calculable.
The photon wave function can be written as:

$$|\gamma >= c_{bare}|\gamma_{bare} > + \sum_{V=\rho^0,\omega,\phi,J/\psi} c_V|V > + \sum_{q=u,d,s,c,b} c_q|q\overline{q} > + \sum_{l=e,\mu,\tau} c_l|l^+l^- > \qquad (4.8)$$

The coefficients c_i depend on the scale μ used to probe the photon. Thus $c_l^2 \sim (\alpha_{em}/2\pi)(2/3)ln(\mu^2/m_l^2)$. Introducing a cut-off parameter k_0 to separate the low- and the high-virtuality parts, one obtains $c_q^2 \sim (\alpha_{em}/2\pi)(2e_q^2)ln(\mu^2/k_0^2)$. The VMD part corresponds to the range of $q\overline{q}$ fluctuations below k_0 and it is μ-independent (assuming $\mu > k_0$). In conventional notation $c_V^2 = 4\pi\alpha_{em}/f_V^2$ with $f_V^2/4\pi$ determined experimentally.[1] The k_0 parameter is constrained by fits to the parton distributions of the photon to be $k_0 \approx 0.6$ GeV. c_{bare} is fixed by unitariety: $c_{bare}^2 \equiv Z_3 = 1 - \sum c_V^2 - \sum c_q^2 - \sum c_l^2$ and it is always close to unity.
The above superposition corresponds to the existence of three main event classes in γp events (see fig. 4.5):

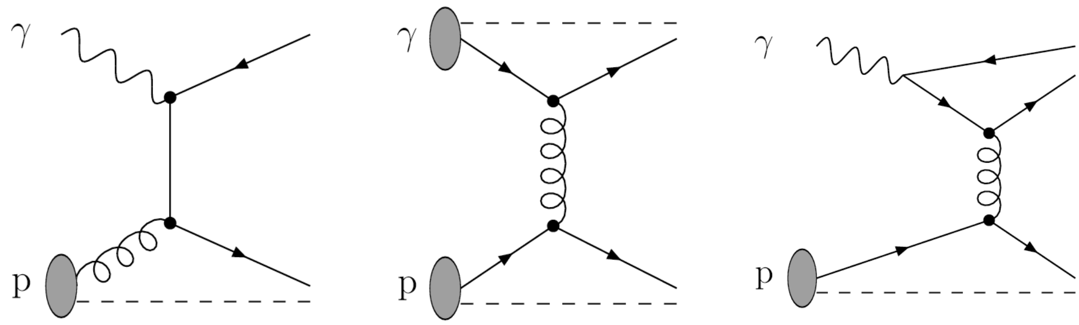

(a) direct (b) vmd (c) gvmd

Figure 4.5: Contributions to hard γp interactions: a) direct, b) VMD and c) anomalous. Only the basic graphs are illustrated; additional partonic activity is allowed in all three processes. The presence of spectator jets has been indicated by dashed lines, while full lines show partons that may give rise to high-$p_\perp$ jets.

a) a 'direct' photon process, wherein the bare photon $|\gamma_{bare}>$ interacts directly with a parton from the proton. The process is perturbatively calculable and no parton distributions of the proton are involved. Although virtual photons can also be absorbed by partons of the nucleon in the leading order (LO) DIS process, see next paragraph, for real photons, only higher-order Photon-Gluon Fusion and QCD Compton scattering are allowed.

b) a VMD process where the photon fluctuates into a vector meson, predominantly a ρ^0 is 'resolved', with the same quantum numbers as the photon before the interaction with the nucleon. The description is that of hadron-hadron scattering where processes like elastic and diffractive scattering, but also soft and hard non-diffractive processes are included. Hard non-diffractive VMD processes proceed via the exchange of a hard gluon. The initial (beam) partons are generated according to parton distribution of the *vector meson*. In soft non-diffractive VMD processes, the (valence-like) parton distributions of the vector meson as well as that of the nucleon are modeled using SU(3). A soft gluon is exchanged between the two partons and the final state hadrons are smeared in transverse momentum only by the hadronization process.

c) anomalous or GVMD (Generalized VMD) photon processes, in which the photon fluctuates into a $q\overline{q}$ pair of larger virtuality then in the VMD class. The photon is 'resolved' but it splits into partons perturbatively, and one of these partons interacts with a parton of the nucleon. Then all kinds of QCD $2 \to 2$ processes are allowed, such as $q_i q_j \to q_i q_j$,

[1] 2.20 for ρ^0, 23.6 for ω, 18.4 for ϕ and 11.5 for J/ψ.

$q\overline{q} \to gg$ and so on. The difference to the hard non-diffractive processes in a) is that here the parton distribution of the photon are relevant.

The leptonic $|l^+l^- >$ states can be neglected in the study of hadronic final states.
The three event classes are distinguished by means of their beam remnants. Usually the nucleon will always leave a remnant with the 'spectator' partons. The direct photon does not leave a remnant, all its energy goes into the hard subprocess. In contrast, resolved photons will leave a beam remnant, except for the very distinct case of elastic and single diffractive VMD events. In soft, non-diffractive VMD processes the remnant will normally have small primordial k_T (transverse momentum) smearing, whereas for the anomalous class the 'beam remnant' coming from the $\gamma \to q\overline{q}$ splitting has a well defined k_T from some cutoff k_0 onwards.
The total γp cross section is the sum of the three contributions

$$\sigma_{tot}^{\gamma p} = \sigma_{direct}^{\gamma p} + \sigma_{VMD}^{\gamma p} + \sigma_{anomalous}^{\gamma p} \tag{4.9}$$

Total hadronic cross sections show a characteristic fall-off at low energies and a slow rise at higher energies. This behavior for a general process $A + B \to X$ can be parameterized by the form:

$$\sigma_{tot}^{AB}(s) = X^{AB}s^{\epsilon} + Y^{AB}s^{-\eta} \tag{4.10}$$

The powers ϵ and η are universal, with fit values:

$$\epsilon \approx 0.0808 \qquad\qquad \eta \approx 0.4525 \tag{4.11}$$

while the coefficients X^{AB} and Y^{AB} are process-dependent. Equation A.6 can be interpreted within the Regge theory, where the first term corresponds to pomeron exchange and gives the asymptotic rise of the cross section. The low energy region is described by the second term, the reggeon.

The VMD part of the cross section can be written as:

$$\sigma_{VMD}^{\gamma p}(s) = \sum_{V=\rho^0,\omega,\phi,J/\psi} \frac{4\pi\alpha_{em}}{f_V^2}\sigma_{tot}^{Vp}(s) \tag{4.12}$$

This contribution corresponds to approximately 70% of the total γp cross section at high energies, with the remaining 20% shared among the direct and anomalous event classes.
The anomalous contribution can be written as:

$$\sigma_{anomalous}^{\gamma p}(s) = \frac{\alpha_{em}}{2\pi}\sum_q 2e_q^2 \int_0^{\infty} \frac{dk_\perp^2}{k_\perp^2}\frac{k_{V(q\overline{q})}^2}{k_\perp^2}\sigma^{V(q\overline{q})p}(s) \tag{4.13}$$

with $k_{V(q\overline{q})}$ a free parameter introduced for dimensional reasons and associated with the typical $k_\perp$ inside the vector meson V formed from a $q\overline{q}$ pair. This equation takes into account the probability for the photon to split into a $q\overline{q}$ state of transverse momenta $\pm k_\perp$ and the cross section for this $q\overline{q}$ pair to scatter against the proton.
To leading order, the direct events come in two kinds:

- QCD Compton $\gamma q \to qg$ (QCDC)
- photon-gluon fusion $\gamma g \to q\overline{q}$ (PGF).

The admixture of these events classes is done according to the scales involved, introduced in fig.4.6. Here $k_\perp$ is related to the $\gamma \to q\overline{q}$ vertex while $p_\perp$ is the hardest QCD $2 \to 2$ subprocess of the ladder between the photon and the proton. The allowed phase space can then conveniently be represented by a two-dimensional plane (see fig.4.6(b))

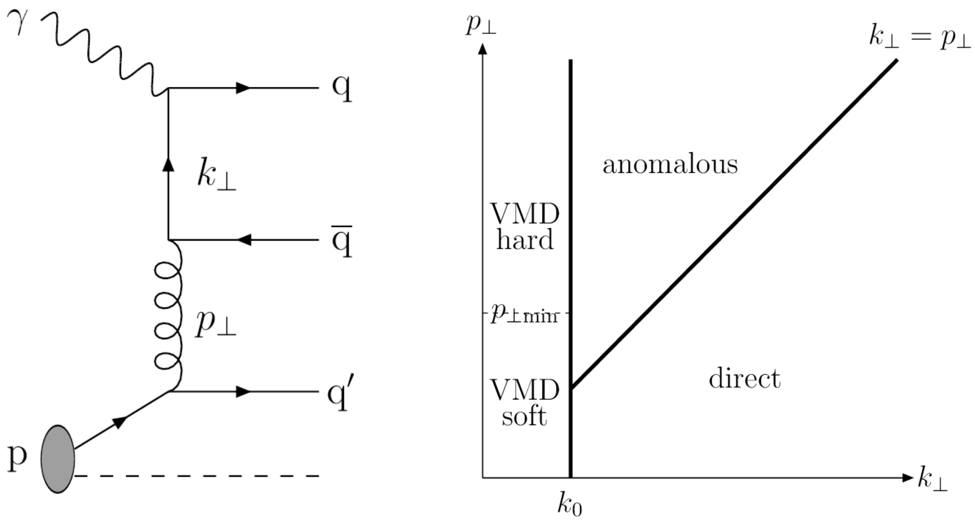

(a) direct (b) vmd

Figure 4.6: (a) Schematic graph for a hard γp process. (b) The allowed phase space for this process with the subdivision into events classes.

- if $k_\perp < k_0$, the transverse momentum at the $\gamma \to q\overline{q}$ vertex is small and the process is VMD.
- if $k_\perp > k_0$, there are two possibilities:
  a) $k_\perp > p_\perp$, then the hard process would be $\gamma q \to q\overline{q}$, with the gluon being part of the gluon distribution in the nucleon, and the photon is direct.
  b) $k_\perp < p_\perp$, then the hard process would be $q\overline{q}' \to q\overline{q}'$, a completely different process, where the $q\overline{q}$ at the photon vertex is the part of the quark distribution inside the photon. This is an anomalous process.

The direct and anomalous event classes are thus subdivided by $k_\perp = p_\perp$ line.

DIS ($Q^2 \to \infty$)

The photon virtuality Q^2 introduces a further scale to the process, showed in fig.4.7.

An additional classification needs to be done for virtual photons, comparing Q^2 with $k_\perp^2$ and $p_\perp^2$:

- the LO DIS process is usually considered when $Q^2 > k_\perp^2 > p_\perp^2$

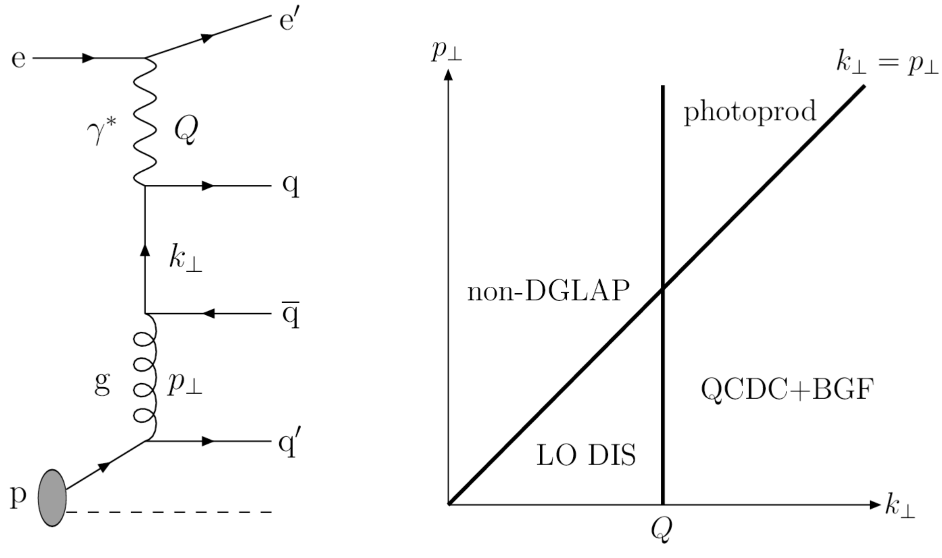

(a) direct (b) vmd

Figure 4.7: (a) Schematic graph for a hard $\gamma^* p$ process. (b) Event classification in the large Q^2 limit.

- the situation when $k_\perp^2 > Q^2 \gg p_\perp^2$ corresponds to $\mathcal{O}(\alpha\alpha_s)$ corrections to LO DIS, the two processes $\gamma^* g \to q\overline{q}$ (PGF) and $\gamma^* g \to qg$ (QCDC). For large enough Q^2 this process is implicitly included in the total DIS cross section and shows up in the (logarithmic) scaling violation of F2. The dividing line $k_\perp^2 > Q^2$ is somewhat arbitrary and was introduced to extrapolate to the region of small $Q^2 \to 0$ where the LO DIS process should be vanishing, but not the $\mathcal{O}(\alpha_s)$ processes.

The DIS cross section can be subdivided into:

$$\sigma_{tot}^{\gamma^* p} \simeq \left(\frac{Q^2}{Q^2 + m_p^2}\right)^m \frac{4\pi\alpha_{em}^2}{Q^2} \; F_2(x, Q^2) = \sigma_{F_2}^{\gamma^* p} \simeq \sigma_{DIS}^{\gamma^* p} = \sigma_{LODIS}^{\gamma^* p} + \sigma_{PGF}^{\gamma^* p} + \sigma_{QCDC}^{\gamma^* p} \quad (4.14)$$

$m = 0, 1, 2$ can be changed by a switch in PYTHIA. The PYTHIA default is $m = 2$. When $Q^2 \to 0$ the last two terms in eq.4.14 become dominant and this could lead to $\sigma_{LODIS}^{\gamma^* p} < 0$ if calculated by subtracting the QCDC and PGF terms from the total DIS cross section. In order to avoid this, the LO DIS cross section is exponentially suppressed by a Sudakov form factor:

$$\sigma_{LODIS}^{\gamma^* p} = \sigma_{DIS}^{\gamma^* p} - \left(\sigma_{PGF}^{\gamma^* p} + \sigma_{QCDC}^{\gamma^* p}\right) \quad \to \quad \sigma_{DIS}^{\gamma^* p} exp\left(-\frac{\sigma_{PGF}^{\gamma^* p} + \sigma_{QCDC}^{\gamma^* p}}{\sigma_{DIS}^{\gamma^* p}}\right) \quad (4.15)$$

At HERMES energies, the scales $p_\perp$, $k_\perp$ and Q^2 might be close to each other such that it is sometimes not possible to unambiguously choose an event type. There is a variety of possible treatments and suppression factors to avoid double counting in those cases. The factor

$$\left(\frac{W^2}{W^2 + Q^2}\right)^n = (1 - x)^n \quad (4.16)$$

with $n \simeq 3$ being a tunable parameter is used to suppress VMD with respect to the LO DIS process in the region where $Q^2 > k_\perp$, but $k_\perp < k_1$, i.e. a region where it cannot easily be decided whether the event still belongs to the resolved or already to the direct class. Altogether, the PYTHIA cross section model for $\gamma^* p$ interactions forms like this:

$$\sigma_{tot}^{\gamma^* p} = \sigma_{DIS}^{\gamma^* p} exp\left(-\frac{\sigma_{PGF} + \sigma_{QCDC}}{\sigma_{DIS}}\right) + \sigma_{PGF}^{\gamma^* p} + \sigma_{QCDC}^{\gamma^* p} + \left(\frac{W^2}{W^2 + Q^2}\right)^n \left(\sigma_{VMD}^{\gamma^* p} + \sigma_{GVMD}^{\gamma^* p}\right) \tag{4.17}$$

The conversion of $\sigma^{\gamma^* p}$ to σ^{ep} is done by weighting with a photon flux in the Weixs$\ddot{a}$cker - Williams approach [93], [94] and [95]:

$$\frac{d^2\sigma^{ep}}{dydQ^2} = \Phi(y, Q^2) \cdot \sigma_{tot}^{\gamma p} \tag{4.18}$$

with

$$\Phi(y, Q^2) = \frac{\alpha_{em}}{2\pi Q^2} \left(\frac{1 + (1-y)^2}{y} - \frac{2(1-y)}{y} \cdot \frac{Q^2_{min}}{Q^2}\right) \tag{4.19}$$

where Q^2 is the negative square of the photon 4-mometum, or the virtuality of the photon. The minimum photon virtuality is $Q^2_{min} = (m_e y)^2/(1-y)$. Integrating over Q^2 up to the maximum experimentally accepted value Q^2_{max}, gives:

$$\frac{d\sigma^{ep}}{dy} = \frac{\alpha_{em}}{2\pi} \left[\frac{1 + (1-y)^2}{y} \cdot ln\left(\frac{Q^2_{max}}{Q^2_{min}}\right) - \frac{2(1-y)}{y} \cdot \left(1 - \frac{Q^2_{min}}{Q^2_{max}}\right)\right] \sigma_{tot}^{\gamma p} \tag{4.20}$$

where $Q^2_{max} = 4E^2(1-y)$ is the maximum experimentally accepted value.

4.3.5 PYTHIA parameters

The physical processes described above can be selected by setting some general PYTHIA parameters.

MSEL	selects the type of processes used to generate events. The choice MSEL$= 2$ selects all QCC processes, including low-p$_\perp$, single and double diffractive and elastic scattering (see tab.4.1). For the photoproduction events the process 95, low $p_\perp$ production is the most probable one ($\sim 89\%$ for the production in 4π and $\sim 80\%$ for the production in the HERMES acceptance), while when the scattered lepton is required the process number 99, Deep Inelastic Scattering, becomes dominant ($\sim 80\%$).
MSTP(13)	(Default $= 1$) Choice of Q^2 range over which electrons are assumed to radiate photons. The setting MSTP(13) $= 2$, used at HERMES corresponds to a user-defined Q^2_{max}.This choice is normally more appropriate for photoproduction events.
MSTP(14)	(Default $= 30$) Choice of the photon structure. MSTP(14) $= 30$, used at HERMES, correspond to a mixture of all the $\gamma^* p$ available components.

MSTP(15)	(Default $= 0$) Possibility to modify the nature of the anomalous photon component with respect to the scale choices and cut-offs of hard processes (the value used at HERMES is the default one).
MSTP(16)	(Default $= 1$) Choice of the definition of the fractional momentum taken by a photon radiated off a lepton. The value MSTP(16) $= 1$, used at HERMES, corresponds to the y variable, i.e. the light-cone fraction.
MSTP(18)	(Default $= 3$) Choice of $p_{\perp min}$ for direct processes to be distinguished from VMD/GVMD processes (the value used at HERMES is the default one).
MSTP(19)	(Default $= 4$) Choice of the partonic cross section in the DIS process (ISUB 99). The value MSTP(19) $= 4$, used at HERMES, corresponds to the DIS parton model cross section modified by the factor $Q^2/(Q^2+m_p^2)$ to provide a finite cross section in the limit $Q^2 \to 0$. It also include the factor $1/(1-x)$ for the conversion from F_2 to σ.
MSTP(20)	(Default $= 3$) Suppression of resolved VMD and GVMD cross section, introduced to compensate for an overlap with DIS processes in the region of intermediate Q^2 and small W^2. The suppression factor is $(W^2/(W^2+Q^2))^{MSTP(20)}$.
MSTP(32)	(Default $= 8$) Definition of Q^2 in hard scattering for $2 \to 2$ processes. The value MSTP(32) $= 8$, used at HERMES, corresponds to $Q^2 = p_\perp^2 + (P_1^2 + P_2^2 + m_3^2 + m_4^2)/2$, with P_1^2 and P_2^2 the virtualities of the two incoming particles and m_3 and m_4 the masses of the outgoing particles.
MSTP(38)	(Default $= 5$) Handling of masses in quark loops (the value used at HERMES is MSTP(32) $= 4$).
MSTP($51/52$)	(Default $= 7/1$) Choice of the proton parton distribution set (the values used at HERMES are MSTP(51) $= 4046$ and MSTP(52) $= 2$).
MSTP($53/54$)	(Default $= 3/1$) Choice of the pion parton distribution set (the values used at HERMES are the default ones).
MSTP($55/56$)	(Default $= 5/1$) Choice of the photon parton distribution set (the values used at HERMES are the default ones).
MSTP(57)	(Default $= 1$) Choice of Q^2 dependence in parton distribution functions. The value MSTP(57) $= 1$, used at HERMES corresponds to the parameterized Q^2 dependence.
MSTP(58)	(Default $= min(5, 2 \times MSTP(1))$) Maximum number of quark flavors used in parton distributions (the value used at HERMES is MSTP(58) $= 4$).
MSTP($91/94$)	Switchs for beam remnant treatment.
MSTP(101)	(Default $= 3$) Structure of the diffractive system (the value used at HERMES is MSTP(101) $= 1$).
MSTP(102)	(Default $= 1$) Decay of a ρ^0 meson produced by elastic scattering of an incoming γ (the value used at HERMES is the default one).
MSTP(111)	(Default $= 1$) Switch for fragmentation and decay (the value used at HERMES is the default one).
MSTP(121)	(Default $= 0$) Calculation of kinematics selection coefficients and differential cross section maxima for included subprocesses (the value used at HERMES is MSTP(121) $= 1$).

PARP(2)	(Default $=10$ GeV) Lowest c.m. energy for the event as a whole (the value used at HERMES is PARP(2) $=7$).
PARP(18)	(Default $=0.4$ GeV) Suppression factor for GVMD processes compared with VMD processes (the value used at HERMES is PARP(18) $=0.17$).
PARP($81-90$)	Parameters for multiple interactions.
PARP($91-100$)	Parameters for beam remnant treatment.
PARP(104)	(Default $=0.8$ GeV) Minimum energy above the threshold for which hadron-hadron total, elastic and diffractive cross sections are defined (the value used at HERMES is PARP(104) $=0.3$).
PARP(111)	(Default $=2$ GeV) Minimum invariant mass of the remnant hadronic system (the value used at HERMES is PARP(111) $=0$).
PARJ(1)	(Default $=0.10$) Suppression of diquark-antidiquark pair production in the color field compared with the quark-antiquark production (the value used at HERMES is PARJ(1) $=0.029$).
PARJ(2)	(Default $=0.30$) Suppression of s quark pair production in the field compared with u or d pair production (the value used at HERMES is PARJ(2) $=0.283$).
PARJ(3)	(Default $=0.4$) Extra suppression of strange diquark production compared with the normal suppression of strange quarks (the value used at HERMES is the default one).
PARJ($41-45$)	(Default $=0.3/0.5$) Parameters for the symmetric Lund fragmentation function (the values used at HERMES are PARJ(41) $=1.94$ and PARJ(45) $=1.05$).
MSTJ(1)	(Default $=1$) Choice of the fragmentation scheme. The value MSTJ(1) $=1$ corresponds to the string fragmentation according to the LUND model (the value used at HERMES is the default one).
MSTJ(12)	(Default $=2$) Choice of the baryon production model (the value used at HERMES is MSTJJ(12) $=1$).

The original JETSET parameters that regulate the fragmentation in the Lund model have been tuned for high energy e^+e^- collisions. The model has been adjusted to the HERMES energies in [76] and [77]. In particular the a and b parameters of the Lund fragmentation function and the Gaussian width σ of the transverse momentum distribution were tuned to the yields of positive and negative hadrons. The resulting model was tested by comparing the P_z distrinutions from data and from Monte Carlo after correcting the former for the acceptance function of the detector (see Sec.6.7).

ISUB	**Process**	**PhotoProduction** (%)	**DIS** (%)
Hard QCD processes			
11	$f_i f_j \to f_i f_j$	1.8	1.0
53	$gg \to f_k \overline{f}_k$	0.007	0
68	$gg \to gg$	0.5	0.19
Soft QCD processes			
92/93	Single Diffraction	0.89	0.24
95	low $p_\perp$ production	81	13
Deep Inelastic Scattering			
99	$\gamma^* q \to q$	9	80
Photon Induced			
131	$f_i \gamma^*_T \to f_i g$ (QCDC)	3.5	2.9
135	$g \gamma^*_T \to f_i \overline{f}_i$ (PGF)	0.91	0.46

Table 4.1: Summary table of some physics processes implemented in PYTHIA.

Chapter 5

The HERMES experiment at HERA

HERMES is a fixed-target experiment located in the east hall of the HERA storange ring at DESY in Hamburg. HERA consists of two rings, one for the lepton beam (27.5 GeV electrons or positrons) and the other for the 900 GeV proton beam. HERMES shares the ring with three other experiments (a sketch of the ring setup is showed in fig 5.1): H1 and ZEUS, which, being collider experiments, use the two colliding beams, and HERA-B which uses the proton beam only.

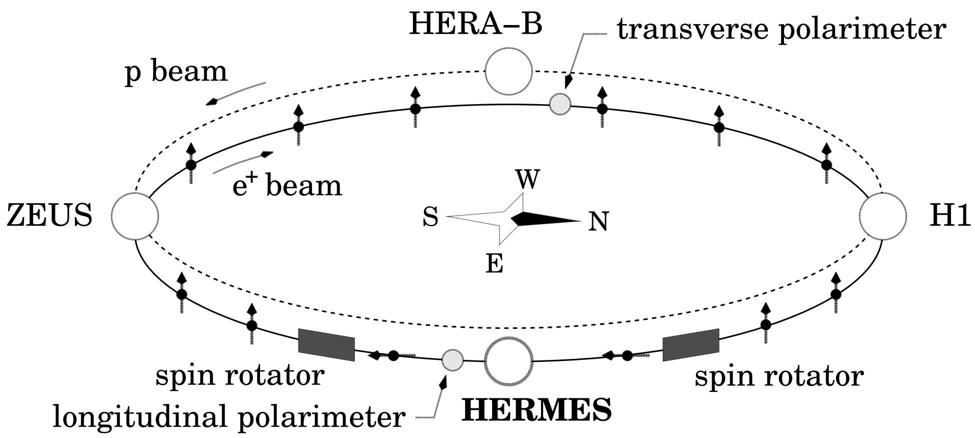

Figure 5.1: Sketch of the HERA storage ring (in the setup for the years 1995 to 2000) with the four experiments. The spin rotators around HERMES switch the positron/electron spin from transverse to longitudinal and back. Also shown are the polarimeters used to measure the transverse and longitudinal polarization of the beam

The positron or electron beam and a fixed gaseous target internal to the beam line are used by HERMES. This experiment was designed to optimize the measurements of quantities related to the nucleon's inner spin distribution. To this purpose high beam current, high values of target and beam polarization, high target density and a relatively large detector acceptance are required.

5.1 The Beam Polarization

The conventions for the HERA coordinate system are: the proton beam momentum defines the z direction; the $+x$ axis points away from the center of the ring and the $+y$ axis points upward. The electron beam consists of up to 220 bunches with a length of 27 ps separated by 96 ns. Typical currents at injection of the beam were around 35 mA in the $1996/1997$ data taking period and up to almost 50 mA in the 2000 data taking period. Over the beam lifetime of about 10 hours the current decreases exponentially and the beam is finally dumped when the current has reached ~ 13 mA.
Electrons or positrons are injected unpolarised at 12 GeV into the HERA storage ring and are subsequently ramped up to the nominal beam energy of 27.5 GeV. The lepton beam is transversely polarised by the *Sokolov-Ternov effect* (ST) [96] which causes the leptons to predominantly aligne their spins in the vertical direction, parallel to the magnetic field of the storage ring, by radiating photons.
The *longitudinal* polarization necessary for HERMES can be obtained by rotating the spin vectors of the positrons (electrons) from the transverse direction to a direction parallel to the beam orbit. A detailed description of the beam polarization and of its diagnostic is reported in Appendix A.0.6.

5.2 The Internal Gas Target

One of the strengths of the HERMES experiment is its target [97], because of its purity and its position internal to the beam-pipe, so that the electron beam does not encounter any unpolarized material before colliding with the target atoms. Basically it has three components:

- an atomic beam source (ABS) producing polarized hydrogen or deuterium atoms
- a storage cell around the central axis of the positron beam
- two diagnostic devices, one to measure the polarization (Breit-Rabi Polarimeter, BRP) and the other one to measure the atomic fraction of the gas (Target Gas Analyzer, TGA).

A schematic view of the target and of the setup with these components is shown in fig. 5.2 and fig. 5.3.

5.2.1 The Atomic Beam Source

The ABS [98] is a device which makes use of the Stern-Gerlach effect [99] to generate atomic polarization of hydrogen or deuterium. First, the molecular gas is dissociated by means of radio frequency dissociator, with dissociation degree up to 80% (from 2000 on a microwave dissociator was used instead) causing a discarge inside a glass tube. The H/D atoms flow through a cooled nozzle with a temperature of 100 K. A thin layer of frozen water on the nozzle surface helps to prevent recombination. The atomic gas then enters a sextupole magnet system with a radial field dependence. Due to the Stern-Gerlach effect atoms crossing a magnetic field with a gradient perpendicular to their motion experience different forces according to their magnetic moments. Those atoms having a positive magnetic moment are focused toward the axis of the magnet, those with a negative magnetic moment are defocused toward the pole tips. Thus the sextupole magnets select only those atoms having electrons with spin projection $m_s = +\frac{1}{2}$. In

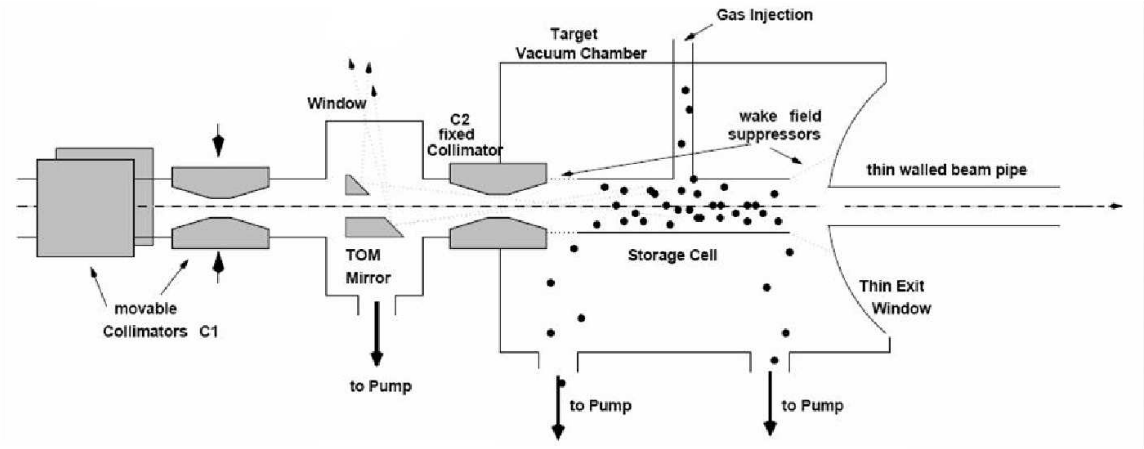

Figure 5.2: Scheme of the HERMES gas target

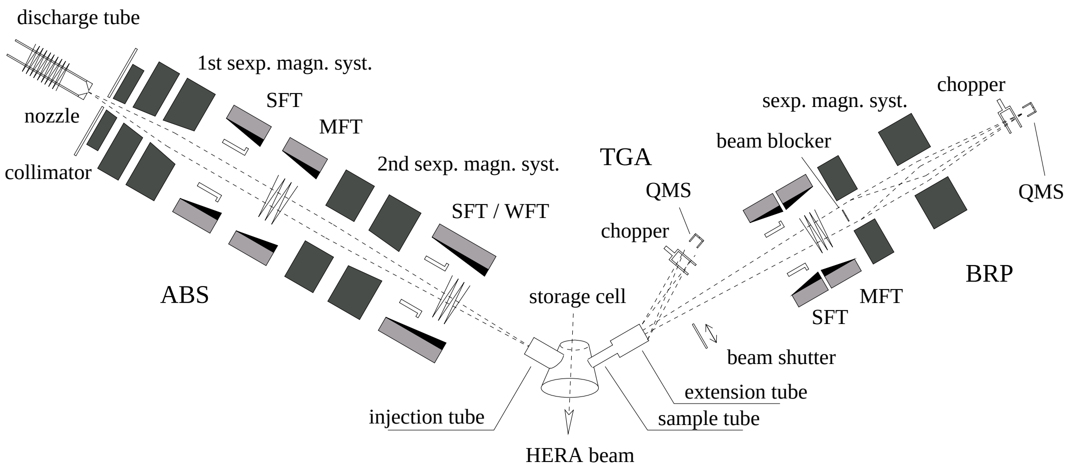

Figure 5.3: Representation of the Atomic Beam Source (ABS), Breit-Rabi Polarimeter (BRP) and Target Gas Analyzer (TGA) with the storage cell in the center.

order to obtain *nuclear* polarization, transitions between hyperfine states are induced. The relative energies of the four (six) hyperfine states of hydrogen (deuterium) are displayed in fig.5.4 as a function of the ratio of the external magnetic field B to the critical field B_c.

In figure 5.4 m_I is the spin projection number of the nucleon ($\pm\frac{1}{2}$ for proton, ± 1, 0 for deuterom), m_s that of the electron ($\pm\frac{1}{2}$) and $m_F = m_s + m_I$ is the total spin projection. F is the spin of the combined system.
The combination of injected states can be changed within a fraction of a second. The nucleon polarization is being flipped randomly on the time scale of a minute, fast enough to reduce systematic influences on asymmetry measurements to a minimum and slow enough to avoid synchronization problems in the data acquisition. The atoms with polarised nucleons and unpolarised shell electrons are injected in the storage cell with fluxes of up to $6.5 \cdot 10^{16}$ atoms/s.

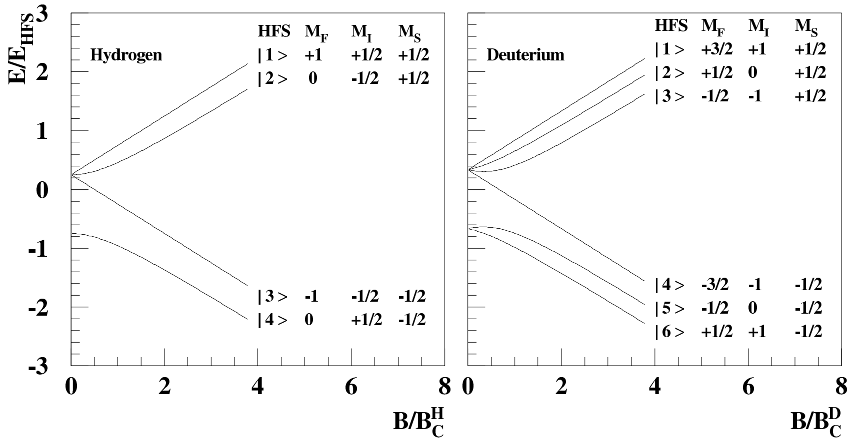

Figure 5.4: Hyperfine splitting of Hydrogen (left) and Deuterium (right) energy levels as a function of the magnetic holding field B relative to the critical field B_c. The energy is given relative to the hyperfine splitting at $B = 0$.

5.2.2 The Storage Cell

After the selection of the hyperfine states the gas is fed into a storage cell whose purpose is the increase of the areal target density by about two orders of magnitude compared to a free jet target. The areal target density obtained is about 10^{14} $atoms/cm^2$. The storage cell is an open ended elliptical tube (40 cm long, 29 mm wide and 9.8 mm high) made of thin (75 μm) ultra pure aluminum. It is being cryogenically cooled in order to reduce the termal velocities of the gas atoms inside. A feed tube through which the polarized gas atoms are injected into the cell is installed perpendicular to the beam axis at the center of the cell. After a number of wall collisions the atoms diffuse into the ultra high vacuum of the lepton beam line where they are pumped away by a high speed differential pumping system. During the diffusion process the atoms cross the lepton beam many times. The cell is coated with a radiation hard hydrophobic silicon based polymer called Drifilm in order to reduce depolarization and recombination of atoms due to wall collisions. As the Drifilm ages and gets damaged after a few weeks of HERMES running, a monolayer f H_20/D_20 forms on the interior of the cell. This layer was found to compensate for the loss of the Drifilm. The cell axis coincides with the lepton beam orbit and the target density has a triangular shape with the maximum in correspondence of the position of the injection tube. The cooling of the storage cell is set to the optimal value for hydrogen of 100 K where recombination and depolarization effects are low. In addition to the injection tube a smaller sampling tube exists which extracts about 5% of the gas for analysis in the TGA and BRP. This sampling tube is installed opposite to the injection tube at an angle of $120°$. The distance between injection and sampling tube allows for the thermalization of the gas with the storage cell wall. A vented extension at the downstream end of the tube ensures that all scattered particles in the HERMES acceptance traverse the same amount of material in the cell walls. In front of the storage cell and behind its extension so-called wake-field suppressors provide a gradual electrical transition between the storage cell and the beam pipe. Without the wake-field suppressors the bunched positron beam in HERA would cause strong radio frequency fields to be emitted at the discontinuity of the beam pipe impendance. These wake-field would not only heat up the target cell but also destabilise the beam orbit.
For the 2000 data taking period, the storage cell was replaced by a smaller one (21 mm wide

instead of 29 mm) which resulted in an additional increase of areal target density by a factor 1.6. An uniform magnetic holding field of 335 mT along the beam axis generated by a superconducting magnet.

5.2.3 The Target Gas Analyser TGA

The main component of the TGA [100] is a $90°$ off-axis quadrupole mass spectrometer (QMS) which is used for the measurement of the atomic and molecular content of the gas sampled at the center of the storage cell. In front of the QMS a chopper periodically blocks the sample beam to allow subtraction of the residual gas signal. In order to avoid interference with the BRP measurement the TGA is tilted by $7°$ with respect to the sampling tube. The measured normalised nucleon flow rates for atoms (ϕ_a) and molecoules (ϕ_m) yield the degree of dissociation of the sample beam:

$$\alpha_T GA = \frac{\phi_a}{\phi_a + \phi_m} \tag{5.1}$$

which is measured roughly once per minute. Together with calibration measurements which are performed during the breaks between fills, two quantities can be calculated: the degree of dissociation, also called *atomic fraction*, in the absence of recombination within the cell, α_0, and the fraction of atoms surviving recombination in the cell, α_r. Both values are necessary for the determination of the density-averaged nuclear polarisation P_T in the cell.

5.2.4 The Breit-Rabi Polarimeter BRP

A second measurement using the gas extracted by the sampling tube is performed by the BRP [101]. The BRP consists of a pair of radio frequency transitions - a strong (SFT) and a medium field transition (MFT) - which can be tuned for different hyperfine state transitions. A sextupole magnet system focuses atoms with $m_s = +\frac{1}{2}$ towards the detector unit and defocuses atoms with $m_s = -\frac{1}{2}$. To prevent atoms which enter on the symmetry axis of the sextupole magnet system (where the field gradient is zero) from entering the detector unit, a beam blocker is installed in front of the first magnet of the sextupole system. As in the TGA, a QMS together with a chopper for background subtraction is used for the detection. From the measured relative populations of the hyperfine states of hydrogen atoms, the atomic polarization P_a can be deduced.
The value of the polarization P_a measured with the BRP is the polarization at the center of the storage cell. It must be related to the polarization averaged along the cell, P_{BRP}, by sampling corrections c_P:

$$P_{BRP} = c_P \cdot P_a \tag{5.2}$$

the sampling corrections are obtained with the help of the Monte Carlo simulations of the balistic flow of the target gas atoms in the storage cell [102]. Using the BRP and TGA measurements the averaged target polarization P_T as seen by the electron beam can be calculated:

$$P_T = \alpha_0[\alpha_r + (1 - \alpha_r)\beta] \cdot P_{BRP} \tag{5.3}$$

Here β is the ratio of the nuclear polarization of molecules produced by recombination and the nuclear polarization of the atoms. A direct measurement of the remnant polarization contained in the molecules is not possible at HERMES as the BRP is capable only of atomic polarization measurements. In dedicated measurements at higher storage cell temperature of 260 K and by boundary considerations, the range of β could be restricted to a range of $\beta = [0.45, 0.83]$. The uncertanty on β is part of the systematic uncertanty of the target poalrization value.

5.2.5 The Target Magnet

The target magnet surrounding the storage cell provides a holding field defining the polarization axis. It also suppresses spin relaxation due to the splitting of the hyperfine energy levels. While a holding field parallel to the lepton beam has no effect on the beam and a marginal effect on the scattered particle trajectories, for a transverse holding field different effects have to be taken into account. The deflection of the beam requires compensation by correction coils and limits the strength of the magnetic field due to the amount of synchrotron radiation generated by the beam. Not only the beam but also the scattered particles are deflected. Hence, the reconstructed vertex position and scattering angles must be corrected for the deflection.
In addition to the influence on the particle trajectories, depolarizations effects occur due to the bunched strcture of the HERA positron beam. The time period of 96.1 ns between two adjacent lepton bunches corresponds to a bunch frequency of 10.41 MHz. The induced magnetic high frequency field around the lepton beam contains a large number of harmonics because of the short bunch length of 30 ps. The energy splitting and hence the resonance frequency between the hyperfine states of the target atoms depends on the strength of the magnetic holding field *B*. If a harmonic of the beam induced field matches such a transition frequency, the target polarization decreases. In order to avoid depolarization, the holding field must be set to a value between such resonances. Two kinds of transitions, π and σ, exist for beam induced fields perpendicular and parallel to the holding field, respectively. For nuclear π ($\Delta m_I = \pm 1, \Delta m_s = 0$) transitions which are possible for both longitudinal and transverse holding fields, the spacing ΔB between two resonances is of the order of 50 mT for a field strength around $B = 300$ mT. σ ($\Delta m_I = \pm 1, \Delta m_s = \mp 1$) transitions occur only in case of a transverse holding field and have a very small spacing ($\Delta B = 0.37$ mT at $B = 300$ mT). Hence, the transverse magnetic holding field needs a good homogeneity over the storage cell to minimize the bunch field induced depolarization.
The longitudinal target magnet was operated at a field strength $B^{\parallel} = 335$ mT with maximum deviations around 10 mT within the storage cell. For the transverse target a homogeneity of $\Delta B^{\perp} \leq 0.15$ mT was required at a field value of 297 mT. With the magnet configuration in 2002 maximum deviations of $\Delta B_z^{\perp} = 0.05$ mT, $\Delta B_y^{\perp} = 0.15$ mT and $\Delta B_x^{\perp} = 0.60$ mT were achieved. This setup was improved by an additional correction coil installed in 2003 which reduced the deviations to $\Delta B_y^{\perp} = 0.05$ mT and $\Delta B_x^{\perp} = 0.30$ mT [103]. A dedicated measurements showed that the depolarization because of the σ resonance could be reduced by roughly $\frac{1}{3}$ of the total effect [104].

5.2.6 The Unpolarised Gas Feed System (UGFS)

Alternatively to the injection of polarised atoms from the ABS, the storage cell can be filled with unpolarised gas using the **Unpolarised Gas Feed System (UGFS)**. Adjustable densities and the possibility to inject the gas also into the target chamber (as opposed to the storage cell) furthermore allow various calibration measurements necessary for the determination of the target polarisation and the different contributions to its systematic uncertainty.

5.3 The HERMES Spectrometer

The HERMES experiment uses an open forward magnetic spectrometer for the detection of the scattered positron and a large fraction of the hadronic final states. The spectrometer is capable of the detection in a broad kinematic region with a good angular and momentum resolution [105]. It consists of two identical halves above and below the HERA beam pipe. It has three main components: the spectrometer magnet, the tracking system consisting of three sets of tracking chambers in front, inside and behind the spectrometer magnet and a particle identification (PID) system. The location of the various detectors is shown in fig. 5.5.

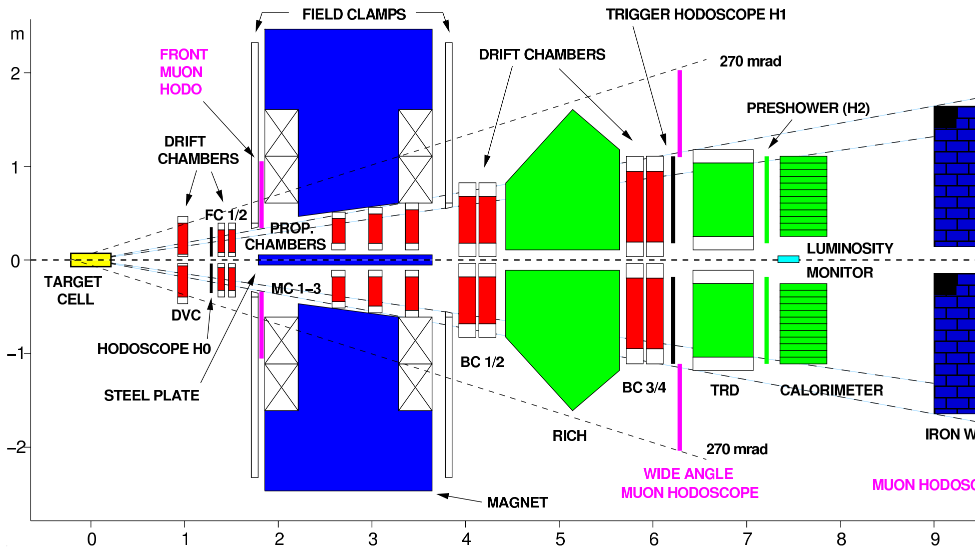

Figure 5.5: A two dimensional, vertical cut of the HERMES spectrometer. Until 1997 a threshold Cherenkov detector was in place of the Ring Imaging Cherenkov (RICH), the silicon detector was not installed until 2001

A detailed description of the detector components can be found in Ref. [97]. The Axes for the HERMES coordinate system are defined such that the z direction is along the incident lepton momentum, x points towards the center of the HERA ring and y points upward.

5.3.1 The spectrometer Magnet

During data taking the spectrometer magnet is operated at a deflecting power of $\int Bdl = 1.3$ Tm. The magnetic dipole field is oriented in the vertical direction, deflecting charged particles horizontally. The influence of the field on the HERA beams is minimised by a 11 cm thick steel plate surrounding the beam pipe. The remaining effects are compensated by a correction coil. Field clamps in front and behind the magnet reduce fringe fields in the adjacent detectors. The aperture of the magnet limits the geometrical acceptance of the spectrometer to ± 140 mrad in the vertical and ± 170 mrad in the horizontal direction. To maintain good acceptance for low momentum particles the acceptance of the detector in the horizontal plane is increased by ± 100

mrad starting from the center of the magnet. The lower limit on the vertical acceptance of ± 40 mrad is given by a septum plate in the horizontal plane that shields both HERA beams from the field of the spectrometer magnet.

5.3.2 The Tracking Devices

Except for the silicon detector right next to the target, all tracking devices are wire chambers, each consisting of seeral planes. The planes come with three different wire orientations, vertical and tilted by ± 30 with respect to the vertical axis. The two most important chambers are the **Front Chambers** (FC) [106] at about 1.6 m from the target center, just in front of the magnet, and the **Back Chambers** (BC) [107] that are combined into two groups in front and behind the RICH detector. Each of their modules consists of six wire planes, where one set of planes has the wire positions staggered by half the drift cell size with respect to the other to help resolve left-right ambiguities.
The two modules of the **FC** have drift cells of 7 mm width and 8 mm depth. They are filled with a mixture of 90% Ar, 5% CO_2 and 5% CF_4. The choise of this particular mixture results from three requirements: non-flammability, fast electron drift velocities, small aging effects (assured by the CF_4 component). The resolution per plane is 225 μm, the single plane efficiency ranges from 97% to 99% depending on the position in the cell.
The **BC**s have a drift cell size of 15×16 mm and the same gas mixture as the FCs. The resolutions are 210 μm for $BC1/2$ and 250 μm for $BC3/4$. For positrons, the BC plane efficiency was found to be well above 99%, while it is somewhat smaller for hadrons (about 97%) because of their reduced ionization density.
The three **Magnet Chambers** (MC) [108] are located in the gap of the magnet. Initially they were intended to help resolve multiple tracks in case of high track occupancies. This turned out not to be necessary because of the low background. Still, they are helpful in determining the momentum of low energy particles (for istance from Λ decays) that do not reach the back part of the detector due to the large deflection in the magnet. The MCs are multi-wire proportional chambers (MWPC) able to operate in a strong magnetic field. Each chamber has three planes with a cell width of 2 mm, providing a resolution of 700 μm. A digital single bit-per-wire readout was chosen to accommodate the readout electronics for a large number of channels (5504) within a very restricted space volume.
Another set of **Drift Vertex Chambers** (DVC) was installed 1.1 m downstream of the target between the 1996 and 1997 data taking periods. These chambers consist of six planes of conventional drift chambers with a design similar to that of the FCs, albeit smaller, and the same gas mixture as the Fcs. The acceptance is somewhat larger though, extending vertically from ± 35 to ± 270 mrad and horizontally to ± 220 mrad. The planes have a wire spacing of 6 mm and a resolution of 220 μm per plane.
The Silicon detector (**Lambda-Wheels**) [109] has been installed in 2002. Two sets of disk-shaped silicon detectors are mounted 45 and 50 cm downstream of the target cell. The disks have a diameter of 33.6 cm and a hole of 9 cm leaving space for the beam pipe and wake field suppressors around it. This detector increases the acceptance for longer living particles such as Λ, Λ_c, K_s that decay outside the target region.

The combined information of many tracking detectors is needed for an unambiguously track reconstruction. At HERMES, a three-search algorithm is applied for fast and efficient track finding. The principle of this method is to look at the whole hit pattern of the detectors in several iterative steps, doubling the resolution at each step. For a given resolution, the algorithm checks if the hit pattern contains a subpattern consistent with an allowed track, by comparing with all sets of allowed patterns stored in a database. If this is the case, the procedure is repeated at increased resolution, otherwise the pattern is rejected. The HERMES reconstruction program (HRC) [110] needs about 11 iterations to find a track. This is done indipendently for the hits in the front and back part of the detector, resulting in a set of front and back partial tracks. In a next step, all combinations of front and back partial tracks are tested if they match spatially in the x - y plane within a defined tolerance. Matching combinations are refitted to form a full track. The track momentum is determined by comparing the position of the track in front and its slope in front and behind the magnet with numbers in a look-up table. This look-up table contains the momentum of a given track as a function of the relevant track parameters. Using interpolation methods, the contribution of HRC to the precision of track momentum determination is less than $\Delta p/p = 0.5\%$. The overall resolutions are somewhat lower due to multiple scattering and bremsstrahlung in the spectrometer material. In many of the data productions the information of the DVCs was not used. Instead, a slightly different method was developed to reconstruct tracks using only the FC and BC hits. The matching of the front and back partial tracks is first done with a larger tolerances. Then, by fixing the matching point to that of the higher quality back track in the middle of the magnet, the front track parameters are recalculated. In an iterative procedure thus the momentum resolution can be considerably improved. This method is called force bridging, i.e. the front track is forced to match the back track in the center of the magnet. In 1998 the threshold Cherenkov detector in between BC$1/2$ and BC$3/4$ was replaced by the RICH. The RICH material has a considerably larger radiation length than that of the Cherenkov, resulting in an increase of the total radiation length of the spectrometer by a factor 20. As a consequence, the resolution of the data taken with the RICH decreased by up to a factor of 2 with respect to data taken with the Cherenkov counter.

5.3.3 The Particle Identification (PID) Devices

The HERMES PID system consists of four different particle identification (PID) detectors, a lead glass calorimeter, a preshower detector, a transition radiation detector (TRD) and a threshold Cherenkov detector that was replaced by a Ring Imaging Cherenkov detector (RICH) in (1998). A probabilistic algorithm which uses the responses of these detectors provides a very clean ($> 98\%$) separation of the scattered positrons from hadrons. The cherenkov detector has been used to separate pions from other hadrons as well as for lepton/hadron separation at low momenta. The main task of the RICH detector is the positive identification of pions, kaons and protons, but it will be shown below that it can help to identify positrons as well.

The Electromagnetic Calorimeter

The calorimeter consisting of 420 lead glass blocks in ech detector half is located at the downstream end of the spectrometer. The length of the lead glass blocks is 50 cm and corresponds to 18 radiation lengths. Each block is viewed from the rear by a photomultiplier tube (PMT) measuring the amount of Cherenkov light produced by secondary leptons generated in an electromagnetic shower. The gain of the PMTs is monitored continuously by a dye laser sending light pulses through glass fibers to every PMT as well as to reference a photo diode. A comparison of the PMT signals to that of the reference diode measures the relative gain of the PMTs.

The energy resoultion of the calorimeter can be parametrized as

$$\frac{\sigma(E)}{E}[\%] = \frac{5.1 \pm 1.1}{sqrtE(GeV) + (1.5 \pm 0.5)}$$

The spatial resolution of the impact point is $\sigma \approx 0.7$ cm.

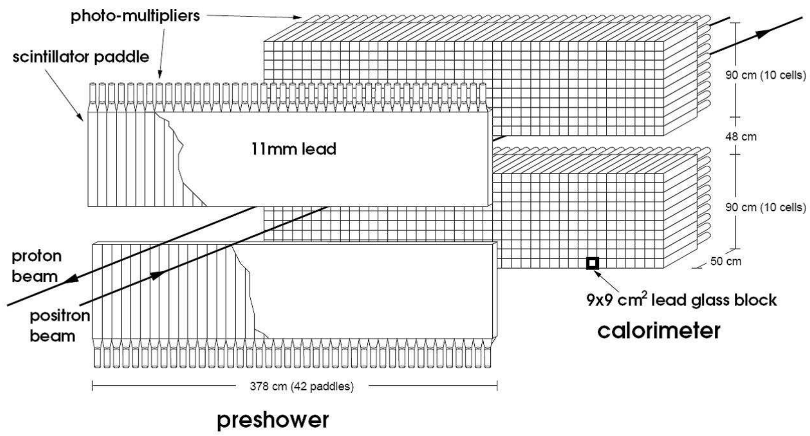

Figure 5.6: A three dimensional view of the HERMES Electromagnetic Calorimeter.

Besides for PID the calorimeter is used for detection and energy determination of photons and it is part of the first level trigger. For particle identification the ratio E/p of the deposited energy to the momentum of the particle is considered. In contrast to leptons (positrons or electrons) which produce electromagnetic showers contining almost all their energy, hadrons only deposit a fraction of their energy due to ionization losses and nuclear interactions.
The top-right panel of the fig. 5.11 shows the probability distributions for hadrons and positrons to deposit a fraction E/p of their energy in the calorimeter. The positrons have a distinct peak at $E/p \simeq 1$, while the hadron distribution is much wider and mostly to lower values. If positrons with high momentum radiate bremsstrahlung photons in the detector material in front or inside the magnet, the photons will travel along the positron path and may hit the same calorimeter cluster as the positron. Thus the detected energy in the calorimeter can be larger than the positron momentum determined by the magnet *after* the photon emission (this explain the large tail at $E/p > 1$).

The Preshower Detector

Right in front of the calorimeter a preshower detector consisting of a wall of 42 vertically oriented plastic scintillator paddles behind an 11 mm thick lead plate (corresponding to 2 radiation lengths) is installed. Adjacent paddles are staggered with some overlap for maximum efficiency. Each paddle is read out individually by a PMT. Positrons may initiate electromagnetic showers in the lead plate and deposit energy with a mean of $20 - 40\ MeV$ in the scintillators whereas hadrons only produce a minimum ionizing signal of 2 MeV. The probability distribution for the preshower signal is also shown in fig. 5.11.

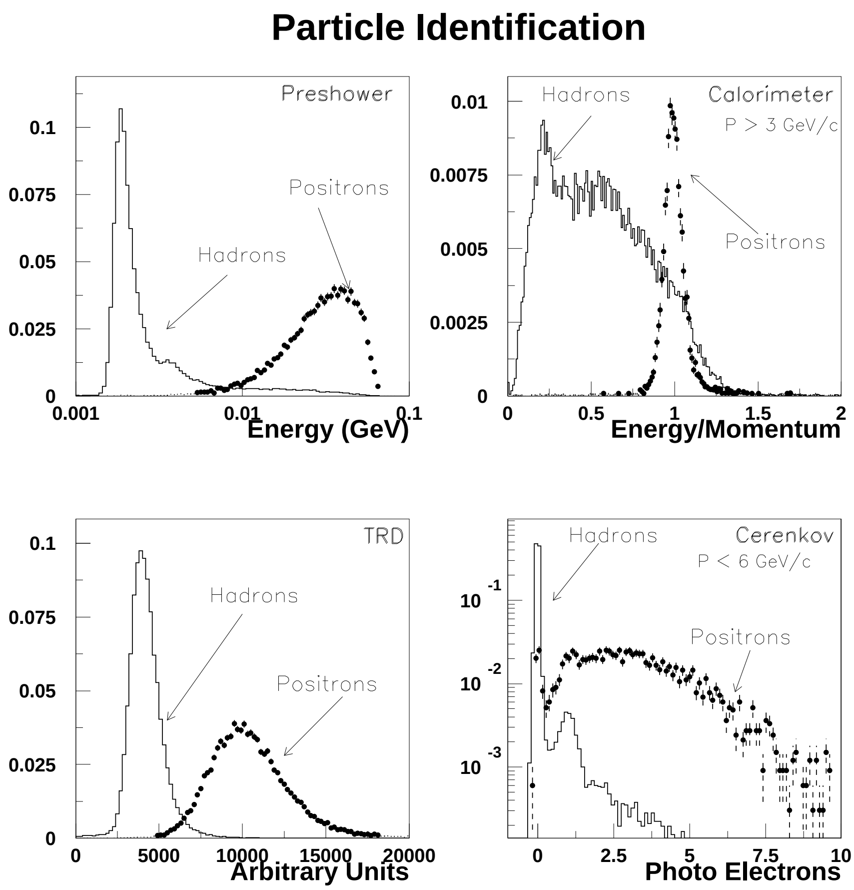

Figure 5.7: The probability distributions for the four PID detectors installed until the end of 1997

.

The Transition Radiation Detector (TRD)

The Transition Radiation Detector (TRD) is a particle identification detector used for the separation of electron from hadrons. When a relativistic paticle passes through the interface between two dielectric media with dielectric constants ϵ_1 and ϵ_2 it emits radiation in the forward direction at an angle ϕ proportional to $1/\gamma$, where γ is the Lorentz factor E/m and E and m being the energy and the mass of the particle. The transition radiation (TR) for ultra- relativistic particles is in the X-ray region (several keV), useful for particle physics applications. In the passage from vacuum to a medium with electron density n_e, the probability of emission of a transition radiation photon in the ultra-relativistic regime is given by:

$$W_{TR} = \frac{8\pi\alpha^2\gamma n_e}{3m_e} \tag{5.4}$$

where α is the fine structure constant and m_e is the electron mass. The linear dependence of W_{TR} on γ enables a separation of highly relativistic particles ($\beta \simeq 1$) in a way that would require a much longer Cherenkov detector for the same separation power. For istance a 5 GeV electron has a $\gamma = 10000$ while for a pion $\gamma = 35$, so that the prbability that the electron emits a TR photon will be 300 times larger than for the pion. Fig. 5.8 shows how the measurements of the TR improves the separation of electrns from pions.

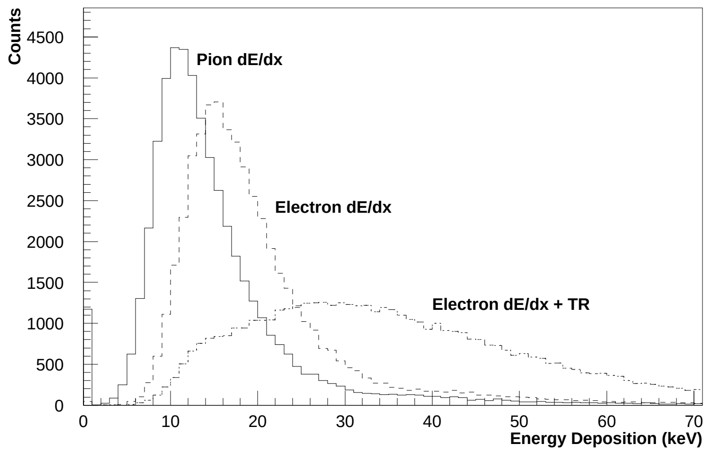

Figure 5.8: Response of a single TRD module. The energy dE/dx deposited in the TRD due to ionization is not able to provide a clear separation between pions and electrons. When the transition radiation is included, the electron peak moves to higher energies and the separation improves.

The dependence of W_{TR} on the square of $\alpha = 1/137$ implies that in order to achieve a considerable probability for the emission of a TR photon, many radiator layers are needed, and the dependence on n_e implies the use of a material with high electron density. The radiator also needs to be highly transparent to X rays, in order to avoid self-absorption. A polypropylene fiber radiator satisfies all requirements, while the last problem is also solved by building a sandwich structure of radiators and X-rays detectors (one single module is shown in fig. 5.9). The radiator is a loosely packed array of polypropylene fibers with a diameter of $17 - 20$ μm, arranged in roughly 300 two-dimensional layers, with a total thickness of 6.35 cm.
The detector consists of 12 modules, 6 above and 6 below the beam pipe. The outer dimensions of the two halves are $401 \times 112 \times 61$ cm^3. Each module is made of a radiator and a wire chamber, separated by a flush-gap where CO_2 circulates in order to avoid the diffusion of oxigen and nitrogen into the chambers, thus protecting them from the ambient atmosphere. The gas in the wire chambers needs to have high atomic number, in order to achieve best X-ray absorption, thus a mixture of 90% Xenon and 10% Methane, the latter acting as a quencher to avoid the creation of electron avalanches in the chamber is used.

The TRD detector reaches a *hadron rejection factor* (defined as the ratio of the total number of hadrons to the number of hadrons misidentified as leptons, for a given energy cut) of 100 for 90% lepton efficiency (the number of leptons above the cut over the total number of leptons). The discrimination can be improved by a factor 3 with a probability analysis ([111]).

The Cherenkov Detector and the RICH

Until the end of 1997 a threshold Cherenkov counter was used to provide positron identification below the threshold momentum for pions ($p < 4$ GeV). Each of the counters in top and bottom consisted of a glass radiator, a system of 20 spherical mirrors and 20 matching photomultiplier tubes mounted on the outside of the aluminum enclosure containing the mirrors and the gas. The threshold velocity of a charged particle to radiate Cherenkov light in a medium with a refractive index n is given by:

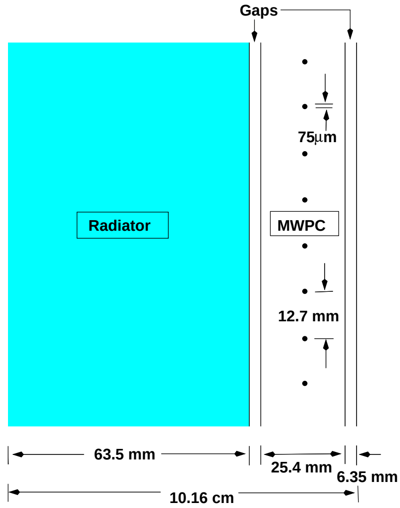

Figure 5.9: Schematic drawing of one TRD module (top view). The effective area of each module is 325 cm^2.

$$v \geq \frac{c}{n} \quad \text{corresponding to} \quad p_{th} = \beta_{th}\gamma_{th}m_0 = m_0\sqrt{\frac{1}{n^2-1}}, \tag{5.5}$$

where p_{th} is the threshold momentum for a particle with mass m_0 ($\beta = p/E$). The radiator gas was a mixture of 70% N_2 and 30% C_4F_{10}, resulting in a p_{th} of 20.9 MeV for $e^{\pm}$, 3.8 GeV for pions and 13.9 GeV for kaons. For tracks classified as a hadron by the other PID detectors, the Cherenkov detector could be udes to identify pions in a momentum range from 3.9 to 13.9 GeV. The number of photons radiated by a particle with momentum p is proportional to $1-1/(\beta^2n^2)$, i.e. it increases with momentum from the threshold on and has a maximum for $\beta = 1$. Positrons at all momenta normally caused signals with 5 to 6 photoelectrons, while pions below 4 GeV left no signal in the PMts and above the threshold the mean number of photoelectrons was roughly 3.
During the shutdown break in the Spring of 1998, the Cherenkov counter was replaced by a Ring Imaging Cherenkov detector. It uses the same support structure as the Cherenkov counter. Two radiators with rather significantly different refractive indices are used, enabling the identification of pions, kaons and protons over a momentum range from 1 to 15 GeV. The first radiator is a wall of 10.5×10.5 cm^2 aerogel tiles with an entire thickness of 5.5 cm, installed right behind the entrance window. They are stacked in 5 layers with 5 horizontal rows and 17 vertical columns. Aerogel is a silica gel foam, i.e. containing air, with refractive index 1.0304. The second radiator is a heavy gas, C_4F_{10} with a refractive index of 1.0014, filling the volume of the detector. Cherenkov photons are reflected from a spherical mirror array onto a photon detector in the focal plane above the gas radiator. The photon detector is an array of 1934 photomultipliers with a diameter of 18.6 mm, arranged in a exagonal closed packed matrix. Each of the PMTs is surrounded by an aluminized plastic foil funnel to maximize light collection. A schematic view of the top RICH detector is shown in fig. 5.10 (a).

For hadron identification, the threshold behavior in the two radiators as well as the information about the photon angles are used. Cherenkov photons are emitted in a cone around the particle trajectory, with an opening angle

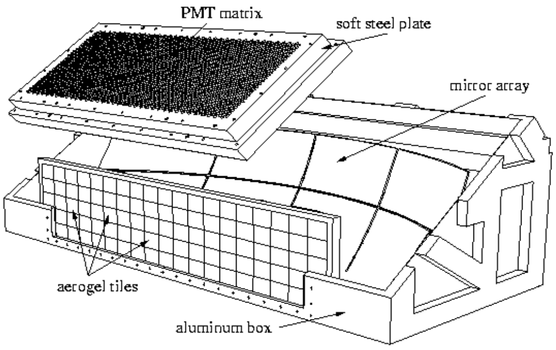

(a) RICH

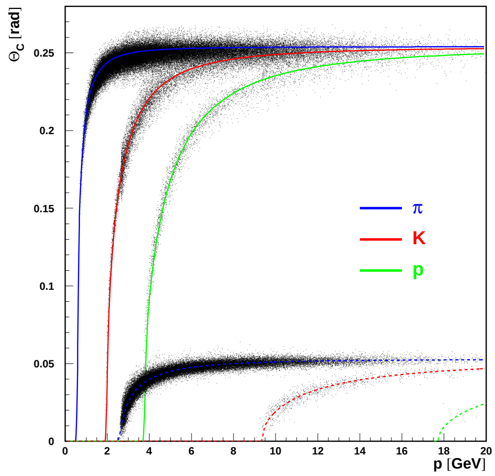

(b) RICH

Figure 5.10: (a): the RICH detector. (b): angle of Cherenkov emission as a function of momentum for pions, kaons and protons, in aerogel and gas. The aerogel gives a better discrimination among hadrons in the low momenta region, while the gas is good at high momentum, where the aerogel curves tend to overlap.

$$cos\theta_c = \frac{1}{\beta n} \tag{5.6}$$

As shown in fig. 5.10 (b), the two radiators have a different momentum window in which they give a good separation between pions, kaons and protons: momenta lower than approximately 10 GeV are below the threshold for Cherenkov radiation with a gas radiator, while in this range the aerogel has its greatest discriminating power. At higher momenta the curves for aerogel saturate and it is not possible anymore to distinguish among hadrons based on aerogel information, and the gas is used instead.

Since the RICH was optimized to provide a good hadron separation, an important piece of information on lepton/hadron discrimination at momenta below 4 GeV was missing that was filled before by the threshold Cherenkov counter. The calorimeter and the TRD, providing the bulk of information above 4 GeV, are not optimized for momenta below that. Low energy hadrons can leave a high fraction of their energy in the calorimeter due to an enhanced probability of nuclear interactions. In the TRD, the TR created by low momentum positrons has to compete with the ionization losses of hadrons of the same order. In fact the RICH information can be used similarly to that of the threshold Cherenkov detector for lepton/hadron separtion at low momwnta. A positron with $p > 0.5$ GeV emits photons in the aerogel and in the gas, at angles close to the maximum ($\beta \to 1$) of $\theta_A \simeq 250$ mrad for aerogel and $\theta_G \simeq 50$ mrad for the gas respectively. The threshold for pions to radiate Cherenkov light is $p > 0.6$ GeV in the aerogel and $p > 3.8$ GeV in the gas. The average angle of photons emitted by pions in the aerogel is still smaller and the number of photons is less than for electrons. A discriminating signal for the RICH can such be the number of hit PMTs in a window defined by a ring with a radius corresponding to the expected Cherenkov angle for a positron and a width of $\pm 2\sigma_\theta$

around that radius. The resolution $\sigma_\theta \simeq 8$ mrad is mostly dominated by the size of a pixel, i.e. the diameter of the photo multiplier tubes. Since below $p = 3.8\ GeV$ pions do not radiate Cherenkov photons in the gas, the signal in window around the expected positron gas angle should be quite unambiguous.

The PID algorithm

From the response of the particle identification detectors it is possible to generate a quantity PID (Particle IDentification), that is related to the probability of a particle to be a hadron or a lepton. From the deflection of the particle in the magnet it is possible to calculate its momentum p. In each PID detector the particle will leave some energy E. The issue is then to find the probability $P(l(h)|Ep)$, given E and p, that the particle is a lepton l or a hadron h.
Bayes theorem relates such a probability to the observable probabilities $P(l(h)|p)$ that a particle with momentum p is a lepton (hadron), and $P(E|l(h)p)$ that a lepton (hadron) with a momentum p deposits an energy E in the detector:

$$P(l(h)|Ep) = \frac{P(l(h)|p)P(E|l(h)p)}{P(l|p)P(E|lp) + P(h|p)P(E|hp)} \tag{5.7}$$

The probability distributions $P(E|lp)$ and $P(E|hp)$, called $parentdistributions$, can be measured in a test beam facility by measuring the response of the detectors to a beam of leptons or hadrons. Another way, which is commonly used in HERMES, consists to place 'hard' cuts on the response of the other detectors, to be sure that the response of the detector under consideration is generated by a certain type of particle. This way has the advantage of taking into account possible aging effects of the detectors. The cuts have to be hard enough to define a clean sample but also they need to have enough statistics, so the cut values vary for each data production, being tighter only for the productions with more data like 1998, 1999 and 2000, and less tight for 1996 and 1997, as it is shown in Table 5.3.3.

	1996-1997		1998-2000	
	Leptons	Hadrons	Leptons	Hadrons
CALO	$0.92 < E/p < 1.10$	$0.01 < E/p < 0.80$	$0.92 < E/p < 1.05$	$0.01 < E/p < 0.50$
PRE	$E > 0.025$ GeV	$E < 0.004$ GeV	$E > 0.03$ GeV	$E < 0.003$ GeV
TRD	$E > 26$ keV	$0.1 < E(keV) < 14$	$E > 26$ keV	$0.1 < E(keV) < 13$

Fig. 5.11 shows the response of these detectors and the cuts identifying leptons and hadrons in 1996-1997. The plots are obtained using data from 1996. A track is included if it has a good data quality, it is Trigger 21 (the DIS trigger in HERMES), and its vertex originates from the target region. From the parent distributions one can create the quantity PID. The flux ratio (ratio of hadrons over leptons) and the PID for each detector D are defined as:

$$\phi = \frac{\phi_h}{\phi_l} = \frac{P(h|p)}{P(l|p)} \qquad\qquad PID_D = log_{10}\frac{P_D(E|lp)}{P_D(E|hp)}, \tag{5.8}$$

where P_D are the conditional probabilities for a detector D.
When one considers the response of more detectors then one gets a better discrimination between hadrons and leptons, so we can define as PID the combined PID for more then one detector:

$$PID' = log_{10} \prod_{D} \frac{P_D(E|lp)}{P_D(E|hp)} = \sum_{D} PID_D \tag{5.9}$$

the most common PID combinations used in HERMES are:

$$\begin{aligned} PID2 &= PID_{CALO} + PID_{PRE} \\ PID3 &= PID_{CALO} + PID_{PRE} + PID_{CER} \\ PID5 &= PID_{TRD} = \sum_{i=1}^{n} PID_{TRD_i}, \end{aligned} \tag{5.10}$$

where the last sum runs over the 6 TRD modules per detector half.
After the 1997 production, the Cerenkov was upgraded to a RICH detector, and the information coming from it no longer enters into the PID, as now it is mainly used for hadron identification. The quantity

$$PID = log_{10} \frac{P(l|Ep)}{P(h|Ep)} \tag{5.11}$$

is clearly positive if the probability of being a lepton is higher than that of being a hadron, and vice-versa for a hadron. Eq. refpid can be rewritten in terms of PID' and the flux ratio as:

$$PID = log_{10} \frac{P(E|lp)}{P(E|hp)} \cdot \frac{P(l|p)}{P(h|p)} = PID' - log_{10}\phi \tag{5.12}$$

5.3.4 Luminosity Measurement

The HERMES luminosity monitor consists of two small calorimeters, located on both sides of the beam pipe in the horizontal plane, about 7.2 m downstream of the target. The luminosity monitor is particularly sensitive to Bhabha scattering ($e^+e^- \rightarrow e^+e^-$) and annihilation processes ($e^+e^- \rightarrow \gamma\gamma$) between beam positrons and the shell electrons af the target atoms. For an electron beam, as in 1998, the measurable process would be Moller scattering ($e^-e^- \rightarrow e^-e^-$). Events from these processes can be separated from background by requiring coincident high energy clusters in each calorimeter. The calorimeters consist of 3×4 arrays of radiation resistant $NaBi(WO_4)_2$ crystals, each of which is read out by an individual photo multiplier. The very well known cross section of the scattering and annihilation processes is integrated and folded with the detector acceptance and efficiency. From this and the coincidence rate the luminosity can be determined with an accuracy of $\Delta L/L \simeq 6\%$. For asymmetry measurements only the relative luminosity from data with two different spin configurations is relevant, here the uncertanty is much smaller, $\Delta R/R \simeq 0.9 - 1.5\%$. In [112] a detailed description of the luminosity monitor and the contribution of systematic uncertainties to the luminosity measurement is given.

5.4 Trigger System

The HERMES trigger system selects events interesting for physics analysis. Additional triggers are used for detector monitoring and calibration. The first level trigger decision is made

within about 400 nsec after the event occurred, using some combinations of signals from the scintillator hodoscopes ($H0$ directly upstream of the FCs, $H1$ directly in front of BC$3/4$ and $H2$ the preshower detector), some of the wire chambers and the calorimeters. The main trigger selects candidates for the scattered positron in deep inelastc scattering by requiring coincident signals in the three hodoscopes in one detector half and a minimum energy deposited in two adjacent calorimeter columns in the same half. From the middle of the 1996 running period on, for running with a polarized target the trigger energy threshold of the calorimeter has been set to 1.4 GeV. Before that period, it was at 3.5 GeV. The high threshold suppresses events with only hadrons (i.e. photoproduction events where the small angle of the scattered positron prevents it from detection), because their energy deposition in the calorimeter is usually smaller. For running with unpolarized gas at higher densities, the threshold is usually set to 3.5 GeV to reduce trigger rates. In order to extend the range of possible measurements, photoproduction triggers were introduced, selecting events with two or more hadrons. These triggers usually require coincident signals in the top and bottom half of the spectrometer in all three hodoscopes as well as the BCs or MCs.
Not all the generated triggers can be accepted by the HERMES data acquisition system (DAQ). During the time needed for readout, newly generated triggers cannot be accepted, leading to a 'dead time' of the trigger system. The dead time is defined as the ratio of rejected trigger requests to the total number of generated triggers. The DAQ system digitizes the analog and timing information for an accepted trigger in the ADC and TDC modules located in Fastbus crates. The information from the Fastbus modules is then sent to a Linux PC farm and stored on hard disks. During the breaks in between HERA fills the data on these disks are copied to tapes for permanent storage. The HERMES DAQ is capable of reading out the detector information at rates up to 500 Hz with dead time below 10%.

5.4.1 Trigger Logic

The trigger logic is summarized in table 5.4.1 where the subscript T(B) refers to the top (bottom) detector half. (Here H0, H1 and H2 are the three hodoscopes, MCs are the magnet chambers, BC are the backward chambers, see Sec.5.3). The symbol 'CA' means the requirement of an energy deposit of 1.4 (3.5) GeV in two adjacent columns of blocks in the calorimeter. All triggers have to be generated within a time window corresponding to the passage of a HERA electron bunch through the interaction point (HERA clock).

5.4.2 Trigger Efficiencies for Cross Section

For the analysis of cross sections it is necessary to know the trigger efficiencies for a certain type of events, and to correct the corresponding observed yields for these inefficiencies. As there is no clear way to exclude accidental hits which could fire a trigger, it is necessary to define event topologies for which the trigger efficiencies are going to be calculated. Care has to be taken so that the topology of the events that have to be corrected is exactly the same of the events used to derived the efficiencies. It is possible to distinguish two classes of events of interest:

- inclusive and semi-inclusive DIS events. The trigger efficiency of this type of events is dominated by the probability of the scattered positron to generate a trigger 21 signal, if the positron energy is above the calorimeter threshold. In 80% of the DIS events the produced hadrons escape the acceptance of the detector, and the event consists of only one positron

Trigger (Year)	Logic
17 (1998)	(HM · H0 · H1 · H2)$_T$ + (HM · H0 · H1 · H2)$_B$
17 (1999/00)	(HM · 2H0 · 2H1)$_T$ + (HM · 2H0 · 2H1)$_B$
17 (2000)	(HM · 2H0 · 2H1 · 2H2)$_T$ + (HM · 2H0 · 2H1 · 2H2)$_B$
18 (1998)	(H1 · H2 · CA)$_T$ + (H1 · H2 · CA)$_B$
18 (1999/00)	(H1 · H2 · CA · MC)$_T$ + (H1 · H2 · CA · MC)$_B$
19 (1998/99)	(H0 · H2 · CA)$_T$ + (H0 · H1 · CA)$_B$
19 (2000)	(H0 · H2 · CA · MC)$_T$ + (H0 · H2 · CA · MC)$_B$
20 (1998/99)	(H0 · H1 · CA)$_T$ + (H0 · H2 · CA)$_B$
20 (2000)	(H0 · H1 · CA · MC)$_T$ + (H0 · H1 · CA · MC)$_B$
21	(H0 · H1 · H2 · CA)$_T$ + (H0 · H1 · H2 · CA)$_B$
22 (1998)	/H0G8 [(H0 · H1 · H2 · MC)$_T$ * (H0 · H1 · H2 · MC)$_B$]
22 (1999/00)	/H0G8 [(H0 · H1 · MC)$_T$ * (H0 · H1 · MC)$_B$]
24	(H0 · H1 · H2 · CA)$_T$
25 (2000)	(H0 · H1 · H2 · CA)$_B$
27 (1998/99)	/H0G8 [(2H0 · 2H1 · 2H2 · MC · 3BC)$_T$ + (2H0 · 2H1 · 2H2 · MC · 3BC)$_B$]
27 (2000)	/H0G8 [(2H0 · 2H1 · MC · 3BC)$_T$ + (2H0 · 2H1 · MC · 3BC)$_B$]
28 (1998)	/H0G8 [(H0 · H1 · H2 · BC)$_T$ * (H0 · H1 · H2 · BC)$_B$]
28 (1999/00)	/H0G8 [(H0 · H1 · BC)$_T$ * (H0 · H1 · BC)$_B$]

Table 5.1: Trigger logic for the main physics and calibration triggers for the years $1996/97$ and 2000. The '*(·)' and '+' signs stand for logical 'AND' and 'OR'

.

track. In about 85% of the semi-inclusive events the hadron(s) are detected in the detector half opposite to that where the positron was scattered. For such events it is possible that a trigger 28 was generated as well. In general, the probability to fire any of the triggers 21, 22 or 28 is higher if more charge particles are present in the event.

- inclusive photoproduction events. These events are usually characterized by one or more hadron tracks. In most of the events with two or more tracks there is at least one track in each half. The generated triggers are a mixture of trigger 21 and 27.

In this thesis photoproduction events are considered and the efficiencies of triggers 21 and 27 were calculated. The analysis was restricted to only one event topology, for which both triggers are enabled.

events with at least two long hadron tracks in the same detector half.

5.4.3 Triegger Efficiency Calculation

The efficiencies of triggers 21 and 27 for a particular class of events (DIS or photoproduction events) can be calculated from the efficiencies of the detector components taking part in the trigger. These can be retrieved from the count rates of the calibration triggers 18, 19 and 20 in combination with those of trigger 21. For istance, for 2000 one gets the efficiencies:

$$\epsilon(H0) = \frac{N_{18\&21}}{N_{18}}, \qquad \epsilon(H1) = \frac{N_{19\&21}}{N_{19}}, \qquad \epsilon(H2) = \frac{N_{20\&21}}{N_{20}}, \tag{5.13}$$

For the calorimeter efficiency no separate calibration trigger exist. In principle this would have been trigger 17 as it was defined in 1997, however, the rates were extraordinary high such that events that fired *only* trigger 17 were disregarded already by the track reconstruction program. The calorimeter efficiency can instead be extracted from events with trigger 27:

$$\epsilon(CA) = \frac{N_{27\&21}}{N_{27}} \tag{5.14}$$

but here care has to be taken since the event topologies for trigger 27 and trigger 21 are very different such that the efficiency may be biased. The signature for a trigger 27 event would be at least two tracks in the top *or* two tracks in the bottom half of the detector. For a trigger 21 *in coincidence* with trigger 27 only either of the tracks had to produce a trigger signal for trigger 21. Given the calorimeter efficiency, the total efficiency of trigger 21 can be calculated as:

$$\epsilon(Tr21) = \epsilon(H0) \cdot \epsilon(H1) \cdot \epsilon(H2) \cdot \epsilon(CA) \tag{5.15}$$

The efficiency for trigger 27 is given by:

$$\epsilon(Tr27) = (\epsilon(H0)) \cdot (\epsilon(H1)) \cdot (\epsilon(H2)) \cdot \epsilon(H0mult \cdot MC \cdot BC) \tag{5.16}$$

the efficiency for the specific hit multiplicity in the H0 and topology of hits in the BCs and MCs $\epsilon(H0mult \cdot MC \cdot BC)$ can only be calculated for the top-bottom combination using coincidences with trigger 21:

$$\epsilon(H0mult \cdot MC \cdot BC) = \frac{N_{21\&27}}{N_{21}} \tag{5.17}$$

Error Calculation

The error on the trigger efficiencies is the error on quantities of the form:

$$\epsilon = \frac{N_A}{N_B} \tag{5.18}$$

the error formula used is [113]:

$$\delta\epsilon = sqrt\frac{(N_A + 1)(N_B - N_A + 1)}{(N_B + 2)^2(N_B + 3)} \tag{5.19}$$

This formula takes into account the fact that there are bins in which N_A and N_B are very small numbers, so that the usual error formulas may not be valid, since they usually apply in the limit of large numbers. In this limit it takes the usual form of the binomial error:

$$\delta\epsilon\sqrt{\frac{(1-\epsilon)\epsilon}{N_B}} \tag{5.20}$$

The errors will be plotted as asymmetric since the efficiency cannot be larger than 1.

5.4.4 Time Dependence of Trigger Efficiencies

The time dependent trigger efficiencies shown below were calculated for each run and averaged over a fill (see Sec.5.4.7). The trigger efficiencies are shown for the years 1998, 1999 and 2000 and for the Λ hyperon.
As expected, the efficiencies are constant in time. The Calorimeter efficiency is the most contributing to the total trigger 21 efficiency, while the three hodoscopes show a stable efficiency very close to one. In 2000 the efficiency of the Magnet Chambers and the Backward Chambers drops to zero in the region of fill $170 - 230$ where the trigger 27 was prescaled. The efficiencies of the two triggers look similar in the three years, possible differences were taken into account in the evaluation of the systematic error of the production cross section (see Sec.6.5.3).

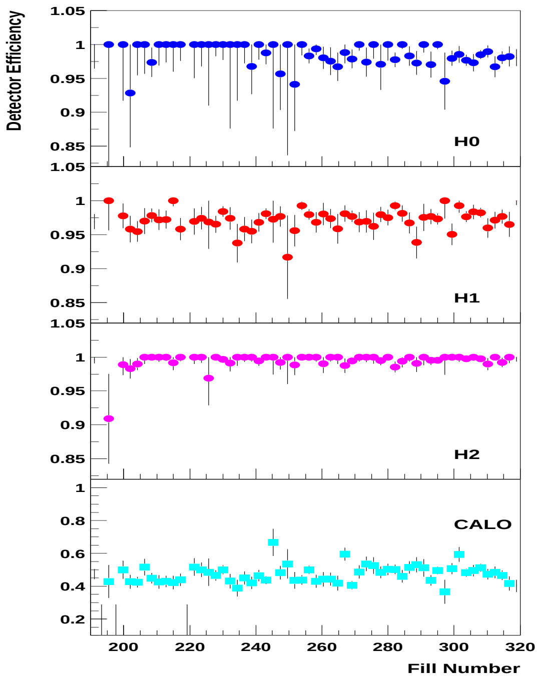

Figure 5.11: Plot of the efficiencies of the detectors used to define the trigger 21 as a function of the fill number for the $98d0$ data production.

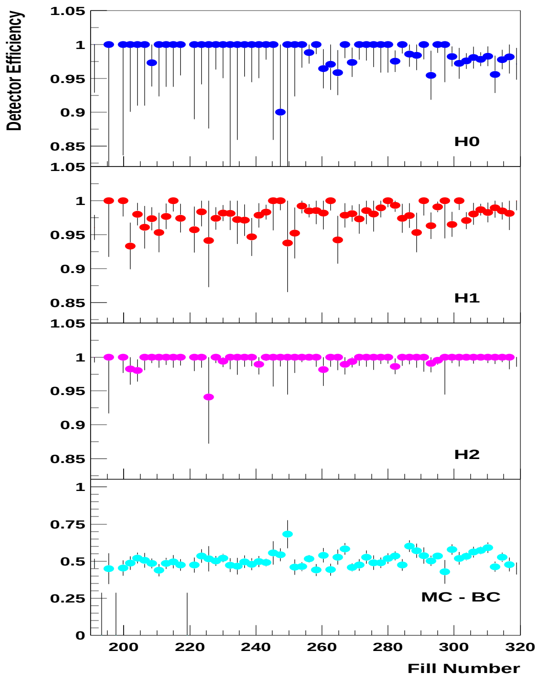

Figure 5.12: Plot of the efficiencies of the detectors used to define the trigger 27 as a function of the fill number for the $98d0$ data production.

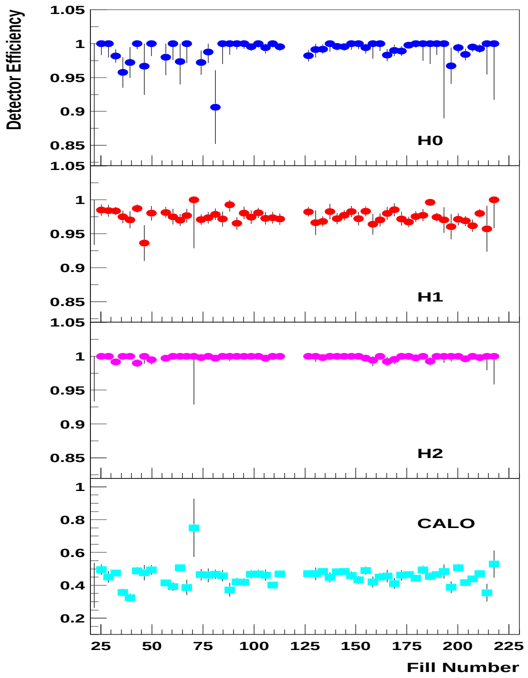

Figure 5.13: Plot of the efficiencies of the detectors used to define the trigger 21 as a function of the fill number for the 99d0 data production.

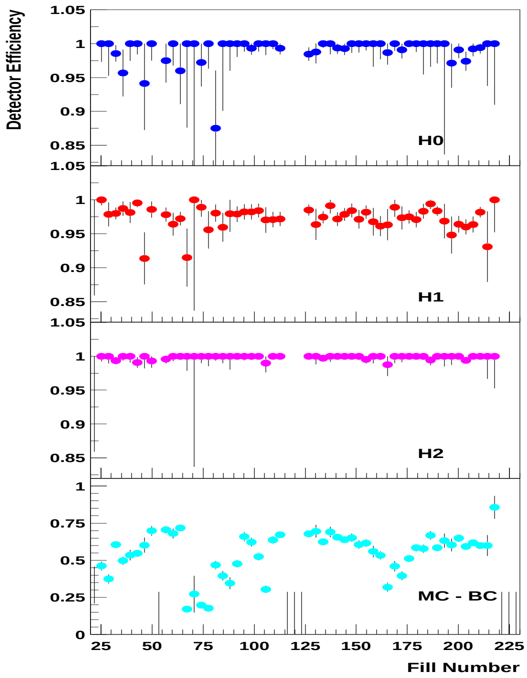

Figure 5.14: Plot of the efficiencies of the detectors used to define the trigger 27 as a function of the fill number for the 99d0 data production.

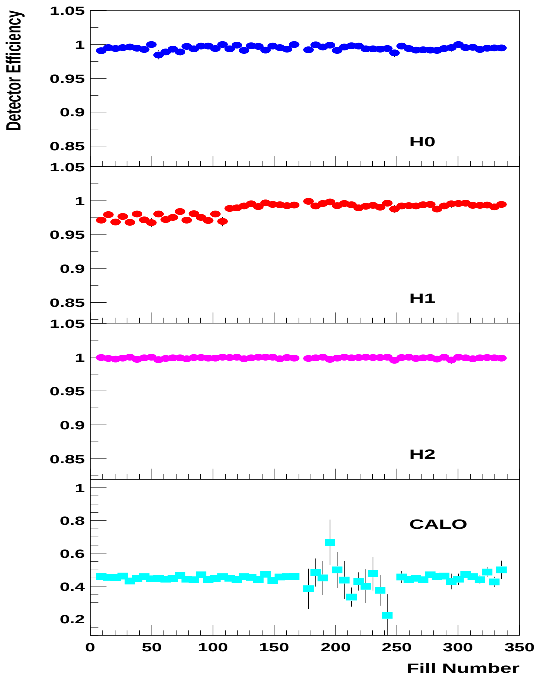

Figure 5.15: Plot of the efficiencies of the detectors used to define the trigger 21 as a function of the fill number for the 00c0 data production.

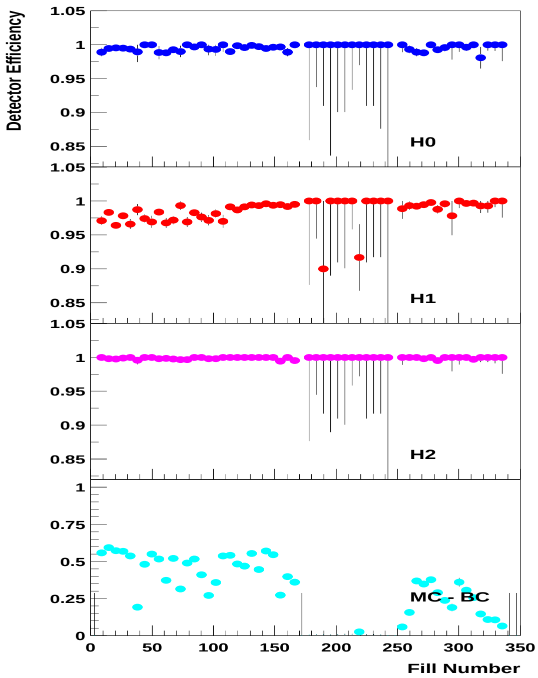

Figure 5.16: Plot of the efficiencies of the detectors used to define the trigger 27 as a function of the fill number for the 00c0 data production.

5.4.5 Trigger Efficiencies for the 1998, 1999 and 2000 data productions

The efficiencies are obtained as a function of proton momentum, in 1 GeV bins from 2 to 15 GeV. The fig. 5.17 show the efficiency for the two triggers, respectively. The efficiencies of H0 and H2 show similar shape, very close to one for both the triggers. The efficiency of the H1 hodoscope instead show a gradual decrease at lower proton momentum. Although the energy deposit in the calorimeter for hadrons is not clearly correlated to the momentum, the calorimeter efficiency decreases at lower momentum. The calorimeter efficiency provides the most important contribution to the total trigger21 efficiency.

The total efficiency of the two triggers, obtained multiplying the efficiencies of the detector components, is shown in fig. 5.18, 5.20 and 5.22 for the three data productions respectively.

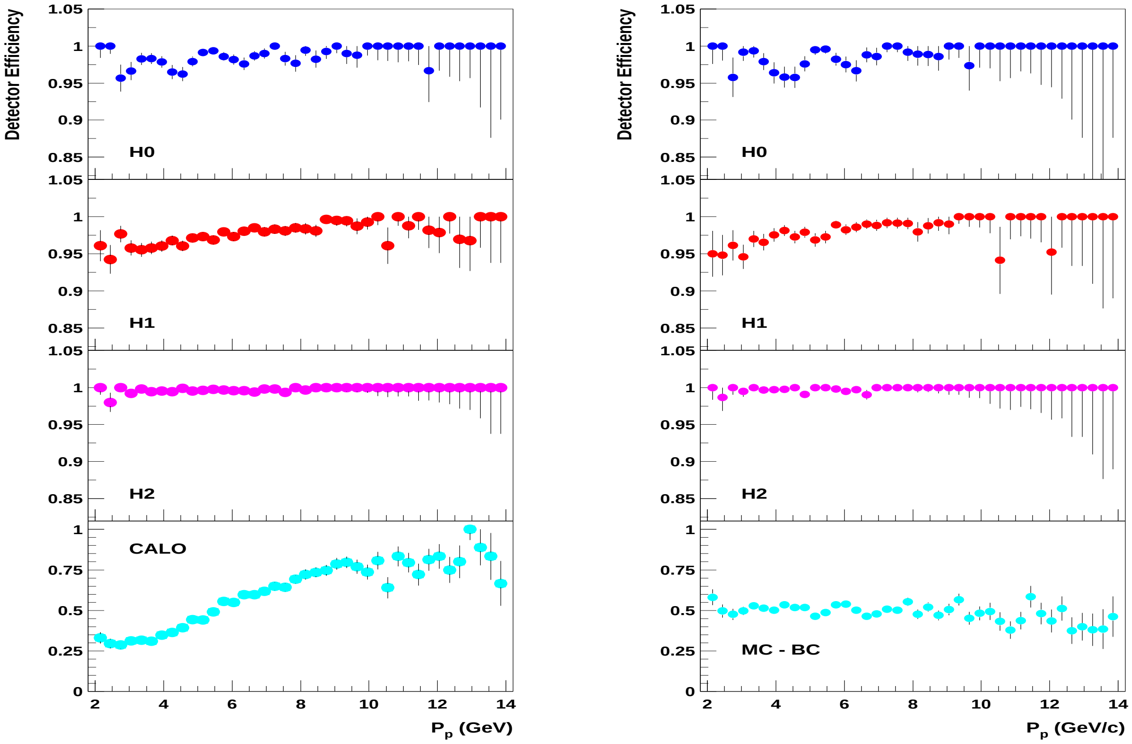

(a) Trigger 21 (b) Trigger 27

Figure 5.17: The efficiency of the detectors that take part to the Trigger 21 (left) and 27 (right) definition is shown as a function of the proton momentum for the $98d0$ data production.

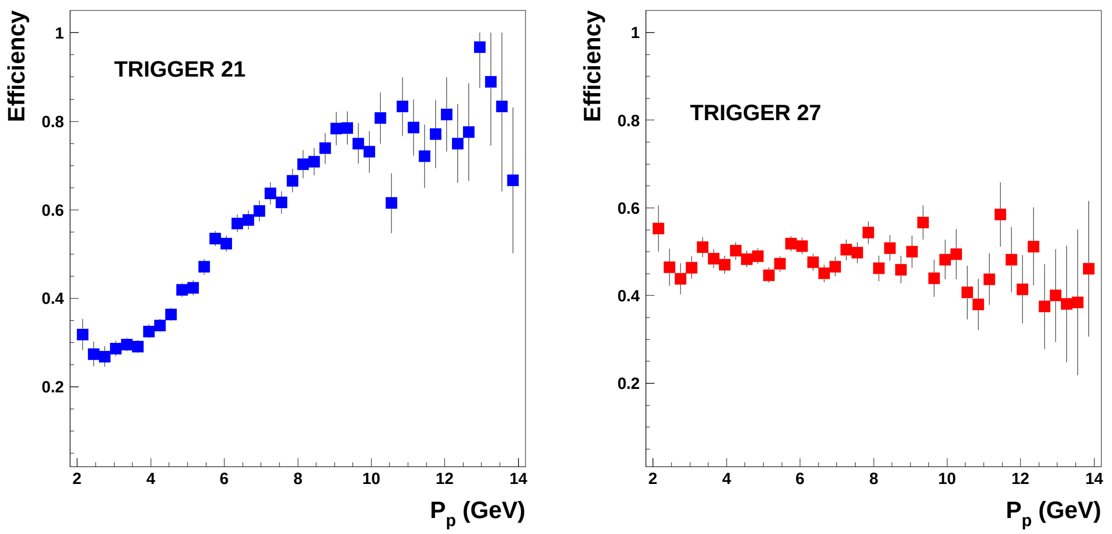

(a) Trigger 21 (b) Trigger 27

Figure 5.18: The efficiency of the Trigger 21 (left) and 27 (right) is shown as a function of the proton momentum for the $98d0$ data production

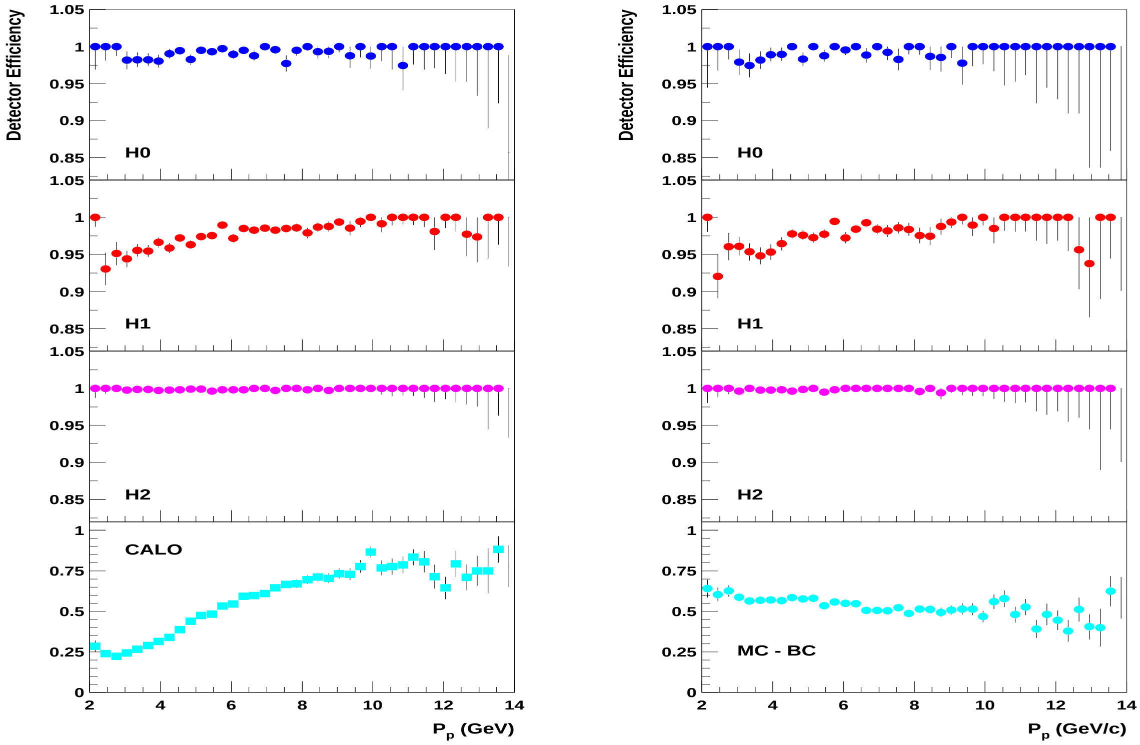

(a) Trigger 21 (b) Trigger 27

Figure 5.19: The efficiency of the detectors that take part to the Trigger 21 (left) and 27 (right) definition is shown as a function of the proton momentum for the $99c0$ data production.

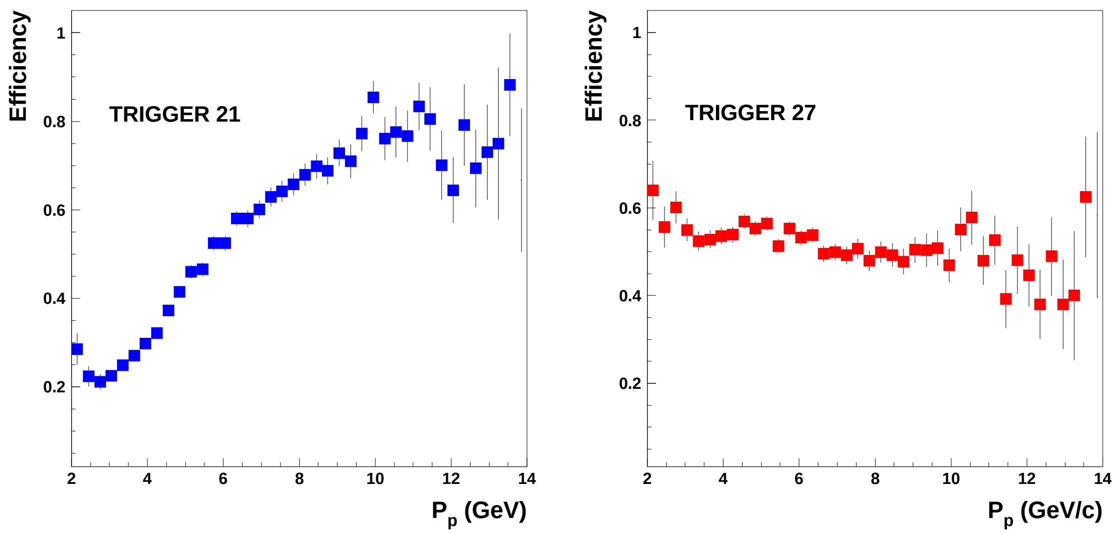

(a) Trigger 21 (b) Trigger 27

Figure 5.20: The efficiency of the Trigger 21 (left) and 27 (right) is shown as a function of the proton momentum for the $99c0$ data production

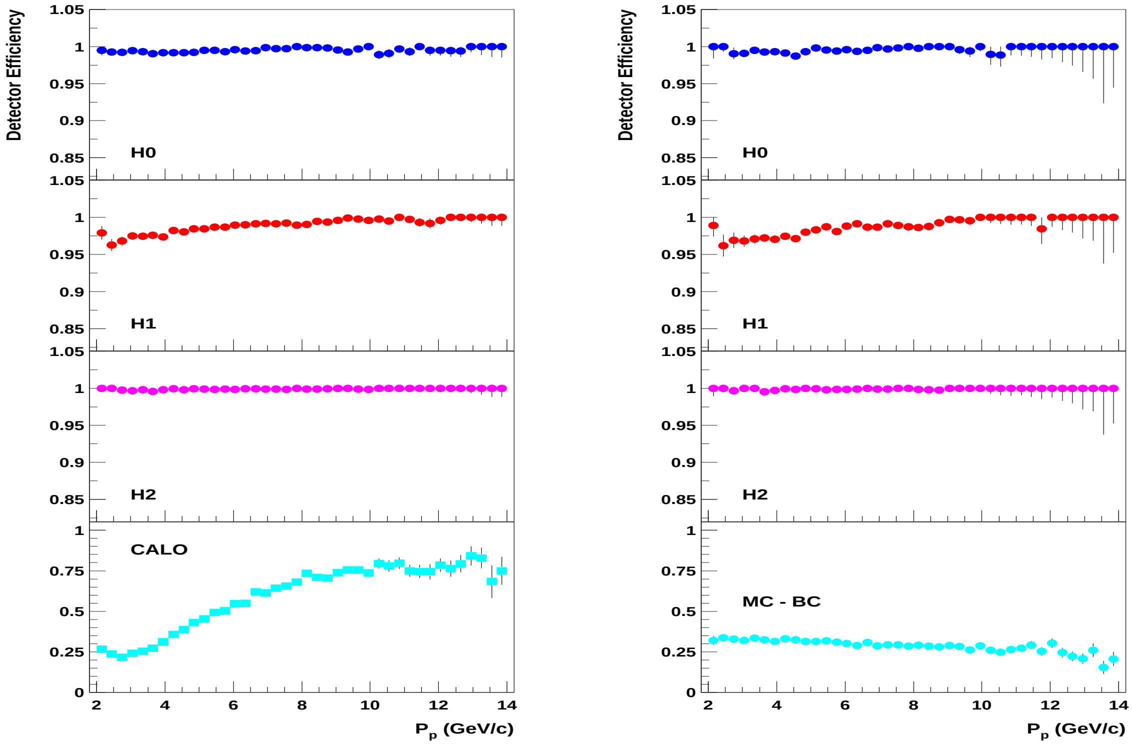

(a) Trigger 21 (b) Trigger 27

Figure 5.21: The efficiency of the detectors that take part to the Trigger 21 (left) and 27 (right) definition is shown as a function of the proton momentum for the $00d0$ data production.

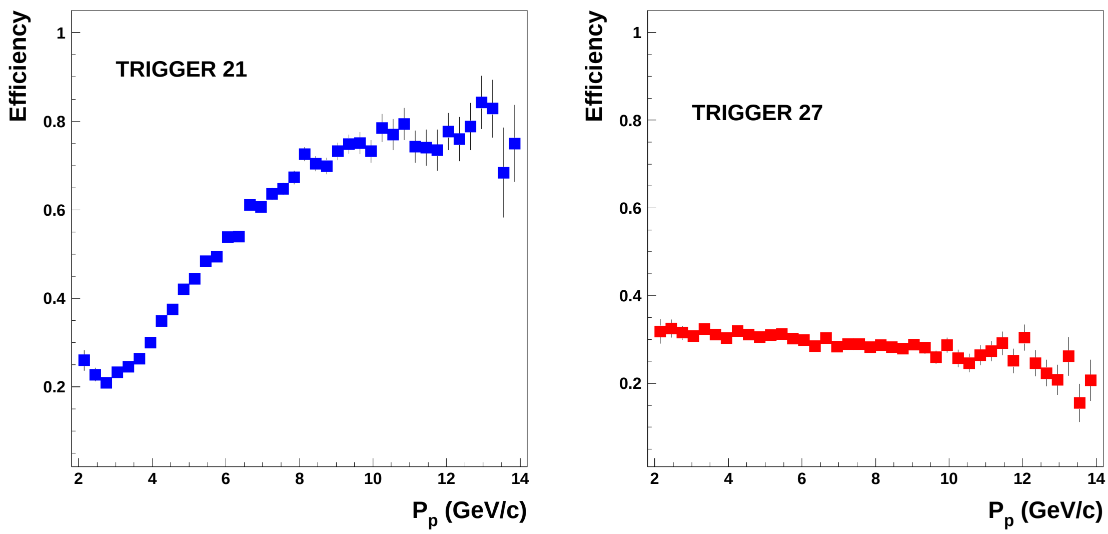

(a) Trigger 21 (b) Trigger 27

Figure 5.22: The efficiency of the Trigger 21 (left) and 27 (right) is shown as a function of the proton momentum for the $00d0$ data production

5.4.6 Trigger Efficiency for the heavier hyperons

All the hyperons studied in this analysis decay in a Λ plus some others particles. For this reason, The trigger 21 and 27 were identified as relevant triggers also in the analysis of the heavier hyperons. The corresponding efficiencies were calculated for each hyperon separately and are shown in the following sections as a function of the momentum of the proton coming from the Λ decay.

Σ^0 Hyperon

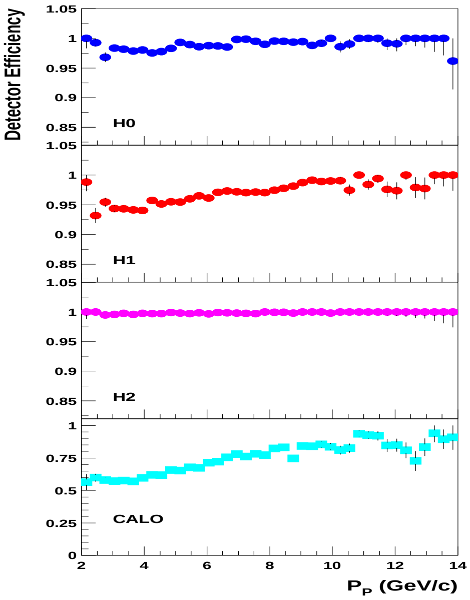

(a) Trigger 21

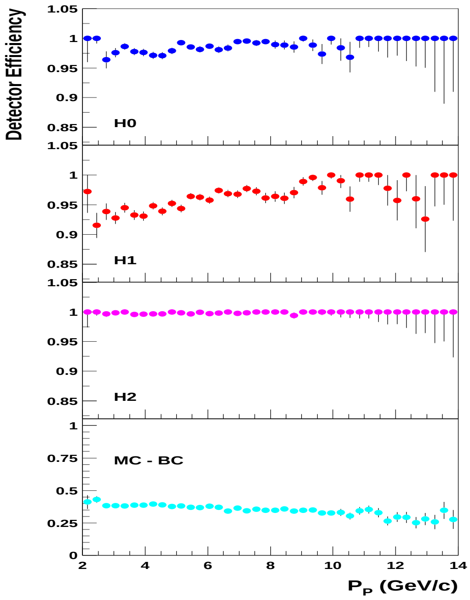

(b) Trigger 27

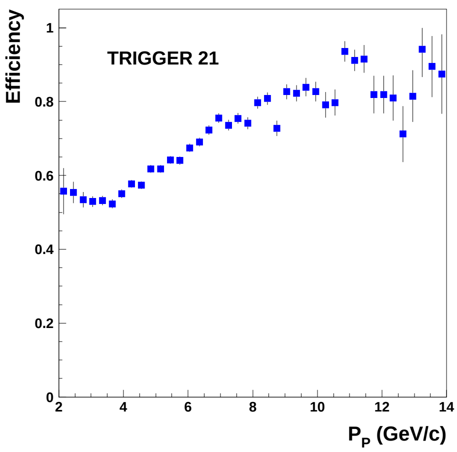

(c) Trigger 21

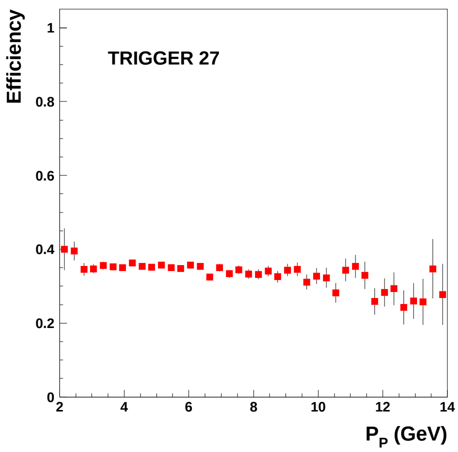

(d) Trigger 27

Figure 5.23: The efficiency of the detectors that take part to the Trigger 21 (left) and 27 (right) definition is shown as a function of the proton momentum for the Σ^0 hyperon.The efficiency of the Trigger 21 (left) and 27 (right) is shown as a function of the proton momentum for the Σ^0 hyperon.

Ξ^- and Σ^{*-} Hyperons

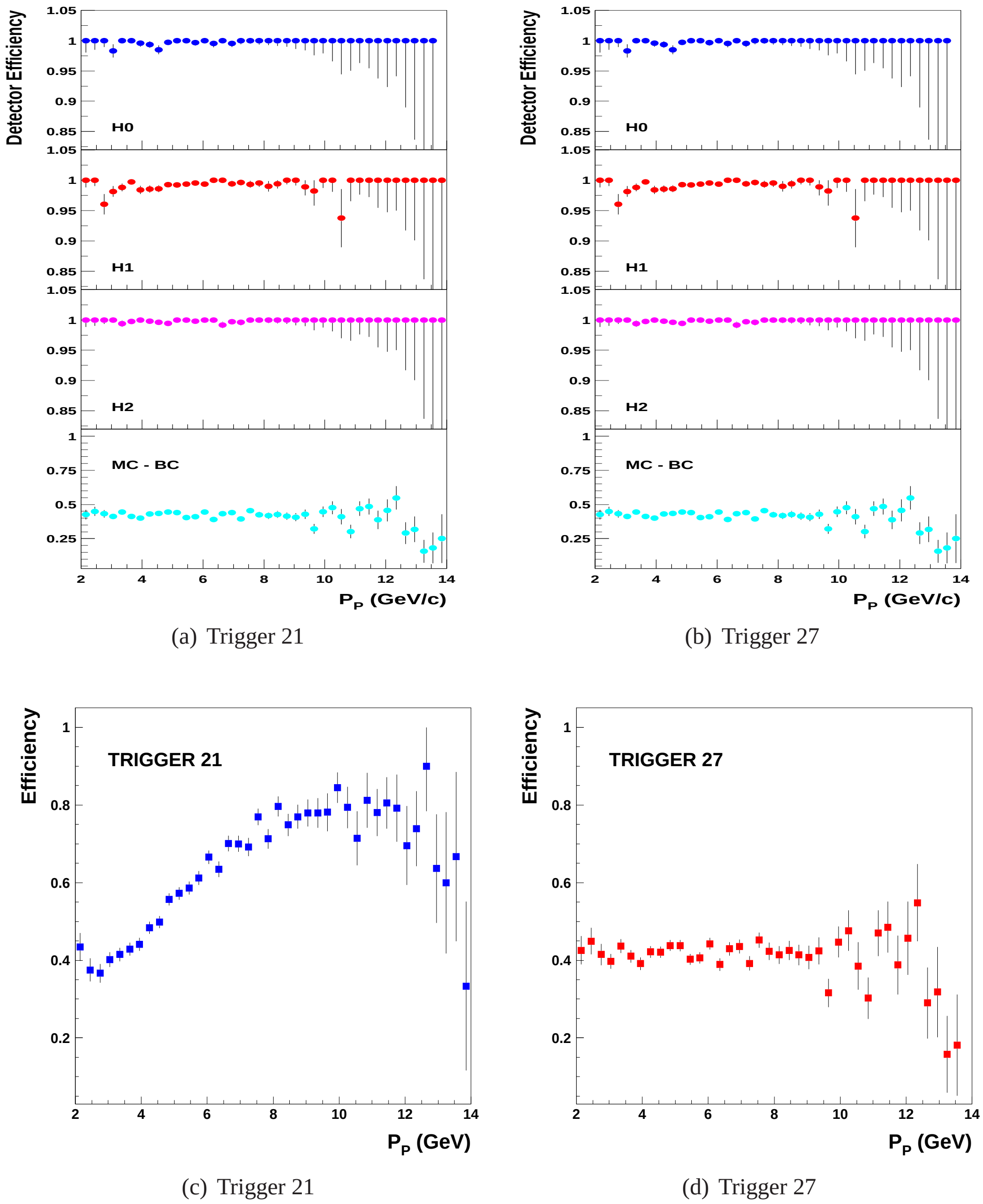

(a) Trigger 21 (b) Trigger 27

(c) Trigger 21 (d) Trigger 27

Figure 5.24: The efficiencies of the detectors that take part to the Trigger 21 (left) and 27 (right) definition and the trigger efficiencies are shown as a function of the proton momentum for the Ξ^- and Σ^{*-} hyperons.

5.4.7 Data Acquisition and Processing

The readout of the detector is carried out by specific readout electronics hosted in FastBus crates which are located in an electronic trailer close to the spectrometer. For the timing and

analogue information LeCory 1881M FastBus ADCs (analogue-to-digital converter) are in use. The magnet chambers and the RICH are read out by the LeCroy PCOS4 system. The data from the FastBus crates are bundled by event builder modules and sent over fast opticals links cluster (a DEC Alpha cluster before 2002), where they are stored on staging disks and on data tapes. So-called slow control data, like information from the luminosity monitor, the polarimeters, the target, detector temperatures, voltage settings, etc., is recorded in addition. The slow control data are read out once every ~ 10 sec, independent of triggers from the spectrometer. All raw data is buffered in EPIO format on hard disks in the Linux cluster and backed up regularly on data tapes. It is transferred to a taping robot at DESY main site after the end of each HERA positron fill using a FDDI (Fast Distributed Data Interface) link.
From the electronic detector signals, the hit positions, energy depositions, etc., are determined with the HERMES decoder (HDC) using mapping, geometry and calibration of the individual detectors. All required information is stored in an ADAMO [114] database, which is an enetity-relationship database allowing structured and portable data storage. In a next step the HERMES reconstruction (HRC) program finds tracks in the spectrometer. Using a timing signal that is written to the event data and slow control data streams, both data streams can be synchronised. All synchronised data which is useful for physics analyses, is stored in data summary tables, the so-called μDST files.
Different time scales are used in the HERMES data. The shortest time interval is the event containing all reconstructed tracks which are observed when a trigger is generated. All events recorded within approximately 10 sec are grouped into bursts. This is the time scale on which the slow control information is synchronised to the event data. In order to split up the raw data into small enough pieces for storage, burst are combined into a run with a size of about 450 MB. Depending on the luminosity, a run lasts around 10 min. The longest time scale, the fill, is determined by the $8-12$ h storage time of the HERA lepton beam.

The analysis of the data collected in the years 1998, 1999 and 2000 with a polarized positron beam and a longitudinally polarized target and the extraction of the photoproduction cross sections for the Λ, Σ^0, Σ^{*-}, Σ^{*+} and Ξ^- are reported in the following chapters.

Chapter 6

Study of the Λ and $\overline{\Lambda}$ Hyperons

The main steps followed in the extraction of the photoproduction cross section of the Λ and $\overline{\Lambda}$ particles are presented in this chapter.
The experimental data analyzed have been collected in the years 1998, 1999 and 2000, with a positron beam (1998) or electron beam (1999 and 2000) and a longitudinally polarized deuterium target. A high quality of the analyzed data was ensured by applying the suitable data quality cuts.
Tab.6 summarizes the procedure adopted in the data analysis. First of all the photoproduction events were selected and the invariant mass spectrum of the Λ and $\overline{\Lambda}$ were reconstructed from their decay products. Then the combinatorial background was highly reduced by applying several kinematical cuts and the yields of the produced Λs were obtained by fitting the background corrected invariant mass spectrum.
Two triggers were found to be relevant for this analysis; their efficiencies were calculated by using some minimum bias triggers.
The geometrical acceptance of the spectrometer was calculated by means of a Monte Carlo simulation and finally the photoproduction cross section was extracted.

Among the hyperons analyzed, the Λ has the best signal-to-background ratio. For this reason the cross section of the Λ was extracted for each of the three analyzed data production separately. In this way the response of the spectrometer was checked through the years. The values of the cross section corresponding to each data production were used to evaluate the systematic uncertainty taking into account the possible differences in the response of the detector in each year. This systematic uncertainty was used in the Λ analysis and in the study of the heavier hyperons, for which the experimental data from the three data productions were first added together and the cross section was then extracted.

6.1 Events Selection

Data Quality Cuts

Each data production corresponds to a μDST file (see sec.5.4.7) that is labeled by the last two digits of the corresponding year of data taking, a letter to indicate the production and a chiper. In a first step the detector calibrations of the previous data taking periods are used and the data are stored in a a-production. Based on this first production, new detailed detector calibrations are subsequently carried out and the resulting data are stored in a b-production. In the subse-

STEPS	**SECTION**	**PAGE**
Event Selection	6.1	39
Invariant Mass Reconstruction	6.2	41
Fit and Extraction of Λ Events	6.4	46
Trigger Efficiency	6.5	48
Total Efficiency	6.5	47
Extraction of the Photoproduction Cross Section	6.5.3	50

Table 6.1: Schematic overview of the analysis chain, starting from the data selection to the extraction of the photoproduction cross section of the Λ hyperon. For the analysis of the other hyperons a similar scheme was adopted.

quent c or d-productions, additional corrections to the detector responses that rely on proper calibrations are added. The analysis presented here is based on the productions $98d0$, $99c0$ and $00d0$.

The information of the status of each experimental component is available for each burst. This information is summarized in a bit-pattern, in which a given bit identifies whether the condition of a particular part of the experiment was satisfactory for physics analysis or not. The information reported in the shift logbook were checked and a burst was analyzed only if it had:

- a reasonable dead time;
- a reasonable length ($0 < t_{burst} < 11$ s);
- a reasonable beam current ($5 < I_{beam} < 50$ mA);
- a reasonable luminosity ($5 < L < 80$Hz).

Furthermore, the first burst of each run was rejected and a burst was rejected also if a problem in the PID detectors or in some blocks of the calorimeter was registered during the data taking.

Geometry cuts and Particle identification

The standard cuts on kinematics and track parameters are shown in table 6.2:

front field clamp position	$\lvert x_{ffc} \rvert < 31\ cm$
septum plate position	$\lvert y_{sp} \rvert > 7\ cm$
rear field clamp position	$\lvert y_{rfc} \rvert < 54\ cm$
rear clamp position	$\lvert x_{rc} \rvert \leq 100\ cm$ $\lvert y_{rc} \rvert \leq 54\ cm$
calorimeter position	$\lvert x_{calo} \rvert \leq 175\ cm$ $30cm \leq y_{calo} \leq 108\ cm$

Table 6.2: Fiducial volume cuts and kinematical requirements.

These geometry cuts on the particle tracks are applied to ensure that the track reconstruction was not influenced by the edges of the HERMES spectrometer and to suppress the background. The vertical and horizontal positions of the track are checked at the locations of several detector components which limit the HERMES acceptance.
Furthermore, tracks hitting the outer edges of the calorimeter wall are excluded to guarantee that the electromagnetic shower is mostly contained within the calorimeter glass blocks.

In order to identify the particles and correctly separate hadrons and leptons the following cuts are applied (see sec.5.11):

- if $(1 < pid3 + pid5 < 100)$ the particle is identified as a lepton
- if $(pid3 + pid5 < 0)$ the particle is identified as an hadron

There are two different kinds of hadron tracks in the μDST. The first class includes the so-called **long tracks** which are reconstructed in the whole spectrometer; these tracks have a valid PID value and are identified by the RICH. The second class includes those tracks that are only reconstructed in the front part of the spectrometer and in the magnet proportional chambers. These tracks are called **short tracks** and have no valid PID value. In the Λ analysis both kinds of tracks were used.

6.2 Mass Reconstruction

As explained in Sec.2.2.1, the Λ hyperon is the lightest baryon containing a strange quark. It decays through two dominant channels (see Tab 2.2). The HERMES spectrometer is not able to detect neutrons, for this reason the analysis presented in this thesis only considers the decay of the Λ hyperon through the channel $\Lambda \rightarrow p\pi^-$.

The invariant mass of the Λ is given by the formula:

$$M_\Lambda = \sqrt{E_\Lambda^2 - P_\Lambda^2} = \sqrt{(E_p + E_\pi)^2 - (\vec{P}_p + \vec{P}_\pi)^2} \tag{6.1}$$

where E_p and E_π are the energies of the proton and of the pion, respectively, and $\vec{P}_p$ and $\vec{P}_\pi$ are the corresponding three-momenta.

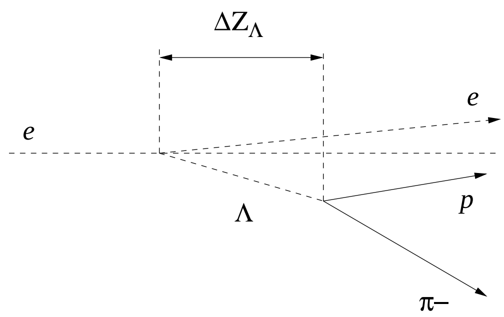

Figure 6.1: Schematic view of the decay of a Λ particle in a proton plus a negative pion. The intersection point of the proton and the pion tracks represents the decay vertex of the Λ while the intersection point of the Λ track and the beam direction represents the production vertex. ΔZ_Λ is the decay length of the Λ hyperon.

All the possible combinations of 1 positive and 1 negative hadron were considered as a Λ candidate for each event. The following kinematical cuts were applied in order to reduce the background:

- the positive hadron is a **proton**:
  1 - it is a long track;
  2 - it is identified by the RICH (smRich.iType=5);
  3 - its momentum is in the range: $2 < P_p < 14$ GeV$/c$
- the negative hadron is a **pion**:
  1 - it can be a long or a short track;
  2 - its momentum is $P_\pi > 0.6$ GeV$/c$

6.2.1 Decay Vertex

Important for the reconstruction of the Λ mass is a correct definition of its primary (i.e. production) and secondary (i.e. decay) vertices.
Due to the finite spatial resolution of the tracking detectors, it is not possible to exactly identify the intersection point of two tracks; for this reason, a new variable was introduced, the **D**istance of **C**losest **A**pproch (dca) between two tracks, that allows to define the decay vertex of the Λ (and $\overline{\Lambda}$) as the mid point between the proton and the pion tracks in correspondence of their dca. The cut applied to this variable, in order to obtain the best reconstruction of the decay vertex,was determined by studying the significance of the peak of the invariant mass spectrum at different values of the DCA. The value of the significance is given by:

$$S = \frac{N_s}{\delta N_s} \tag{6.2}$$

where N_s is the full area under the peak obtained from the fit and δN_s is the fully correlated uncertainty. This ratio measures how far the peak is away from zero in units of its own standard deviation. All correlated uncertainties from the fit, including those of the background parameters, are accounted for in δN_s, as discussed in sec. 3.1.3. The fit of the invariant mass peak at different values of the dca is show in figure 6.3. As shown in fig. 6.2, the significance has a maximum for $dca < 1.5$ cm and this constraint was chosen for the determination of the decay vertex.

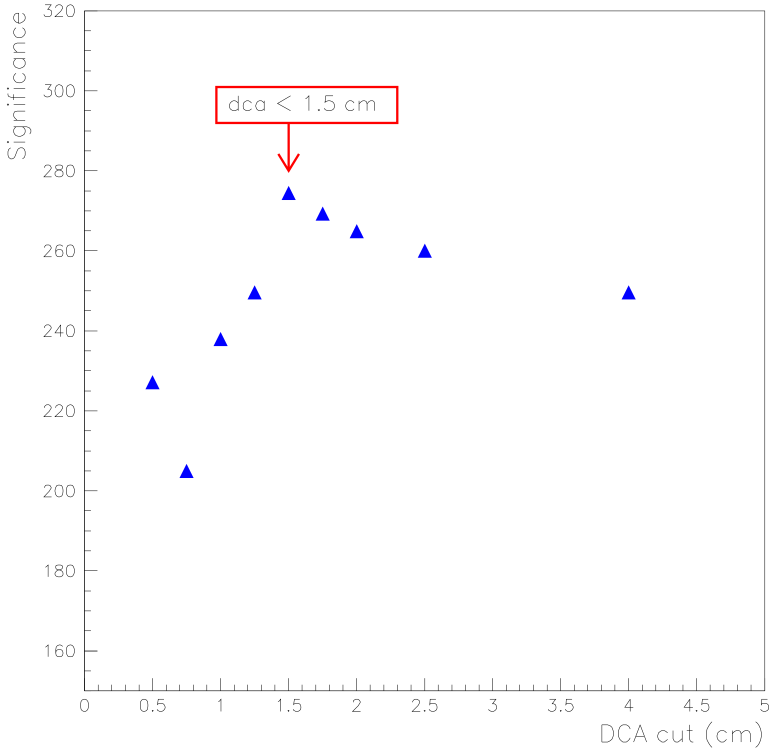

Figure 6.2: Significance for different cuts applied on the distance of closest approach between the proton and the negative pion.

6.2.2 Production Vertex

In a similar way the production vertex was defined as the mid point between the beam direction and the Λ direction in correspondence of the closest approach. The fig.6.4 shows the distribution of the production vertices of the Λ for each of the three data productions considered in this analysis. This distribution reflects the density distribution of the gas into the target cell (40 cm length). The density distribution has a triangular shape, with the maximum at the position of the injection tube, at the center of the cell, and decreases towards the ends. In the plot is also visible a small peak in the negative region from -40 cm to -20 cm which, being outside to the target region, has been discarded in the following analysis by the constraint:

$$-18cm < v_{prod} < 18cm.$$

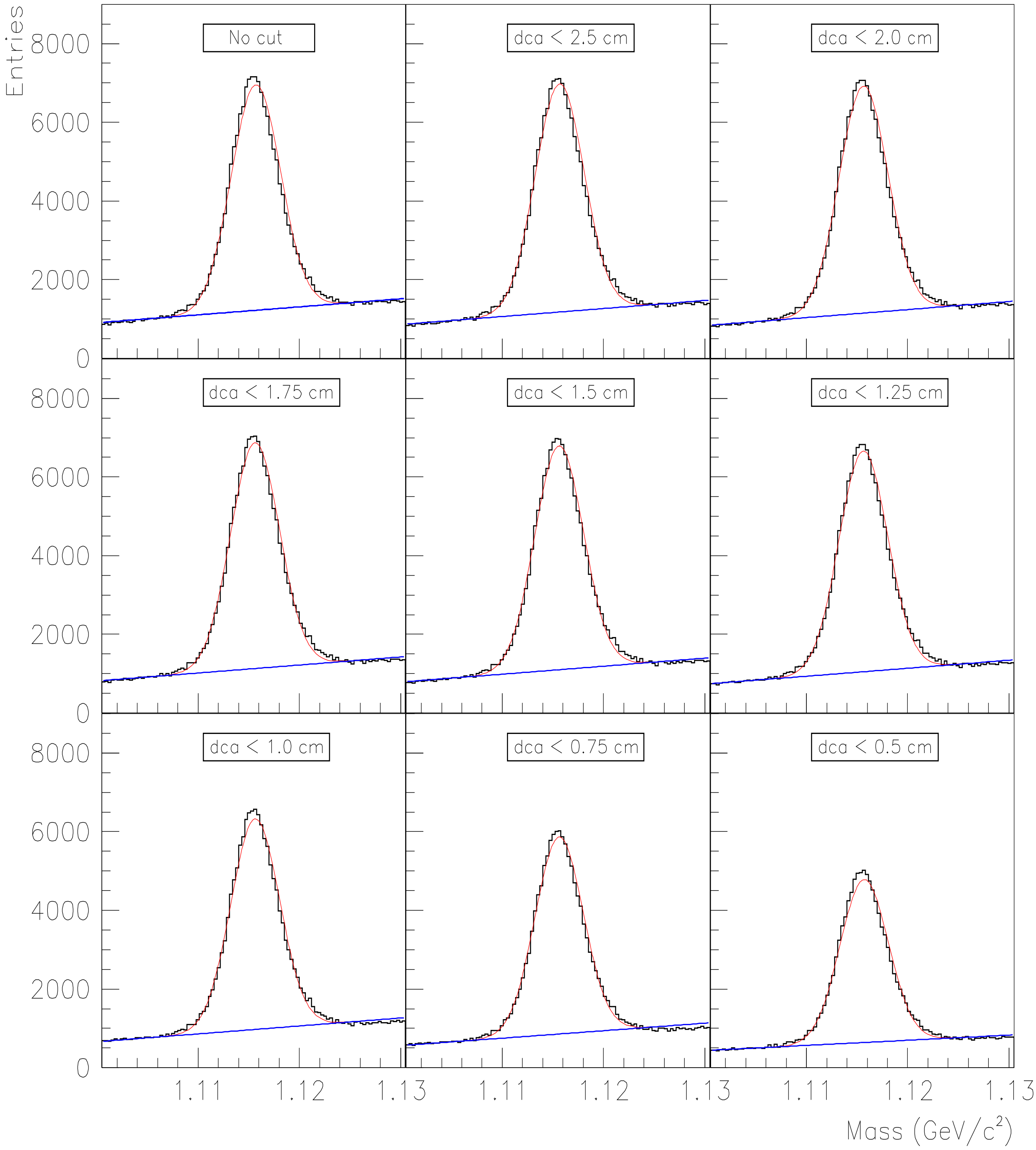

Figure 6.3: The invariant mass spectrum of the Λ reported for different values of the dca.

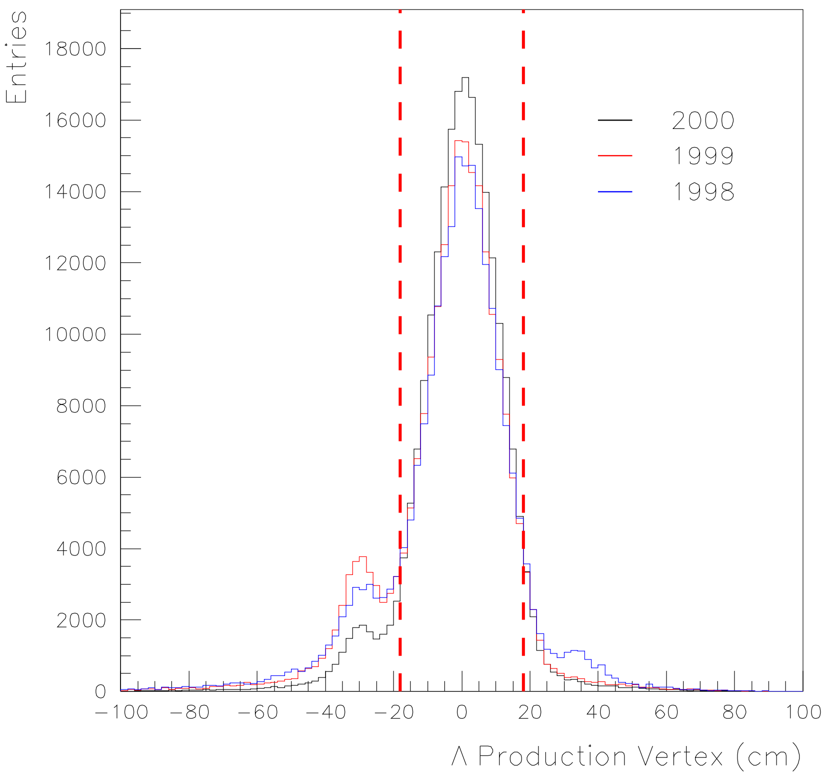

Figure 6.4: The distribution of the production vertex of the Λ for each of the three data taking periods considered in this analysis.

6.3 Extraction of the Photoproduction Cross Section

The photoproduction cross section of the Λ hyperon is given by the formula:

$$\sigma_{\gamma N \rightarrow \Lambda X} = \frac{\sigma_{eN \rightarrow \Lambda X}}{\Phi} \tag{6.3}$$

$$= \frac{N^{\Lambda \rightarrow p+\pi}_{observed}}{\epsilon_{TOT} \cdot BR \cdot \Phi \cdot L} \tag{6.4}$$

where:

- $N^{\Lambda \rightarrow p+\pi}_{observed}$ is the total number of Λ events;
- $BR = 0.642$ is the branching ratio for Λ decaying into a proton plus a negative pion;
- Φ is the Flux Factor, a quantity that connects the DIS cross section to the Photoproduction cross section;
- ϵ_{tot} is the total efficiency
- L is the integrated Luminosity

Luminosity calculation

The Luminosity was calculated for each of the data productions separately. It was evaluated by using the equation:

$$Lumi = L_{rate} \cdot l_{burst} \cdot DT_{corr} \cdot C_{lumi} \tag{6.5}$$

where:

- L_{rate} is the luminosity rate measured by the luminosity monitor;
- l_{burst} is the length of the burst;
- DT_{corr} is the correction for the dead time;
- C_{lumi} is a normalization constant, that relates the luminosity measurement to the known Bhabba scattering cross section and takes the efficiency and the acceptance of the luminosity monitor into account. It has been determined to $C_{lumi} = 250$ mb^{-1} for 1998 and $C_{lumi} = 417 \pm 30$ mb^{-1} for $1999 - 2000$.

The values corresponding to the three data productions are reported in table 6.3.

Data Production	Luminosity (pb^{-1})
$98d0$	30.1
$99c0$	40.3
$00d0$	187.7

Table 6.3: Values of the integrated Luminosity for each of the three data productions analyzed.

(see Sec.6.3).

Calculation of the Photon Flux Factor

The photon flux factor was calculated by using the formula reported in Sec. 4.3.4. Integrating over the ranges $1.7 < \nu < 25$ GeV and between Q^2_{min} and Q^2_{max} yields to a photon flux factor of 0.10.

6.4 Fit and Extraction of the Λ Events

The application of the mentioned cuts significantly reduced the background. The invariant mass spectrum of the Λ hyperon was then fitted with the following function:

$$\begin{aligned} f(x) &= Signal + Background = \\ &= \frac{1}{\sqrt{2\pi}\sigma} \cdot N_\Lambda \Delta x \cdot exp(-\frac{1}{2}(\frac{x-m}{\sigma})^2) + \\ & a + b \cdot x + c \cdot x^2 \end{aligned} \tag{6.6}$$

A Gaussian distribution (normalized to unity) was used to fit the signal region, σ and m represent the *root mean squared* and the *mean* of the distribution, Δx is the width of the bin and N is the parameter that provides the number of '$\Lambda - events$'. The product $N_\Lambda \cdot \Delta x$ represents the total area under the peak. A second order polynomial was used to fit the remaining background. Figs.6.5 and 6.6 show the result of the fit for the $98d0$, $99c0$ and $00d0$ data production, respectively, together with the relevant fit parameters.
In the same way, the number of detected Λ is extracted for the $98d0$ and $99c0$ productions.

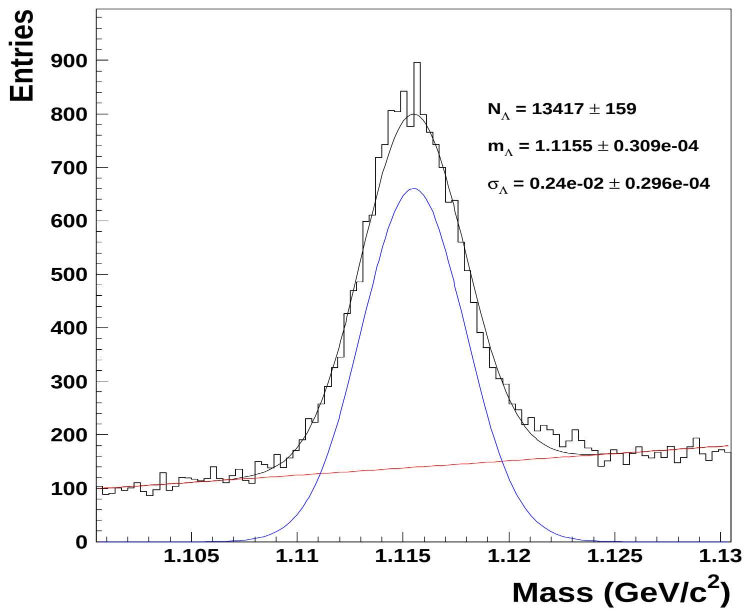

Figure 6.5: Invariant mass spectrum of the Λ with the corresponding fit for the production $98d0$.

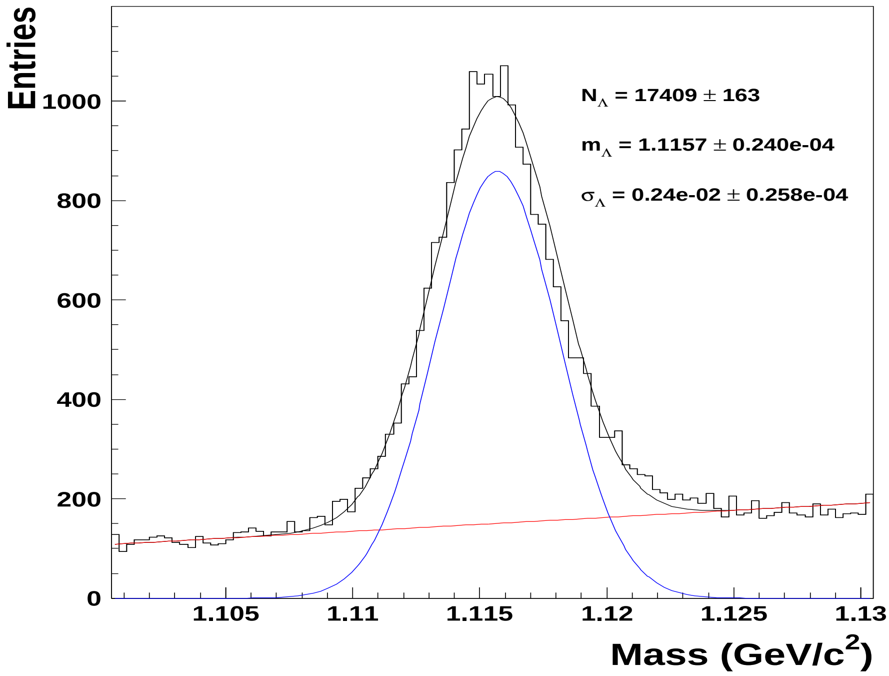

(a)

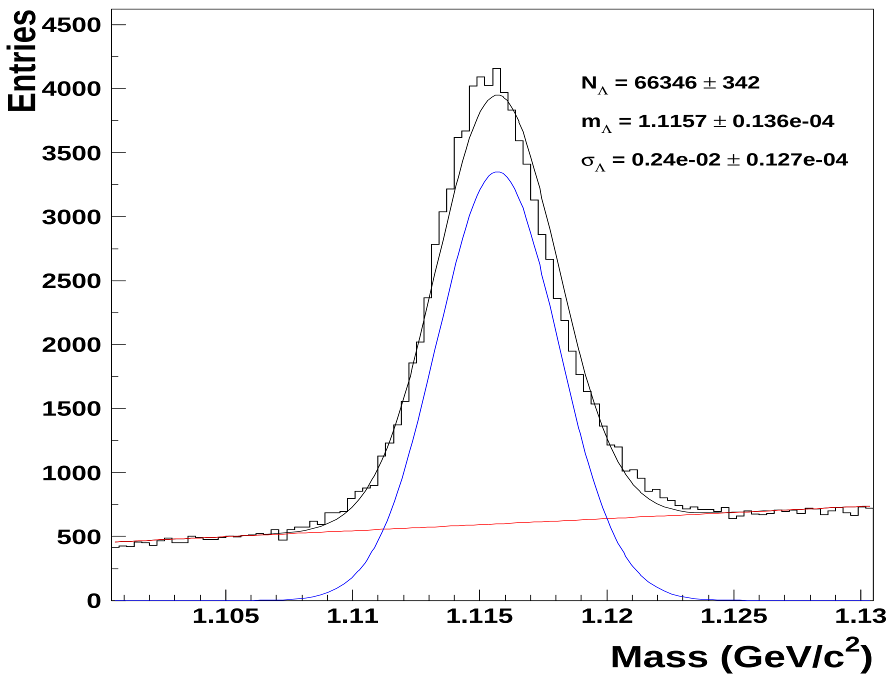

(b)

Figure 6.6: Invariant mass spectra of the Λ with the corresponding fits for the productions (a) $99c0$ and (b) $00d0$.

6.5 Calculation of the Total Efficiency

The total efficiency needed to extract the photoproduction cross section is given by the combination of the geometrical acceptance of the spectrometer, the trigger efficiency, the RICH efficiency and the kinematical cuts efficiency:

$$\epsilon_{tot} = \epsilon_{Geom.Acc.} \cdot \epsilon_{Trigger} \cdot \epsilon_{RICH} \cdot \epsilon_{Exp.Cuts} \tag{6.7}$$

6.5.1 Geometrical Acceptance

The angular acceptance was determined by means of a Monte Carlo simulation. 1000000 of Λ events, i.e. events with at least 1 proton and 1 pion coming from the decay of a Λ particle, were generated both in the detector acceptance and in 4π. In order to take into account the RICH efficiency, a complete simulation of the RICH detector was included. The resulting efficiency, that includes also the RICH efficiency, the geometrical cuts efficiency was defined as:

$$\epsilon_{Geom.Acc.} \cdot \epsilon_{RICH} \cdot \epsilon_{Exp.Cut} = \frac{N^{\Lambda}_{accep.}}{N^{\Lambda}_{4\pi}} \tag{6.8}$$

where:

- $N^{\Lambda}_{accep.}$ is the number of generated Λ within the geometrical acceptance of the detector which are correctly reconstructed and have fulfilled the kinematical cuts applied;
- $N^{\Lambda}_{4\pi}$ is the number of generated Λ in 4π phase space

both numbers were normalized to the corresponding luminosities.

6.5.2 Trigger Efficiency

At this stage, the missing piece is the trigger efficiency. The data used to measure the Λ photoproduction cross section were selected by two dominant triggers: trigger 21 and trigger 27, that are defined, in terms of the detectors involved, as:

Tr21 = (H0 · H1 · H2 · CA)$_T$ or (H0 · H1 · H2 · CA)$_B$

Tr27 = H0G8 [(2H0 · 2H1 · 2H2 · MC · 3BC)$_T$ or (2H0 · 2H1 · 2H2 · MC · 3BC)$_B$]

- **Trigger**21: this is the main trigger in HERMES. It is intended to select potential deep inelastic scattering events using characteristic signals from the scattered lepton. The requirement of coincident hits in all three hodoscopes (H0, H1 and H2) and an energy deposit of more than 1.4 GeV in two adjacent columns of calorimeter blocks have to be fulfilled in the top or in the bottom half of the detector. The coincidence signals in all three hodoscopes prevents triggers to be fired by photons showering in the preshower.
  Also inclusive photoproduction events are selected by this trigger, but, due to the normally rather small average momentum of the particles involved, the efficiency of this trigger is quite low due to the calorimeter threshold for this kind of events.

- **Trigger**27: this trigger is one of the 'photoproduction' triggers, mainly intended for low Q^2 events where the scattered lepton does not leave the beam pipe and hadrons and resonances are produced with a high track multiplicity. Events selected by this trigger should have at least two charged tracks in each detector half leaving coincidence signals in the three hodoscopes and the BCs and the MCs. In addition there is an upper cut on the hit multiplicity in the front hodoscope (H0G8) , necessary for background reduction.

The Trigger efficiency was calculated as explained in Sec.5.4.3, for the events topology that requires at least two long tracks per detector half.
The samples of data enabled by trigger 21 and trigger 27 are partially overlapped. Therefore, in order to evaluate the trigger efficiency of the combination (boolean OR) of the two samples the equation below was used which takes into account the correlation of the two data samples:

$$\epsilon_{OR} = \epsilon_{21} \cdot \epsilon_{27} + \epsilon_{21}(1 - \epsilon_{27}) + \epsilon_{27}(1 - \epsilon_{21}) \tag{6.9}$$

where ϵ_{21} and ϵ_{27} are the efficiencies of trigger 21 and trigger 27, respectively, and ϵ_{OR} is the trigger efficiency of the combined sample.
The three efficiencies, as a function of the proton momentum, are shown in figs.6.7 for the $98d0$, $99c0$ and $00d0$. The trigger21 efficiency is quite low, especially in the lower momentum region, due to the energy threshold in the calorimeter and approaches to $\approx 80\%$ at increasing of the proton momentum. In contrast, the trigger27 efficiency shows no dependence on the proton momentum, its low value is due to the upper cut on the hit multiplicity.

Data Production	ϵ_{21}	ϵ_{27}	ϵ_{OR}
$98d0$	45%	48%	76%
$99c0$	43%	53%	78%
$00d0$	43%	30%	64%

Table 6.4: Average efficiencies of trigger 21, trigger 27 and of the combination of the two triggers.

The values of the total efficiencies (obtained using the Eq.6.7) for the three data productions are listed in Tab.6.5 for both the triggers of interest and for the resulting combination.

Data Production	Total Efficiency - Tr21	Total Efficiency - Tr21	Total Efficiency - Tr21 or Tr27
$98d0$	0.015%	0.017%	0.025%
$99c0$	0.015%	0.019%	0.026%
$00d0$	0.015%	0.011%	0.021%

Table 6.5: Total efficiency for the triggers 21 and 27 and for the combination of the two triggers, for the three data productions.

In order to check the consistency between data and Monte Carlo, some relevant distributions from data and from Monte Carlo have been compared, after correcting the former for the total efficiency. Fig. 6.8 shows the comparison between the proton momentum distributions from the PYTHIA simulation and from the experimental data, corrected for the trigger 21 (top-left panel) and trigger 27 (bottom-left panel) efficiencies. The ratios of the two distributions are also shown (top-right panel for trigger 21 and bottom-right panel for trigger 27 respectively). The momentum distributions of the pion coming from the decay of the Λ particle were compared

too; the comparisons and the ratios are shown in fig. 6.9.
The two data samples selected by trigger21 and trigger27 are independent at 70%. Their efficiencies as a function of the proton momentum are different, see Fig.6.7. Nevertheless, the comparison between data and Monte Carlo looks similar for the two triggers; this lead to the conclusion that the discrepancy between the experimental distributions and the simulated ones is mainly due to a problem in the model used to simulated the photoproduction events.

Using the numbers of total events extracted from the fit and correcting for the corresponding efficiency, the cross sections for the three years have been obtained separately, and are reported in Tab.6.6.

Data Production	Cross Section - Tr21 (μbarn)	Cross Section - Tr27 (μbarn)	Cross Section - Tr21 or Tr27 (μbarn)
$98d0$	30.13 ± 0.32 (stat.)	29.66 ± 0.30 (stat.)	29.90 ± 0.13 (stat.)
$99c0$	27.92 ± 0.27 (stat.)	26.74 ± 0.23 (stat.)	27.33 ± 0.11 (stat.)
$00d0$	28.01 ± 0.13 (stat.)	26.97 ± 0.15 (stat.)	27.49 ± 0.06 (stat.)

Table 6.6: Photoproduction cross sections for triggers 21 and 27 and for the combination of the two triggers, for the three data productions.

The final value of the photoproduction cross section was obtained as the weighted average of the values corresponding to the combination of the two triggers, while the values corresponding to trigger 21 and trigger 27 were used to estimate the systematic uncertainty, as explained in the following section.

$$< \sigma_\Lambda >= 26.96 \pm 0.05\ (stat.)\ \ \mu\text{barn} \tag{6.10}$$

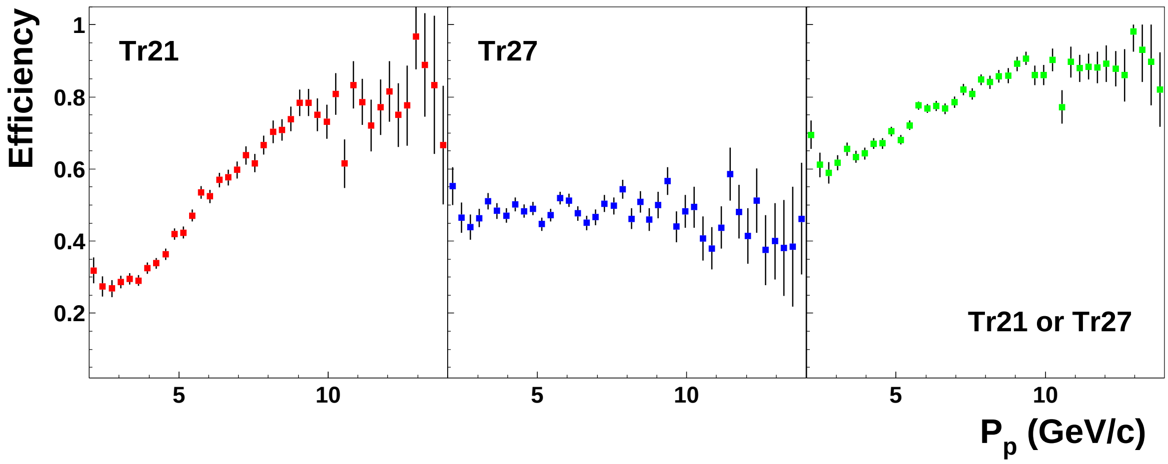

(a) 98d0 production

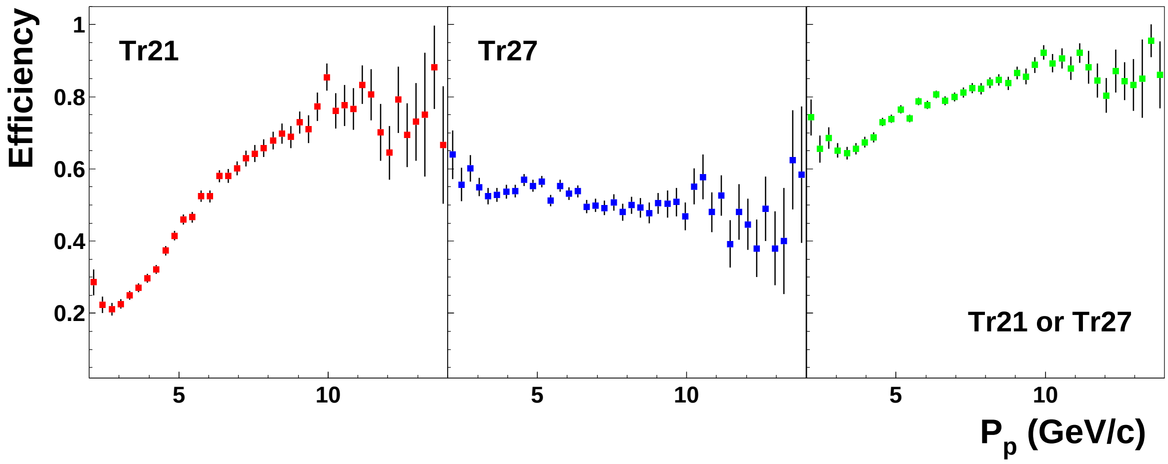

(b) 99c0 production

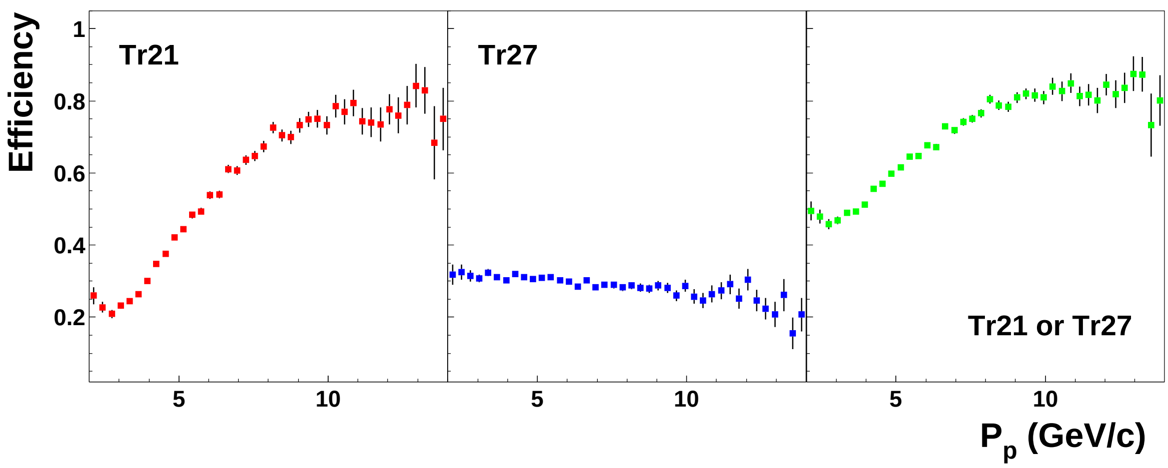

(c) 00d0 production

Figure 6.7: Efficiencies of trigger 21 (left-panel) trigger 27 (center-panel) and of the combination of the two triggers (right-panel) as a function of the proton momentum for the $98d0$ (a), $99c0$ (b) and $00d0$ (c) data productions.

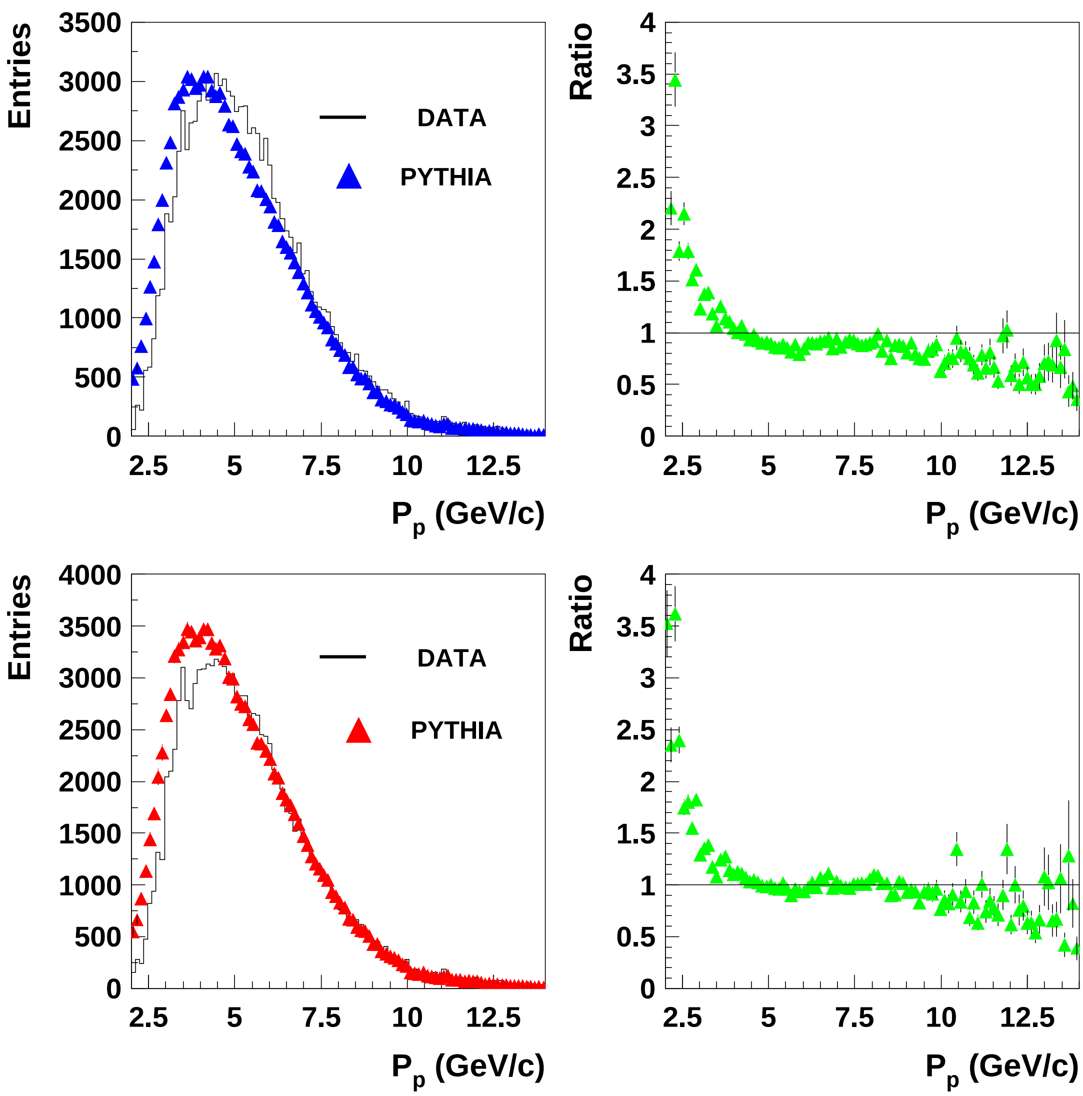

Figure 6.8: Comparison between the momentum distributions from PYTHIA and from the experimental data for the proton coming from the decay of the Λ particles. The experimental data, for the 2000 data production, were corrected for the Trigger 21 (top) and 27 (bottom) efficiencies.

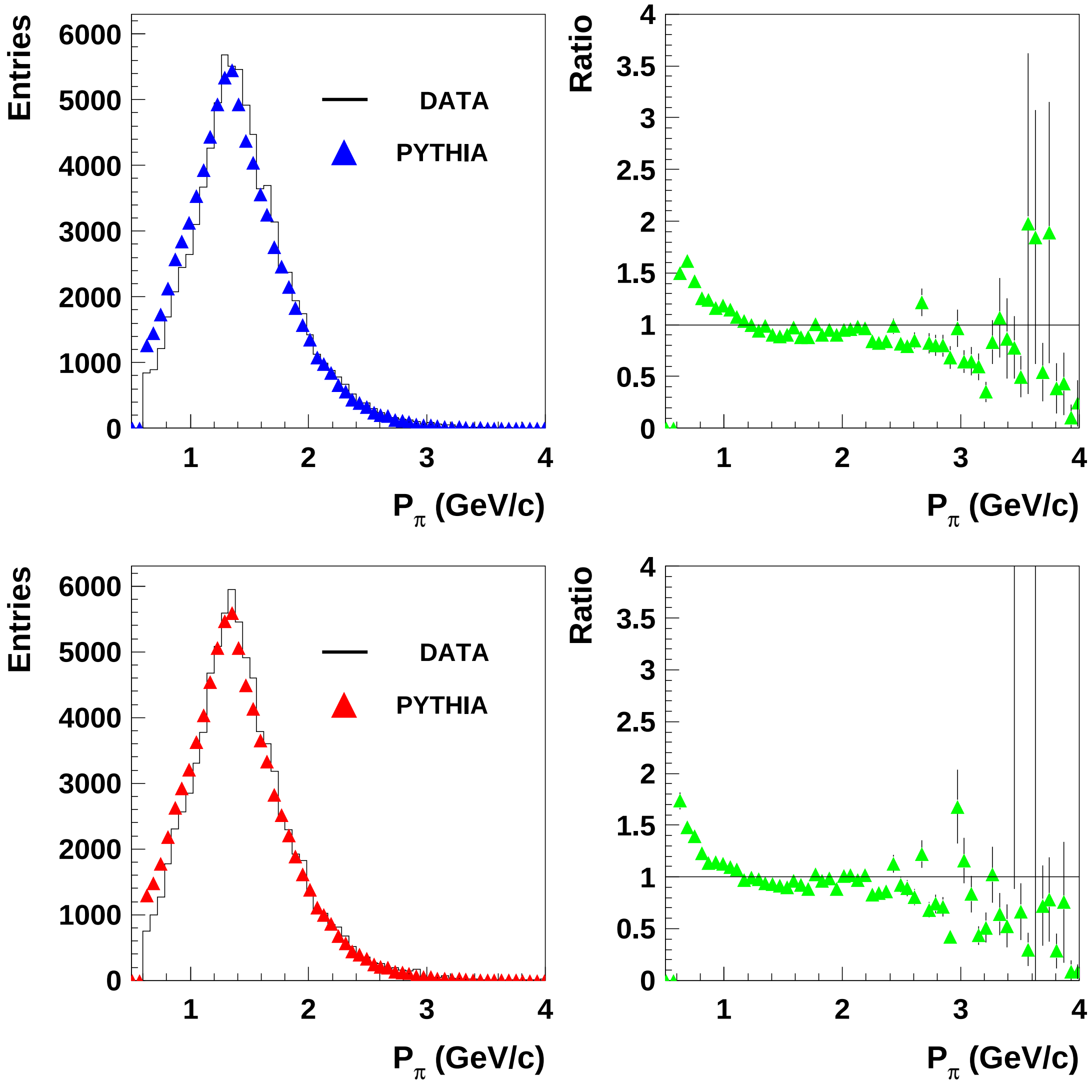

Figure 6.9: Comparison between the momentum distributions from PYTHIA and from the experimental data for the pion coming from the decay of the Λ particles. The experimental data, for the 2000 data production, were corrected for the Trigger 21 (top) and 27 (bottom) efficiencies.

6.5.3 Systematic Uncertainties

Several sources of systematic uncertainties were considered:

- the systematic uncertainty due to the measurement of the Luminosity. There are two possible choices for the determination of the luminosity: the DIS yield (L_{DIS}) or the measurement with the luminosity monitor (L_{lumi}). In [115] the two methods were both used, the deviation from unity of the ratio L_{DIS}/L_{lumi} was used to determine the systematic uncertainty, that was found to be $\sim 5\%$;
- the systematic uncertainty due to the two triggers used in the analysis. It was determined as the half of the difference between the values of the cross sections corresponding to trigger 21 and 27 respectively;
- the systematic error due to the difference between the three data productions: it was estimated as the half of the difference between the highest and the lowest value, corresponding to $98d0$ and $99c0$ productions respectively. This systematic uncertainty, corresponding to $\sim 5\%$ of the total cross section, has been used in the evaluation of the total systematic uncertainty for the heavier hyperons, for which, due to the poor statistics, it was not possible to threat the three data productions separately, as reported in sec. 7.1.3, 7.3.3 and 7.3;
- the systematic error due to the applied cut on the proton momentum: in order to estimate the value of this uncertainty, the cut on the proton momentum was changed. As shown in section (see 4), the ratio between the experimental and the PYTHIA distributions was significantly higher than 1 in the lower momentum region, for this reason the new cut on the proton momentum was set to $4 \div 14$ GeV/c (the old one was $2 \div 14$ GeV/c) and the cross section was calculated again for each of the data productions separately. The values corresponding to the two relevant triggers (21 and 27) were combined as already explained and are reported in table 6.7.

Data Production	Cross Section (μbarn)
$98d0$	$33.60 \pm 0.32(stat.)$
$99c0$	$29.74 \pm 0.26(stat.)$
$00d0$	$30.65 \pm 0.13(stat.)$

Table 6.7: Photoproduction cross sections for triggers 21 and 27 for the three data productions, extracted after applying the new cut on the proton momentum.

The weighted averaged cross section of the three data productions with the new cut is then:

$$< \sigma_\Lambda >= 31.47 \pm 0.10(stat.) \ \ \mu\text{barn} \tag{6.11}$$

The systematic uncertainty due to the applied cut was calculated as the half of the difference between the values of the cross sections corresponding to the two cuts.

The values of the systematic errors were then added in quadrature. The resulting Λ photoproduction cross section, with the corresponding statistical and systematic uncertainties is:

$$< \sigma_\Lambda >= 26.96 \pm 0.07(stat.) \pm 2.98(syst.) \ \ \mu\text{barn}. \tag{6.12}$$

6.6 $\overline{\Lambda}$ Hyperon

The geometrical and kinematical cuts used for the Λ analysis were applied in the study of the $\overline{\Lambda}$. Also in this case, the three data productions were treated separately. The invariant mass spectrum was reconstructed and the number of $\overline{\Lambda}$ was then extracted by fitting the spectrum with a Gaussian distribution and a second order polynomial. In fig.6.10 the mass spectrum of the $\overline{\Lambda}$ for the $00d0$ data production is shown; the fit and the corresponding parameters are also shown.

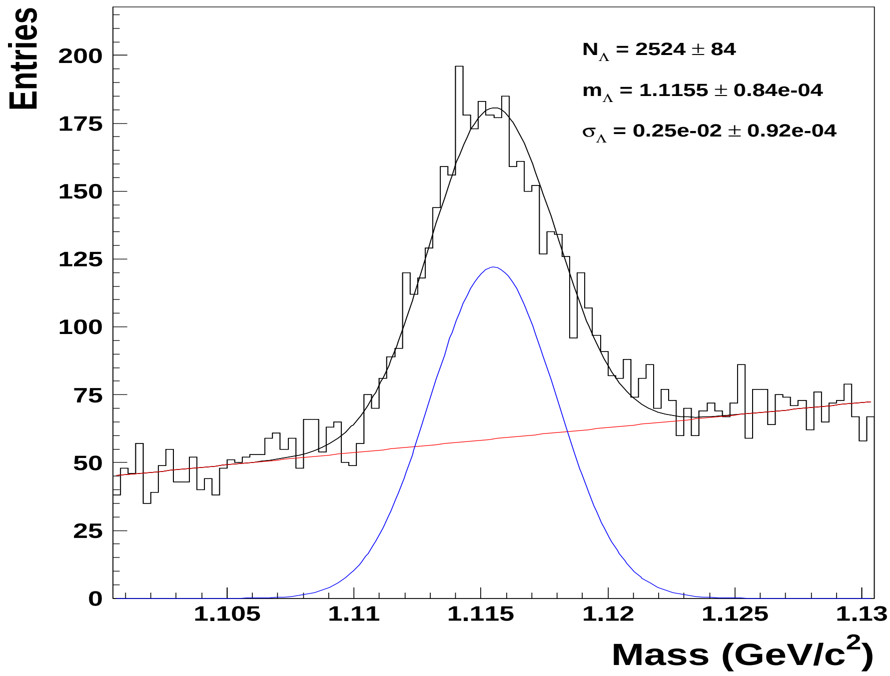

Figure 6.10: The invariant mass spectrum of the $\overline{\Lambda}$ is shown together with the fit.

Trigger 21 and trigger 27 were identified as the relevant triggers. Their efficiencies were calculated for each data production as explained in Sec.5.4.3 for the event topology with at least two long tracks per detector half. The efficiencies of trigger 21 and trigger 27 and of the combination of the two triggers are shown in fig. 6.12 as a function of the anti-proton momentum and their average values are reported in table 6.8.

Data Production	ϵ_{21}	ϵ_{27}	ϵ_{OR}
$98d0$	67%	53%	87%
$99c0$	67%	52%	87%
$00d0$	70%	29%	80%

Table 6.8: Average efficiencies of trigger 21, trigger 27 and of the combination (boolean OR) of the two triggers.

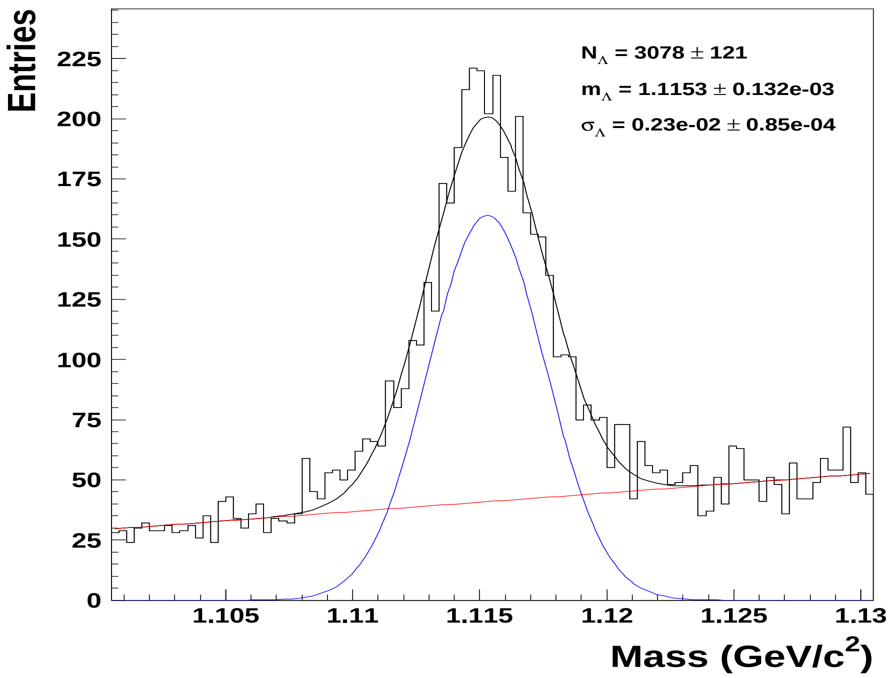

(a)

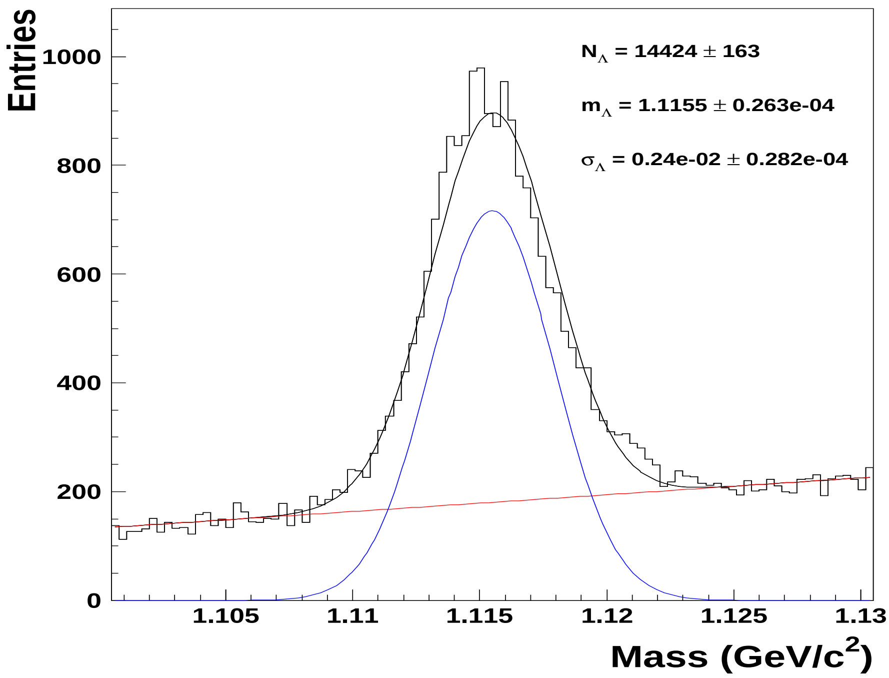

(b)

Figure 6.11: Invariant mass spectra of the $\overline{\Lambda}$ with the corresponding fits for the productions (a) $99c0$ and (b) $00d0$.

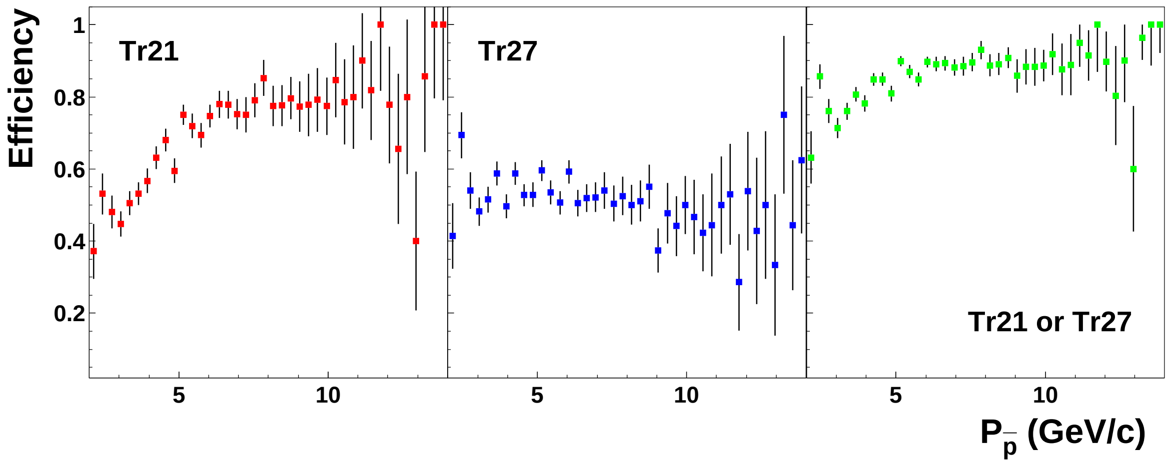

(a) 98d0 production

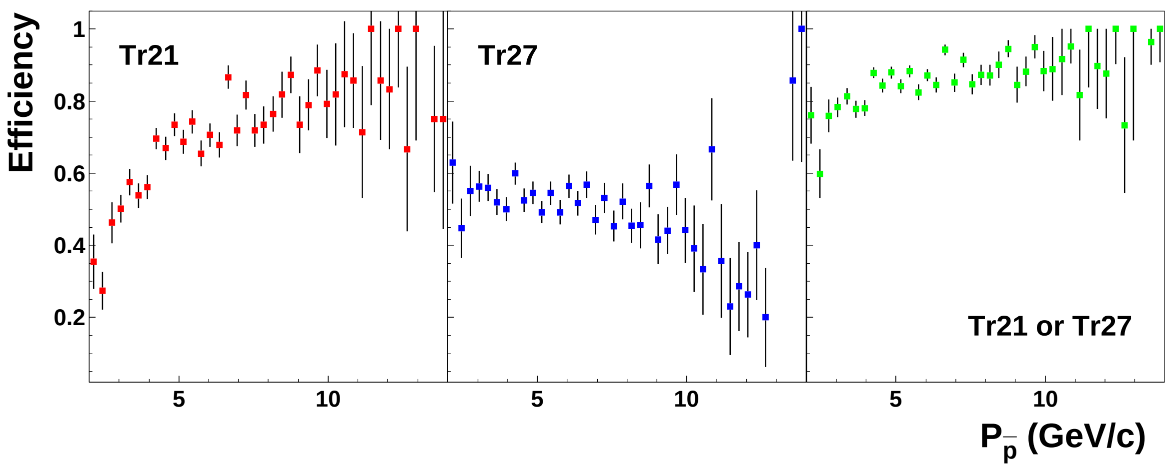

(b) 99c0 production

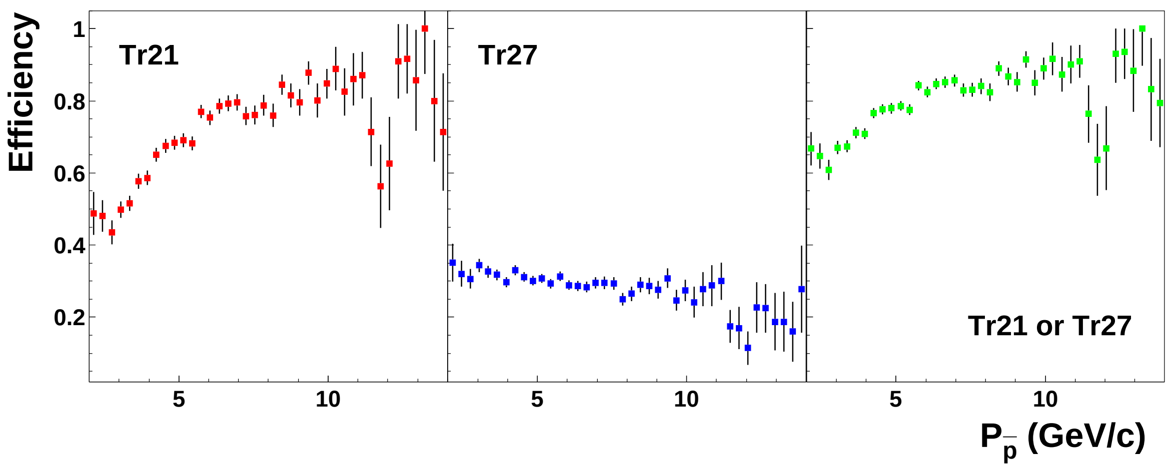

(c) 00d0 production

Figure 6.12: Efficiencies of trigger 21 (left-panel) trigger 27 (center-panel) and of the combination of the two triggers (right-panel) as a function of the proton momentum for the $98d0$ (a), $99c0$ (b) and $00d0$ (c) data productions.

Data Production	Total Efficiency - Tr21	Total Efficiency - Tr21	Total Efficiency - Tr21 $\cup$ Tr27
$98d0$	0.50%	0.38%	0.61%
$99c0$	0.50%	0.37%	0.60%
$98d0$	0.51%	0.21%	0.57%

Table 6.9: Total efficiency for the triggers 21 and 27 and for the combination (boolean OR) of the two triggers, for the three data productions.

The $\overline{\Lambda}$ photoproduction cross section was extracted using the usual formula (eq.6.4). The final value was obtained as the weighted average of the values obtained for the three data productions. The systematic uncertainty was estimated as explained in sec. 6.5.3.

$$< \sigma_{\overline{\Lambda}} >= 0.2102 \pm 0.0014 \pm 0.0172 \ \mu\text{barn} \tag{6.13}$$

6.7 Λ differential cross section

Fig.6.13 shows the distribution of the longitudinal component of the Λ momentum and of the Feynman variable x_F for the two Monte Carlo productions used to calculate the acceptance function needed to extract the photoproduction cross section.

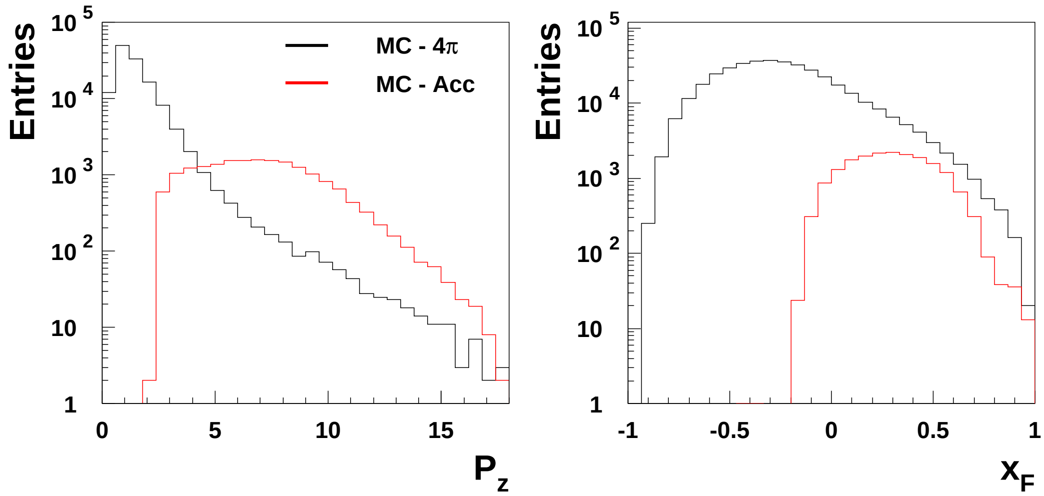

Figure 6.13: Distribution of the longitudinal component of the Λ momentum and of the Feynman variable x_F, in 4π (black line) and within the HERMES acceptance (red line).

A large fraction of the Λ hyperons simulated in 4π are produced in the negative x_F region, which is generally referred to as the 'target fragmentation region' (see Sec.3). On the other hand, the limited angular coverage of the HERMES spectrometer corresponds to a mainly positive x_F interval. Thus, the values of the absolute photoproduction cross section reported for the Λ and $\overline{\Lambda}$ are extrapolated in a x_F region in which it is not possible to test the Monte Carlo distributions with the experimental ones.
Since in the photoproduction regime the information about the scattered leptons are not available, it is not possible to define the x_F variable. However, the application of the cut on the longitudinal momentum of the Λ ($\overline{\Lambda}$):

$$P_z^{\Lambda(\overline{\Lambda})} > 3 \;\; GeV/c \tag{6.14}$$

allows to restrict the data sample to the positive x_F region, corresponding to the so called 'current fragmentation region' (see Fig.6.14).

The acceptance was then calculated as a function of the longitudinal and transverse components of the Λ ($\overline{\Lambda}$) momentum. This information was stored in a 10×10 bins matrix, that, combined with the trigger21 efficiency, provided the total experimental efficiency to be used to correct the experimental data (defined as explained in sec.6.5.2).
The differential cross section extracted in this way was compared with the Monte Carlo one, obtained with two different sets of the PYTHIA parameters:

- the **DEFAULT** parameters, tuned by fitting the data from e^+e^- collider experiments;
- the parameters tuned to the HERMES data by measuring hadron multiplicities versus various variables (as described in [76] and [77]):

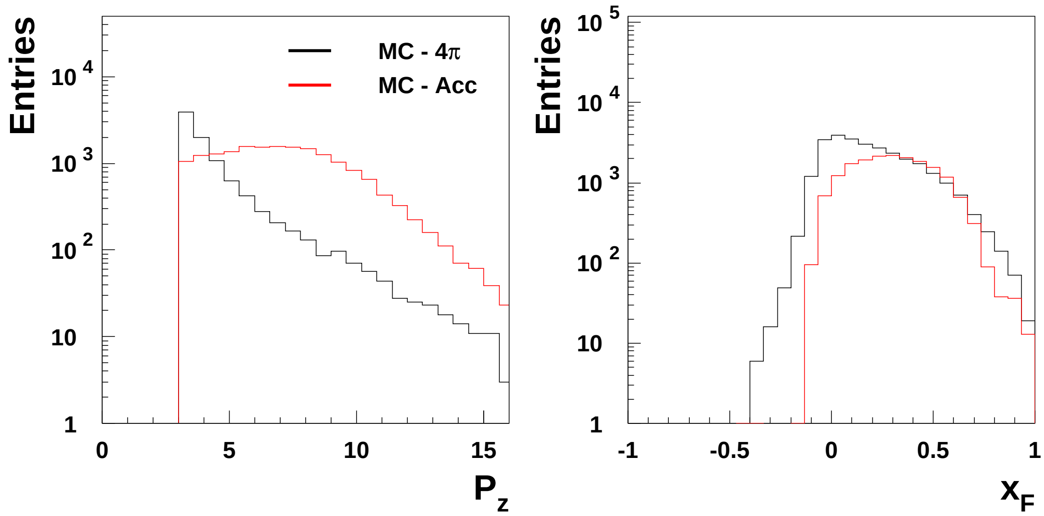

Figure 6.14: Distribution of the longitudinal component of the Λ momentum and of the Feynman variable x_F, in 4π (dark line) and within the HERMES acceptance (light line).

1 - PARJ $1 = 0.029$ (default = 0.1)
2 - PARJ $2 = 0.283$ (default = 0.3)
3 - PARJ $3 = 1.2$ (default = 0.4)
4 - PARJ $21 = 0.36$ (default = 0.4)
5 - PARJ $41 = 1.94$ (default = 0.3)
6 - PARJ $42 = 0.544$ (default = 0.58)
7 - PARJ $45 = 1.05$ (default = 0.5)

The meaning of the parameters above is explained in Chapter 4.
The results of the comparison are shown in Figs. 6.15 and 6.16 for the two sets of parameters, respectively. The differential cross sections look similar in shape but differ in the absolute values (a factor of 8.16 for the production with the **DEFAULT** parameters and a factor of 7.32 (3.82)for the production with the HERMES parameter settings).
The comparison between the data and the Monte Carlo P_z distributions slightly improves when the HERMES settings are used. The improvement is due to the change in PARJ$41 - 42$ that correspond to the parameters a and b of the symmetric LUND fragmentation function (see Sec. 4.2). These parameters have a substantial impact on the share of the available energy to the produced hadrons. Higher values of a shift the hadron distribution toward lower values of z while the increase of b causes the opposite effect (see [76]). The residual disagreement between data and Monte Carlo in the lower longitudinal momentum region suggests that a still too high value of the a parameter was used in the new parameterization.
In contrast, the comparison of the transverse momentum distributions does not improve when using the HERMES settings. This is due to the fact that the PARJ21 parameter, which corresponds to the width of the Gaussian p_x and p_y transverse momentum distribution, was not substantially changed during the tuning of the model to the HERMES kinematics. Indeed any major change of this parameter resulted in a dramatic worsening in the agreement between P_t and rapidity (see Sec. 3.1) distributions from data and Monte Carlo.

Thanks to the relatively high statistics the extraction of the differential cross section was also possible for the Λ ($\overline{\Lambda}$) hyperon. In contrast, due to their lower statistics, only the extraction of the absolute cross section was possible for the heavier hyperons, as reported in the next chapter.

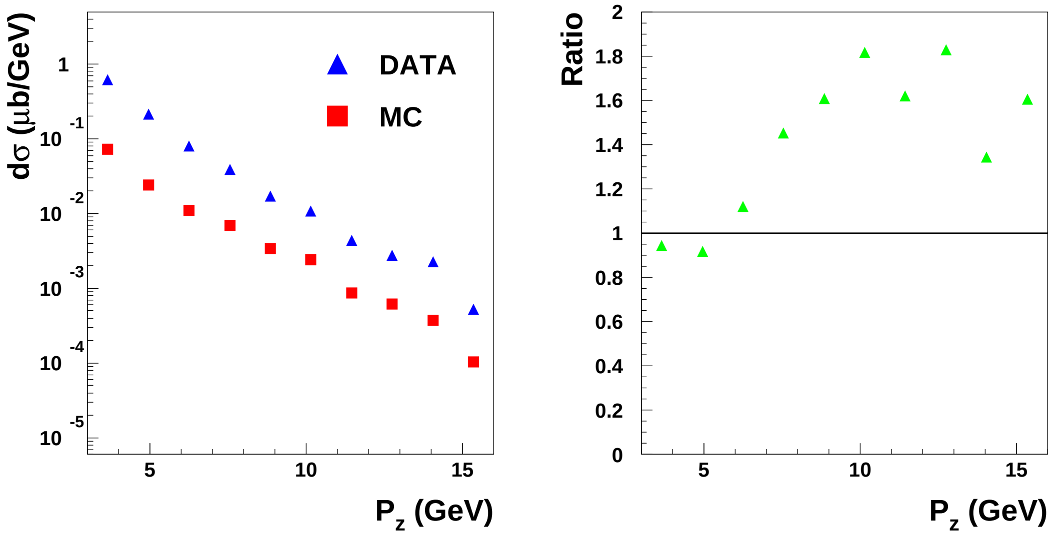

(a)

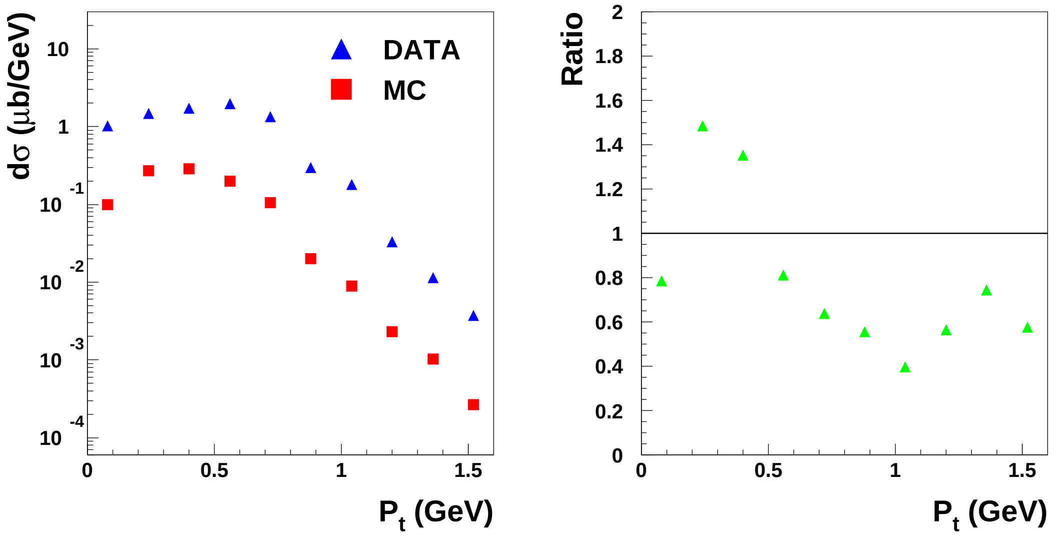

(b)

Figure 6.15: Differential cross section as a function of P_z^{Λ} (a) and P_t^{Λ} (b) for data and MC, produced by using the **DEFAULT** PYTHIA parameters.(left panels). Ratio between the differential cross section from data and MC (right panels).

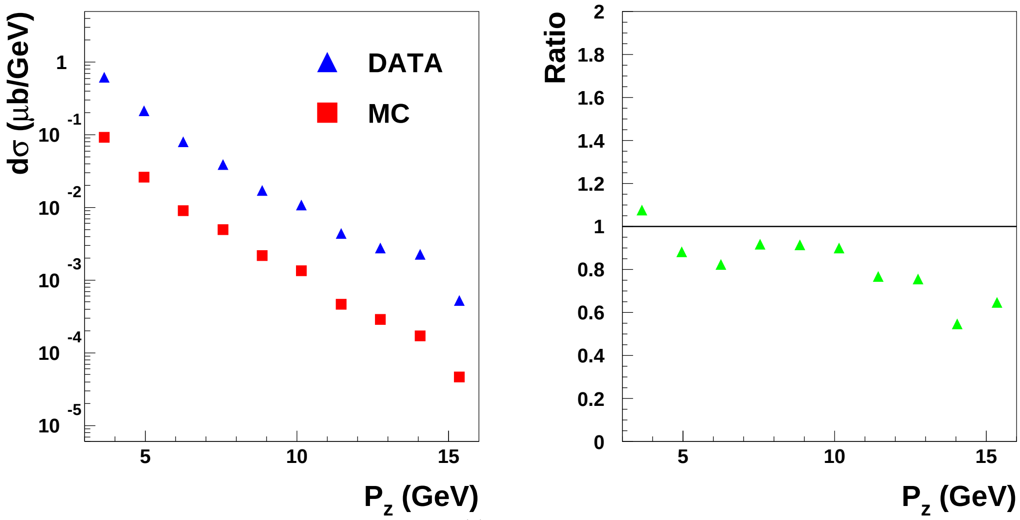

(a)

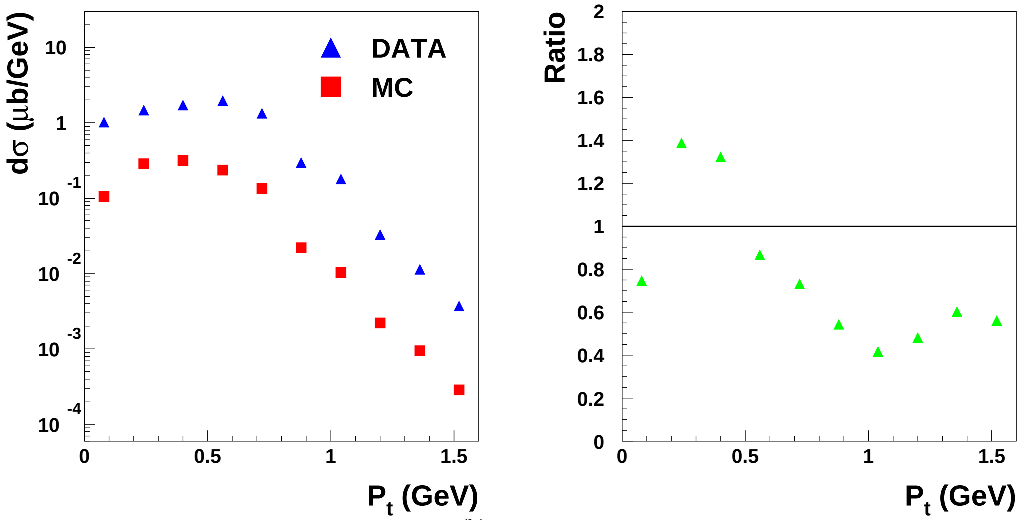

(b)

Figure 6.16: Differential cross section as a function of P_z^Λ (a) and P_t^Λ (b) for data and MC, produced by using the HERMES PYTHIA parameters (left panels). Ratio between the differential cross section from data and MC (right panels).

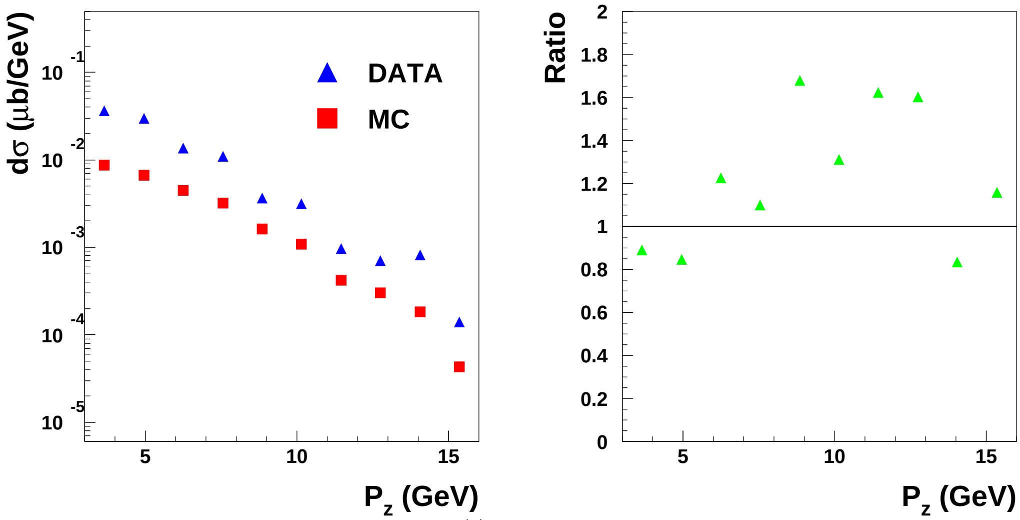

(a)

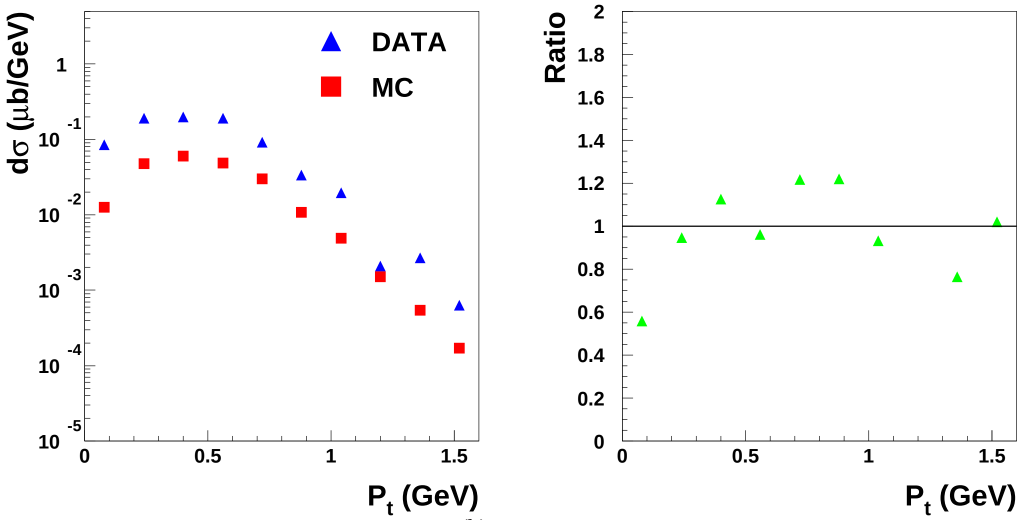

(b)

Figure 6.17: Differential cross section as a function of P_z^{Λ} (a) and P_t^{Λ} (b) for data and MC, for $\overline{\Lambda}$ particle, produced by using the HERMES PYTHIA parameters (left panels). Ratio between the differential cross section from data and MC (right panels).

Chapter 7

Heavier Hyperons

The main steps needed for the extraction of the photoproduction cross section of the heavier hyperons decaying into a Λ are described in this chapter.
The data quality cuts and the kinematical cuts explained in Sec.6.1 were used to reconstruct the mass spectra.
Each of the hyperons analyzed here presents a signal-to-background ratio worse than that of the Λ, for this reason a detailed study of the background was performed by means of a Monte Carlo simulation. The background subtracted spectra were then fitted in order to extract the number of observed events.
The photoproduction events were selected by two main triggers, whose efficiency was calculated by using some calibration triggers. The geometrical acceptance of the HERMES spectrometer was estimated by means of a Monte Carlo simulation.
The photoproduction cross sections were then extracted for the hyperons reported in Tab.2.2 and for the corresponding antihyperons.

7.1 Σ^0 Hyperon

The Σ^0 hyperon decays in a Λ plus a photon with a branching ratio of 100% (see Tab.2.2).
The data quality cut reported in Sec.6.1 were applied for the selection of the Σ^0 candidates. The following geometrical cuts on the electromagnetic calorimeter have been included in order to identify the photon and to reduce the background:

calorimeter fiducial volume	$\lvert x_{calo} \rvert \leq 125\ cm$ $33cm \leq y_{calo} \leq 105\ cm$

Table 7.1: Fiducial volume cuts for the electromagnetic calorimeter.

Furthermore, the following cuts were applied:
The mass spectrum of the Λs satisfying the cuts applied for the selection of the Σ^0 hyperon is shown in fig.7.2 (a). It is possible to define two regions depending on the Λ mass range. The region between 1.108 and 1.123 GeV/c^2 ($\pm 3\sigma$, where σ is the experimental width determined by fitting the Λ mass spectrum and equal to $0.24 \cdot 10^{-2}$ GeV) identifies the so-called '**SIGNAL-REGION**'; the two regions between 1.1005 and 1.108 GeV/c^2 and between 1.123 and 1.1305 GeV/c^2 are the so-called **SIDE - BAND REGIONS**, and, as described in Sec.7.1.3 are used to subtract the background of the Σ^0.

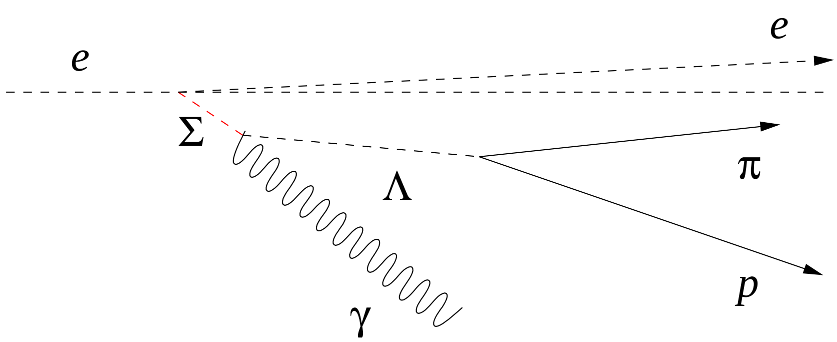

Figure 7.1: Schematic view of the Σ^0 production and decay vertices.

Proton Track	
	Long track
PID	Positively identified by the RICH
Momentum	$2 < P_p < 14$ GeV/c
Pion Track	
	Long or short track
Momentum	$P_\pi > 0.6$ GeV/c
Photon Track	
Momentum	$P_\gamma > 0.8$ GeV/c
Λ Particle	
Mass	$1.108 < M_\Lambda < 1.123$ GeV/c^2
dca (p - π)	< 1.5 cm
Production Vertex	-18 cm $< v_{prod} < 18$ cm

Table 7.2: Cuts applied for the selection of Σ^0 candidates.

The mass spectrum of the Σ^0 (shown in Fig.7.2 (b)) was reconstructed selecting the produced Λ in the signal-region.

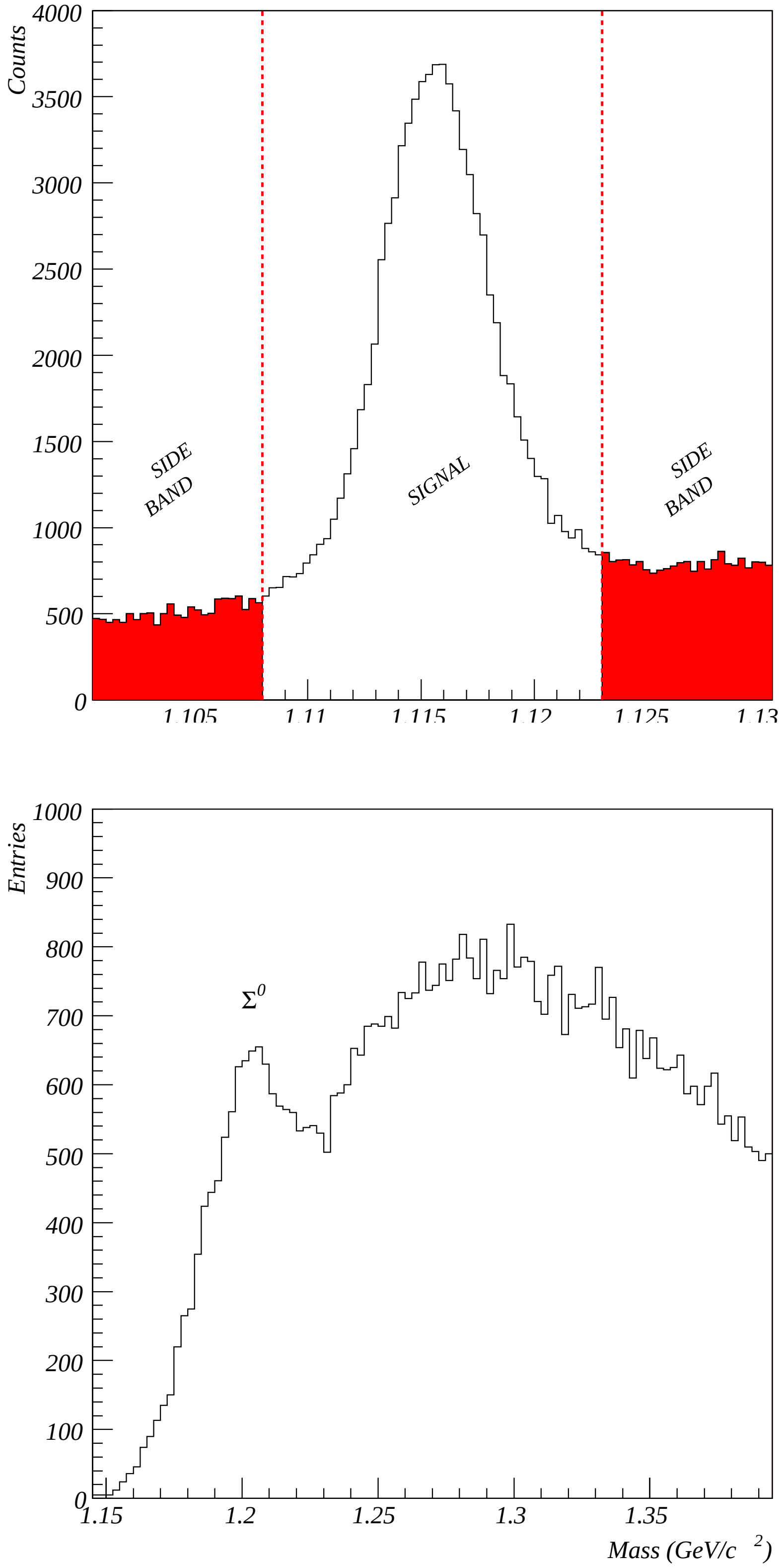

(b)

Figure 7.2: (a) Invariant mass spectrum of the Λs coming from the decay of the Σ^0. (b) Invariant mass spectrum of the Σ^0 hyperon.

7.1.1 Extraction of the Photoproduction Cross Section

The photoproduction cross section of the Σ^0 hyperon was calculated using the formula:

$$\sigma_{\gamma N \to \Sigma^0 X} = \frac{\sigma_{eN \to \Sigma^0 X}}{\Phi} \tag{7.1}$$

$$= \frac{N^{\Sigma^0 \to \Lambda+\gamma}_{observed}}{\epsilon_{TOT} \cdot BR_{\Lambda} \cdot BR_{\Sigma^0} \cdot \Phi \cdot L} \tag{7.2}$$

where:

- $N^{\Sigma^0 \to \Lambda+\gamma}_{observed}$ is the total number of Σ^0 events;
- ϵ_{TOT} is the total efficiency
- BR_{Λ} and BR_{Σ^0} are the branching ratios for the Λ decay ($BR_{\Lambda \to p+\pi} = 0.642$) and for the Σ^0 decay ($BR_{\Sigma^0 \to \Lambda+\gamma} = 1$) respectively;
- Φ is the Photon Flux Factor;
- L is the total Luminosity integrated over the three data productions analyzed.

The calculation of the total Luminosity and the determination of the Photon Flux Factor are explained in Secs.6.3 and 6.3.

7.1.2 Calculation of the Total Efficiency

The total efficiency for the Σ^0 hyperon was defined as:

$$\epsilon_{tot} = \epsilon_{Geom.Acc.} \cdot \epsilon_{RICH} \cdot \epsilon_{Kin.Cuts} \cdot \epsilon_{Trigger} \tag{7.3}$$

The combination of the geometrical acceptance, the RICH efficiency and the kinematical cuts efficiency was calculated by using a Monte Carlo simulation, including the RICH, after applying the same kinematical cuts used for the selection of the Σ^0 candidates. It was defined as the ratio:

$$\epsilon_{Geom.Acc.} \cdot \epsilon_{RICH} \cdot \epsilon_{Kin.Cuts.} = \frac{N^{\Sigma^0 gen.}_{acc.}}{N^{\Sigma^0 gen.}_{4\pi}} \tag{7.4}$$

where $N^{\Sigma^0 gen.}_{acc.}$ is the number of Σ^0 particles generated by PYTHIA, tracked through the detector and satisfying the above cuts, and $N^{\Sigma^0 gen.}_{4\pi}$ is the number of Σ^0 particles generated in 4π.

The missing piece is the efficiency of the triggers involved in the analysis. Two relevant triggers, 21 and 27, have been used. The efficiencies of these triggers were calculated as explained in Sec.5.4.3 and then were combined as explained in Sec.6.3. Also in this case, the efficiency was calculated only for the event topology with at least two long tracks per detector half. The trigger 21 efficiency shows a behavior similar to that of the Λ, but the mean efficiency is higher in this case; this is probably due to the presence of the photon in the Σ^0 events, that increases the probability to satisfy the calorimeter threshold. The trigger 27 efficiency shows no dependence from the proton momentum.

The efficiencies for the triggers 21 and 27 and for the combination of the two triggers are shown in Fig.7.3.

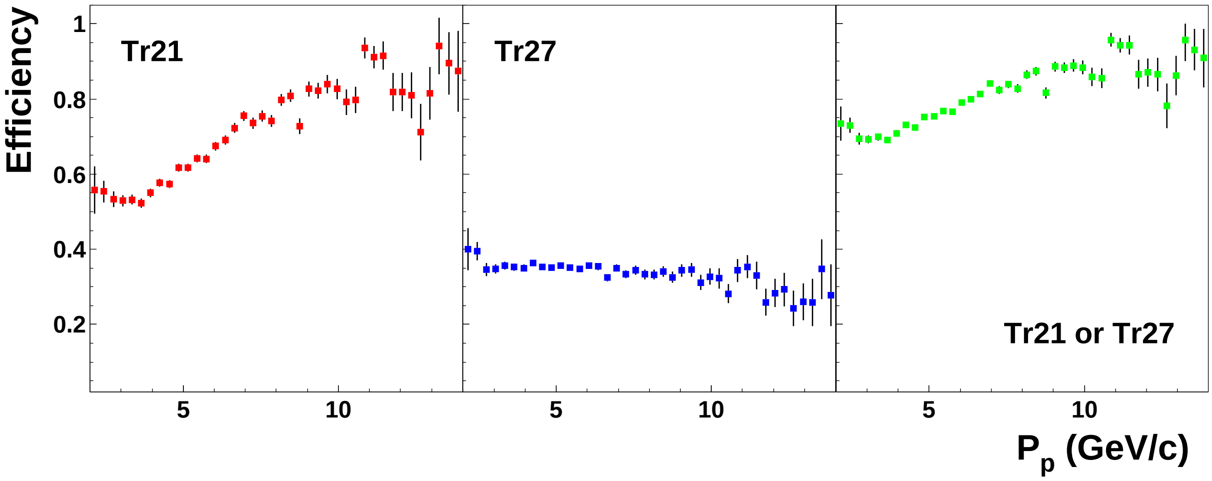

Figure 7.3: Efficiencies of trigger 21 (left-panel), trigger 27 (center-panel) and of the combination of the two triggers (right-panel) as a function of the proton momentum.

Data Production	Trigger 21	Trigger 27	Trigger 21 or 27
$98d0 + 99c0 + 00d0$	66%	35%	78%

Table 7.3: Total efficiency for the triggers 21 and 27 and of the combination of the two triggers.

Data Production	Total Efficiency - Tr21	Total Efficiency - Tr27	Total Efficiency - Tr21 or 27
$98d0 + 99c0 + 00d0$	0.0029%	0.0014%	0.0033%

Fig.7.4 shows the comparison between the proton momentum distributions from the PYTHIA simulation and from the experimental data, corrected for the trigger 21 (top-left panel) and trigger 27 (bottom-left panel) efficiencies. The ratios of the two distributions are also shown (top-right panel for trigger 21 and bottom-right panel for trigger 27 respectively). The momentum distributions of the pion coming from the decay of the Λ particle were compared too; the comparisons and the ratios are shown in Fig.7.5. The comparison between data and Monte Carlo looks similar to that obtained for the Λ.

7.1.3 Extraction of the Σ^0 events

The total number of Σ^0 events was extracted using two different methods:

- the subtraction of the total background;
- the fit of the invariant mass spectrum.

The two methods are described in the following sections.

Background Subtraction

Two possible sources of combinatorial background were identified:

- the combination of a 'fake' Λ with an uncorrelated photon;
- the combination of a 'true' Λ with an uncorrelated photon.

The first kind of background can be reproduced with the so-called 'SIDE-BAND' method: the invariant mass spectrum of the Σ^0 is reconstructed requiring a Λ from the side-band regions (see Fig.7.2(a)). The second kind of background can be simulated with a Monte Carlo program: the invariant mass spectrum of the hyperon is reconstructed in this case combining a 'true' Λ (i.e. identified by the PYTHIA LUND type) with a photon, with the requirement that the resulting hyperon is not a 'true' Σ^0 (i.e. not identified by the PYTHIA LUND type).
Fig 7.6 shows the invariant mass spectrum of the Σ^0, that satisfying the applied cuts, and the two backgrounds. The background due to the "fake" Λs coming from the Λ's SIGNAL REGION was extrapolated from the Λ SIDE BANDE REGION under the assumption of a homogeneous background within and outside the SIGNAL REGION (see Fig.7.2(a)). As a first step this contribution to the total background was subtracted from the uncorrected Sigma0 spectrum. The resulting spectrum was further corrected for the combinatorial background simulated by the Monte Carlo after normalizing the latter to the former in the mass range $1.25 - 1.35$ GeV/c^2. (Fig.7.8(b)).

Fit of the invariant mass spectrum

The total number of observed events can be accessed, in a different way, by fitting the total 'signal spectrum' with the following function in the mass range $1.145 - 1.395\ GeV/c^2$:

$$\begin{aligned} f(x) &= Signal + Background = \\ &= \frac{1}{\sqrt{2\pi}\sigma} \cdot N_{\Sigma^0} \cdot \Delta x \cdot exp(-\tfrac{1}{2}(\tfrac{x-m}{\sigma})^2) + \\ &(a + b \cdot x + c \cdot x^2 + d \cdot x^4) \cdot exp(f \cdot (x+g)) \end{aligned} \tag{7.5}$$

The Gaussian function was used to fit the peak and the total number of Σ^0, N_{Σ^0} was directly provided by the fit. The product $N_{\Sigma^0} \cdot \Delta x$, with Δx the width of the bin, represents the total area under the peak. The background was fitted with a combination of a polynomial and an exponential function, used to fix the end-point of the available phase-space. The result of the fit together with the fit parameters is shown in Fig.7.8.

In both described methods, the photoproduction cross sections were calculated for each of the two triggers separately and then the values were combined as explained in Sec.6.3. The corresponding weighted average cross sections are reported in Tab.7.4.

Method	**Cross Section (μbarn)**
Background Subtraction	$4.68 \pm 0.26(stat.)$
Fit	$5.18 \pm 0.23(stat.)$

Table 7.4: Photoproduction cross sections of the Σ^0 hyperon extracted with the two methods.

Both methods are affected by a certain extend of arbitrariness. In fact, in the background subtraction method it was assumed that all the possible sources of background were correctly simulated by PYTHIA, while in the fit method the choice of the function used to fit the background sensibly affects the extraction of the number of events. For this reason, as a criterion, the mean value of the two obtained was taken as the final result of the Σ^0 photoproduction cross section. The highest value of the statistical error was chosen as the final one.

Systematic Uncertainties

Several sources of systematic uncertainties was identified:

- the systematic uncertainties due to the used triggers: it was obtained as half of the difference of the cross sections corresponding, for each method, to trigger 21 and trigger 27, respectively.
- the systematic uncertainty due to to the time stability of the detector: the error estimated in the Λ analysis (see Sec.6.5.3) was propagated (in percentage) to the heavier hyperons;
- the systematic uncertainty due to the different methods, calculated as the half of the difference of the two values reported in Tab.7.4;
- the systematic uncertainty due to the measurement of the luminosity (see Sec.6.5.3)

the four contributions of systematic uncertainties were then added in quadrature.
The weighted averaged photoproduction cross section of the Σ^0 hyperon is then:

$$< \sigma_{\Sigma^0} >= 4.93 \pm 0.23(stat.) \pm 0.63(syst.) \quad \mu\text{barn} \tag{7.6}$$

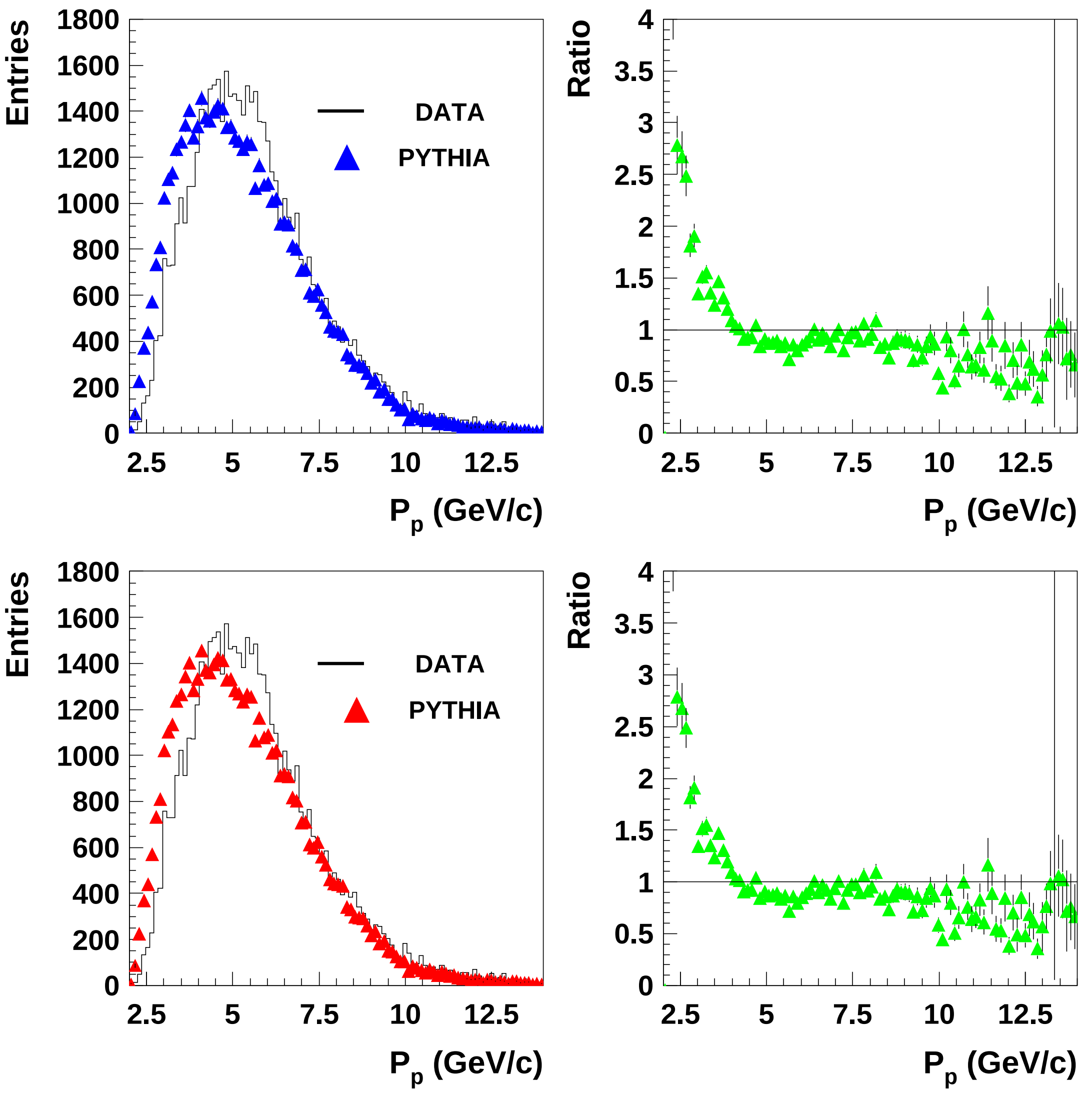

Figure 7.4: Comparison between the momentum distributions from PYTHIA and from the experimental data for the proton of the Λ particles coming from the decay of the Σ^0 hyperon. The experimental data, were corrected for the Trigger 21 (top) and 27 (bottom) efficiencies.

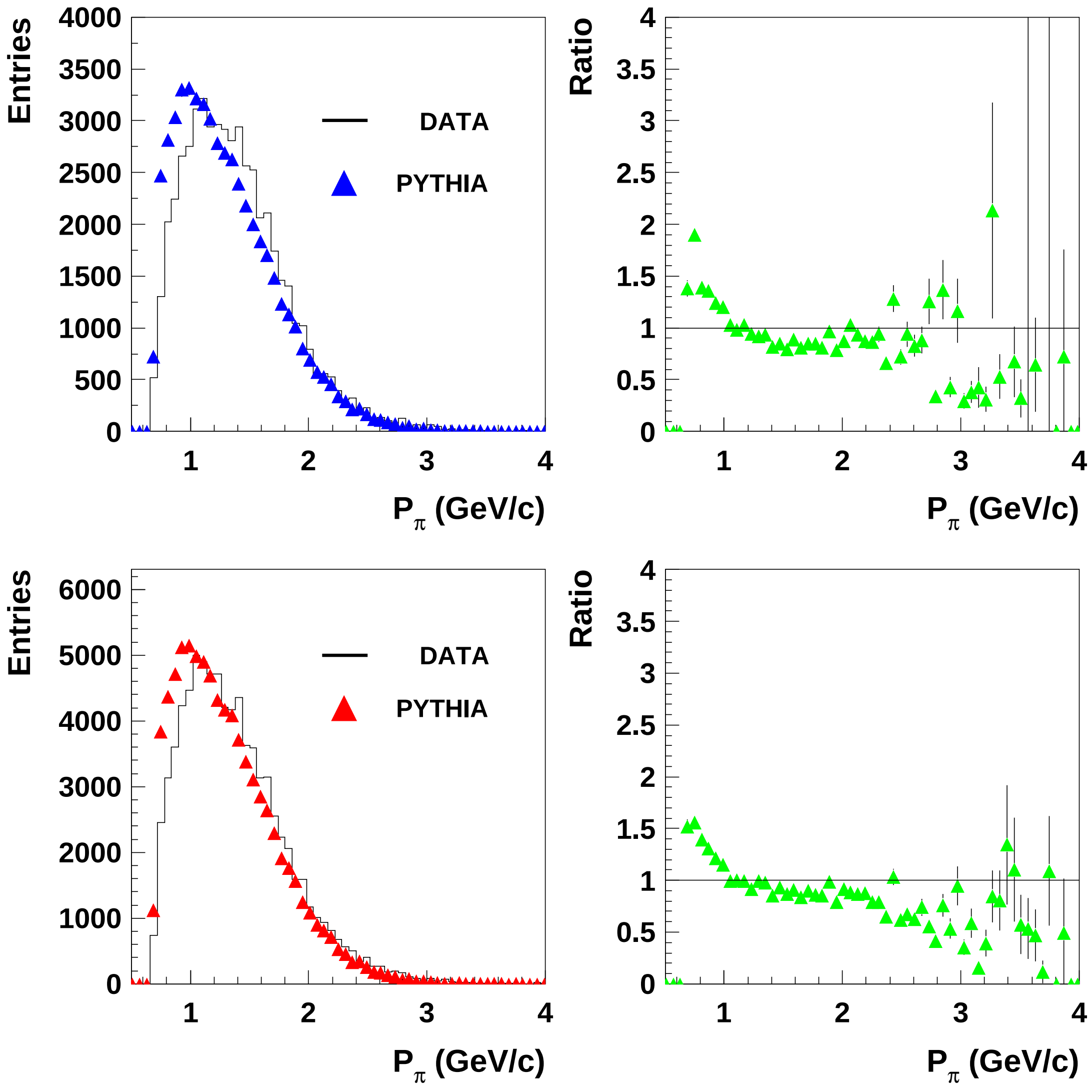

Figure 7.5: Comparison between the momentum distributions from PYTHIA and from the experimental data for the pion of the Λ particles coming from the decay of the Σ^0 hyperon. The experimental data, were corrected for the Trigger 21 (top) and 27 (bottom) efficiencies.

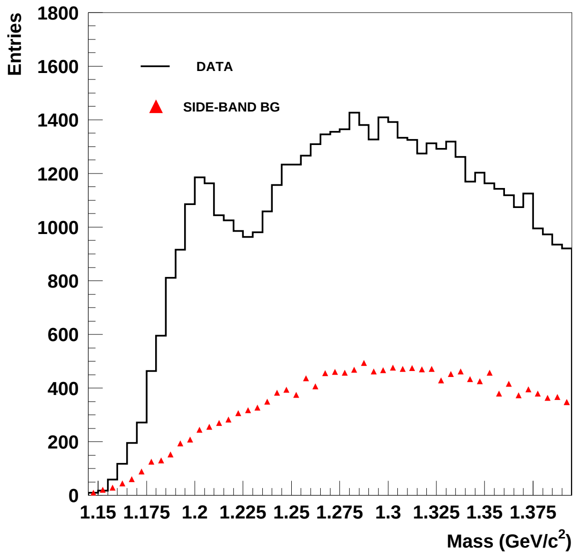

(a) SIDE-BAND background

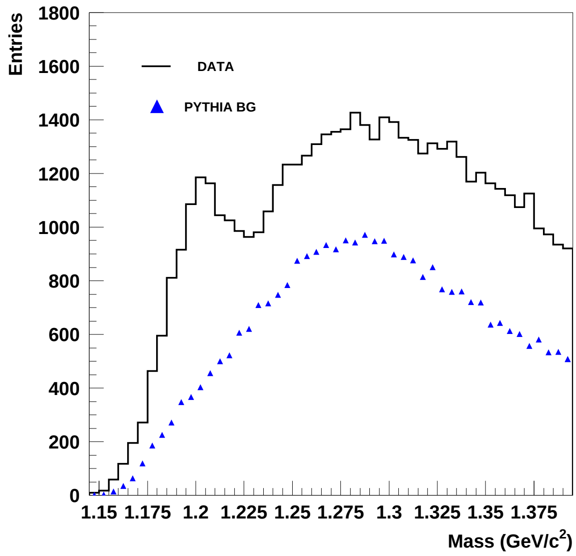

(b) PYTHIA background

Figure 7.6: The background obtained by using the SIDE-BAND method (a) and the one obtained with a Monte Carlo simulation (b).

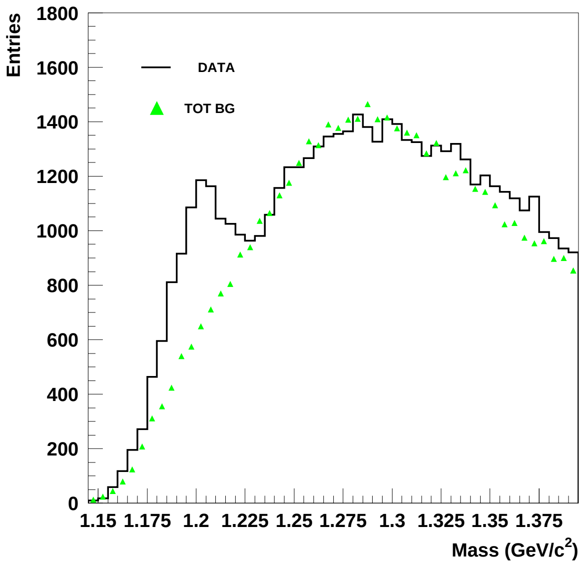

Figure 7.7: The total background resulting from the combination of the two contributions obtained using the SIDE-BAND method and the Monte Carlo simulation.

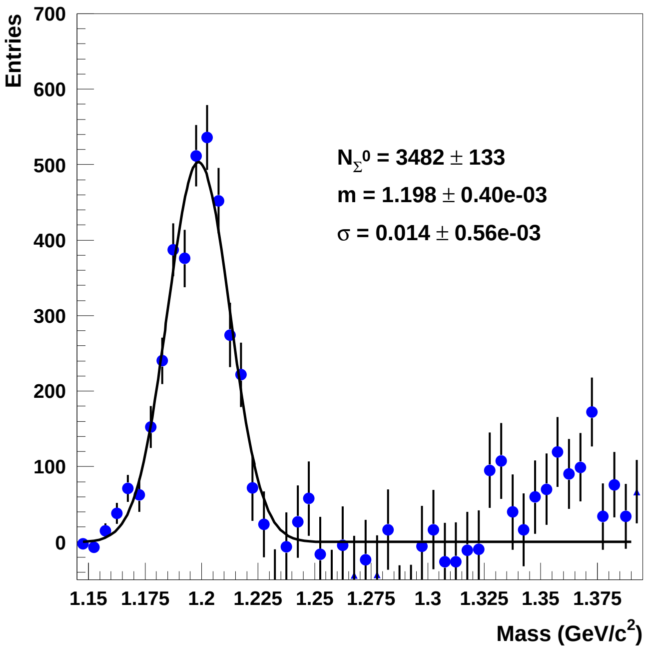

(a) Background subtraction Method

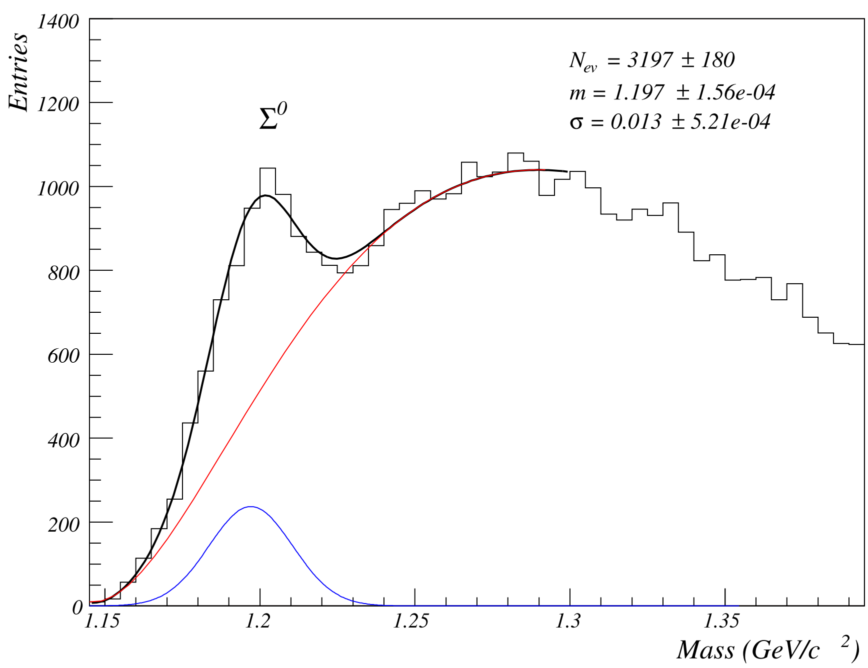

(b) Fit Method

Figure 7.8: Gaussian fit of the mass spectrum after the subtraction of the total background (a). Fit of the invariant mass spectrum of the Σ^0 (b).

7.1.4 $\overline{\Sigma}^0$ Hyperon

The $\overline{\Sigma}^0$ candidates were selected by applying the cuts reported in Tab.7.2. The triggers 21 and 27 were used. The efficiencies of these two triggers and of their combination as a function of the anti-proton momentum are shown in fig. 7.9. The average values of the trigger efficiencies are reported in Tab.7.5

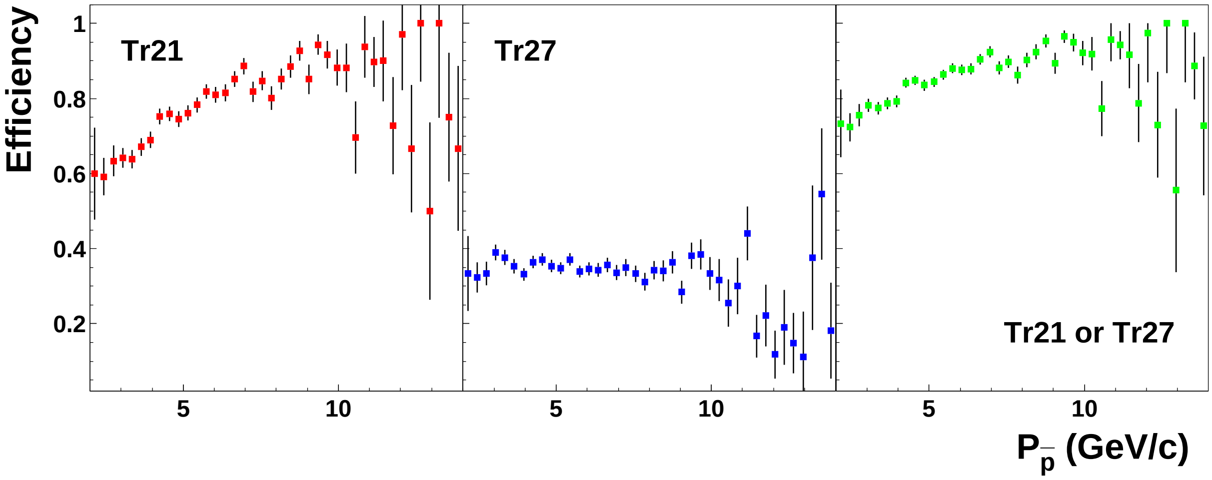

Figure 7.9: Efficiencies of trigger 21 (left-panel), trigger 27 (center-panel) and of the combination of the two triggers (right-panel) as a function of the anti-proton momentum.

Data Production	Trigger 21	Trigger 27	Trigger 21 or 27
$98d0 + 99c0 + 00d0$	79%	35%	87%

Table 7.5: Average values of the efficiencies for the triggers 21 and 27 and for the combination of the two triggers.

In the following steps, needed for the extraction of the cross section, only the combination of the two triggers was considered. The value of the total efficiency, $\epsilon_{tot}^{21or27} = 0.043\%$, was calculated as explained in Sec.6.3 and was used to correct the experimental data.
The number of $\overline{\Sigma}^0$ events was extracted with the two methods used in the analysis of the Σ^0 hyperon:

- the background subtraction method
- the fit method

The total simulated background, normalized to the data, is shown in Fig.7.10 (c), while the difference between the signal and the background, together with the fit of the peak, is shown in Fig.7.11.
The fit of the total spectrum and the fit parameters are shown in Fig.7.12. The values of the photoproduction cross section obtained with the two methods are reported in table 7.6.

Hyperon	**Method**	**Cross Section (μbarn)**
$\overline{\Sigma}^0$	Background Subtraction	$0.075 \pm 0.014(stat.)$
	Fit	$0.071 \pm 0.023(stat.)$

Table 7.6: Photoproduction cross sections of the $\overline{\Sigma}^0$ obtained with the two methods.

The final value was obtained as a weighted average of the values obtained with the two methods. The systematic uncertainty was estimate as explained in sec. 7.1.3.

$$< \sigma_{\overline{\Sigma}^0} >= 0.073 \pm 0.014(stat.) \pm 0.007(syst.)\mu\text{barn} \quad (7.7)$$

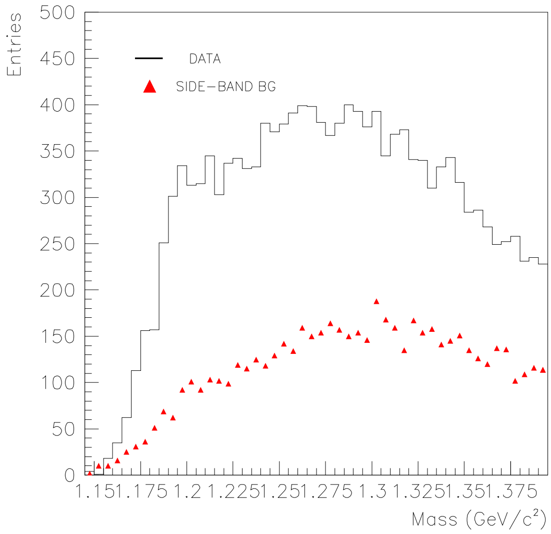

(a) SIDE-BAND background

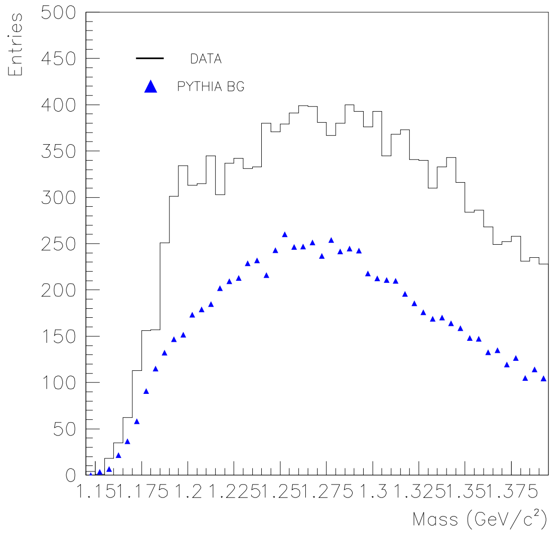

(b) PYTHIA background

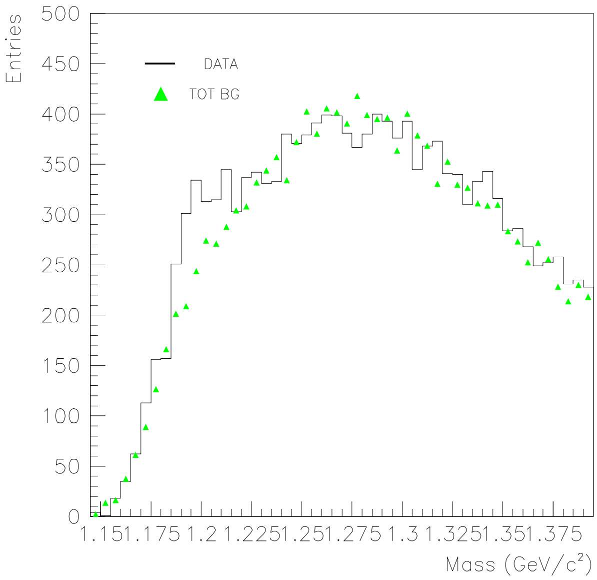

(c) Total background

Figure 7.10: Contributions to the total background obtained by using the SIDE-BAND method (a) and the Monte Carlo simulation (b). Total background (c)

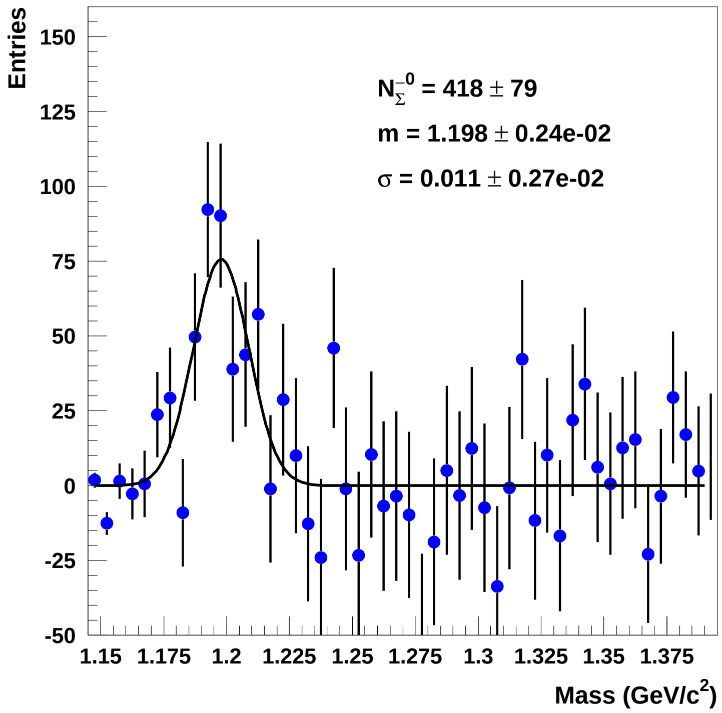

Figure 7.11: Gaussian fit of the peak after the background subtraction.

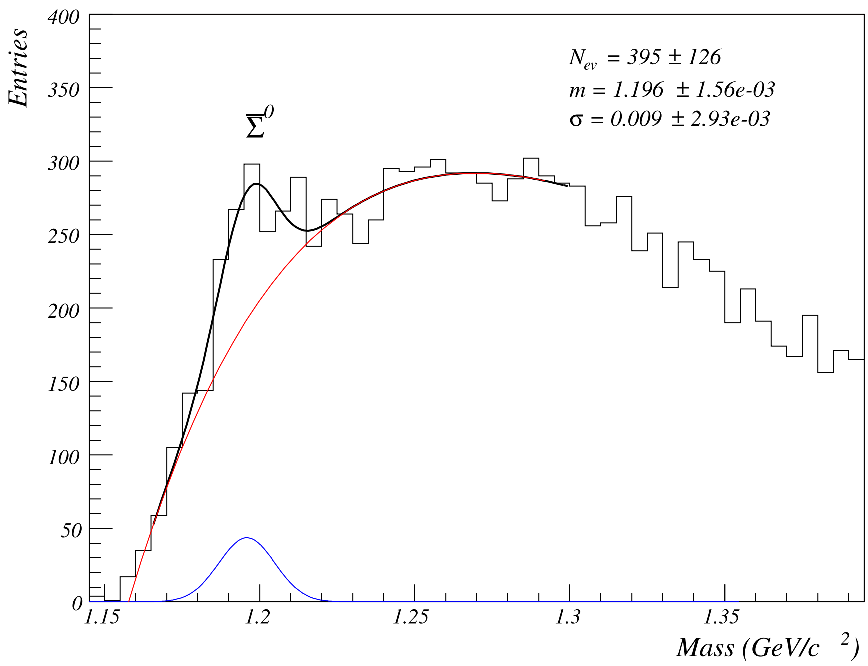

Figure 7.12: Fit of the invariant mass spectrum of the $\overline{\Sigma}^0$; the parameters from the fit are also reported.

7.2 Ξ^- and Σ^{*-} hyperons

The decay of the Ξ^- and Σ^{*-} hyperons in a Λ plus a negative pion is shown in Fig.7.13.

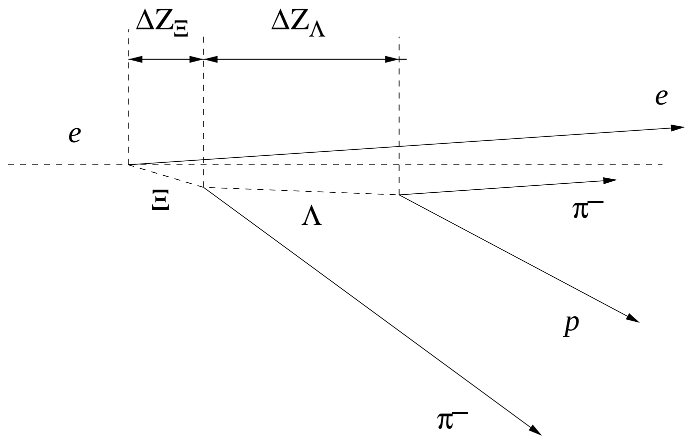

Figure 7.13: Schematic view of production and decay vertices of the Ξ^- and Σ^{*-} hyperons.

In order to select the two hyperons candidates and reduce the background, the following cuts were applied:

Proton Track	
	Long track
PID	Positively identified by the RICH
Momentum	$2 < P_p < 14$ GeV/c
Pion Tracks	
	Long or short track
Momentum	$P_\pi > 0.6$ GeV/c
Λ Particle	
Mass	$1.108 < M_\Lambda < 1.123$ GeV/c^2
dca (p - π)	< 1.5 cm
Production Vertex	-18 cm $< v_{prod} <$ 18 cm
Decay Length	$v_{decay} - v_{prod} > 7.5$ cm

Table 7.7: Cuts applied for the selection of Ξ^- and Σ^{*-} candidates.

The invariant mass spectrum of the Λ satisfying the cuts applied for the selection of the two hyperons is shown in Fig. 7.14 (a). Depending on the mass range of the Λ, it is possible to identify two regions, the 'SIGNAL-REGION' ($\pm 3\sigma$, experimental width) and the 'SIDE-BAND REGION'. The invariant mass spectra of the Ξ^- and Σ^{*-}, shown in Fig.7.14 (b), were reconstructed requiring Λs in the 'SIGNAL-REGION'.

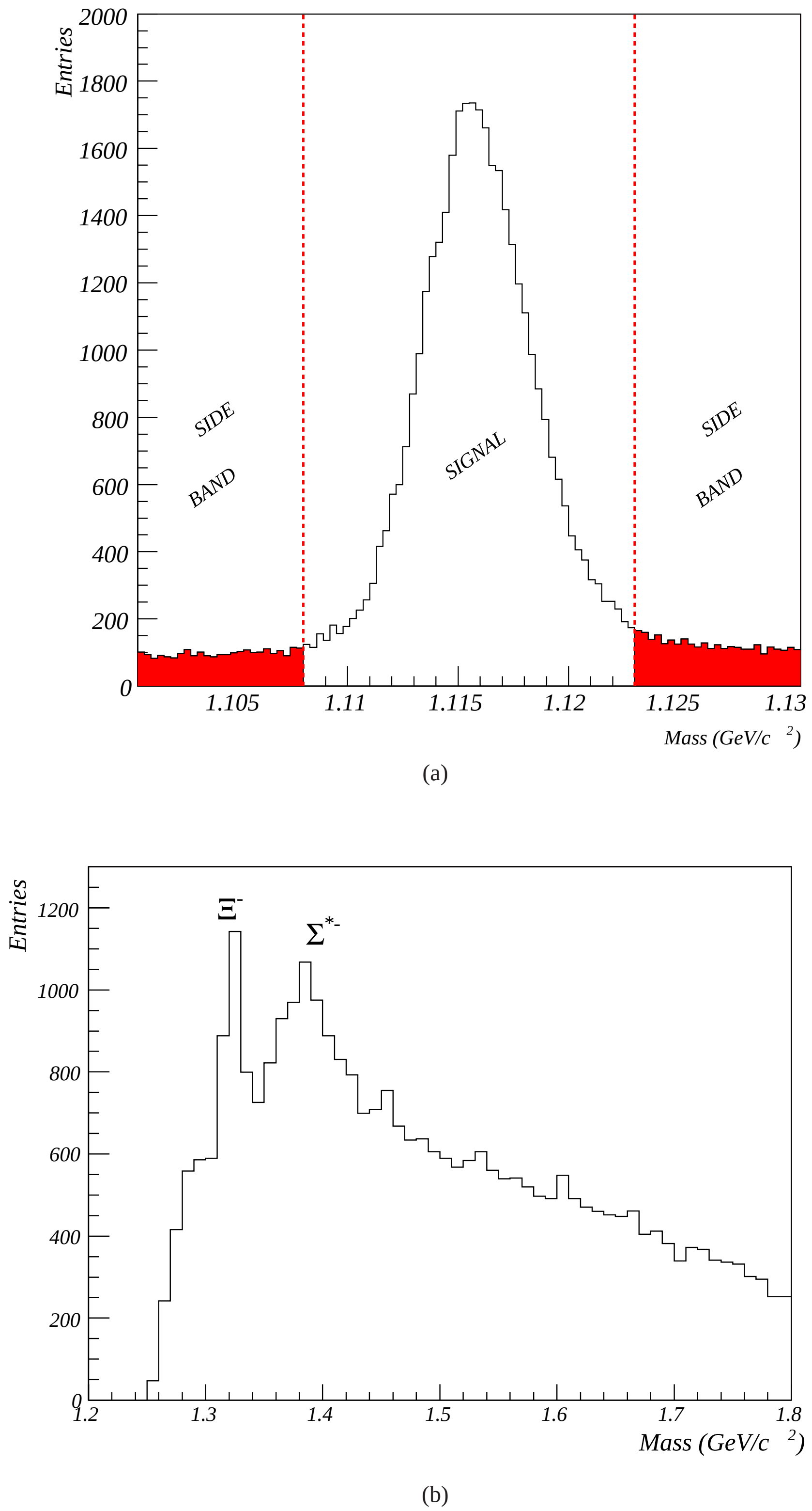

Figure 7.14: (a) Invariant mass spectrum of the Λ satisfying the cuts applied for the selection of the Ξ^- and Σ^{*-} hyperons. (b) Invariant mass spectrum of the Ξ^- and Σ^{*-} hyperons.

7.2.1 Extraction of the Photoproduction Cross Section

The Ξ^- and Σ^{*-} photoproduction cross sections were extracted using the usual formula:

$$\sigma_{\gamma N \to YX} = \frac{\sigma_{eN \to YX}}{\Phi} \tag{7.8}$$

$$= \frac{N^{Y \to \Lambda+\pi}_{observed}}{\epsilon_{TOT} \cdot BR_\Lambda \cdot BR_Y \cdot \Phi \cdot L} \tag{7.9}$$

where:

- $N^{Y \to \Lambda+\pi}_{observed}$ is the total number of Ξ^- or Σ^{*-} observed events;
- ϵ_{TOT} is the total efficiency;
- BR_Y is the branching ratio for the Ξ^- or the Σ^{*-} decaying in a Λ plus a negative pion (99.887% and 88% respectively), while BR_Λ is the branching ratio of the Λ decay ($BR_{\Lambda \to p+\pi} = 0.642$);
- Φ is the Photon Flux Factor;
- L is the total Luminosity integrated over the three data productions analyzed.

The determination of the Photon Flux Factor and the calculation of the total Luminosity were explained in Secs.6.3 and 6.3.

7.2.2 Trigger Efficiency

The total efficiency is given by the product of the geometrical acceptance, the RICH efficiency, the kinematical cuts efficiency, and the trigger efficiency. The combination of the first three terms was obtained as explained in Sec.7.1.2
The triggers 21 and trigger 27 were used and the corresponding efficiencies were calculated as explained in **APPENDIX A**, for the event topology with at least two long tracks per detector half. The two efficiencies were then combined as explained in Sec.6.3. The efficiencies as a function of the proton momentum are shown in Fig.7.15. The lower value of the trigger21 efficiency, with respect to the Σ^0 hyperon, could be explained with the absence of photons in the selected events, this makes more difficult to satisfy the calorimeter threshold. In contrast, the higher value of the trigger 27 efficiency, again with respect to the Σ^0 hyperon, could be due to the higher track multiplicity of the selected events. The trigger efficiencies and the total efficiencies are reported in Tabs.7.8 and 7.10.

Data Production	Trigger 21	Trigger 27	Trigger 21 or 27
$98d0 + 99c0 + 00d0$	58%	42%	78%

Table 7.8: Average vales of the trigger efficiencies.

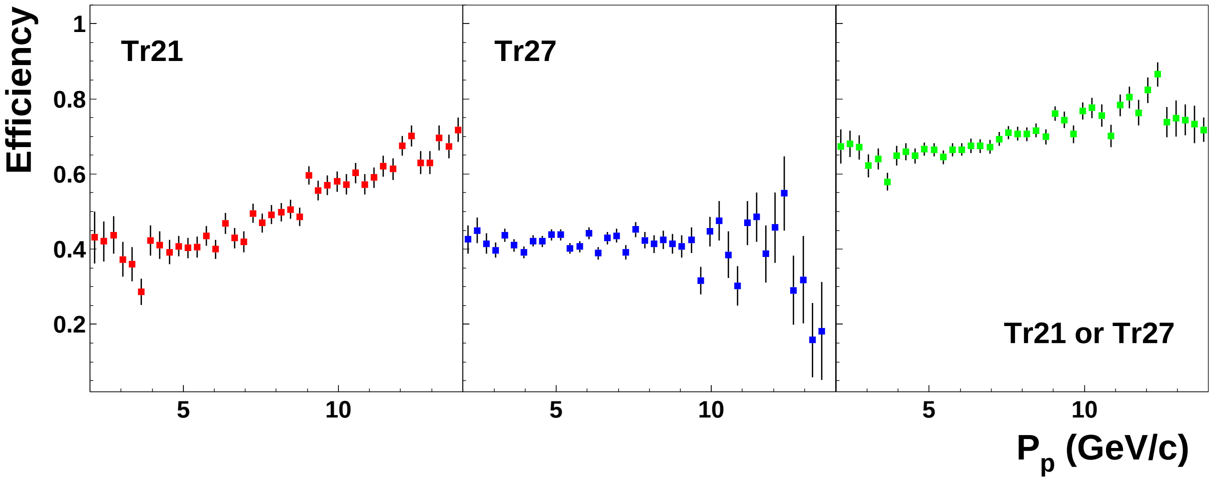

Figure 7.15: Efficiencies of trigger 21 (left-panel), trigger 27 (center-panel) and of the combination of the two triggers (right-panel) as a function of the proton momentum.

Data Production	Total Efficiency - Tr21	Total Efficiency - Tr27	Total Efficiency - Tr21 or 27
$98d0 + 99c0 + 00d0$	0.10%	0.07%	0.14%

Table 7.9: Total efficiency for the triggers 21 and 27 and for the combination of the two triggers for the three data productions for the Ξ^- hyperon.

7.2.3 Extraction of the Ξ^- and Σ^{*-} events

The total number of Ξ^- and Σ^{*-} events was extracted using two different methods:

- the subtraction of the total background;
- the fit of the invariant mass spectrum.

The two methods are described in the following sections; the second one was used in order to estimate the systematic uncertainty on the value of the photoproduction cross section.

Background Subtraction

The total combinatorial background can be described as the sum of two major contributions:

- the background generated by the combination of a 'fake' Λ and an uncorrelated pion; this first contribution can be obtained with the SIDE-BAND method;
- the background generated by the combination of a 'true' Λ and an uncorrelated pion; this second contribution can be simulated with a Monte Carlo based on PYTHIA.

The two contributions are shown in fig. 7.16. The two contributions were first normalized to the 'signal' spectrum within the mass range $1.45 - 1.6\ GeV/c^2$ and then summed. The simulated background was then subtracted from the 'signal' spectrum. The number of Ξ^- and Σ^{*-} events

Data Production	Total Efficiency - Tr21	Total Efficiency - Tr27	Total Efficiency - Tr21 or 27
$98d0 + 99c0 + 00d0$	0.0015%	0.0012%	0.0021%

Table 7.10: Total efficiency for the triggers 21 and 27 and for the combination of the two triggers for the three data productions for the Σ^{*-} hyperon.

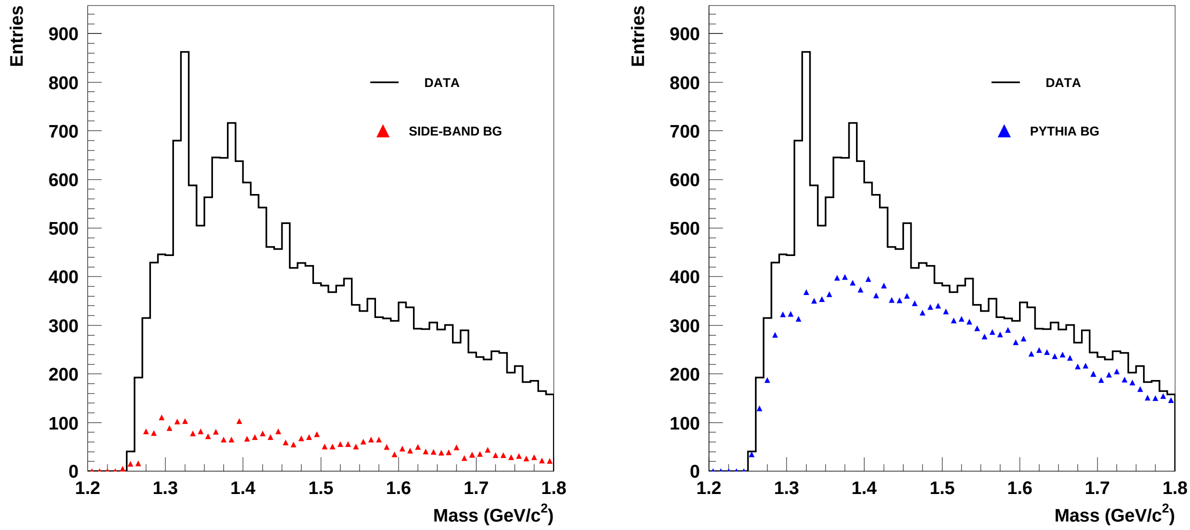

(a) SIDE-BAND Background

(b) PYTHIA Background

Figure 7.16: Contributions to the total background obtained with the SIDE-BAND method (a) and with the Monte Carlo simulation (b).

were then extracted by fitting the remaining peaks with two Gaussian distributions. The result of the fit is shown in fig. 7.18.

Fit of the invariant mass spectrum

The second method used to extract the number of observed Ξ^- and Σ^{*-} events consists in a fit of the invariant mass spectrum. In this case the two hyperons were studied separately.

- Ξ^- **hyperon**: After produced in the interaction of the lepton beam with the proton target, the Σ^{*-} immediately decays in a Λ plus a negative pion; in contrast, the Ξ^- travels for 4.91 cm. A cut on the decay length of the Ξ^- can be applied, in this way the Σ^{*-} signal is completely suppressed and only the Ξ^- peak remains visible in the invariant mass spectrum. In fig. 7.19 the resulting spectrum after applying the cut

$$\Delta z = (v_{decay} - v_{prod}) > 10 \text{ cm}$$

is shown. The spectrum was then fitted with a Gaussian distribution and a second order polynomial. The fit and the corresponding parameters are shown in fig. 7.19.

The total number of Ξ^- events provided by the fit was then corrected for the decay length cut efficiency (0.70), calculated from the Monte Carlo simulation.

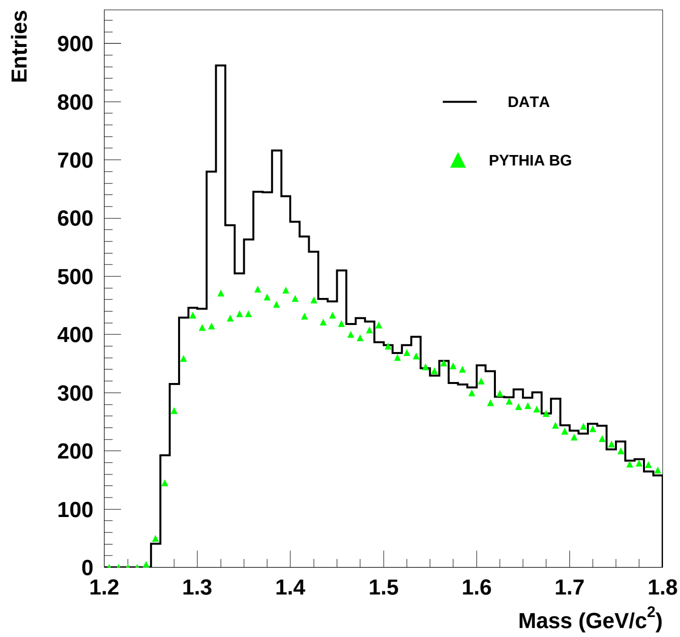

Figure 7.17: The total background obtained as the sum of the two contributions.

- Σ^{*-} **hyperon**: in order to extract the number of Σ^{*-} events, the total experimental mass spectrum, without applying the cut on the decay length, was fitted with the function:

$$\text{f(x)} = \text{Signal} + \text{Background} =$$

$$= \frac{1}{\sqrt{2\pi}\sigma_{\Xi^-}} \cdot N_{\Xi^-} \cdot \Delta x \cdot exp\left(-\frac{1}{2}\left(\frac{x-m_{\Xi^-}}{\sigma_{\Xi^-}}\right)^2\right) +$$

$$\frac{1}{\sqrt{2\pi}\sigma_{\Sigma^{*-}}} \cdot N_{\Sigma^{*-}} \cdot \Delta x \cdot exp\left(-\frac{1}{2}\left(\frac{x-m_{\Sigma^{*-}}}{\sigma_{\Sigma^{*-}}}\right)^2\right) +$$

$$(a + b \cdot x) \cdot exp(c \cdot (x - d)) \tag{7.10}$$

Here two Gaussian distributions were used to fit the signal while the combination of a polynomial and an exponential function was used to fit the background. The following parameters of the Gaussian used to fit the Ξ^- signal were fixed to the values obtained from the fit of the spectrum after applying the cut on the decay length:

- m_{Ξ^-} was fixed to the value $1.322\ GeV/c^2$
- σ_{Ξ^-} was fixed to the value $4.02 \cdot 10^{-2}\ GeV/c^2$.

The parameter $N_{\Sigma^{*-}}$ provides the number of Σ^{*-} events, $m_{\Sigma^{*-}}$ and $\sigma_{\Sigma^{*-}}$ correspond to the mean and the width of the Gaussian distribution, respectively. The product $N_{\Sigma^{*-}} \cdot \Delta x$ represents the total area under the peak. The parameters of the fit are shown in fig. 7.20.

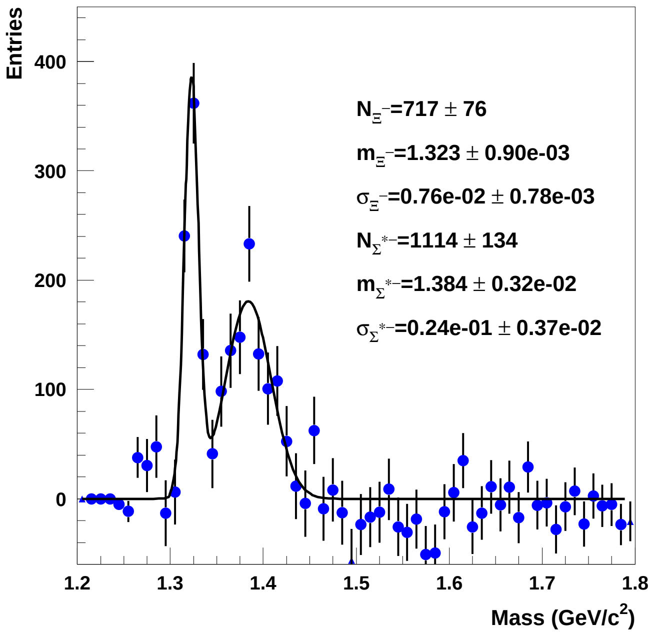

Figure 7.18: Fit of the signal spectrum after subtracting the total simulated background.

The photoproduction cross section was calculated for each of the two relevant triggers separately, the values obtained were then combined as explained in sec.6.3. The results of the two methods are summarized in table 7.11.

Hyperon	**Method**	**Cross Section (μbarn)**
Ξ^-	Background Subtraction	$0.111 \pm 0.011(stat.)$
	Fit	$0.093 \pm 0.006(stat.)$
Σ^{*-}	Background Subtraction	$4.41 \pm 0.49(stat.)$
	Fit	$4.32 \pm 0.45(stat.)$

Table 7.11: Photoproduction cross sections of the Ξ^- and the Σ^{*-} obtained with the two methods.

Systematic Uncertainties

Several sources of systematic uncertainties was identified:

- the systematic uncertainties due to the used triggers: it was obtained as half of the difference of the cross sections corresponding, for each method, to trigger 21 and trigger 27, respectively.

- the systematic error due to to the time stability of the detector: the error estimated in the Λ analysis (see Sec.6.5.3) was propagated (in percentage) to the heavier hyperons;

- the systematic uncertainty due to the different methods, calculated as the half of the difference of the two values reported in Tab.7.11;

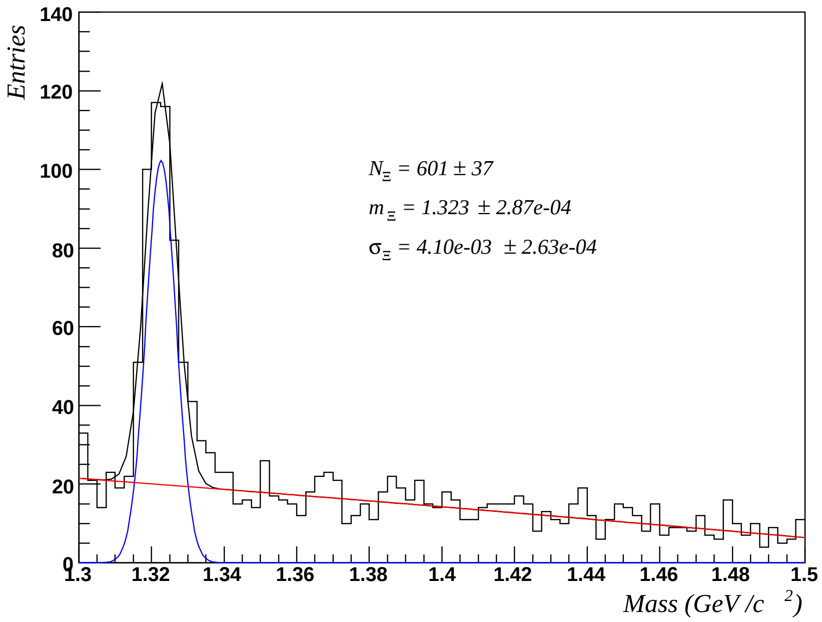

Figure 7.19: Fit of the invariant mass spectrum after applying the cut on the decay length.

- the systematic uncertainty due to the measurement of the luminosity (see Sec.6.5.3)

The four contributions were then added in quadrature.
The final values of the photoproduction cross section of the Ξ^- and Σ^{*-} hyperons, with the corresponding statistical and systematic uncertainties, are:

$$< \sigma_{\Xi^-} >= 0.102 \pm 0.011(stat.) \pm 0.020(syst.) \quad \mu\text{barn} \tag{7.11}$$

$$< \sigma_{\Sigma^{*-}} >= 4.36 \pm 0.49(stat.) \pm 0.39(syst.) \quad \mu\text{barn} \tag{7.12}$$

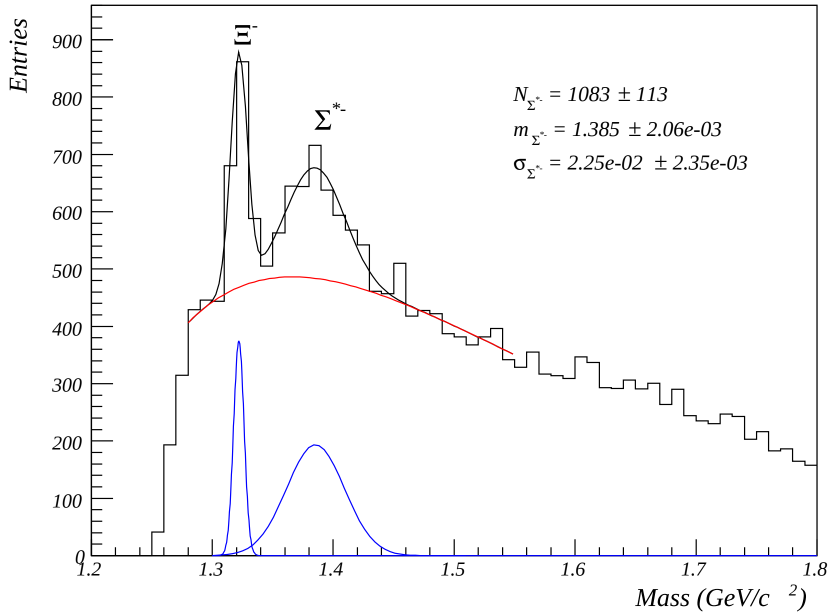

Figure 7.20: Fit of the total invariant mass spectrum.

7.2.4 $\overline{\Xi}^{+}$ and $\overline{\Sigma}^{*+}$ Hyperons

The cuts reported in Tab.7.7 were applied in order to select the $\overline{\Xi}^{+}$ and $\overline{\Sigma}^{*+}$ hyperons candidates. The trigger 21 and 27 were used. The efficiencies of the two triggers and of their combination as a function of the anti-proton momentum are shown in Fig.7.21. The average values of the trigger efficiencies are reported in table 7.12

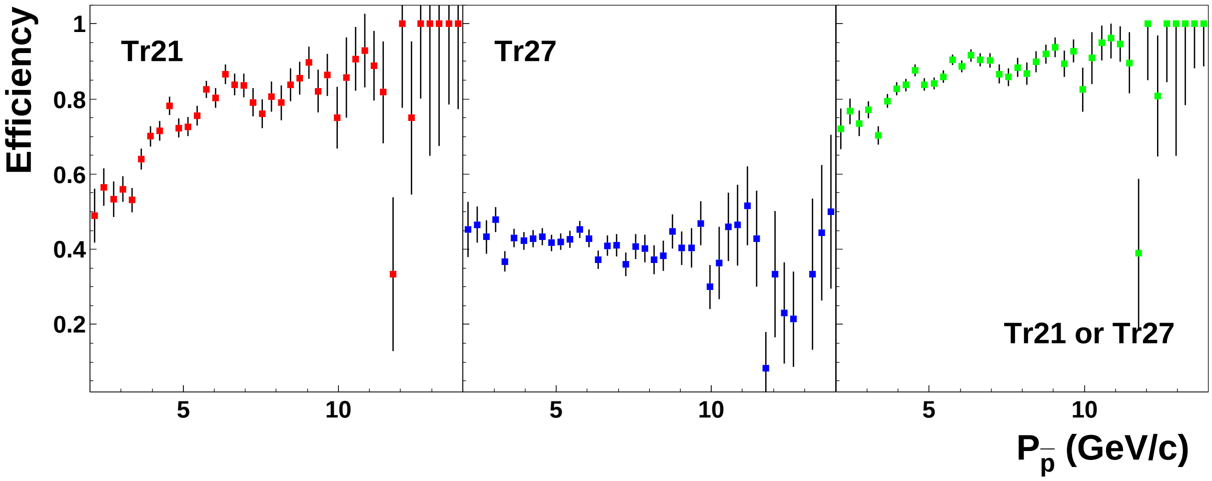

Figure 7.21: Efficiencies of trigger 21 (left-panel), trigger 27 (center-panel) and of the combination of the two triggers (right-panel) as a function of the anti-proton momentum.

Data Production	Trigger 21	Trigger 27	Trigger 21 or 27
$98d0 + 99c0 + 00d0$	76%	41%	87%

Table 7.12: Total efficiency for the triggers 21 and 27 for the three data productions.

Only the combination of the two triggers was considered for the extraction of the cross section. The value of the total efficiency, $\epsilon_{tot}^{21or27} = 0.13\%$, was calculated as explained in Sec.6.3 and was used to correct the experimental data.
The number of observed the $\overline{\Xi}^{+}$ and $\overline{\Sigma}^{*+}$ events was extracted with the two methods:

- the background subtraction method
- the fit method

The total simulated background, normalized to the data, is shown in Fig.7.23, while the difference between the signal and the background, together with the fit of the peak, is shown in Fig.7.24.
The fit of the total spectrum is shown in Fig.7.26 together with the parameters from the fit.
The values of the photoproduction cross section obtained with the two methods are reported in the following table.

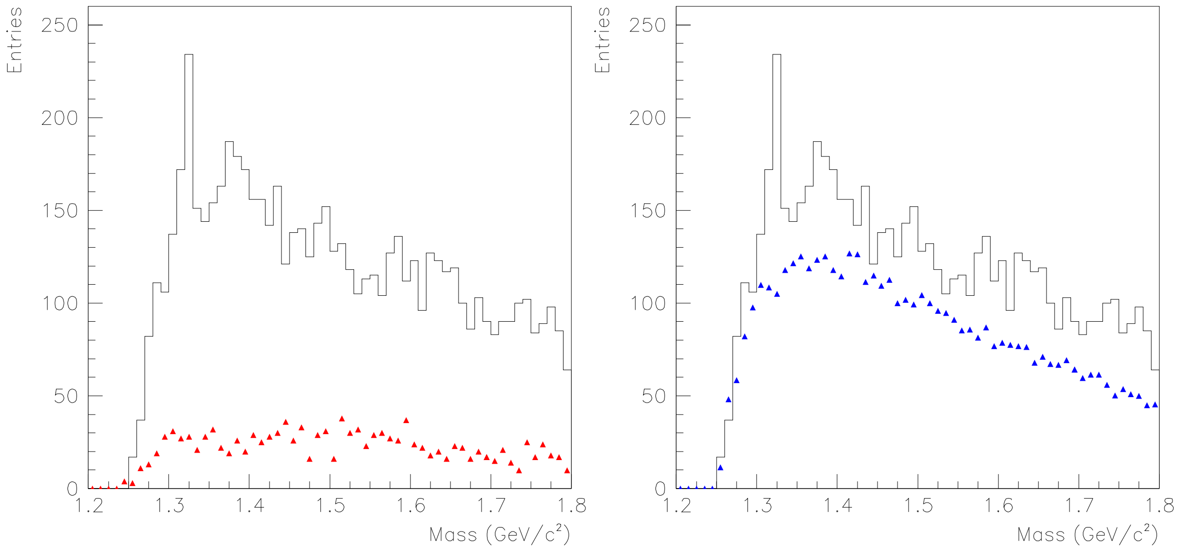

(a) SIDE-BAND background (b) PYTHIA background

Figure 7.22: Contributions to the total background obtained by using the SIDE-BAND method (a) and the Monte Carlo simulation (b).

Hyperon	**Method**	**Cross Section (μbarn)**
$\overline{\Xi}^{+}$	Background Subtraction	$0.0269 \pm 0.0054(stat.)$
	Fit	$0.0277 \pm 0.0031(stat.)$
$\overline{\Sigma}^{*+}$	Background Subtraction	$0.0098 \pm 0.0053(stat.)$
	Fit	$0.0096 \pm 0.0034(stat.)$

The final value was obtained as a weighted average of the values obtained with the two methods. The systematic uncertainty was estimate as explained in sec. 7.2.3.

$$< \sigma_{\overline{\Xi}^{+}} >= 0.0273 \pm 0.0031(stat.) \pm 0.0029(syst.) \quad \mu\text{barn} \tag{7.13}$$

$$< \sigma_{\overline{\Sigma}^{*+}} >= 0.0097 \pm 0.0034(stat.) \pm 0.0007(syst.) \quad \mu\text{barn} \tag{7.14}$$

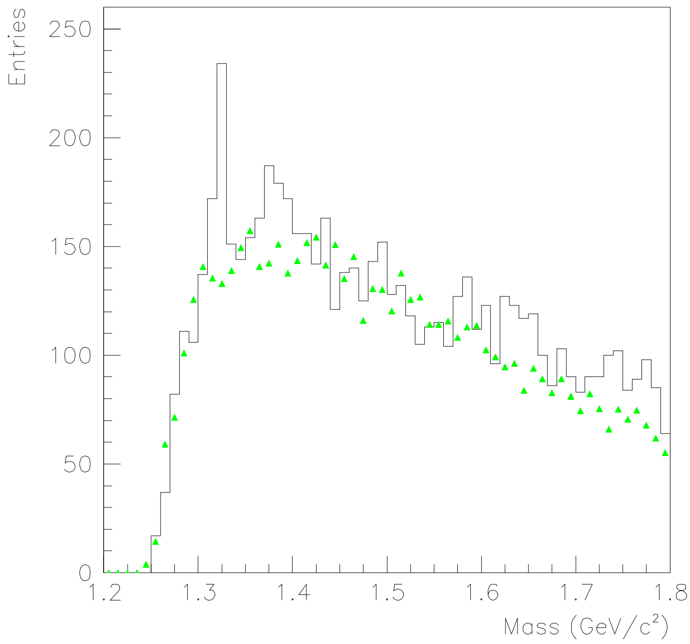

Figure 7.23: Total background resulting from the combination of the two contributions obtained with the SIDE-BAND method and the Monte Carlo simulation.

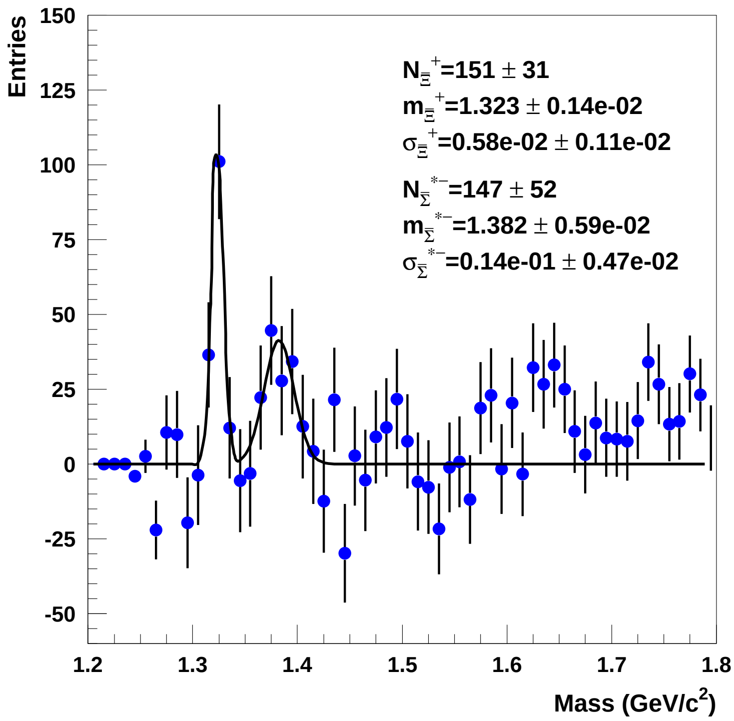

Figure 7.24: Gaussian fit of the peaks ($\overline{\Xi}^{+}$ left and $\overline{\Sigma}^{*+}$ right) after the background subtraction.

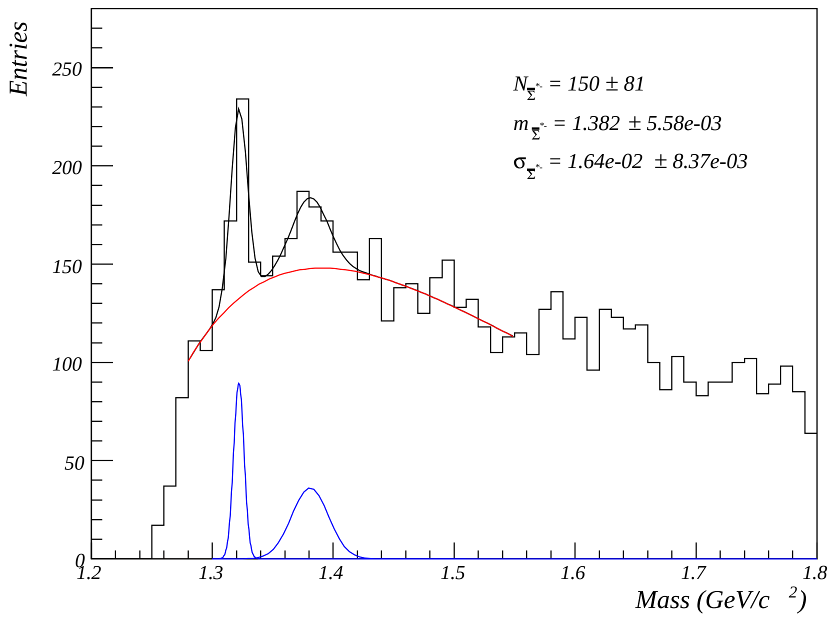

Figure 7.25: Fit of the invariant mass spectrum of the $\overline{\Xi}^{+}$ and $\overline{\Sigma}^{*+}$, together with the parameters from.

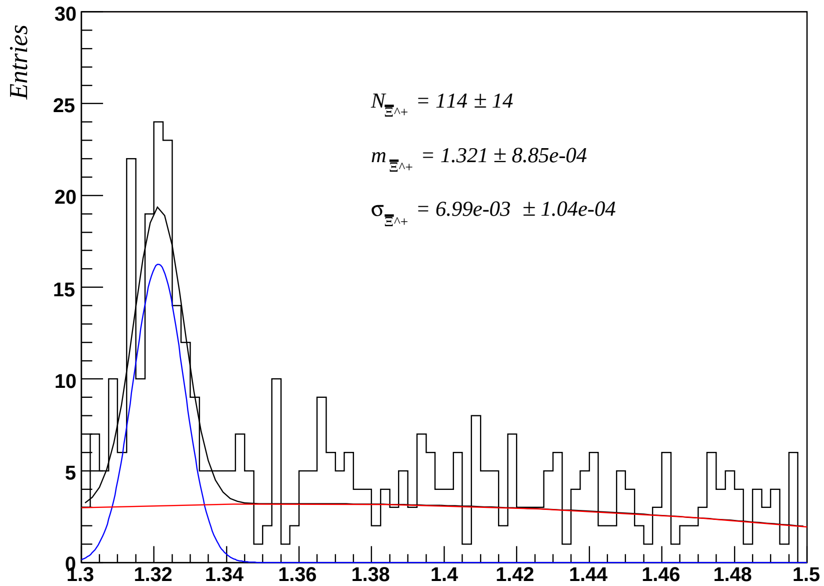

Figure 7.26: Fit of the invariant mass spectrum of the $\overline{\Xi}^{+}$ after applying the cut on the decay length, together with the parameters from the fit.

7.3 Σ^{*+} hyperon

The decay of the Σ^{*+} hyperon in a Λ plus a positive pion is shown in Fig.7.27.

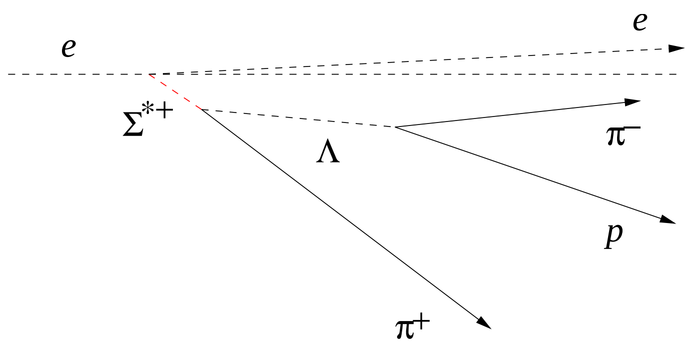

Figure 7.27: Schematic view of the Σ^{*+} production and decay vertices.

The Σ^{*+} candidates were selected by applying the cuts reported in Tab.7.13.

Proton Track	
	Long track
PID	Positively identified by the RICH
Momentum	$2 < P_p < 14$ GeV/c
Pion Tracks	
	Long or short track
Momentum	$P_\pi > 0.6$ GeV/c
Λ Particle	
Mass	$1.108 < M_\Lambda < 1.123$ GeV/c^2
dca (p - π)	< 1.5 cm
Production Vertex	-18 cm $< v_{prod} < 18$ cm
Decay Length	$v_{decay} - v_{prod} > 7.5$ cm

Table 7.13: Cuts applied for the selection of the Σ^{*+} candidates.

The invariant mass spectrum of the Λ satisfying the cuts applied for the selection of the hyperon is shown in Fig. 7.28 (a). Depending on the mass range of the Λ, it is possible to identify two regions, the 'SIGNAL-REGION' ($\pm 3\sigma$, experimental width) and the 'SIDE-BAND REGION'. The invariant mass spectra of the Σ^{*+}, shown in Fig.7.28 (b), was reconstructed requiring Λs in the 'SIGNAL-REGION'.

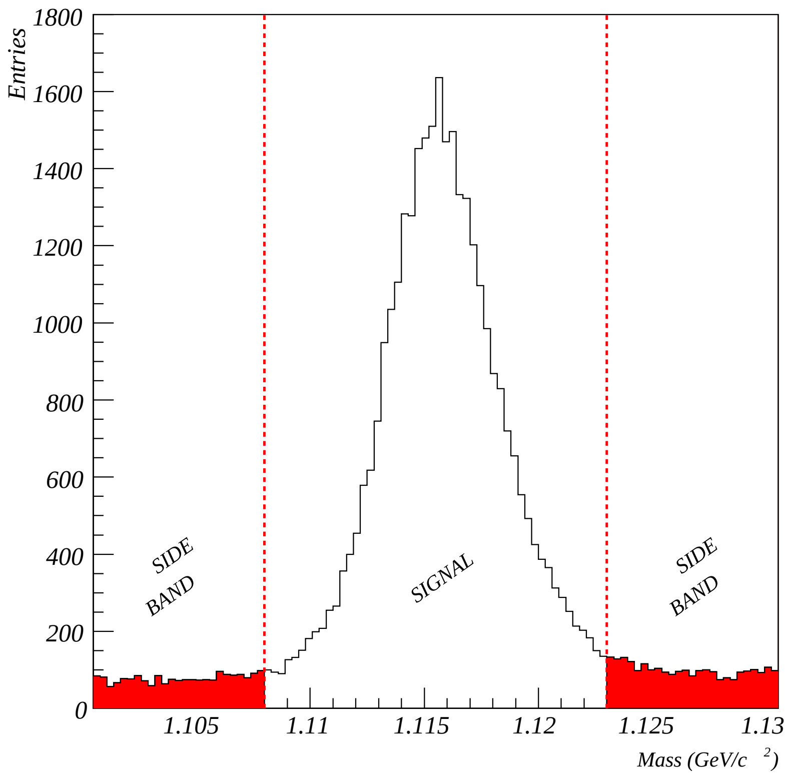

(a)

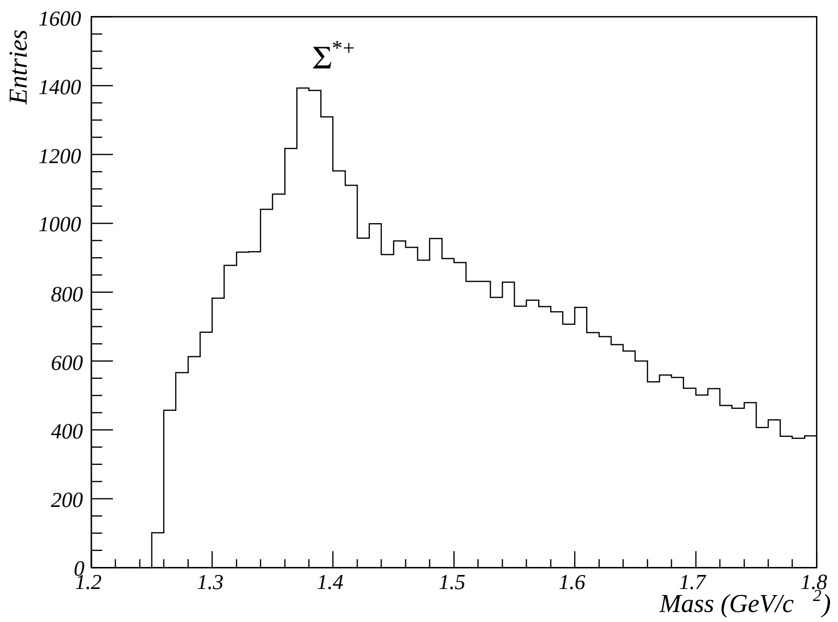

(b)

Figure 7.28: (a) Invariant mass spectrum of the Λ satisfying the cuts applied for the selection of the Σ^{*+} hyperons. (b) Invariant mass spectrum of the Σ^{*+} hyperons.

7.3.1 Extraction of the Photoproduction Cross Section

The Σ^{*+} photoproduction cross section was extracted using the usual formula:

$$\sigma_{\gamma N \to \Sigma^{*+} X} = \frac{\sigma_{eN \to \Sigma^{*+} X}}{\Phi} \tag{7.15}$$

$$= \frac{N^{\Sigma^{*+} \to \Lambda + \pi}_{observed}}{\epsilon_{TOT} \cdot BR_{\Lambda} \cdot BR_{\Sigma^{*+}} \cdot \Phi \cdot L} \tag{7.16}$$

where:

- $N^{\Sigma^{*+} \to \Lambda + \pi}_{observed}$ is the total number of Σ^{*+} observed events;
- ϵ_{TOT} is the total efficiency;
- $BR_{\Sigma^{*+}}$ is the branching ratio for the Σ^{*+} decaying in a Λ plus a positive pion (88%), while BR_{Λ} is the branching ratio of the Λ decay ($BR_{\Lambda \to p+\pi} = 0.642$);
- Φ is the Photon Flux Factor;
- L is the total Luminosity integrated over the three data productions analyzed.

The determination of the Photon Flux Factor and the calculation of the total Luminosity were explained in Secs.6.3 and 6.3.

7.3.2 Trigger Efficiency

The total efficiency is given by the product of the geometrical acceptance, the RICH efficiency, the kinematical cuts efficiency, and the trigger efficiency. The combination of the first three terms was obtained as explained in Sec.7.1.2
The triggers 21 and trigger 27 were used and the corresponding efficiencies were calculated as explained in **APPENDIX A**, for the event topology with at least two long tracks per detector half. The two efficiencies were then combined as explained in Sec.6.3. The efficiencies as a function of the proton momentum are shown in Fig.7.29. The trigger efficiencies and the total efficiencies are reported in Tabs.7.14 and 7.15.

Data Production	Trigger 21	Trigger 27	Trigger 21 or 27
$98d0 + 99c0 + 00d0$	57%	41%	77%

Table 7.14: Average values of the trigger efficiencies.

Data Production	Total Efficiency - Tr21	Total Efficiency - Tr27	Total Efficiency - Tr21 or 27
$98d0 + 99c0 + 00d0$	0.0015%	0.0012%	0.0021%

Table 7.15: Total efficiency for the triggers 21 and 27 for the three data productions.

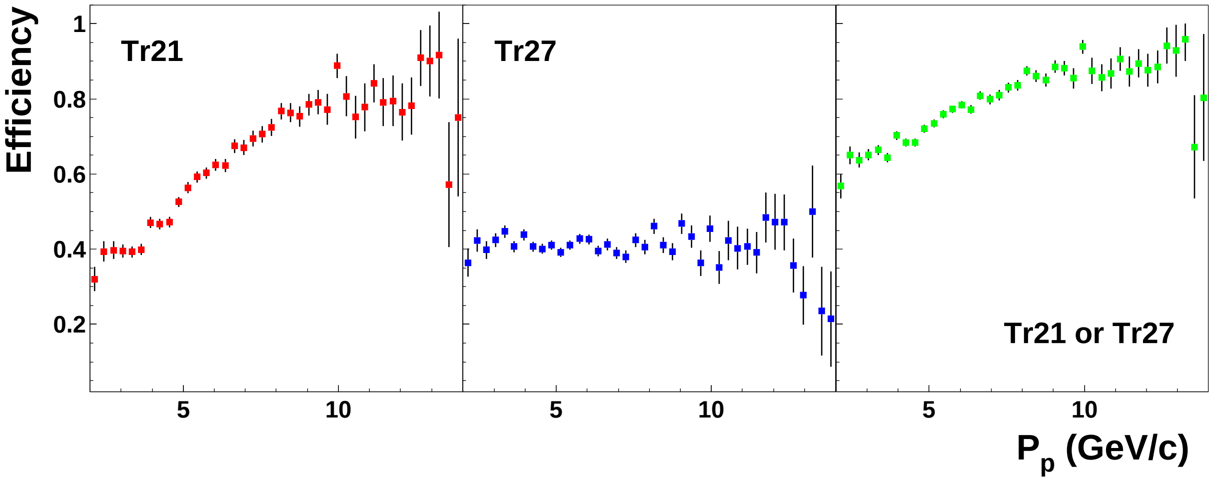

Figure 7.29: Efficiencies of trigger 21 (left-panel), trigger 27 (center-panel) and of the combination of the two triggers (right-panel) as a function of the proton momentum.

7.3.3 Extraction of the Σ^{*+} events

The total number of the Σ^{*+} events was extracted using two different methods:

- the subtraction of the total background;
- the fit of the invariant mass spectrum.

The two methods are described in the following sections; the second one was used in order to estimate the systematic uncertainty on the value of the photoproduction cross section.

Background Subtraction

The total combinatorial background can be described as the sum of two major contributions:

- the background generated by the combination of a 'fake' Λ and an uncorrelated pion; this first contribution can be obtained with the SIDE-BAND method;
- the background generated by the combination of a 'true' Λ and an uncorrelated pion; this second contribution can be simulated with a Monte Carlo based on PYTHIA.

The two contributions are shown in Fig. 7.30 for the data sample corresponding to the combination of the two triggers. The two contributions were first normalized to the 'signal' spectrum within the mass range $1.45 - 1.6\ GeV/c^2$ and then summed. The simulated background was then subtracted from the 'signal' spectrum. The number of Σ^{*+} events was then extracted by fitting the remaining peak with a Gaussian distribution. The result of the fit is shown in Fig.7.32.

Fit of the invariant mass spectrum

The second method used to extract the number of observed Σ^{*+} events consists in a fit of the invariant mass spectrum by using the function:

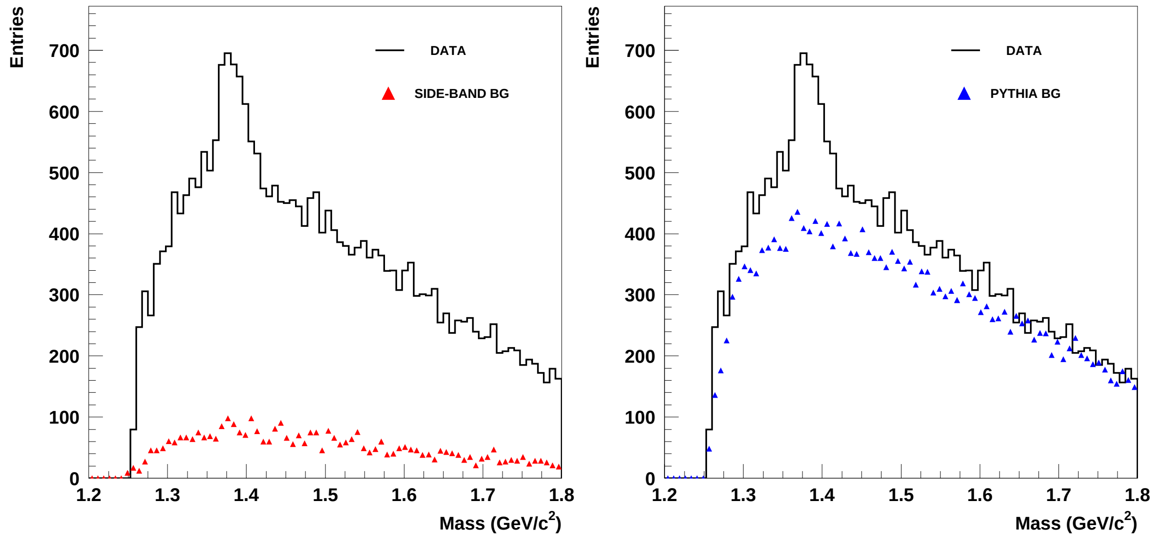

(a) SIDE-BAND background (b) PYTHIA background

Figure 7.30: Background obtained by using the SIDE-BAND method (a) and background obtained with a Monte Carlo simulation (b).

$$\text{f(x)} = \text{Signal} + \text{Background} =$$
$$\frac{1}{\sqrt{2\pi}\sigma_{\Sigma^{*+}}} \cdot N_{\Sigma^{*+}} \cdot \Delta x \cdot exp\left(-\frac{1}{2}\left(\frac{x - m_{\Sigma^{*+}}}{\sigma_{\Sigma^{*+}}}\right)^2\right) +$$
$$(a + b \cdot x + c \cdot x^2)) \tag{7.17}$$

The Gaussian distribution was used to fit the signal while the polynomial function was used to fit the background.
The parameter $N_{\Sigma^{*+}}$ provides the number of Σ^{*+} events, $m_{\Sigma^{*+}}$ and $\sigma_{\Sigma^{*+}}$ correspond to the mean and the width of the Gaussian distribution, respectively. The product $N_{\Sigma^{*+}} \cdot \Delta x$ represents the total area under the peak. The parameters of the fit are shown in fig. 7.33.
The values of the resulting photoproduction cross section for the two methods are summarized in table 7.16:

Hyperon	**Method**	**Cross Section (μbarn)**
Σ^{*-}	Background Subtraction	$4.67 \pm 0.50(stat.)$
	Fit	$4.79 \pm 0.44(stat.)$

Table 7.16: Photoproduction cross sections of the Σ^{*+} obtained with the two methods.

Systematic Uncertainties

Several sources of systematic uncertainties was identified:

- the systematic uncertainties due to the used triggers: it was obtained as half of the difference of the cross sections corresponding, for each method, to trigger 21 and trigger 27, respectively.

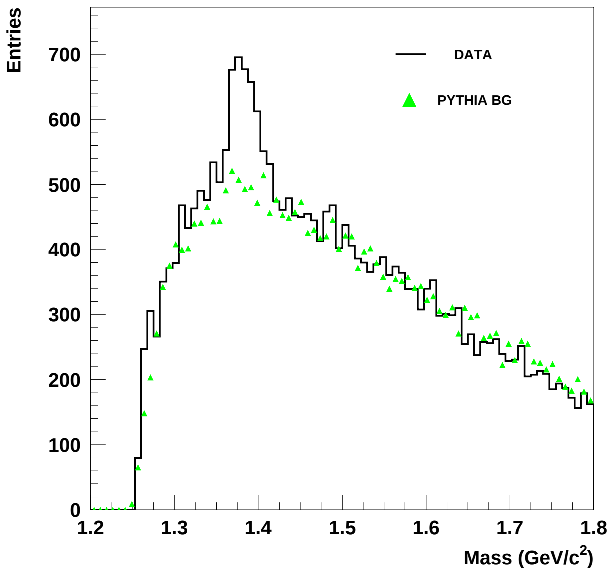

Figure 7.31: The total background resulting from the combination of the SIDE-BAND method and the Monte Carlo simulation.

- the systematic error due to to the time stability of the detector: the error estimated in the Λ analysis (see Sec.6.5.3) was propagated (in percentage) to the heavier hyperons;
- the systematic uncertainty due to the different methods, calculated as the half of the difference of the two values reported in Tab.7.16;
- the systematic uncertainty due to the measurement of the luminosity (see Sec.6.5.3)

The four contributions were then added in quadrature.
The final value of the photoproduction cross section of the Σ^{*+} hyperons, with the corresponding statistical and systematic uncertainties, is:

$$< \sigma_{\Sigma^{*+}} >= 4.72 \pm 0.50(stat.) \pm 1.18(syst.) \quad \mu\text{barn} \tag{7.18}$$

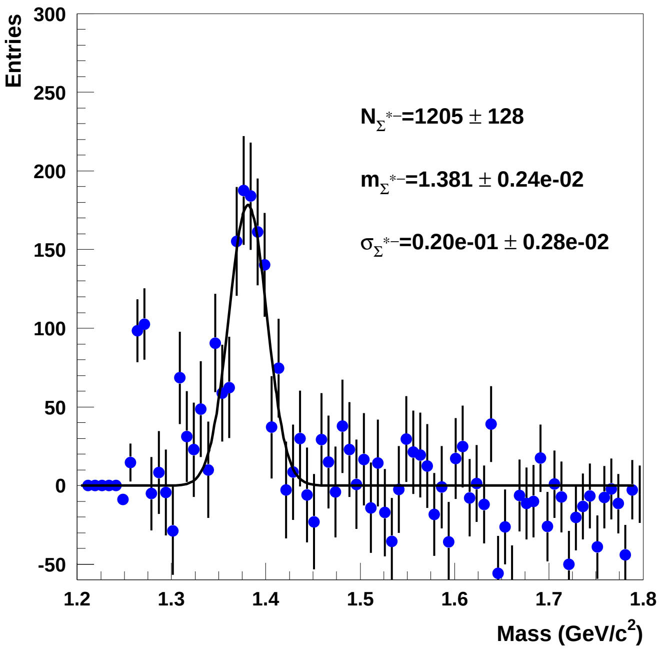

Figure 7.32: Fit of the resulting peak after subtracting the total background.

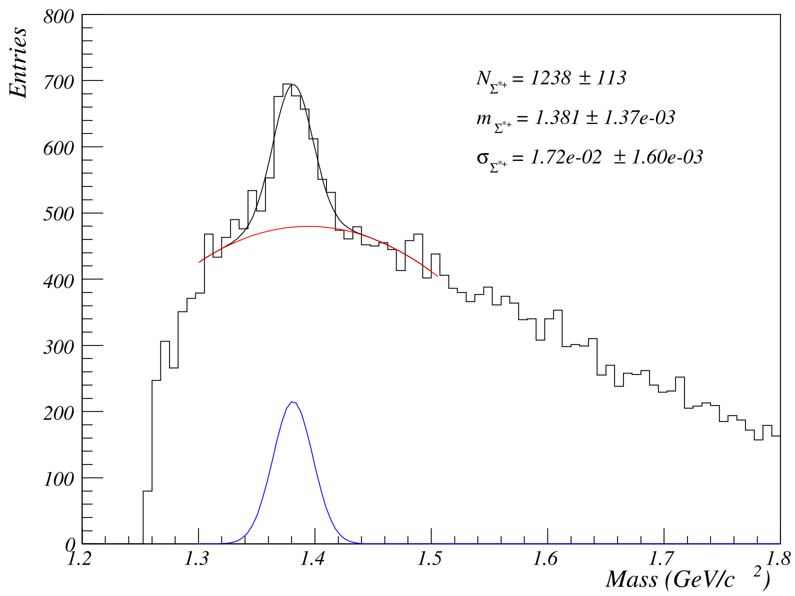

Figure 7.33: Fit of the mass spectrum of the Σ^{*+} hyperon.

7.3.4 $\overline{\Sigma}^{*-}$ Hyperon

The cuts reported in Tab.7.13 were applied in order to select the $\overline{\Sigma}^{*-}$ hyperon candidates. The trigger 21 and 27 were used. The efficiencies of the two triggers and of their combination as a function of the anti-proton momentum are shown in Fig.7.34. The average values of the trigger efficiencies are reported in table 7.17

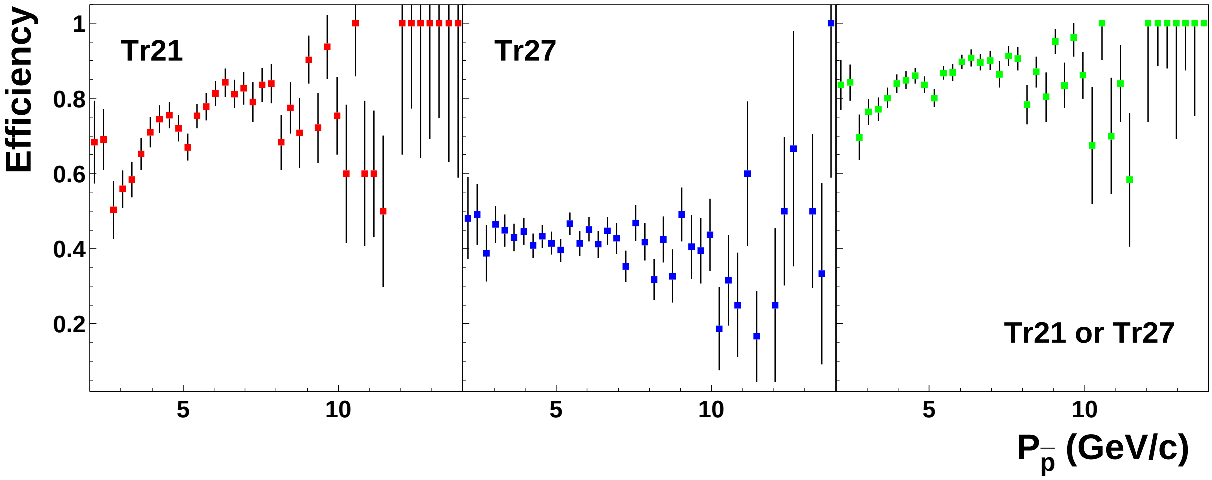

Figure 7.34: Efficiencies of trigger 21 (left-panel), trigger 27 (center-panel) and of the combination of the two triggers (right-panel) as a function of the anti-proton momentum.

Data Production	Trigger 21	Trigger 27	Trigger 21 or 27
$98d0 + 99c0 + 00d0$	75%	42%	86%

Table 7.17: Total efficiency for the triggers 21 and 27 for the three data productions.

Only the combination of the two triggers was considered for the extraction of the cross section. The value of the total efficiency, $\epsilon_{tot}^{21or27} = 0.13\%$, was calculated as explained in Sec.6.3 and was used to correct the experimental data.
The number of observed $\overline{\Sigma}^{*-}$ events was extracted with the two methods:

- the background subtraction method
- the fit method

The total simulated background, normalized to the data, is shown in Fig.7.35, while the difference between the signal and the background, together with the fit of the peak, is shown in Fig.7.36.
The fit of the total spectrum is shown in Fig.7.37 together with the parameters from the fit.
The values of the photoproduction cross section obtained with the two methods are reported in the following table.

Hyperon	**Method**	**Cross Section (μbarn)**
$\overline{\Sigma}^{*-}$	Background Subtraction	$0.0117 \pm 0.0027(stat.)$
	Fit	$0.0115 \pm 0.0024(stat.)$

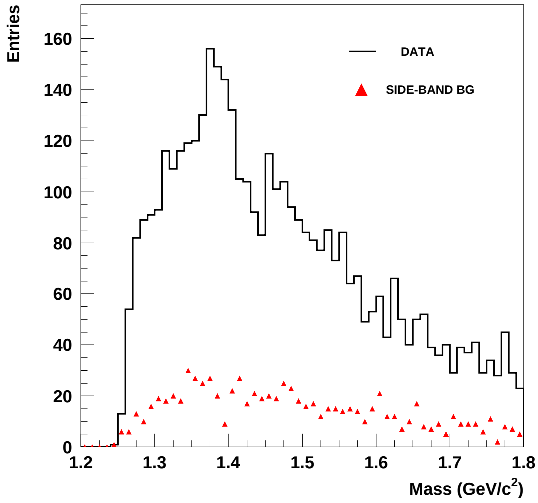

(a) SIDE-BAND background

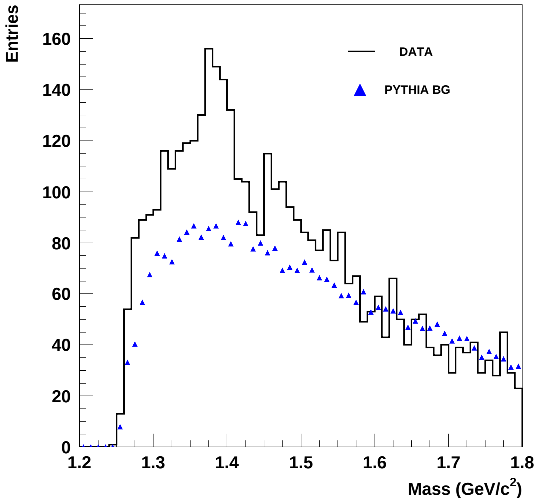

(b) PYTHIA background

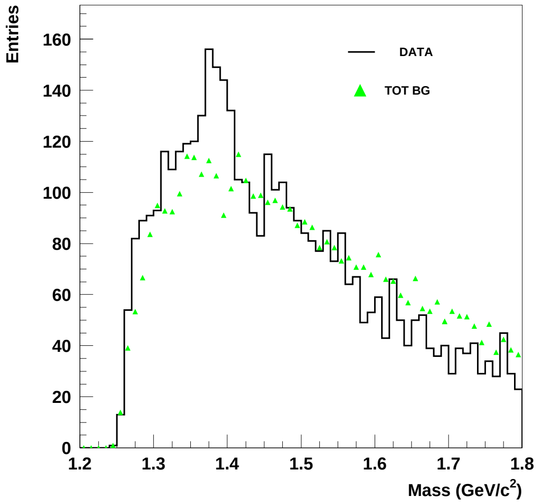

(c) Total background

Figure 7.35: Contributions to the total background obtained by using the SIDE-BAND method (a) and the Monte Carlo simulation (b). Total background (c).

The final value was obtained as a weighted average of the values obtained with the two methods. The systematic uncertainty was estimate as explained in sec. 7.3.3.

$$< \sigma_{\overline{\Sigma}^{*-}} >= 0.0116 \pm 0.0024(stat.) \pm 0.0027(syst.) \quad \mu\text{barn} \tag{7.19}$$

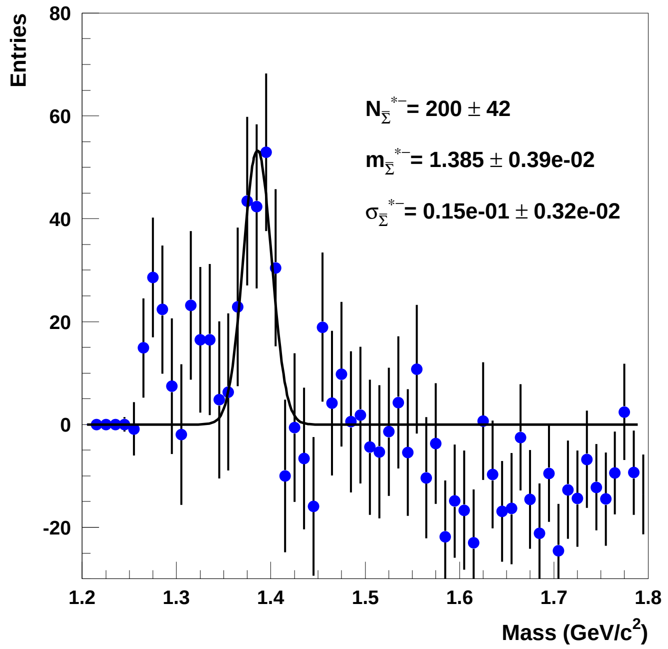

Figure 7.36: Gaussian fit of the $\overline{\Sigma}^{*-}$ peak after the background subtraction.

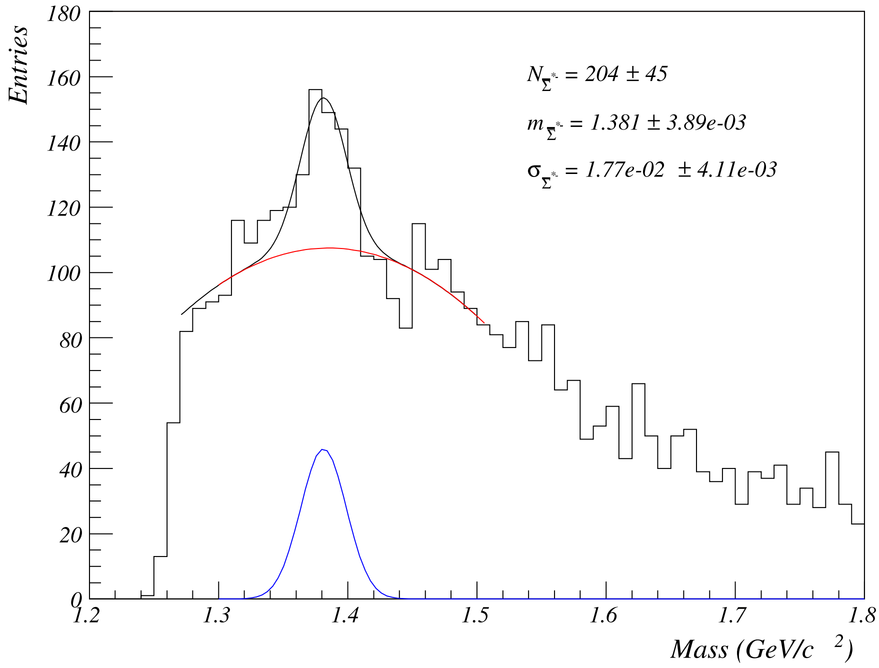

Figure 7.37: Fit of the invariant mass spectrum of the $\overline{\Sigma}^{*-}$ together with the parameters from the fit.

The extracted values of the photoproduction cross section of all the hyperons (antihyperons) analyzed in this thesis have been compared with results available in literature: [116], [117] and references wherein for the γp and πp interactions and [47] for e^+e^- interactions. The comparison is shown in Fig. 7.38. The results of this thesis are reported both with and without the P_z cut ($P_z > 3$ GeV) (see Sec. 6.7) and are summarized in Tabs. 7.18 and 7.19. The huge difference in the values of the cross section between these two cases is a consequence of the fact that the target remnant contribution, which is dominant in the $P_z < 3$ GeV region, is relevant for the Λ, Σ^0 and $\Sigma^{*\pm}$ production mechanism. However, being the latter poorely described in the PYTHIA model adopted, the cross section can be safely measured at HERMES only in the forward region ($x_F > -0.1$ which corresponds to $P_z > 3$ GeV). As noticeable in Fig. 7.38, this is no longer true for the Ξ^- hyperon and all the antihyperons analyzed since the fragmentation process is dominated by the sea quarks contribution in this case.

Hyperon	**Cross section** (μbarn)	**Cross Section ($P_z > 3$ GeV)** (μbarn)
Λ	$26.96 \pm 0.07(stat.) \pm 2.98(syst.)$	$1.94 \pm 0.01(stat.) \pm 0.21(syst.)$
Σ^0	$4.93 \pm 0.23(stat.) \pm 0.63(syst.)$	$0.681 \pm 0.032(stat.) \pm 0.086(syst.)$
Σ^{*+}	$4.72 \pm 0.50(stat.) \pm 1.18(syst.)$	$0.632 \pm 0.066(stat.) \pm 0.158(syst.)$
Σ^{*-}	$4.36 \pm 0.49(stat.) \pm 0.39(syst.)$	$0.553 \pm 0.062(stat.) \pm 0.050(syst.)$
Ξ^-	$0.102 \pm 0.011(stat.) \pm 0.020(syst.)$	$0.093 \pm 0.010(stat.) \pm 0.018(syst.)$

Table 7.18: Summary of the Photoproduction cross sections of the hyperons analized.

Hyperon	**Cross section** (μbarn)	**Cross Section ($P_z > 3$ GeV)** (μbarn)
$\overline{\Lambda}$	$0.210 \pm 0.001(stat.) \pm 0.017(syst.)$	$0.147 \pm 0.001(stat.) \pm 0.001(syst.)$
$\overline{\Sigma}^0$	$0.073 \pm 0.014(stat.) \pm 0.007(syst.)$	$0.051 \pm 0.016(stat.) \pm 0.005(syst.)$
$\overline{\Sigma}^{*+}$	$0.0097 \pm 0.0034(stat.) \pm 0.0007(syst.)$	$0.0082 \pm 0.0045(stat.) \pm 0.0006(syst.)$
$\overline{\Sigma}^{*-}$	$0.0116 \pm 0.0024(stat.) \pm 0.0027(syst.)$	$0.0115 \pm 0.0026(stat.) \pm 0.0026(syst.)$
$\overline{\Xi}^+$	$0.0273 \pm 0.0031(stat.) \pm 0.0029(syst.)$	$0.0213 \pm 0.0042(stat.) \pm 0.0023(syst.)$

Table 7.19: Summary of the Photoproduction cross sections of the antihyperons analized.

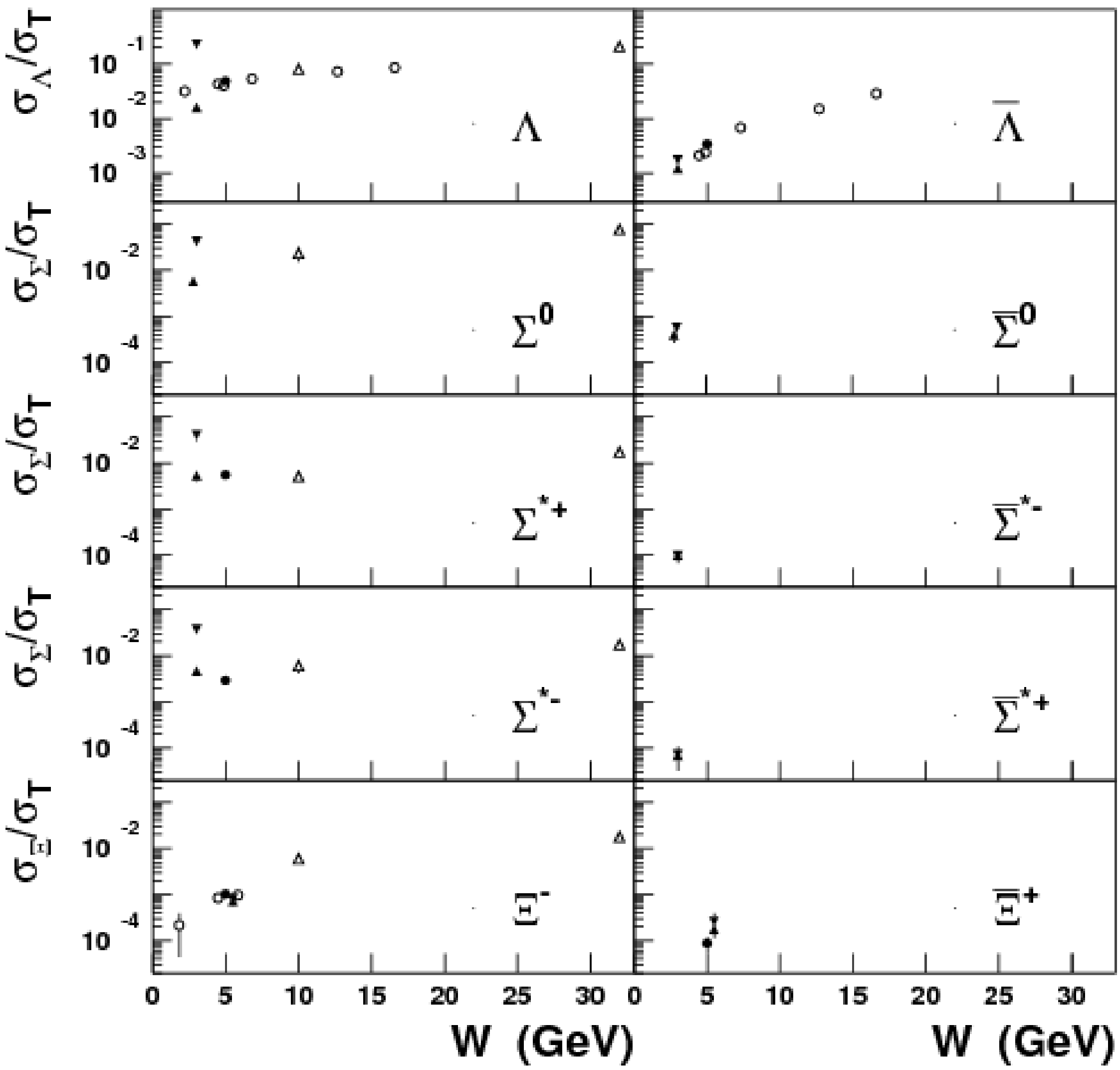

Figure 7.38: The production cross section of Λ, Σ^0, $\Sigma^{*\pm}$ and Ξ^- hyperons, and their corresponding antihyperons, are plotted as a function of the center of mass energy W. Different experimental conditions are compared. The open circles show the results of experiments with pion beams (the average between results with π^+ and π^- beams of the same energy is plotted). The open triangles show the results at e^+e^- colliders where the combined production of particle and antiparticle is measured. The black circles show the results of an experiment with a real gamma beam. The black triangles show the results of this work, with (upward) and without (downward) the threshold on P_z ($P_z > 3$ GeV).

Chapter 8

Conclusion

This thesis presents the study of strange hyperon production mechanism in photoproduction processes, which have been poorly explored so far. The work can be split into two major parts: the study of the Λ ($\overline{\Lambda}$) differential cross section as a function of the longitudinal and transverse momentum, that allows to constrain the unpolarized fragmentation functions, and the measurement of the production cross section of several strange baryons and the respective antiparticles. In the extraction of the differential and absolute cross sections a big effort has been done to estimate the possible sources of inefficiencies and in controlling the systematic uncertainty. In particular, an algorithm for the calculation of the trigger inefficiencies, which can be generally neglected in the standard analysis of spin asymmetries of cross-section at HERMES, has been developed. Furthermore, a simulation of the RICH detector allowed to fully take into account the inefficiencies in the particles identification. Finally, a Monte Carlo simulation based on PYTHIA6.2 genertator [78] and GEANT3 [79] was used to estimate the effects of the relatively small angular acceptance of the HERMES spectrometer.

The differential cross section and the related hadron multiplicities are the observables used to extract the fragmentation functions which describe the quark hadronization (or how the confinement arises) and should be used when extracting the original partonic informations from measured quantities. The multiplicities of different mesons and non-strange baryons produced in the fragmentation process at HERMES, have been extracted in [76] and [77]. The tuning of the LUND model parameters to describe the HERMES kinematic regime, was based on these studies, and results in a substantial improvement of the agreement between the experimental and simulated distributions for pions and antiprotons. This tuning, however, was found to be not fully satisfying for the description of the kaons and protons distributions.
The extraction of the differential cross section of the Λ ($\overline{\Lambda}$) particle, which is a strange baryon decaying into a proton plus a pion, and the comparison between experimental and simulated distributions represent a useful tool to test the parametrization of the fragmentation function related to baryons and strangeness and suggest a way to further improve the model. The disagreement in the P_z distributions from data and Monte Carlo suggests that a too high value of PARJ41 (which corresponds to the a parameter of the symmetric LUND fragmentation function see Sec. 6.7) was probably used in [76] and [77].

The second part of this work concerns the extraction of the absolute photoproduction cross sections of the Σ^0, Σ^{*+}, Σ^{*-} and Ξ^- hyperons and the relative antiparticles. Here a great effort was made in order to correctly estimate the background, which is relatively small for the Λ hyperon but sizable in the case of heavier hyperons. A combination of Monte Carlo simulations and investigations of off-shell mass candidates allowed to perform a detailed study of the combinatorial background. The comparison between the measured photoproduction cross sections, and the cross sections obtained from the Monte Carlo simulation, represents a way to test the assumptions and the parameters used in the LUND model. The measured cross sections allow to investigate the production mechanism of strange baryons in photoproduction processes and to correlate it with other processes like pion-nucleon scatterings and e^+e^- annihilations.

Acnowledgements

Now that my thesis is over I would like to thank all the people whose help was indispensable to complete my PhD. First of all I would like to thank my internal tutor Prof. Francesco Riggi for giving me the opportunity to spend a large part of my PhD at the University of Ferrara, thus making it possible for me to join an exciting experiment such as the HERMES experiment at HERA. Then, of course, I would like to thank my group leader Prof. Paola Ferretti Dalpiaz for inviting me to be part of the HERMES group of Ferrara and for transmitting me her experience and enthusiasm in hadron physics.

Joining the Ferrara group has been really useful and exciting for me. There I had the opportunity to learn a lot of concepts and techniques not only related to my major activity: data analysis, but also concerning different fileds like the working priciple and the characterization of an Atomic Beam Source and the practical and theoretical problems related to the polarization of a high energy antiproton beam, needed for the future experiments at FAIR. But, most importantly, I had the opportunity to enter the HERMES experiment and to spend several periods in the international environment of the DESY research facility in Hamburg.

Concerning my work in the data analysis I really would like to thank Elke-Caroline Aschenauer for being always available regarding the Monte Carlo producitons and for answering in a very clear and comprehensive way all my questions and dubts. A particular thanks to Michelle Stancari and expecially to Marco Contalbrigo, for being always available to give me the right hints and for indicating me the (... sometimes tortuous and stressful) way toward the extraction of my final results. In particular I am indebted with Marco Contalbrigo for his extraordinary efforts to make this analysis successfully completed in only one and a half year.

I would also like to thank my collegues Francesca Giordano and Diego Pelliccia for sharing with me the stress and the excitement of the last months during our coffee breaks at 'Bar di Ingegneria'.

Tutto il mio amore va alla mia famiglia e a mio marito per avermi supportato e sopportato in questi tre anni.

Appendix A

A.0.5 Regge poles and confinement

Regge poles have been introduced in particle physics in the beginning of 60-ies [118, 119] and up to present time are widely used for description of high-energy interactions of hadrons and nuclei. Regge approach establishes an important connection between high energy scattering and spectrum of particles and resonances. It served as a basis for introduction of dual and string models of hadrons. A derivation of Regge poles in QCD is a difficult problem closely related to the nonperturbative effects in QCD and the problem of confinement.In the first paragraph of this Appendix there is a short introduction to the reggeon concept, while the second paragraph contains elementary considerations on the connections between Regge trajectories and string

The Reggeon concept

The complex angular momentum method was first introduced by Regge in nonrelativistic quantum mechanics.[120] In relativistic theory it connects a high energy behavior of scattering amplitudes with the singularities in the complex angular momentum plane of the partial wave amplitudes in the crossed (t) channel. This method is based on the general properties of the S-matrix - unitarity, analyticity and crossing. The simplest singularities are poles (Regge poles). The formal definition of Reggeon is the pole in the partial wave in t-channel of the scattering process. For example, for $\pi^+ + p$ elastic amplitude the Reggeon is a pole in the partial wave of the reaction: $\pi^+ + \pi^- \rightarrow p + \bar{p}$, namely, the amplitude of this process can be written in the form:

$$f_l(t) = \sum_{l=0}^{\infty} f_l(t)\,(2l + 1)\,P_l(z)\;, \tag{A.1}$$

where $z = cos\theta$ and θ is the scattering angle from initial pion to final proton (antiproton). Reggeon is the hypothesis that $f_l(t)$ has a pole of the form

$$f_l(t) = \frac{g_1(t)\,g_2(t)}{l - \alpha_R(t)} \tag{A.2}$$

where function $\alpha_R(t)$ is the Reggeon trajectory which experimentally has a form:

$$\alpha_R(t) = \alpha_R(0) + \alpha'_R(0)\,t\;, \tag{A.3}$$

where $\alpha_R(0$ is the intercept of the Reggeon and $\alpha'_R(0)$ is its slope.

A Regge-pole exchange is a natural generalization of a usual exchange of a particle with spin J to complex values of J. So this method established an important connection between high energy scattering and the spectrum of hadrons. This is a t-channel point of view on Regge poles. On the other hand asymptotic behavior of scattering amplitudes at very high energies is

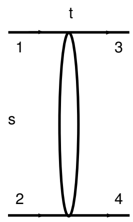

Figure A.1: A diagram for a binary reaction.

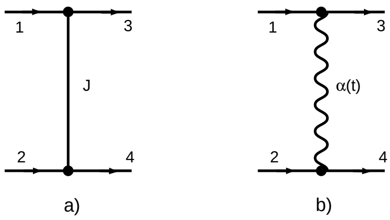

Figure A.2: a) Exchange by a particle of spin J in the t-channel. b) Exchange by a Regge pole in the t-channel.

closely related to the multiparticle production. This is the s-channel point of view on reggeons. Let us consider first the t-channel point of view in more details.
The binary reaction $1 + 2 \to 3 + 4$ (A.1) is described by the amplitude $T(s,t)$, which depends on invariants $s = (p_1 + p_2)^2$ and $t = (p_1 - p_3)^2$. At high energies $s \gg m^2$ and fixed momentum transfer $t \sim m^2$ an exchange by a particle of spin J in the t-channel (Fig.2a)) leads to an amplitude of the form

$$T(s,t) = g_{13} \cdot g_{24} \cdot (s)^J/(M_J^2 - t) \tag{A.4}$$

where g_{ik} are the coupling constants and M_J is the mass of the exchanged particle.

For a partial wave expansion of amplitudes

$$f(s, cos\theta) = \frac{T(s,t)}{8\pi\sqrt{s}} = \frac{1}{p}\sum_{l=0}^{\infty}(2l+1)f_l(s)P_l(cos\theta) \tag{A.5}$$

the unitarity relation leads to the constraints

$$\Im f_l(s) \geq | f_l(s) |^2; \quad | f_l(s) | \leq 1 \tag{A.6}$$

It follows from eq.(1) that for an exchange of a particle with a spin $J \geq 2$ the partial wave amplitude increases with energy $\sim s^{(J-1)}$ for large s and violates unitarity as $s \to \infty$.

This problem can be solved by introduction of Regge poles. It should be taken into account that the expression (1) for the amplitude is valid, strictly speaking, only close to the pole position $t \approx M_J^2$ and can be strongly modified away from the pole. Regge pole model gives an exact form of this modification and absorbs in itself exchanges by states of different spins (Fig2b)). The corresponding amplitude has the form

$$T(s,t) = f_{13}(t) \cdot f_{24}(t) \cdot (s)^{\alpha(t)} \cdot \eta(\alpha(t)) \tag{A.7}$$

where $\alpha(t)$ is the Regge-trajectory, which is equal to spin J of the corresponding particle at $t = M^2$. The function $\eta(\alpha(t)) = -(1 + \sigma exp(-i\pi\alpha(t))/\sin(\pi\alpha(t))$ is a signature factor and $\sigma = \pm 1$ is a signature. It appears due to the fact that in relativistic theory it is necessary to consider separately analytic continuation of partial wave amplitudes in the t-channel to complex values of angular momenta J from even $(\sigma = +)$ and odd $(\sigma = -)$ values of J. This factor is closely related to the crossing properties of scattering amplitudes under interchange of s to $u = (p_1 - p_4)^2$. Amplitudes with $\sigma = +$ are even under the interchange $s \leftrightarrow u$ $(s \leftrightarrow -s$ for high energies), while for $\sigma = -$ amplitudes are antisymmetric under this operation. It should be emphasized that the single Regge exchange corresponds to an exchange of particles or resonances which are "situated" on the trajectory $\alpha(t)$. For example if $\alpha(t) = J$, where J is an even (odd) integer for $\sigma = +(-)$ for $t = M_J^2$ and M_J^2 is less than the threshold for transition to several hadrons ($4m_\pi^2$ for particles which can decay into two pions), then the Regge amplitude eq.(4) transforms into the particle exchange amplitude eq.(1) with $g_{13}g_{24} = f_{13}(M_J^2) \cdot f_{24}(M_J^2)2/\pi\alpha'(M_J^2)$.

If M_J is larger than the threshold value then $\alpha(t)$ is a complex function and can be written for $t \approx M_J^2$ in the form

$$\alpha(t) = J + \alpha'(M_J^2) \cdot (t - M_J^2) + iIm\alpha(M_J^2) \tag{A.8}$$

In this case for $Im\alpha(M_J^2) \ll 1$ Regge pole amplitude eq.(4) corresponds to an exchange in the t-channel by a resonance and has the Breit-Wigner form

$$T(s,t) = -g_{13} \cdot g_{24}(s)^J/(t - M_J^2 + iM_J\Gamma_J) \tag{A.9}$$

with a width $\Gamma_J = Im\alpha(M_J^2)/M_J\alpha'(M_J^2)$.

Thus a reggeization of particle exchanges leads to a natural resolution of the above mentioned problem with a violation of the unitarity, -Regge trajectories, which correspond to particles with high spins can have $\alpha(t) \leq 1$ in the physical region of high energy scattering $t < 0$ and the corresponding amplitudes will increase with s not faster than s^1, satisfying the unitarity. The experimental information on spectra of hadrons and high energy scattering processes nicely confirms this theoretical expectation. The only exception is the Pomeranchuk pole (or the Pomeron), which determines high energy behavior of diffractive processes.

A.0.6 Bosonic and fermionic Regge poles, vacuum exchange

Let us consider the main properties of Regge poles.
a)Factorization. Regge poles couple to external particles in a factorizable way, which is manifest in eq.(4).
b)Regge poles have definite conserved quantum numbers like the baryon quantum number, parity P, isospin e.t.c. As it was mentioned above they have also a definite signature σ.

An information on trajectories of Regge poles can be obtained for $t < 0$ from data on two-body reactions at large s and for $t > 0$ from our knowledge of the hadronic spectrum. We have seen that a bosonic trajectory corresponds to particles and resonances for those values of t where it passes integer values $(Re\alpha(t) = n)$ even for $\sigma = +$ and odd for $\sigma = -$. While for fermionic trajectories particles correspond to $Re\alpha(t) = \frac{n}{2} = J$ and signature $\sigma = (-1)^{J-\frac{1}{2}}$. There can be many trajectories with the same quantum numbers indicated above, which differ by a quantum number analogous to the radial quantum number. Such trajectories are usually called "daughter" trajectories and masses of corresponding resonances (with the same value of J) for them are higher than those for the leading trajectory with given quantum numbers.

Trajectories for some well established bosonic Regge poles are shown in Fig.3. Note that all these trajectories have $\alpha_i(0) \leq 0.5$ for $t \leq 0$. One of the most interesting properties of these

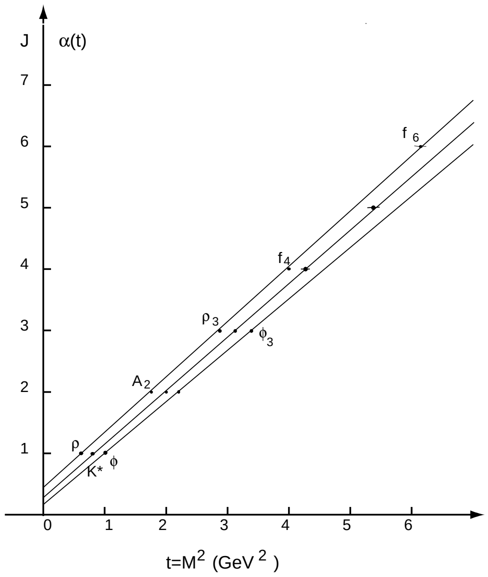

Figure A.3: Trajectories for some well-known Regge poles.

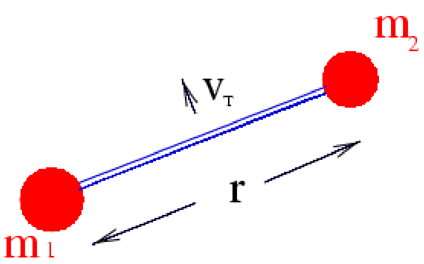

Figure A.4: *Picture of the quark-antiquark bound state in the string model.*

trajectories is their surprising linearity. This usually interpreted as a manifestation of strong forces between quarks at large distances, which lead to color confinement. The linearity of Regge trajectories indicates to a string picture of the large distance dynamics between quarks and it was a basis of dual models for hadronic interactions.

Confinement

Up to now, free quarks have not been detected. The upper limit on the cosmic abundance of relic quarks, n_q, is $n_q/n_p < 10^{-27}$, n_p being the abundance of nucleons, while cosmological models predict $n_q/n_p < 10^{-12}$ for unconfined quarks. The fact that no free quarks have been ever detected hints to the property of quark confinement. Hence, the interaction among quarks has to be so strong at large distances that a $q\bar{q}$ pair is always created when the quarks are widely separated. From the data it is reasonable to expect that a quark typically comes accompanied by an antiquark in a hadron of mass $1\,\mathrm{GeV}$ at a separation of 1 fm ($\simeq \Lambda_{QCD}^{-1}$). This suggests that between the quark and the antiquark there is a linear energy density of order

$$\sigma = \frac{\Delta E}{\Delta r} \simeq 1\frac{\mathrm{GeV}}{\mathrm{fm}} \simeq 0.2\,\mathrm{GeV}^2. \tag{A.10}$$

A theoretical framework is provided by the string model, Nambu (1974). In this model the hadron is represented as a rotating string with the two quarks at the ends. The string is formed by the chromoelectric field responsible for the flux tube configuration and for the quark confinement (see Fig. A.4) Buchmüller (1982).

The evidence for linear Regge trajectories (see Fig. A.6) supports this picture.

When the spin J of mesons is plotted as a function of squared meson mass m^2, it turns out that the resulting points can be sorted into groups which lie on straight lines, and that the slopes of these lines are nearly the same, as shown in Fig. A.3. These lines are known as "linear Regge trajectories," and the particles associated with a given line all have the same flavor quantum numbers. Similar linear trajectories are found for the baryons, out as far as $J = 11/2$.

This remarkable feature of hadron phenomenology can be reproduced by a very simple model. Suppose that a meson consists of a straight line-like object with a constant energy density σ per unit length, having a nearly massless quark at one end of the line, and a nearly massless antiquark at the other. The quark and antiquark carry the flavor quantum numbers of the system, and move at nearly the speed of light. For a straight line of length $L = 2R$, whose ends rotate at the speed of light, the energy of the system is

$$m = E = 2\int_0^R \frac{dr}{\sqrt{1-v^2(r)}} \tag{A.11}$$

$$= 2\int_0^R \frac{dr}{\sqrt{1-r^2/R^2}} \tag{A.12}$$

$$= \pi R \tag{A.13}$$

while the angular momentum is

$$J = 2\int_0^R \frac{rv(r)dr}{\sqrt{1-v^2(r)}} \tag{A.14}$$

$$= \frac{2}{R}\int_0^R \frac{r^2dr}{\sqrt{1-r^2/R^2}} \tag{A.15}$$

$$= \pi R^2 \tag{A.16}$$

Comparing m and J, we find that

$$J = \frac{m^2}{2\pi} \tag{A.17}$$

which means that this very simple model has caught the essential feature, namely, a linear relationship between m^2 and J. From the particle data, the slope of the Regge trajectories is approximately

$$= \frac{1}{2\pi} \approx 0.9\, GeV^{-2} \tag{A.18}$$

implying an energy/unit length of the line between the quarks, which is known as the "string tension", of magnitude

$$\approx 0.18\, GeV^2 \approx 0.9\, GeV/fm \tag{A.19}$$

Of course, the actual Regge trajectories don't intercept the x-axis at $m^2 = 0$, and the slopes of the different trajectories are slightly different, as can be seen from Fig. A.6. But the model can also be modified by allowing for finite quark masses. Note that since a crucial aspect of the model is that the quarks move at (nearly) the speed of light, the low-lying heavy quark states (charmonium, "toponium", etc.), composed of the c, t, b quarks, would not be expected to lie on linear Regge trajectories. Another way of making the model more realistic would be to allow for quantum fluctuations of the line-like object in directions transverse to the line. Those considerations lead to (and in fact inspired) the formidable subject of string theory.

QCD can be made agree with the simple phenomenological model if, for some reason, the electric field diverging from a quark is collimated into a flux tube of fixed cross-sectional area. In that case the string tension is simply

$$= \int d^2x_\perp \, \vec{E}^a \cdot \vec{E}^a \tag{A.20}$$

where the integration is in a plane between the quarks, perpendicular to the axis of the flux tube. The problem is to explain why the electric field between a quark and antiquark pair should be collimated in this way, instead of spreading out into a dipole field, as in electrodynamics, or simply petering out, as in a spontaneously broken theory.

In fact, as already emphasized, the color electric field of a quark or any other color charge source *does* peter out, eventually. If a heavy quark and antiquark were suddenly separated by a large distance (compared to usual hadronic scales), the collimated electric field between the quarks would not last for long. Instead the color electric flux tube will decay into states of lesser energies by a process of "string breaking" (Fig. A.5), which can be visualized as production of light quark-antiquark pairs in the middle of the flux tube, producing two or more meson states. The color field of each of the heavy quarks is finally screened by a bound light quark. This process also accounts for the instability of excited particle states along Regge trajectories.

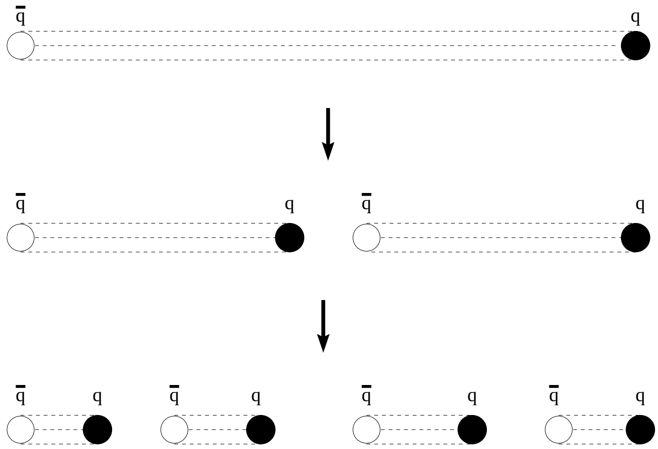

Figure A.5: String breaking by quark-antiquark pair production.

Pair production, however, is suppressed if all quarks are very massive. Suppose the lightest quark has mass m_q. Then the energy of a flux tube state between nearly static quarks will be approximately L, while the mass of the pair-produced quarks associated with string-breaking will be at least $2m_q$. This means that the flux tube states will be stable against string breaking up to quark separations of approximately

$$L = 2m_q \tag{A.21}$$

Concluding, Light mesons (as well as baryons) of a given internal symmetry quantum number but with different spins obey a simple spin (J)-mass (M) relation. They lie on a Regge trajectory

$$J(M^2) = \alpha_0 + \alpha' M^2 \tag{A.22}$$

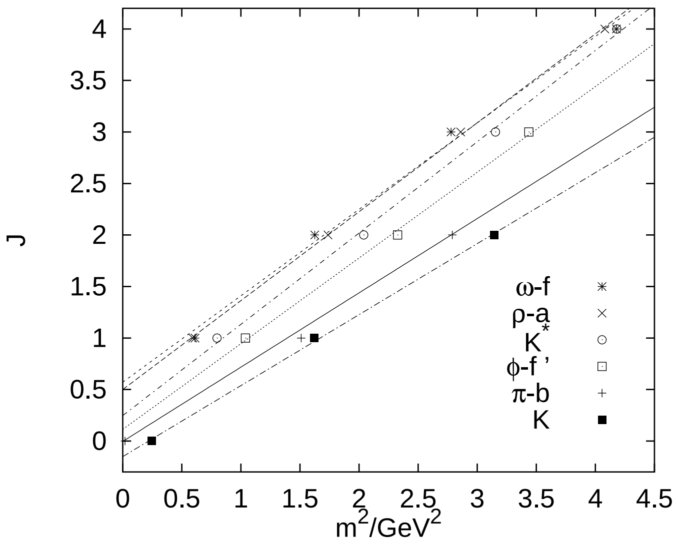

Figure A.6: Regge trajectories for the low-lying mesons (figure from Bali, ref. [121]).

with $\alpha' \simeq 0.8 - 0.9\,\mathrm{GeV}^{-2}$.

It is possible to establish the relation

$$\alpha' = \frac{1}{2\pi\sigma} \tag{A.23}$$

between the slope of the Regge trajectories and the string tension. The string tension σ emerges as a key phenomenological parameter of the confinement physics.

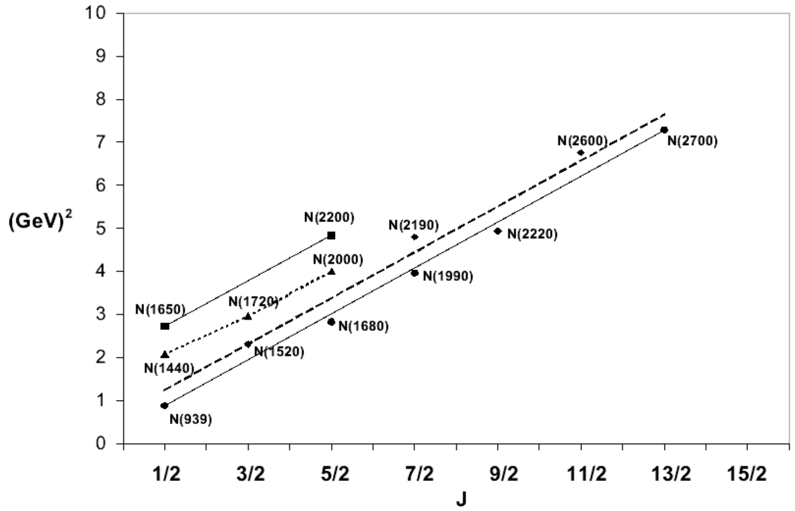

Figure A.7: Regge trajectories for nucleons.

Appendix A

The beam polarization

A.1 The Beam Polarization

Electrons or positrons are injected unpolarised at 12 GeV into the HERA storage ring and are subsequently ramped up to the nominal beam energy of 27.5 GeV. The lepton beam is transversely polarised by the *Sokolov-Ternov effect* (ST) [96] which causes the leptons to predominantly aligne their spins in the vertical direction, parallel to the magnetic field of the storage ring, by radiating photons.
The time dependence of the beam polarization follows an exponential law::

$$P_{ST}(t) = P_{\infty}\left(1 - e^{\frac{t}{\tau}}\right) \tag{A.1}$$

for a circular machine with a perfectly flat orbit. The theoretical maximum of the polarization has been calculated to be:

$$P_{ST}^{\infty} = \frac{8}{5\sqrt{3}} = 92.38\% \tag{A.2}$$

with an associated rise-time constant:

$$\tau_{ST} = \frac{8}{5\sqrt{3}}\frac{m_e^2 c^2 \rho^3}{e^2 \hbar \gamma^5} = 37min \tag{A.3}$$

where γ is the Lorentz factor, ρ is the bending radius of the orbit, m_e and e are the electron mass and charge, c is the speed of light, $\hbar$ is the Planck constant and E is the positron energy.
For rings such as HERA with the spin rotators needed to get longitudinal polarization at experiment P_{ST}^{∞} can be reduced substantially below 92.38% and τ_{ST} can be modified too. Synchrotron radiation also causes depolarization which competes with the ST effect with the result that the equilibrium polarization is reduced even further. Moreover the depolarization is strongly enhanced by the presence of the small but non-vanishing misalignments of the magnetic elements and the resulting vertical orbit distorsions.
The strength of this depolarization can be summarized into a depolarizing time constant τ_{dep}, such that the asymptotic polarization becomes:

$$P_{max}(t) = P_{ST}^{\infty}\frac{\tau_{dep}}{\tau_{dep} + \tau_{ST}} \quad and \quad \tau = \tau_{ST}\frac{\tau_{dep}}{\tau_{dep} + \tau_{ST}} \tag{A.4}$$

and

$$\tau = \tau_{ST} \frac{\tau_{dep}}{\tau_{dep} + \tau_{ST}} \tag{A.5}$$

As a result, the maximum achievable polarization becomes smaller and the rise time shorter, while Eq. (1.1) stays valid when exchanging $P_{ST}^{\infty} \rightarrow P_{max}$ and $\tau_{ST} \rightarrow \tau$. Efforts taken at HERA to empirically optimize the positron orbit helped to achieve polarization values of 50% to 60% during the data taking periods 1995 to 1997.

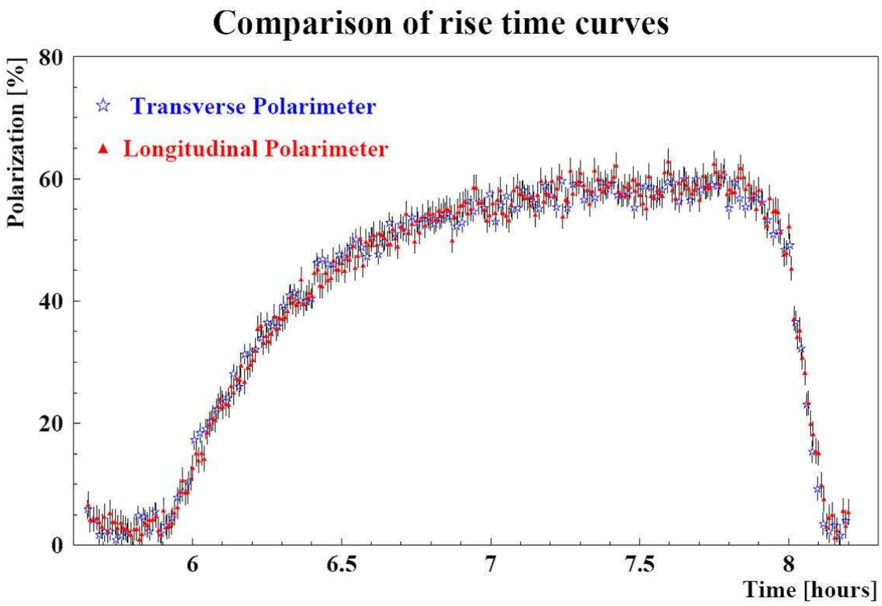

Figure A.1: Polarization build-up through the Sokolov-Ternov effect. Within a rise time of about 22 minutes typically polarizations between 50% and 60% are reached.

The *longitudinal* polarization necessary for HERMES can be obtained by rotating the spin vectors of the positrons (electrons) from the transverse direction to a direction parallel to the beam orbit. This is done with a spin rotator, a device consisting of six interleaved horizontal and vertical dipole magnets generating a pattern of vertical and horizontal orbit deflections. After passing through a spin rotator a positron will not have its beam trajectory changed, but the orbit kicks will cause a series of rotations of the spin vector such that it is finally turned by $90°$. Between 1995 and 2000 two rotators were installed, one before the HERMES Interaction Point (IP), turning the spin into the axis of the beam momentum, and one after the HERMES IP, turning the spin back to the transverse direction.

A.1.1 Transverse and Longitudinal Polarimeters

The uncertanty in the beam polarization constitues an important part of the systematic uncertanty for precision measurements of polarized cross section, asymmetries etc. Therefore it is essential to provide precise and frequent measurements of the beam polarization. At HERA, two polarimeters are in operation. Both polarimeters make use of a cross section asymmetry in the Compton scattering of circularly polarized photons off polarized electrons/positrons.

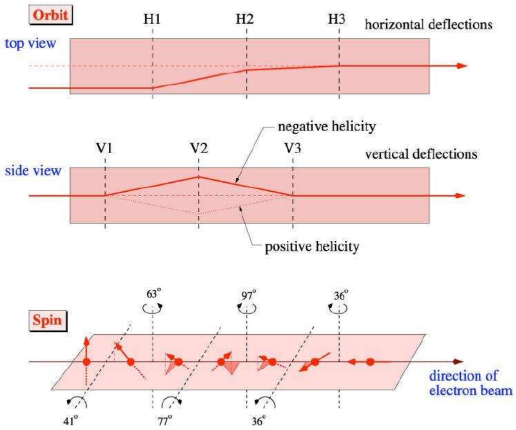

Figure A.2: A schematic diagram showing the operation principle of one spin rotator. A sequence of vertical and horizontal magnetic fields move the beam orbit (top) and rotate the positron (electron) polarization direction (bottom). The sequence is chosen such that the vertical position of the orbit in unchanged by the rotator, but the spin receives a net rotation to the longitudinal direction.

The **Transverse Polarimeter (TPOL)** was installed in the HERA east hall in 1992 and measures the transverse polarization, (a detailed description can be found in refs [122],[123]). Circularly polarized light from a continuous Argon ion laser (514 nm, E=2.41 eV) is directed against the positron beam at a shallow angle, with its helicity being switched with a frequency of 83.8 Hz. The backscattered photons are detected with a tungsten-scintillator sandwich calorimeter consisting of two identical halves separated along the beam plane. If the positron polarization is in the y direction (i.e. perpendicular to the orbit plane), the Compton scattered photons are distributed asymmetrically along the y direction. The asymmetry is proportional to the sine of the azimuthal photon scattering angle around the beam axis and to the positron polarization into the y-direction [124]. By measuring the asymmetry in the energy deposition of backscattered photons between the top and the bottom halves of the calorimeter the mean average vertical position $\langle y \rangle$ can be inferred. From the difference

$$\Delta y = \frac{\langle y \rangle_R - \langle y \rangle_L}{2} \sim P_y \Pi_y \tag{A.6}$$

of the mean values $\langle y \rangle$ measured with right (R) and left (L) circularly polarized light, the transverse positron polarization P_y can be derived. The analyzing power Π_y is derived from the spin-dependent cross section if both the light and the positrons were completely polarized. Within one minute the positron polarization can be determined with an absolute statistical error of about 0.01. The absolute calibration is performed with dedicated measurements of the rise-time τ using the relation:

$$\frac{\tau}{\tau_{ST}} = \frac{P_{max}}{P_{ST}} \tag{A.7}$$

The uncertanty of the rise-time calibrations dominates the systematic uncertanty of the TPOL and are in the order of 3.4% for $1996/1997$.

The **Longitudinal Polarimeter (LPOL)** measures the longitudinal polarization behind the HERMES IP in the East Right straight section of the HERA positron ring. It was installed in $1995/1996$. The setup is similar to that of the TPOL: it consists of a pulsed Nd:YAG Laser

($\lambda = 532$ nm) generating polarized light with alternating helicity at each pulse. The light crosses the beam 53 m downstream of the HERMES target at an angle of about 9 mrad. Several thousand photons are backscattered when the laser pulse crosses a electron/positron bunch. Their energy sum is measured by a radiation hard calorimeter consisting of an array of four NABi(W0)$_2$ crystals of 20 cm length. For a longitudinal positron polarization the Compton cross section is indipendent of the azimuthal scattering angle, but switching the laser helicity will modify the energy spectrum. The asymmetry of the energy weighted sums of backscattered photons ζ determines the longitudinal positron polarization P_z:

$$A = \frac{\zeta_L - \zeta_R}{\zeta_L + \zeta_R} \sim P_z \Pi_z \tag{A.8}$$

Again, Π_z is the analyzing power, i.e. the Compton cross section asymmetry for the case of fully polarized laser light and positrons, folded with the response function $r(E_\gamma)$ (efficiency) of the calorimeter. The largest systematic uncertanty comes from the knowledge of the response function which had been determinded correctly only after 1998. For the years 1999 and 2000 the fractional systematic uncertanty of the LPOL was 1.6%. From 1996 to 1998 the systematic error was larger, $\delta P_z/P_z \simeq 4\%$, mainly arising from the fact that the absolute calibration was performed with rise time measurements. A detailed description of the setup and the performance of the LPOL can be found in ref [125].

List of Figures

List of Tables

Bibliography

[1] E.D.Bloom et al., *High Energy Inelastic e - p Scattering at* 6° *and* 10°, Phys. Rev. Lett. **23** (1969) $930 - 934$.

[2] H. Fritzsch and M. Gell-Mann, in *Proceedings of the XVI Conference on High-Energy Physics*, Chicago, 1972 (J.D. Jackson, A. Roberts, eds.), **hep-ph/0208010**.

[3] G. 't Hooft, in *High Energy Physics*, ed. A.Zichici (Editrice Compositori, Bologna, 1976); S.Mandelstam, Phys.Rept. **C23,** (1976) 245.

[4] G. 't Hooft, Nucl.Phys.**B190** (1981) 455.

[5] J.Ambjorn and P.Oleson, Nucl.Phys.**B170** (1980) 265.

[6] D.I.Diakonov and V.Yu.Petrov, Nucl.Phys.**B245,** (1984) 259.

[7] G.K.Savvidy, Phys.Lett. **B71,** (1977) 133.

[8] M.Creutz, Phys. Rev. **D21** (1980) 2308.

[9] P.Cea and L.Cosmai, Phys.Rev.**D43,** (1991) 620; H.D.Trottier and R.M.Woloshyn, Phys.Rev.Lett. **70,** (1993) 2053.

[10] J.W.Negele, **hep-lat/9804017**.

[11] R.Hagedorn, Nuovo Cim Suppl.**3** (1965) 147.

[12] N.Cabibbo and G.Parisi, Phys Lett.**B59** (1975) 67.

[13] D.Bailin and A.Love Phys Rep. **107** (1984) 325.

[14] R.Rapp et al., Phys Rev. Lett.**81** (1998) 53.

[15] N.Stergioulas, Living Rev. Relativity **6**, (2003), 3 and references therein.

[16] I.Bombaci,I.Parenti and I.Vidana, Astr.Journ. **614** (2004), L.Lindbum and B.J Owen, Phys. Rev. **D65** 063006.

[17] ALICE Collaboration Reports.

[18] The STAR Collaboration, **nucl-ex/0501009**.

[19] B. Friman, W. Nörenberg, and V.D. Toneev, Eur. Phys. J.**A3** (1998) 165.

[20] W. Cassing and E.L. Bratkovskaya, '*Hadronic and electromagnetic probes of hot and dense nuclear matter*', Phys. Rep. **308** (1999) 65.

[21] Yu.B.Ivanov, V.N.Russkikh, and V.D.Toneev, Phys.Rev. **C73** (2006) 044904.

[22] M. Gazdzicki and M.I. Gorenstein, Acta Phys. Polon. **B30** (1999) 2705.

[23] P. Braun-Munzinger, J. Cleymans, H. Oeschler, and K. Redlich, Nucl. Phys. **A697** (2002) 902 .

[24] M.Gazdzicki et al., (NA49 Collaboration) J. Phys. **G30** (2004) S701.

[25] M.Asakawa and K.Yazaki, Nucl. Phys.**A504** (1989) 668 .

[26] Z. Fodor and S.D. Katz, JHEP **203** (2002) 14; JHEP **404** (2004) 50.

[27] M.Stephanov, K.Rajagopal and E.Shuryak, Phys.Rev. **D60** (1999) 114028.

[28] FAIR *An International Accelerator Facility for Beams of Ions and Antiprotons*, http://www.gsi.de/fair/

[29] N.Antoniou et al., CERN-SPSC-2006-001, CERN-SPSC-P-329 (Letter of Intent of NA49-future collaboration).

[30] A.Cho, Science **312** (2006) 190.

[31] D.H.Perkins, *Introduction to high Energy Physics*, 1987.

[32] L.G.Hyman et al., *Measurement of the* Λ^0 *Mass*, Phys. Rev. **D5** (1972) 1063.

[33] B.Bhowmik and D.P.Goyal, Nuovo Cimento **28** (1963) 1494.

[34] P.Schmidt, Phys. Rev. **140** (1965) $B1328$.

[35] G.W.London et al, Phys. Rev. **143** (1966) 1034.

[36] C.Mayeur, E.Tompa and J.Wichens, Universit Libre de Bruxelles Bulletin **32** (1967).

[37] C.Baltay et al, Phys. Rev. **140** (1965) $B1027$.

[38] C.Y.Chien et al, Phys. Rev. **152** (1966) 1171.

[39] J.Badier et al, Phys. Lett. **25B** (1967) 152.

[40] P.F.Schultz et al, Phys. Rev. **168** (1968) 1509.

[41] G.S.Abrams et al, Phys. Rev. **175** (1968) 1967.

[42] E.P.Hartouni et al, *Precise Measurement of the* Λ^0 *and* $\overline{\Lambda}^0$ *Masses and a Test of CPT Invariance*, Phys. Rev. Lett. **72** (1994) 1322.

[43] G.Poulard et al, *New measurement of the* Λ *lifetime*, Phys. Lett. **46B** (1973) 135.

[44] Particle Data Grup, Rev. Mod. Phys., **45**, Part II (1973).

[45] E.F.Clayton et al, *A high-statistics determination of the* Λ *mean lifetime*, Nucl. Phys. **B95** (1975) 130.

[46] G.Zech et al, *A measurement of the lifetime of the* Ξ^0 *and* Λ *hyperons*, Nucl. Phys. **B124** (1977) 413.

[47] J. Phys. **G33** (2006).

[48] F.S.Crawford et al, Phys. Rev. Lett. **2** (1959) 266.

[49] C.Baltay et al, *Precise Measurement of the Lifetime and Decay Branching Ratio of the* Λ^0 *Hyperon*, Phys. Rev. **D4** (1971) 670.

[50] M.Chretien et al, *Improved Determination of the Neutral Decay Branching Ratio of the* K_1^0 *Meson and the* Λ^0 *Hyperon*, Phys. Rev. **131** (1963) 2208.

[51] J.L.Brown et al, Phys. Rev. **130** (1963) 769.

[52] P.Schmidt, *Precise Hyperon Masses*, Phys. Rev. **140B** (1965) 1328.

[53] M.H.L.S.Wang, *Precise measurement of the* Σ^0 *mass*, Phys. Rev. **D56** (1997) 2544.

[54] F.Didak et al., *Measurement of the* Σ^0 *lifetime*, Nucl. Phys. **B118** (1977) $1-24$.

[55] P.C.Petersen et al., *Measurement of the* Σ^0-Λ *Transition Magnetic Moment*, Phys. Rev. Lett. **57** (1986) 949.

[56] T.Devlin et al., *On Primakoff production of* Σ^0 *hyperon*, Phys. Rev. **D34** (1986) 1626.

[57] J. Colas et al, Nucl. Phys. **B91** (1975) 253.

[58] Feinberg et al, Phys. Rev. **109** (1958) 1019.

[59] R.P.Ely et al., *Spin of* Y_1, Phys. Rev. Lett. **7** (1961) 461.

[60] M.Baubillier et al., *The reactions* $K^-p \rightarrow \pi^\pm\Sigma(1835)^\pm$ *at* 8.25 *GeV/c*, Z. Phys. **C23** (1984) 213.

[61] CLAS Collaboration, Phys. Rev. **C71** (2005) 054609.

[62] Molchanov et al., Phys. Lett. **B590** (2004) 161.

[63] Arik et al., Phys. Rev. Lett. **38** (1977) 1000.

[64] H.Schneider, *Mass and decay parameters of the* Ξ^- *particles*, Phys. Lett. **4** (1963) 360.

[65] F.A.Dibianca and R.J.Endorf, *Study of the* Ξ^- *and* Ω^- *production from* K^-n *and* K^-p *interactions at* 4.93 *GeV/c*, Nucl. Phys. **B98** (1975) $137-150$.

[66] R.J.Hemingway et al., Nucl. Phys. **B142** (1978) 205.

[67] J.C.Collins, *Light-cone variables, rapidity and all that*, **hep-ph/9705393** (1997).

[68] J.D.Bjorken and E.A.Paschos, *Inelastic Electron-Proton and* γ*-Proton Scattering and the Structure of the Nucleon*, Phys.Rev. **185** (1969) $1975-1982$.

[69] R.P.Feynman, *Very high-energy collisions of hadrons*, Phys. Rev. Lett. 23 (1969), $1415-1417$.

[70] E.D.Bloom et al., *Recent Results in Inelastic Electron Scattering*, Presented at the XV International Conference on High Energy Physocs, Kiev, URSS (Aug. 26 - Sep 4, 1970).

[71] J.Callan, C.G. and D.J.Gross, *High Energy electroproduction and the constitution of the electric current*, Phys. Rev. Lett. **22** (1969) $156 - 159$.

[72] V.N.Gribov and L.N.Lipatov, *Deep inelastic ep scattering in perturbation theory*, Sov. J. Nucl. Phys. **15** (1972) $438 - 450$.

[73] L.N.Lipatov, *The parton model and perturbation theory*, Sov. J. Nucl. Phys. **20** (1975) $94 - 102$.

[74] G.Altarelli and G.Parisi, *Asymptotic freedom in parton language*, Nucl. Phys. **B126** (1977) $298 - 318$.

[75] Y.L.Dokshitzer, *Calculation of the structure functions for deep inelastic scattering and e^+e^- annihilation by perturbative theory in quantum chromodynamics*, Sov. Phys. JETPZ. **46** (1977), $641 - 653$.

[76] A. Hillenbrand, *Measurement and Simulation of the Fragmentation Process at HERMES*, Ph.D. thesis, FRIEDRICH-ALEXANDER-Universitaet Erlangen (Germany), September 2005.

[77] B. Maiheu, *Hadronization in electron - proton scattering at HERMES*, Ph.D. thesis, University of Ghent, March 2006.

[78] T.Sjostrand, P.Eden, C.Friberg, L.Lonnblad, G.Miu, S.Mrenna, E.Norrbin, PYTHIA 6.2 Physics and Manual, Computer Physics Commun. **135** (2001) 238.

[79] R.Brun, R.Hagelberg, M.Hansroul and J.C.Lassalle, *GEANT: Simulation Program for Particle Physics Experiments. User Guide and Reference Manual*, (1978), **CERN-DD-78-2-REV**.

[80] S.Weinzierl, *Introduction to Monte Carlo Methods*, **hep-ph/0006269** (2000).

[81] B.Andersson, G.Gustafson, T. Siöstrand, *Baryon Production in Jet Fragmentation and Υ Decay*, Phys. Scripta **32** (1985) $574 - 580$.

[82] P.Edn and G.Gustafson, *Baryon Production in String Fragmentation Picture*, Z. Phys. **C75** (1997), $41 - 49$.

[83] B.Andersson, G.Gustafson, B. Söderberg, *A General Model for Jet Fragmentation*, Z. Phys. **C20** (1983) 317.

[84] R.D.Field and R.P.Feynman, *A Parametrization of the properties of quark jets*, Nucl. Phys. B136 (1978), $1 - 76$.

[85] P.Hoyer, P.Osland, H.G.Sander, T.F.Walsh and P.M.Zerwas, *Quantum chromodynamics and jets in e^+e^-*, Nucl. Phys. **B161** (1979) $349 - 372$.

[86] A.Ali, J.G.Körner, G.Kramer and J.Willrodt, *Heavy quarks in e^+e^- annihilation*, Nucl. Phys. **B168** (1980) 409.

[87] B.R.Webber, *A QCD model for jet fragmentation including soft gluon interference*, Nucl. Phys. **B238** (1984) $492 - 528$.

[88] G.Marchesini and B.R.Webber, *Simulation of QCD jets including soft gluon interference*, Nucl. Phys. **B238** (1984) $1-29$.

[89] G.Corcella et al., *HERWIG6: an eent generator for hadron emission reactions with interfering gluons (including supersymmetric processes)*, JHEP **01** (2001) $010:1-96$.

[90] T.D.Gottschalk and D.A.Morris, *A new model for hadronization and e^+e^- annihilation*, Nucl. Phys. **B288** (1987), $729-781$.

[91] G.A.Schuler and T.Sjöstrand, *Toward a complete description of high-energy photoproduction*, Phys. Lett. **B300** (1993) 169.

[92] C.Friberg and T.Sjöstrand, *Total Cross Section and Event Properties from Real to Virtual Photons*, J. High Energy Phys. (2000), $0009:010$.

[93] E.Fermi, Z. Phys. 29 (1924), 315.

[94] C.Weizsäcker, *ibid* **88** (1934) 612.

[95] E.Williams, Phys.Rev.**45** (1934) 729.

[96] A.Sokolov and I.Ternov, Sov. Phys. Doklady **8** (1964) 1203.

[97] K.Ackerstaff et al., The HERMES Collaboration, *The HERMES Spectrometer*, DESY $98-057$, Nucl. Instr. Meth. **A417** (1998) 230.

[98] A.Nass et al., *The HERMES Polarized Atomic Beam Source*, Nucl. Instr. Meth. **A505/3** (2003) 633.

[99] W.Gerlack, O.Stern, Z. Physik, **8** (1921) 110.

[100] C.Baumgarten et al., *A gas analyser for the internal polarized target of the HERMES experiment*, Nucl. Instr. Meth. **A508** (2003) $268-275$.

[101] C.Baumgarten et al., *An atomic beam polarimeter to measure the nuclear polarization in the HERMES gaseous polarized hydrogen and deuterium target*, Nucl. Instr. Meth. **A482** (2002) $606-618$.

[102] A.Airapetian et al., The HERMES Collaboration, *The HERMES polarized hydrogen and deuterium gas target in the HERA electron storage ring*, Nucl. Instr. Meth. **A540** (2004) $68-101$.

[103] W.Wang, *Improvements of the HERMES Transverse Polarized Hydrogen Target and Calculations of the Sextupole Magnet*, PhD thesis, China Institute of Atomic Energy, (2004), HERMES $04-056$.

[104] P.Tait, *Beam Induced Depolarisation at the HERMES Transversely Polarised Hydrogen Target*, PhD Thesis, Friedrich-Alexander-Universitaet Erlangen-Nurimberg, 2006, in preparation

[105] M.Duren, *The HERMES experiment: from the design to the first results*, Habilitation thesis, Friedrich-Alexander-Universitaet Erlangen-Nurberg, 1995, HERMES $95-002$.

[106] J.T.Brack et al., *The HERMES forward tracking chambers: construction, operation and aging effects*, Nucl. Instr. Meth. **A469** (2001) $47-54$.

[107] S.Bernreuther, *The HERMES Back Drift Chambers*, Nucl. Instr. Meth. **A416** (1998) $45-58$.

[108] A.Andreev et al., *Multiwire Proportional Chambers in the HERMES experiment*, Nucl. Instr. Meth. **A465** (2001) $482-497$.

[109] M.G. van Beuzekom et al., *First experience with the HERMES silicon detector*, Nucl. Instr. Meth. **A461** (2001) $247-250$.

[110] W.Wander, *Rekonstruktion hochergetischer Streuereignisse im HERMES Experiment*, Dissertation, Friedrich-Alexander Universitaet Erlangen-Nurnberg (1996).

[111] F.Menden, MSc. Thesis *Measurement of the Valence Quark Spin Distributions of the Nucleon Using Deep Inelastic Scattering at HERMES*, HERMES internal note 98/001.

[112] T.Benisch et al., *The luminosity monitor of the HERMES experiment at DESY*, Nucl. Instr. Meth. **A471** (2001) 314.

[113] T.Ernst, PhD Thesis, University of Freiburg (1985).

[114] CERN Programming Techniques Group, ADAMO-*Entity-Relationship Programming System*, 1993, User Guide, Version **3.3**.

[115] C.Hadjidakis and D.Hasch, *Total cross section for hard exclusive π^+ prodution*, HERMES internal report.

[116] K.Abe et al., *Inclusive photoproduction of neutral strange particles at 20 GeV*, Phys. Rev. **D29** (1984) 1877.

[117] K.Abe et al., *Inclusive photoproduction of strange baryons at 20 GeV*, Phys. Rev. **D32** (1985) 2869.

[118] V.N.Gribov, ZhETF **41** (1961) 667.

[119] G.F.Chew and S.C.Frautschi, Phys.Rev.Lett.**7** (1961) 394.
R. Blankenbecler and M. Goldberger, Phys. Rev. **126** (1962) 766.

[120] T.Regge, NCA **14** (1959) 951.

[121] G.S.Bali, V.Bornyakov, M.Müller-Preußker, and K.Schilling, Phys.Rev.**D54,** (1996) 2863 .

[122] D.P.Barber et al., *The HERA Polarimeter and the first observation of electron spin polarization at HERA*, Nucl. Instr. Meth. **A329** (1993) 79.

[123] B.Tipton, *Measurement of Polarized Parton Distributions With Spin-dependent Deep Inelastic Scattering*, PhD Thesis, Massachusetts Institute of Technology, Boston (1999)

[124] M.Beckmann, *Extraction of Polarized Quark Distributions of the Nucleon from Deep Inelastic Scattering at the HERMES Experiment*, Dissertation, Albert-Ludwigs-Universitaet Freiburg (2000).

[125] M.Beckmann et al., *The Longitudinal Polarimeter at HERA*, Nucl. Instr. Meth. **A479/2-3** (2002) $334-348$.

[126] M.Baker, *Proc. Confinement III*, TJ Lab.(1998).

[127] T.Banks, R.Myerson, and J.Kogut, Nucl.Phys. **B129,** (1977) 493 .

[128] P.Becher and H.Joos, Z.Phys.**C15** (1982) 343 .

[129] W.Deconinck and F.Giordano, *Analysis report: the search for the* Ξ^{--}, HERMES Internal Report $04-030$ (2004).

[130] T.A.DeGrand and D.Toussaint, Phys.Rev.D **22,** (1980) 2478.

[131] L.Del Debbio, M.Faber, J.Giedt, J.Greensite, and S.Olejnik, **hep-lat/9801027** and references therein.

[132] A.DiGiacomo, **hep-th/9809047**.

[133] H.G.Dosch, Proc.Confinement III, TJ Lab. (1998).

[134] Z.F.Ezawa and A.Iwazaki, Phys.Rev.D **25,** (1982) 2681.

[135] A.S.Kronfeld, G.Schierholz, U.J.Wiese, Nucl.Phys.**B293** (1987) 461.

[136] F.X.Lee, R.M.Woloshyn, and H.D.Trottier, Phys.Rev. **D53** (1996) 1532.

[137] J.Maldacena, Adv. Theor. Math. Phys. **2** (1998) 231, **hep-th/9711200**; O.Aharony, S.Gubser, J.Maldacena, H.Ooguri and Y.Oz, Phys.Rept. **323** (2000) 183, **hep-th/9905111**.

[138] C.Michael, Proc.Confinement III, TJ Lab. (1998), **hep-lat/9809211**.

[139] C.Morningstar, Proc.Confinement III, TJ Lab. (1998), **hep-lat/9809305**; J.E.Paton, *ibid.*; T.JAllen, *ibid.*.

[140] M.Polikarpov, Proc.Confinement III, TJ Lab., (1998).

[141] A.M.Polyakov, JETP Lett.**20** (1974) 194; G. 't Hooft, Nucl.Phys.**B79** (1974) 276.

[142] N.Seiberg and E.Witten, Nucl.Phys. **B426** (1994) 19.

[143] T.Suzuki, Prog.Theor.Phys.**80** (1988) 929.

[144] T.Suzuki, Prog.Theor.Phys.Suppl.**122,** (1996) 75.

[145] $T\chi L$ collaboration: G.S.Bali et al., in preparation.

[146] M.Zach, M.Faber, W.Kainz and P.Skala, Phys.Lett.**B358,** (1995) 325.